MICROSTRUCTURE AND FRACTURE TOUGHNESS OF THE IN-SITU NiAl-Ni_3Al INTERMETALLIC COMPOSITES

by
Qian Gao

A thesis
presented to the University of Waterloo
in fulfilment of the
thesis requirement for the degree of

Doctor of Philosophy

in

Mechanical Engineering

Waterloo, Ontario, Canada, 1997

The University of Waterloo requires the signatures of all persons using or photocopying this thesis. Please sign below, and give address and date.

ABSTRACT

An overview of the toughening mechanisms in the intermetallic-base in-situ composites is presented. Based on the literature review and preliminary research, the two phase ($\beta + \gamma'$) region of Ni-Al system was chosen as a model in-situ composite to study fracture toughness of the in-situ NiAl-Ni_3Al intermetallic composites and explore the fracture toughening mechanisms in these intermetallic materials.

The composition ranges investigated were 25-35 at.% Al for both as-solidified and as-heat-treated composites. To evaluate fracture toughness, a three point bending of Chevron-notched beam (*CNB*) specimens were used. The values of fracture toughness were calculated either directly from the maximum load at unstable crack propagation or by using a modified *J*-integral approach. Compressive testing was also carried out to obtain yield strength of tested in-situ intermetallic composites. Micromechanical properties of individual phases were probed by Vickers microhardness testing. The relationship between fracture toughness (K_{Ivm} , K_{Ivc}) and volume fraction of second phase V_d, in the following form: $K_{Ivc}=f(V_d^n)$ has been established. Also, boron-doped (0.2 and 0.4 at.%) Ni_3Al was fabricated. Fracture mechanisms and boron effect on fracture toughness of the Ni_3Al phase were explored.

The obtained results of fracture toughness (K_{Ivm}, K_{Ivc}) are compared with the existing models, which describe the second phase toughening mechanisms, and rule of mixtures (*ROM*). Weibull analysis is also applied for the analysis of the fracture toughness distribution of the investigated Ni_3Al/NiAl in-situ composites.

The important features of the K-Δa and J-Δa curves by a *CNB* bend test have been explored in this research. The stress intensity factor K decreases with increasing crack extension (Δa) and a PLATEAU usually appears with increasing of the crack extension only

until the critical crack extension (Δa_m), then K starts to increase with increasing crack extension, forming a very special shape which can be called "HOOP HEAD". Particularly, a critical value (J_{Ivc}) of the fracture energy for a *CNB* test can be simply calculated by a horizontal line tangent to the "HOOP HEAD".

It is shown that fracture toughness of Ni_3Al/NiAl increases with increasing volume fraction of Ni_3Al in the in-situ composites according to a general formula $K_{Ivc}=6.1+ 0.7V_d^{0.75}$ (Mpa$\sqrt{m}$) (where V_d - volume % of Ni_3Al). In some Ni_3Al/NiAl composite alloys the Ni_5Al_3 fine particles are formed (so-called "mat-like structure") which exhibits very high Vickers microhardness (≈690 kg/mm^2). The significant yield strength of =1150 kg/mm^2 in the aged $Ni_{65.9}Al_{34.1}$ in-situ composite is also attributed to this needle-like structure of Ni_5Al_3. It is worth of pointing out that a very high yield strength (σ_{YS}≈1150MPa) is combined in aged alloys with a reasonable value of fracture toughness (≈13 MPa$\sqrt{m}$). It indicates that such a new promising alloy can be yielded by an economic and simple casting method followed by a proper heat treatment as shown in this research.

The highest Weibull's modulus m = 23.8 for $Ni_{63.7}Al_{36.3}$ (≈17 vol.% Ni_3Al) indicates that this alloy is a very reliable material for engineering design even with lower fracture toughness value (K_{Im}^{W} = 8 MPa$\sqrt{m}$). The lowest Weibull's modulus m = 5.8 for $Ni_{73.2}Al_{26.8}$ (≈99 vol.% Ni_3Al) means that the fracture toughness of this alloy is highly variable and no single value for K_{Im}^{W} can be assigned easily.

ACKNOWLEDGEMENTS

It has been a great honour for me to have worked under the supervision of Professor R.A. Varin. His invaluable guidance, constant encouragement, immense patience, and friendly personality motivated me in many ways during the course of this study. It has been a rewarding experience for me working with him, and I would like to express my deepest respect and appreciation to him.

I would also like to express my appreciation to the numbers of my examining committee, Prof. Z. Wang (external examiner from University of Toronto), Prof. A. Plumtree. Prof. G. Glinka and Prof. J. Corbett for their valuable suggestions.

I am very grateful for the financial assistance obtained from the Natural Sciences and Engineering Research Council of Canada.

Special thanks to the Materials Science Group's, technical staff members, notably Hans Kamler and Norval Wilhelm for their technical assistance and constructive ideas toward a successful experimental study. I would also wish to thank my fellow grad students, especially L. Zbroniec, Q-Z Hu and J. Biglou for their assistance.

Finally, I would like to thank my Government for giving me this opportunity to study abroad. I would like to thank my dearest parents and my family for their non-ending encouragement and love. Without their support, I would have lost my way during some of my difficult times.

DEDICATION

To

my father Jinhan Gao,

my mother Suyuan Xu,

my wife Qihua,

and my daughter Chao

CONTENTS

Chapter 4

LIST OF FIGURES

LIST OF TABLES

NOMENCLATURE

a	crack length
a^*	half of the maximum crack length
a_0	initial crack length
a_1	slot length of CNB notch
B	thickness of CNB specimen
b	ligament length (uncracked length)
C	reciprocal of the degree of constraint on toughening particle
c	volume concentration of toughening particles
E	Young's modulus of composite
E'	plane strain elastic modulus of composite
G	fracture energy (strain energy release rate) of composite
h	height of process or microcrack shielding zone
J	values of the J-integral
K_c	critical stress-intensity factor of composite
K_{Ic}	plane strain fracture toughness
K_d	K_{Ic} value of ductile phase
K_m	K_{Ic} value of matrix
K_r	crack growth toughness
K_R	K-resistance curve
K_i	initiation toughness
L	bridging length (projected crack length)
$<l>$	average length of shear ligaments
m	Weibull modulus

N	slot width of chevron notch
r_p	plastic zone size
S	half of a single microcrack length
S_1	major span
S_2	minor span
S_m	average value of fracture strength of brittle matrix
u	crack opening
v_P	critical plastic value of the crack-face displacement
V	volume fraction
W	width of a specimen
Y^*	stress intensity factor coefficient
Y_m^*	the minimum value of stress-intensity-factor coefficient

Greek Symbols

γ'	$L1_2$-ordered crystal structure Ni_3Al
β	B2-ordered crystal structure NiAl
α_1	orientation of microcrack with respect to the stress axis
σ_R	residual stress
σ_{YS}	yield strength
σ_F	failure stress of toughening particles
σ_{ym}	yield stresses of matrix
σ_{yd}	yield stresses of ductile phase
$\sigma(u)$	nominal stress
σ_d	ultimate stress of ductile phase
σ_i^P	shear traction

ε_t	total dilatational strain
ε^T_{ij}	stress-free strain
ε_{fm}	effective fracture strain values of matrix
ε_{fd}	effective fracture strain values of ductile phase
γ_f	fracture strain in shear
$\delta^{1/2}$	crack opening displacement
ϕ, θ	crack deflection angle
χ	dimensionless work-of-rupture parameter
τ_f	fracture stress in shear
ν	Poisson's ratio of composite
λ	toughening ratio

Subscripts

m	matrix
ms	microcrack shielding
d	ductile second phase
b	crack bridging
bl	crack blunting
el	elastic deformation
pl	plastic deformation
l	shear ligaments
I	opening mode

CHAPTER 1

INTRODUCTION AND LITERATURE REVIEW

Structural alloys based on the ordered intermetallic compounds such as TiAl, Ti_3Al, Ni_3Al, NiAl and $MoSi_2$ have recently become potential candidate materials for several advanced high-temperature aerospace applications, primarily because of their high specific strength and stiffness which are retained at elevated temperatures exceeding 1000°C. Their structural use, however, is quite limited by low room-temperature ductility and toughness properties; in fact, most of the measured fracture strains under uniaxial tension can be as low as 1% with a fracture toughness below ≈10 MPa$\sqrt{m}$. **Table 1.1** summarizes the fracture toughness K_{Ic} of selected intermetallic alloys and composites. Obviously, most of the single phase intermetallics show low values of K_{Ic}. The low intrinsic fracture toughness of these materials has not been changed through solid solution elemental additions. A composite approach must then be considered in an effort to increase toughness [1].

These intermetallic compounds closest to commercial utilization, such as Ti_3Al, TiAl as

Table 1.1 Room temperature fracture toughness K_{Ic} of selected intermetallic alloys and composites.

Type of material	Name of material and processing technique	Crystallographic structure	Fracture toughness K_{Ic} or K_Q (MPa$\sqrt{m}$)	Refs.
Single Phase	NiAl [001] (Single crystal)	B2 (CsCl)	10	2
	NiAl [011] (Single crystal)	B2 (CsCl)	6	2
	NiAl (Power processed)	B2 (CsCl)	2.7-3.8	3
	NiAl (Extruded cast ingot)	B2 (CsCl)	5.4-5.9	4
	Ti_5Si_3	$D8_8$	2	5
	$MoSi_2$	C11b	4	6
	$MoSi_2$	C11b	4.6	7
	$Al_{66}Ti_{25}Mn_9$	$L1_2$	3.5	8
	$Al_{66}Ti_{25}Cr_9$	$L1_2$	3.5	8
	$Ti_{58}Al_{27}Nb_{15}$	DO_{19}	20	9
	Nb_3Al	A15	1.1	10
Multi-phase	NiAl+5Nb	B2 + ?	12.2-15.4	3
	NiAl+5Ti	B2 + ?	4.7-14.5	3
	Ti_5Si_3/Ti_3Al	$D8_8$+DO_{19}	12	5
	$TiAl_{52}$	$L1_0$+DO_{19}	10	11
	$TiAl_{48}$ (As-extruded)	$L1_0$+DO_{19}	15	7
	$TiAl_{48}$ (Electrode arcmelting)	$L1_0$+DO_{19}	30 (K_Q)	12
	$TiAl_{48}$/(βTi, Nb)	($L1_0$+DO_{19})+20 vol.% (βTi, Nb)	20	7
	$MoSi_2$/Nb	C11b+20 vol.% Nb	5.7	7
	$Ti_{56}Al_{24}Nb_{20}$	DO_{19}+20 vol.% β (B2)	44 (K_Q ?)	9
	$Ti_{58}Al_{27}Nb_{15}$	DO_{19}+70 vol.% β(B2)	26 (K_Q ?)	9
	Nb_3Al/Nb	A15+40 vol.%Nb	6.5	10
	NiAl/TiB_2 (Particulate)	B2+20 vol.% TiB_2	6	13
	NiAl/Al_2O_3	B2+15-25 vol.% Al_2O_3	9	14

well as Ni_3Al, are actually multi-component systems rather than single phases, with highly refined microstructures consisting of a majority strong and sometimes brittle intermetallic phase, in close association with possibly a more to increase toughness [1].

These intermetallic compounds closest to commercial utilization, such as Ti_3Al, TiAl as well as Ni_3Al, are actually multi-component systems rather than single phases, with highly refined microstructures consisting of a majority strong and sometimes brittle intermetallic phase, in close association with possibly a more ductile phase. This is similar to pearlite, the eutectoid microstructure developed between cementite, Fe_3C, and ferrite, a microstructure common in many plain carbon steels and known for its toughness. Multiphase systems such as these can be considered composites, since the two constituent phases usually have differing moduli, thermal expansion and ductility. This realization leads to define the term COMPOSITE, which in the present context will not be straightforward. For our purposes, a composite will be defined as:

any material with multi-component structure for which the phases are manipulated in geometry or volume fraction so as to obtain a desired mix of mechanical properties [1].

Under this broad definition, many practical engineering materials such as titanium and nickel alloys would be defined as composites. We must make this definition, because for intermetallic based materials to become useful, their properties, especially toughness, will need to be enhanced through the proper manipulation of either artificially manufactured composites

in which particles, whiskers or fibres are added, or through natural or in-situ composites in which the reinforcement can be introduced via either solidification or solid state precipitation. Provided that the phase diagram is well understood, directional solidification and/or various thermomechanical treatments can be used to separate and align the reinforcement into the desired geometry. An in-situ intermetallic composite is then obtained. Additional advantage is that these composites are thermodynamically stable. The in-situ intermetallic composites are limited in their constituents by the phase diagrams, which may limit reinforcement volume fraction, chemistry and morphology [1].

Increases in toughness observed in many multiphase intermetallic composites, including the in-situ ones, are shown in **Table 1.1**. As mentioned by Ashby [15], a value of K_{Ic}≈20 MPa√m is often quoted as a minimum for conventional design. Also, Jackson et al. [16] stated that a working hypothesis has been offered that once a material exceeds a threshold of ≈20 MPa√m. toughness in the make-and-assemble stages is not a major issue. This threshold may eventually be relaxed as further experience is gained. Therefore, an important goal is optimising the structure of many intermetallic alloys to obtain the values of K_{Ic} at least about 20 MPa√m, if not better. However, in order to achieve this objective a clear understanding of underlying physical mechanisms of second phase toughening and their description in terms of micromechanical models are urgently needed.

1.1 Mechanisms and Micro-Mechanical Modelling of Toughness Improvements in the In-Situ Intermetallic Composites

An overview of the second phase toughening in the in-situ intermetallic composites is presented. The existing models of the second phase toughening of brittle matrix composites such as crack-tip blunting, crack trapping, crack bridging and so on are discussed with the emphasis on their application for the in-situ intermetallic composites. A comparison of available experimental data on fracture toughness of the in-situ intermetallic composites with the theoretical models of fracture toughness enhancement by the second phase toughening is presented.

As discussed before, an in-situ composite is any alloy with multi-component structure for which the phases are separated ***naturally*** according to the pertinent phase diagram by solidification, precipitation and/or thermomechanical treatment. In the in-situ composites, macrostructural toughening usually involves the incorporation of a ductile second phase in a brittle matrix. The purpose of the ductile phase is to interact with the progression of cracks through the matrix phase. The ductile second phase can take the form of isolated particles, interpenetrating networks or continuous phases such as lamellae or fibres. While the degree of toughening is generally dependent on the volume fraction and morphology of the second phase, the actual characteristics of the ductile phase that will generate optimum toughness have not

yet been adequately established or modelled. The objective of this section is to present the state-of-the-art in the understanding of relationships between microstructure, toughening mechanism, and fracture resistance. To develop microstructure/toughness relationships, important micromechanical variables affecting fracture resistance are elucidated using micromechanical models.

In general, toughening mechanisms in the in-situ intermetallic composites can be considered either as intrinsic or extrinsic [17-20]. The intrinsic mechanisms, which mainly include crack-tip blunting by a ductile phase [18, 21-27], crack-front trapping [28-30], microcracking renucleation [29, 31-32] and interface delamination (debonding) [32-37], as shown in **Figures 1.1a**, **b**, **c** and **d**, originate from properties of the constituents [23] and improve the inherent fracture toughness of the material, thereafter enhance the **initiation toughness**, K_i, as shown in **Figure 1.2**. The term initiation toughness K_i refers to the critical stress intensity at the onset of stable crack growth; it is customarily referred to as the K_{Ic} value when the plane strain condition prevails [17-18, 20]. For the purpose of this work the K_i parameter will be later in the text designated K_{Ic} assuming that a valid, plane strain test is performed to assess fracture toughness of the in-situ composite. The extrinsic mechanisms, which mainly include crack bridging by a ductile phase [38-47], process zone toughening [48, 49], shear ligament toughening [18, 20, 23, 50-51], crack deflection [18, 36, 52-55] and microcrack shielding [18, 23, 48, 49] as shown in **Figures 1.1e**, **f**, **g**, **h** and **i**, impede crack opening in the material and improve fracture resistance by lowering the stress intensity levels in the wake of crack-tip, thereafter affect the **crack growth toughness**, K_r, by inducing a rising

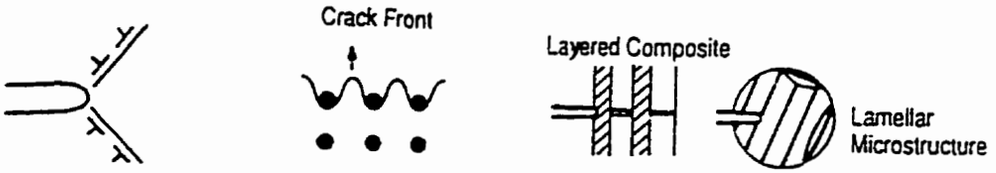

(a) *Crack-Tip Blunting*

(b) *Crack Trapping*

(c) *Microcrack Renucleation*

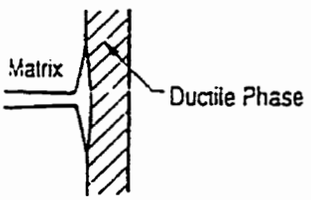

(d) *Interface Delamination*

(e) *Crack Bridging*

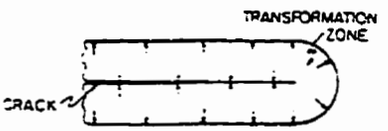

(f) *Process Zone Toughening*

(g) *Shear Ligament Toughening*

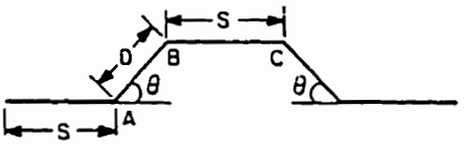

(h) *Crack Deflection*

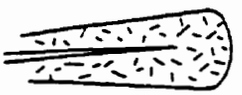

(i) *Microcrack Shielding*

Figure 1.1 Schematic illustration of the possible intrinsic (a to d) and extrinsic (e to i) mechanisms for enhancing the toughness of brittle materials through the addition of a ductile phase [17, 32, 42].

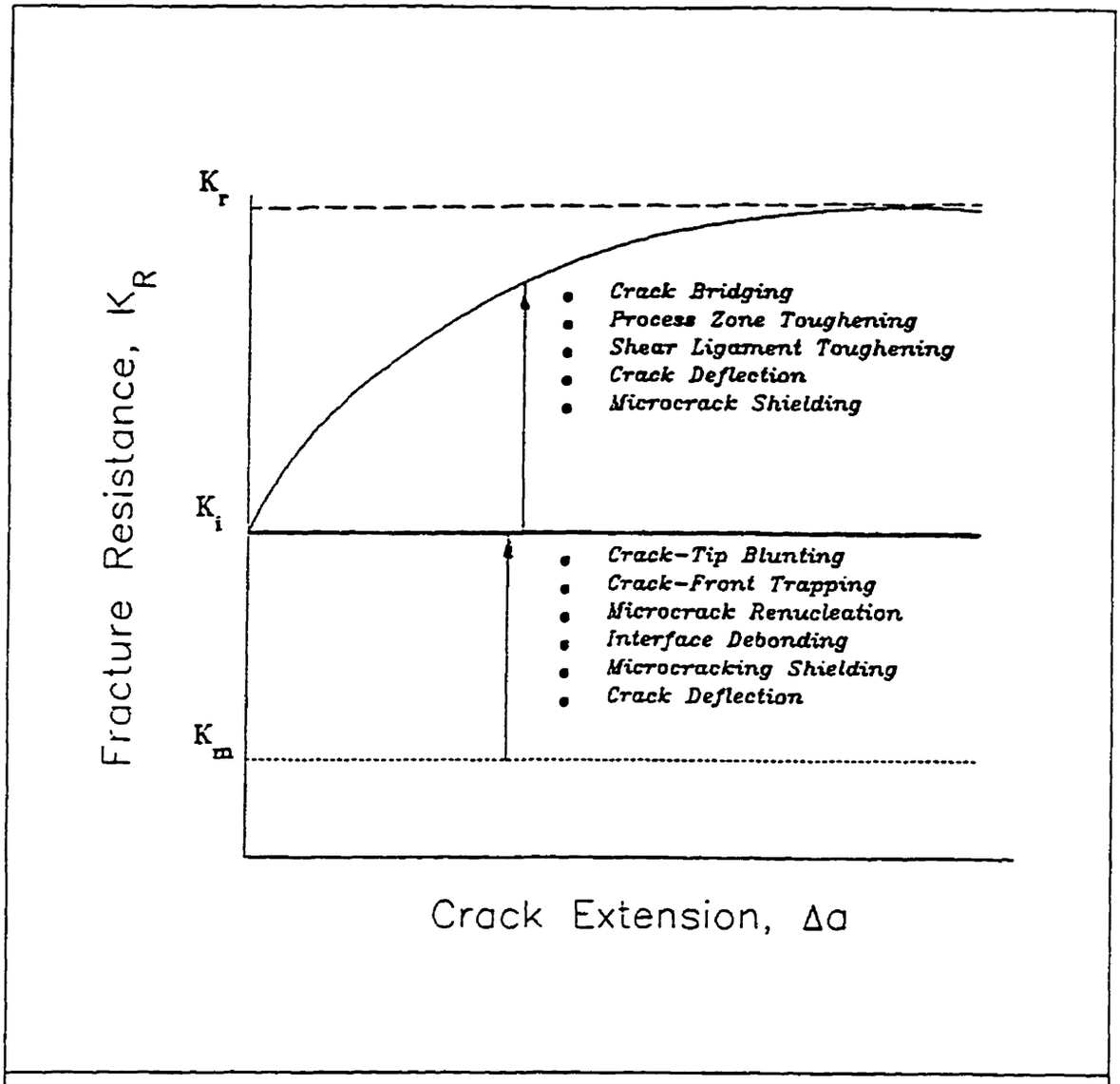

Figure 1.2 Relationships between toughening mechanisms and fracture resistance [17, 29, 32].

crack-growth resistance curve as shown by a rising solid line in **Figure 1.2.** The term crack growth toughness K_r is defined as the maximum value of the K-resistance, K_R, curve at the onset of unstable fracture.

The K_R curve for the single-phase matrix is a lower dotted line with a zero slope (as shown

in **Figure 1.2**). In this thesis, K_m designates the fracture toughness K_{Ic} of the matrix. The two-phase intermetallic alloys and composites shows higher toughness than the single-phase matrix because both the initiation and crack growth toughness can be enhanced by the presence of a ductile phase in the microstructure. This fact is supported by many experiments. A typical example was shown by Rigney et al. [56] from the experiments on Nb_5Si_3/Nb particulate composites compared with the monolithic Nb_5Si_3 (**Figure 1.3**). The mechanisms by which toughening is achieved and the amount of enhancement, however, vary with the morphology, volume fraction, size, and work-of-fracture of the ductile phase, as well as properties of the interface. The various processes by which toughness can be imparted in brittle intermetallic via the use of a ductile phase are elaborated and modelled as follows.

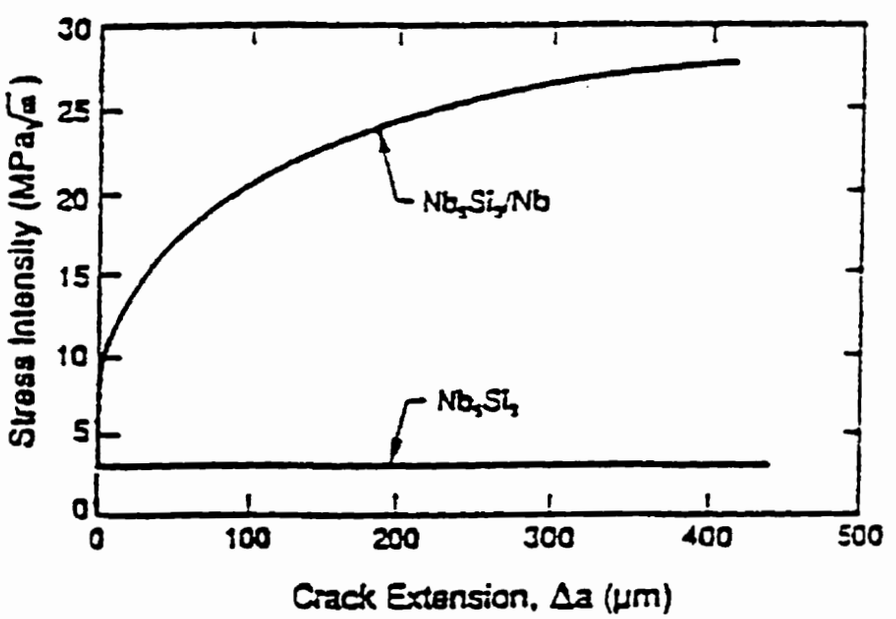

Figure 1.3 Comparison of K-resistance curves of Nb_5Si_3/Nb in-situ composite and the matrix Ni_5Si_3 [17, 56].

1.1.1 Superposition of Toughening Mechanisms

It is interesting to be noted in **Figure 1.2** that *intrinsic* toughening mechanism affect the initiation fracture toughness only, i.e. K_{Ic} value [18]. This effect is expressed by Chan [18] by so-called overall toughening ratio [18]:

$$\lambda = \frac{K_i (\equiv K_\infty \equiv K_{applied})}{K_m} \tag{1.1}$$

In addition, *extrinsic* toughening mechanisms affect the resistance curve behaviour, e.g. K_r in **Figure 1.2**. They should not have impact on K_{Ic} and J_{Ic} [18]. However, in some cases such extrinsic mechanisms as microcrack shielding and crack deflection can also lead to increase in the initiation toughness (K_{Ic}) value, depending on whether or not a deflected crack tip and shielding microcrack exist prior to crack growth [18].

The main intrinsic and extrinsic mechanisms and their models of ductile dispersion toughening in-situ composites have been discussed separately in **Sections 1.1.2** and **1.1.3**, respectively. In fact, a few mechanisms (usually, not all of the above mechanisms as shown in **Figure 1.1**) will always occur in the same material. However, the method to predict the combined effects of multiple toughening mechanisms is still not well established so far. Some selected work on this topic will be presented as follows.

Simple Multiplication

According to Chan [18] the overall toughening ratio for K_{Ic} can be calculated theoretically from the following equation (*Eq.(1.1)*) [18]:

$$\lambda = \lambda_d \bullet \lambda_{ms} \bullet \lambda_b \qquad (1.2)$$

where λ_d, λ_{ms} and λ_b are toughening ratios for crack deflection, microcrack shielding and crack blunting, respectively. Notice that the summation (multiplication) above is *only* for those λ ratios which increase K_{Ic}.

Soboyejo et al. [7, 54] also proposed that the principle of superposition can be applied to predict the toughening combinations of crack bridging and crack deflection by a simple multiplication of the toughening ratios:

$$K_{Ic} = \lambda_b \lambda_d K_m \qquad (1.3)$$

where λ_b and λ_d are toughening ratios of crack bridging and deflection, respectively. However, *Eq.(1.3)* seems to be erroneous because crack bridging, a typical extrinsic mechanism, can not affect K_{Ic}.

Simple Addition

Another superposition model was suggested by Enoki and Kishi [57]. They [57] considered microfracture process for both fully lamellar and duplex TiAl and found

microcracks and subsequent shear ligament formation from the observations and acoustic emission studies. Instead of a simple multiplication such as in *Eq.(1.2)*, they consider the effects of microcrack shielding and shear ligament mechanisms as a simple addition [57]

$$K_{Ic} = K_m + \Delta K_c + \Delta K_l \qquad (1.4)$$

where ΔK_c and ΔK_l are the contributions of microcracking and shear ligaments, respectively. But these two are *extrinsic* and are responsible for K_R curve behaviour. Therefore, the correct toughness in *Eq.(1.4)* is K_r, rather than K_{Ic}. Simple addition is good for *intrinsic* toughening mechanisms plus "microcrack shielding" and "deflection" eventually but *extrinsic* toughening cannot be additive to K_m as to get K_{Ic}.

So far, there is no standard method available for synthesizing the toughening combinations of several mechanisms in an in-situ composite.

1.1.2 Intrinsic Mechanisms

As mentioned above, this type of ductile-phase toughening is expected to improve the initial toughness K_i of in-situ composites when crack extension commences. It is possible to categorize the typical mechanisms of intrinsic toughening into several distinct classes as follows.

Crack-Tip Blunting

Crack-tip blunting as shown in **Figure 1.1a** occurs when the propagation of a crack tip is

impeded as it intersects a ductile particle with a well-bonded interface. Extensive localized plastic deformation by dislocation movement of the second phase causes the stresses at the crack tip to relax sufficiently to blunt the crack and in the ideal case will prevent the crack from propagating further. The crack tip is shielded from the external load. A second phase material with a low yield strength will tend to maximize this effect [17-18, 21-24]. Toughness enhancement resulting form crack-tip blunting by a ductile phase has been modelled by Chan [17-18, 21-23] using the Hutchinson, Rice and Rosengren (HRR) crack tip field [25-27]. In the HRR-field, the near-tip strains are quite large and it is assumed that the yield stress and effective strain of the two-phase microstructure are related to the corresponding properties of the constituent phases according to the rule of mixtures (for a detailed description, see **Appendix A**). Therefore, initiation of crack growth in ductile alloys can generally be considered in terms of a critical strain criterion, which assumes that fracture occurs when the strain at a characteristic distance from the crack tip exceeds a critical value.

To model this mechanism, the initiation fracture toughness, K_i, of a two-phase microstructure consisting of a brittle matrix (m), and a ductile phase (d), can be given by [17-18, 21-23]:

$$\lambda_b = \frac{K_i}{K_m} = [1 + V_d(\Sigma - 1)]^{(n-1)/2n} [1 + V_d(\Lambda - 1)]^{(n+1)/2n} [\frac{E}{E_m}]^{(n+1)/2n} \quad \textbf{(1.5)}$$

with

$$\Sigma = \sigma_{yd} / \sigma_{ym} \quad \textbf{(1.6)}$$

$$\Lambda = \varepsilon_{fd} / \varepsilon_{fm} \quad \textbf{(1.7)}$$

where K_m is the K_{Ic} value of the matrix, V_d is the volume fraction of ductile phase, ε_{fm} and ε_{fd} are effective fracture strain values of matrix and ductile phases, σ_{ym} and σ_{yd} are their yield stresses, n is the inverse of the strain hardening exponent, E and E_m are elastic moduli of the composite and matrix, respectively.

It is interesting to be noted that the initial fracture toughness K_i increases with the volume fraction of ductile phase V_d generally in a nonlinear fashion for this mechanism. Furthermore, this model remains valid for both continuous or discontinuous ductile phases [18].

As a typical example in experimental research on this mechanism, Chan [18, 23] has identified crack-tip blunting from the toughening mechanisms in the Ti-24Al-11Nb in-situ composites as shown in **Figure 1.4**.

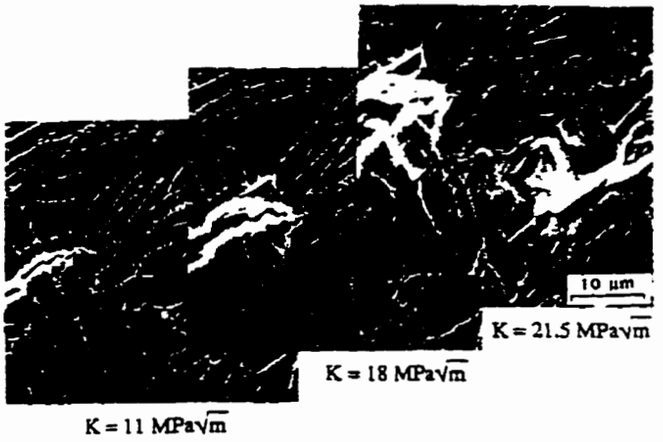

Figure 1.4 Composite *in situ* scanning electron micrographs show that the near-tip fracture process in the coarse basketweave microstructure at 25°C is characterized by blunting of the tips of main crack and the microcracks by continuous ductile phase (light phase, β-Ti). The volume fraction of is 39% [23].

Crack-Front Trapping

Crack-front trapping occurs when the crack front interacts with higher toughness reinforcements, requiring the crack to penetrate between the reinforcements. It is most pertinent when the brittle phase is continuous and the ductile particles take the form of rods or spheroids [17, 28]. When a straight crack intersects a row of tough particles, part of the crack front can bow out and loop around the particles as shown in **Figure 1.1b**. The increased crack curvature increases the local stress intensity factor and can lead to fracture of the ductile particles without the formation of bridging particles in the crack wake if the ratio of ductile-phase toughness (K_d) to matrix toughness (K_m) is less than three [28]. If K_d is considerably greater than K_m, intact particles are left in the crack wake by the looping process, which can lead to an additional toughening by crack bridging. The corresponding initiation toughness, K_i, attainable from the crack trapping mechanism, is given by [17, 28],

$$\lambda_t = \frac{Ki}{Km} = \{1 + \alpha_t V_d [(\frac{Kd}{Km})^2 - 1]\}^{1/2} \qquad (1.8)$$

where K_m and K_d are the K_{Ic} values for the matrix and ductile phase, respectively, α_t is a constant having values of 1 and 1.74 for average and maximum toughening by crack trapping, respectively [17, 28].

It is apparent that the only important variable affecting the initial toughness K_i in crack-front trapping is the volume fraction of ductile phase, V_d, which is summarized in **Figure 1.5**.

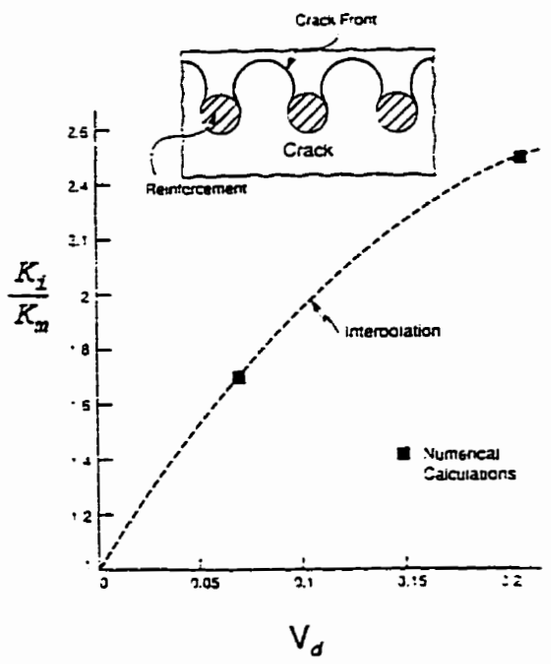

Figure 1.5 Predictions of the influence of crack trapping on the initiation toughness ratio [29].

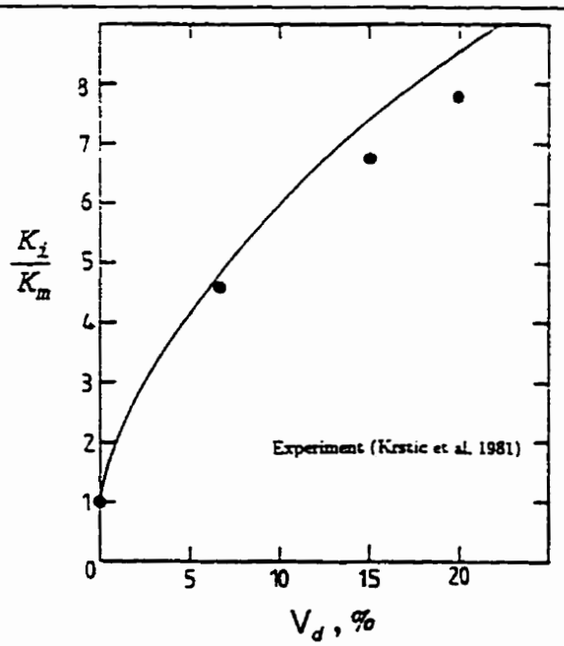

Figure 1.6 Comparison of measured and predicted toughness of a brittle matrix reinforced by tough particles [28].

The excellent agreement of measured and predicted toughness of a brittle matrix reinforced by tough particles has been obtained by Bower and Ortiz [28], and Krstic et al. [30] for the toughness of glass reinforced by partially oxidized aluminium particles as shown in **Figure 1.6.**

As an example, a typical experimental picture of crack-front trapping is also given in **Figure 1.7.**

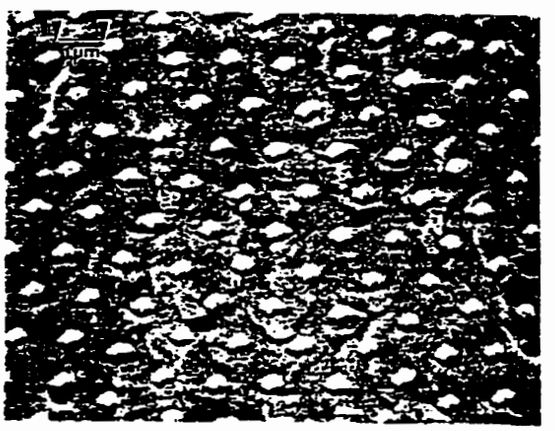

Figure 1.7 Higher-resolution SEM views of the fracture surface of the NiAl/Mo indicating characteristic crack trapping "tails" in the NiAl [29].

Microcrack Renucleation

In a layered in-situ composite as shown in **Figure 1.1c**, the crack front cannot loop around the ductile phase with well-bonded interface. Consequently, a crack renucleation phenomenon must occur before crack growth proceed [29]. The initiation toughness can be determined by the renucleation of microcrack in the matrix ahead of the main crack [17]. Shaw et al. [31] investigated metal/ceramic multilayers and suggested that for composites with thick brittle matrix layers, the corresponding initiation toughness, K_i, can be estimated from

$$K_i = S_m(2\pi\, h_d)^{1/2} \tag{1.9}$$

where S_m and h_d are the average value of the fracture strength of the brittle matrix and the thickness of the ductile layer as shown in **Figure 1.8**, respectively.

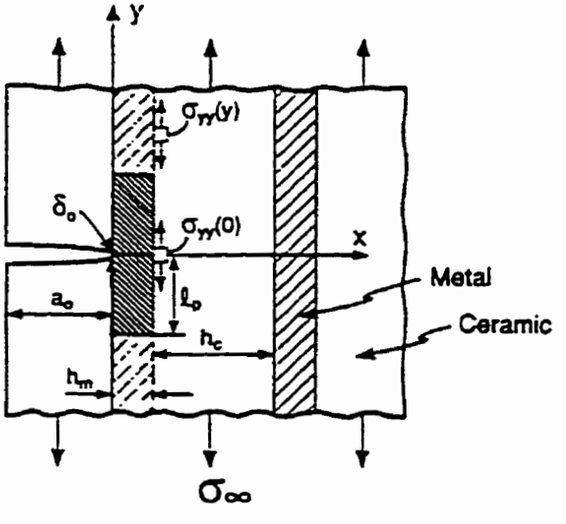

Figure 1.8 Schematic illustrating the crack geometry and the parameters measured from the multilayered alumina/copper and alumina/aluminum composites [31].

Crack-Tip Interface Delamination

Any second phase that is weakly bonded to the matrix has the potential to increase the toughness of the system through crack tip-interface debonding or splitting process [32-37]. As illustrated in **Figure 1.1d**, when a crack encounters a planar interface, slip and debonding along the interface can cause a stress redistribution that is favourable for initiation toughness enhancement. This stress redistribution produces three important effects [17]:

(1) the triaxial stresses near the crack tip are lowered;

(2) a diffuse microcrack zone is created by enlarging the process zone size;

(3) intact ligaments are generated between the main crack and the microcracks. These processes also increase the fracture resistance by crack bridging or ligament toughening as discussed later.

Unfortunately, there is no a quantitative model available to elucidate microstructure/toughness relationships so far. Even though, crack-tip stress analyses have shown that crack-tip interface debonding significantly reduces the normal stresses near the crack tip and shifts the peak stress away from the crack tip as mentioned above [32-36]. In addition, Deve et al. [37] also found that the work of fracture exhibits a linear dependence on the debond length for the TiAl/Nb laminate composite. As discussed by Anderson [38], a sufficient debonding is a necessary precursor for a subsequent crack bridging.

Figure 1.9 shows a selected instance of crack-interface-debonding mechanism from NiAl/Mo in-situ composite.

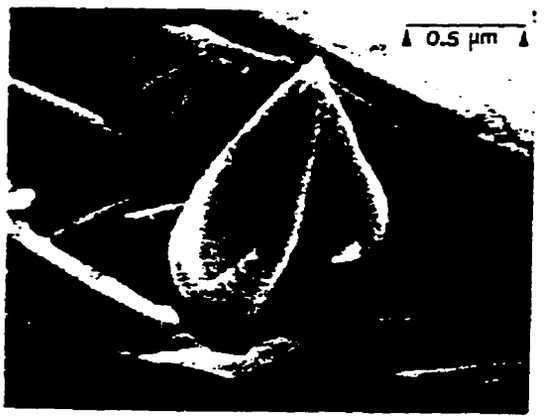

Figure 1.9 SEM fractographs of the NiAl/Mo system showing plastic stretch of the Mo and interface debonding [29].

1.1.3 Extrinsic Mechanisms

Extrinsic in nature, this type of ductile-phase toughening affects the crack growth toughness K_r by inducing a rising resistance curve behaviour through the formation of bridged zone and process zone in crack wake or a deflected or tortuous crack path located ahead of the dominant crack tip (e.g., shear ligaments can form as the result of mismatched planes of microcracks). The typical modelling and mechanisms will be summarized in the following sections.

Crack Bridging

The presence of intact ductile particles in the crack wake can significantly increase the fracture resistance of the composite by crack bridging as shown in **Figure 1.1e**. The mechanics of crack bridging by ductile phase particles are well developed. There are two kinds of popular models available. The earlier ones are *spring models* proposed by Budiansky et al. [39] and Elliott et al. [40]. The others are *energy models* suggested by Ashby et al. [41], Mataga [42], and Flinn et al. [43].

Spring Models

The mechanics of ductile-phase toughening have been analyzed by Budiansky et al. [39] by treating the bridging particles as elastic, elastic/perfectly plastic, or rigid/perfectly plastic springs as shown in **Figure 1.10**. Based on the *J*-integral approach, Budiansky et al. [39] established a model for the elastic/perfectly plastic case, which is identical to the rigid/perfectly plastic) case. as follows

$$\lambda_b = \frac{K_r}{K_m} = [\omega(1-C) + \frac{2CE\sigma_d\delta}{K_m(1-\nu^2)}]^{1/2} \qquad (1.10)$$

with

$$\omega = \frac{E(1-\nu_m^2)}{E_m(1-\nu^2)} \qquad (1.11)$$

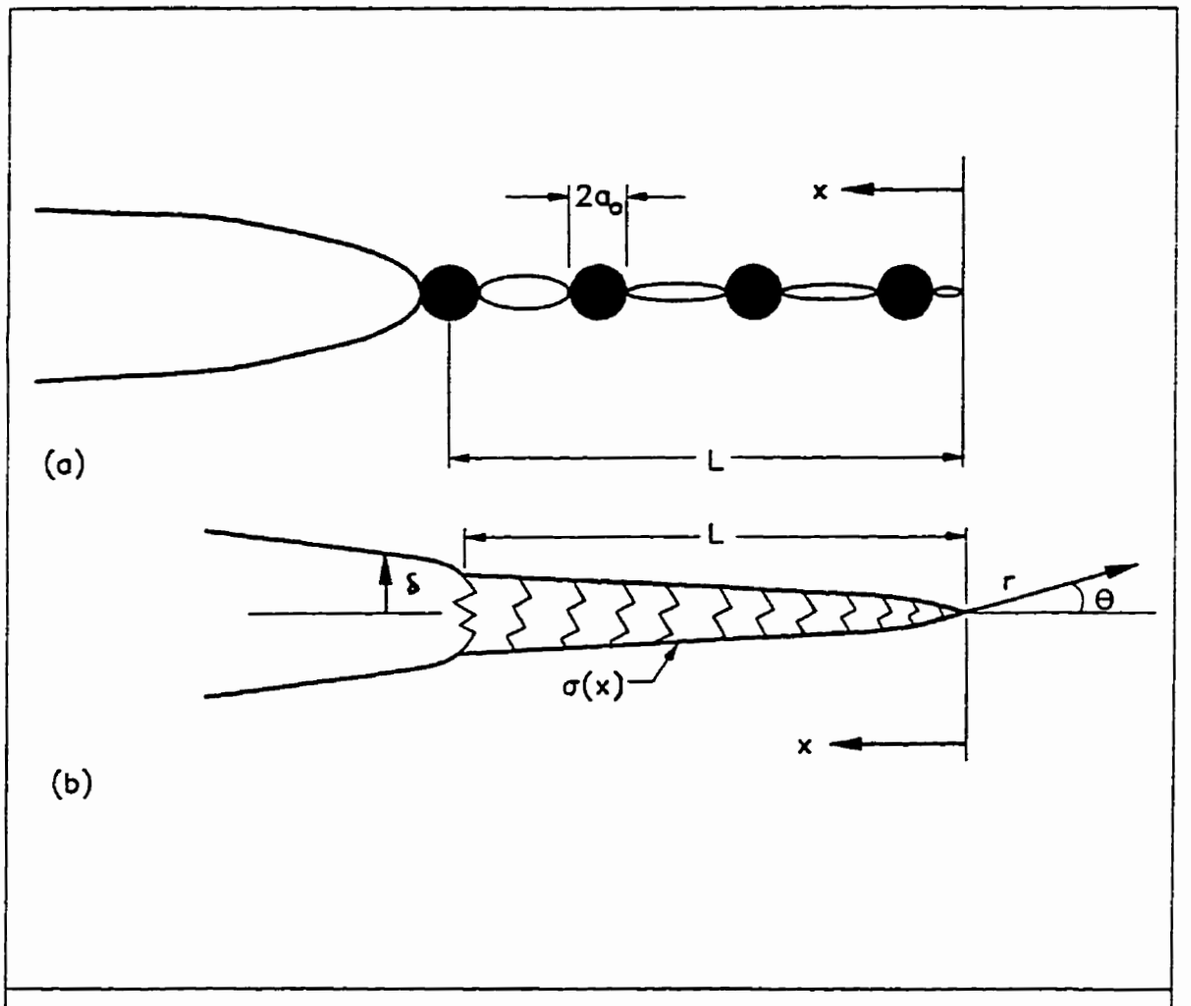

Figure 1.10 (a) Bridged crack and (b) bridging-spring model [39].

Eq.(1.10) increases with increasing of the square root of V_d and the crack opening as fracture resistance K_r of a particulate composite containing a concentration, C, of ductile particles subjected to an ultimate stress σ_c. In *Eq.(1.10)*, C is equivalent to volume fraction of ductile phase, V_d . Therefore, it is evident that K_r from displacement, $\delta^{1/2}$, as shown in **Figure 1.10b**.

Furthermore, based on the *J*-integral approach, the first term within the bracket in *Eq.(1.10)* is the contribution of the matrix to the overall strain energy release rate of the particle-reinforced composite, while the second term is the contribution due to the plastic work consumed in fracture of the ductile particles in the bridging zone.

Based on stress intensity factor approach, Budiansky et al. [39] also gave an alternative expression for this spring model,

$$\lambda_b = \frac{K_r}{K_m} = 1 + 2\sigma_d \left(\frac{2L}{\pi}\right)^{1/2} \tag{1.12}$$

which indicates that the fracture resistance K_r caused by crack bridging is proportional to $L^{1/2}$, where L is the length of the bridged zone as shown in **Figure 1.10**.

Obviously, a very important factor, volume fraction of ductile phase (V_d), in the composite was not considered in *Eq.(1.12)*, which definitely limits its application. Therefore, Elliott et al. [40], Chan [18] and Soboyejo et al. [7, 54] modified *Eq.(1.12)* as,

$$\lambda_b = \frac{K_r}{K_m} = 1 + B V_d \sigma_d \ L^{1/2} \tag{1.13}$$

where, B is a constant for this model of crack bridging. B is equal to $2\sqrt{(2/\pi)} \approx 0.9$ in Ref.[7, 18, 54]. However, B was also chosen as 1.9 depending on crack geometry by Elliott et al. [40], the reason being not clear.

Energy Model

Relatively ductile particles, when strongly bonded to the brittle matrix, undergo extensive stretching in the crack wake (**Figure 1.11**) until they fracture or decohere. The work of stretching contributes to the overall toughness of the solid. The crack growth energy in the composite, ΔG_r, is directly related to the nominal stress, $\sigma(u)$, carried by the stretching particle

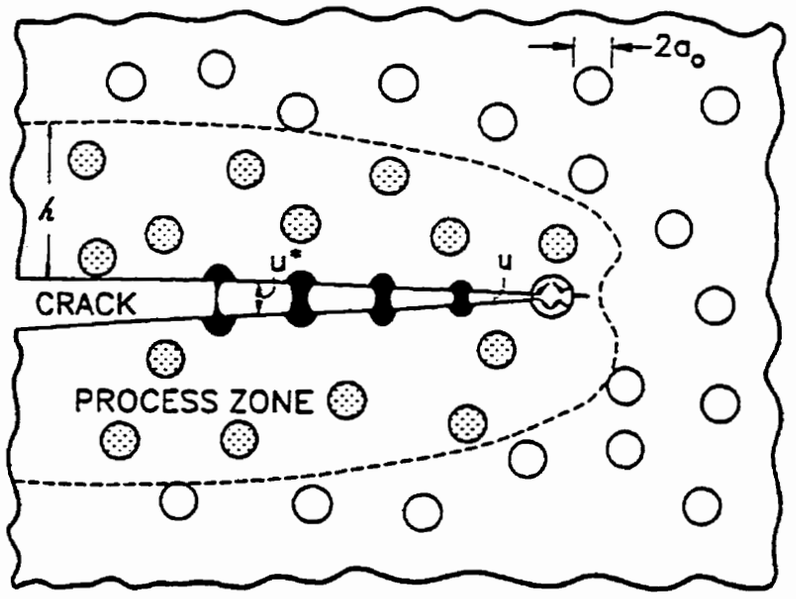

Figure 1.11 A crack in a brittle matrix, intersected by ductile particles. The particles stretch and fail as the crack opens. The work of stretching contributes to the fracture energy of the composite [41-42].

for a given crack opening, u [41-42]

$$\Delta G_r = V_d \int_0^{u^*} \sigma(u) du \tag{1.14}$$

where V_d is the area-fraction of ductile particles intercepted by the crack and u^* is the total crack opening when the ductile particle fails (**Figure 1.11**). Both theoretical considerations and model experiments on the glass matrix (brittle)/lead wire (ductile) composites [41] have shown that the crack growth energy due to crack bridging, ΔG_r, over that of the matrix is given by:

$$\Delta G_r = \chi V_d a_0 \sigma_{YS} \tag{1.15}$$

or using for the plane stress $\Delta K_r = (E\Delta G_r)^{1/2}$

$$\Delta K_r = [\chi a_0 E \sigma_{YS} V_d]^{1/2} \tag{1.16}$$

where a_0 is radius of a spherical second-phase as shown in **Figure 1.11** or simply representative microstructural dimension (e.g., lamellar thickness of ductile phase if it is in the lamellar morphology) [44]. The parameter χ is a dimensionless work-of-rupture parameter which is given by [41, 42]

$$\chi = \int_0^{u^*/a_0} \frac{\sigma(u)}{\sigma_{YS}} d\left(\frac{u}{a_0}\right) \tag{1.17}$$

χ depends on interfacial debonding, the reinforcement ductility and the work hardening coefficient. Experimental studies and calculations have indicated that χ can vary from 0.3 to 8 corresponding to either well-bonded (debonding length, $d \approx 0$) interface or poor-bonded

interface [43-47]. For example, Ashby et al. [41] suggested 1.6 to 6 and Bencher et al. [44] used 2.7 for well-bonded interface, Sun and Yeomans [45] show 0.3 to 1 for well-bonded interface and ductile ligaments that fail by necking to a point.

For plain strain condition elastic modulus in *Eq.(1.16)* should be modified by factor $(1-\nu^2)$ where ν is Poisson's ratio of composite. It is interesting to note that *Eq.(1.16)* suggests a linear relationship between the fracture resistance K_r caused by crack bridging and the square root of ductile-phase volume fraction, $V_d^{1/2}$.

An evidence of crack-bridging zone in an experimental observation is shown in **Figure 1.12.**

Figure 1.12 *SEM* micrograph of the crack profile in the lamellar Nb_3Al/Nb composite microstructure under monotonic loading, showing crack bridging by the ductile Nb phase in the crack wake [43].

Process Zone (Transformation) Toughening

Particles intercepted by the crack, when bonded to the matrix, exhibit extensive plastic stretching in the crack wake as shown in **Figures 1.9** and **1.12**, and contribute to the toughness by inhibiting crack opening. When such a bridging zone exist, residual stress present in the composite, caused by thermal expansion mismatch, can also contribute to the toughness by means of its influence on the initial crack opening force. Simultaneously, plastic straining of particles in a process zone causes crack shielding. Toughening by crack shielding in the process zone (**Figure 1.11**) is fundamentally governed by a critical stress for the onset of nonlinearity, σ_c, in elements near the crack tip and by the total dilatational strain, ε_t [36, 48]. The resulting stress-strain hysteresis of those elements within a process zone then yields fracture-resistance energy given by [36, 48]

$$G_r = 2 V_d h \sigma_c \varepsilon_t \qquad (1.18)$$

where h the process-zone height in steady state (**Figure 1.11**). Transformation and twin toughening mainly fall into the category of process zone toughening because they are all based on the same simplifying assumption and provide equivalent predictions [36, 48]. Recalling that, $K^2(1-\nu^2)/E=G$, it has been demonstrated that G_r given by *Eq.(1.18)* is identical to K_r predicted by the transformation model [48]

$$K_r = 0.22 E V_d \varepsilon_t h^{1/2} / (1-\nu) \qquad (1.19)$$

Sigl et al. [49] also included plastic straining of particles in the process zone as contributing

to the crack tip shielding when particles are very small and have low yield strength. However. the contribution from the latter mechanism usually does not seem to be substantial [49].

It is evident that this mechanism behaves much close relationship with crack bridging because they always occur simultaneously in an in-situ composite toughened by a ductile phase because the bridging zone is always surrounded by a process zone when a crack occurs.

Shear Ligament Toughening

Shear ligament toughening is a process that has been recently identified in both Ti_3Al- and TiAl-base titanium aluminides and used to explain roughness-induced toughness in these alloys [17-18, 23, 50-51]. The toughening mechanism results from deflection of the main crack from the mode I path and the formation of mismatched microcracks ahead of the crack tip. As the main crack zigzags between grains, the angle of deflection and the plane of microcracking are likely to be different among individual grains. As shown schematically in **Figure 1.1g**, the consequence is that the crack planes in the various grains are unconnected at either grain or phase boundaries and are separated by ligaments, which undergo shear deformation.

A theoretical model of shear ligament toughening is based on an energy balance given by [50, 51]

$$J_r = J_m + J_l = J_m + \tau_l \gamma_l < l > V_l \qquad (1.20)$$

where J_r, J_m and J_l are the values of the J-integral supplied by the remote load, exited in the

matrix, and dissipated by the shear ligaments, respectively. V_l and $<l>$ are the volume fraction and average length of the shear ligaments $(=1+(L/l)\tan\phi$, where L is the projected crack length and ϕ is the crack deflection angle as shown in **Figure 1.13**), respectively. τ_l and γ_l are fracture stress and fracture strain in shear, respectively. Recalling that, $K^2(1-\nu^2)/E=J$, the fracture resistance K_r achieved by the crack-wake shear ligaments can be described by [17, 50-51]

$$K_r = \left[\frac{E K_m^2}{E_m} + \frac{V_l < l > E \tau_l \gamma_l}{1-\nu^2}\right]^{1/2} \qquad (1.21)$$

where $K_r=K_m$ when shear ligaments are absent ($V_l=0$). In other words, the second term in *Eq.(1.21)* is the contribution of the shear ligament toughening (K_l). This model indicates that the amount of toughening achieved, increases with the square root of volume fraction, V_l, and the average length, $<l>$, of the shear ligaments in the crack wake.

Evidence for the formation of shear ligaments by mismatched crack planes is presented in **Figure 1.13**. Fracture of the shear ligaments requires additional plastic dissipation leading to a tortuous crack path and a resistance-curve behaviour.

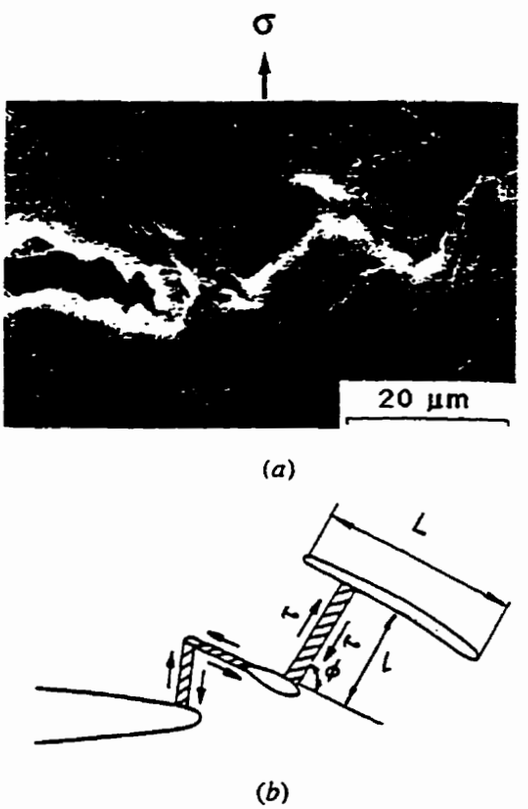

Figure 1.13 Composite figures showing the process by which shear ligament toughening occurs in an in-situ composite (Ti-24Al-11Nb) with an equiaxed $\alpha_2 + \beta$ (the lighter phase in (a)): (a) *SEM* micrograph and (b) a sketch of the ligaments [50].

Crack Deflection

The crack is redirected during the deflection process in such a way that the stress intensity at the crack tip becomes significantly reduced or diminished [18, 36, 52-55]. The toughening by crack deflection is the result of a reduction in the local stress intensity factor when a crack deviates from its original path. For a mode I crack that deviates from a straight path by a deflection angle θ as shown in **Figure 1.1h**, the fracture resistance K_r can be assessed [53]:

$$K_r = \frac{K_m}{\cos^2(\theta/2)} \tag{1.22}$$

where θ is the deflection angle in the model analyzed by Suresh [53] as shown in **Figure 1.1h**. *Eq.(1.22)* was expressed as $\lambda_d = K_\infty/K_m = cos^2(\theta/2)$ by Soboyejo et al. [55] only if crack deflection increases K_{Ic}, i.e. the crack pre-exists as deflection.

Figure 1.14 shows that the calculated values of the toughening ratio increase with increasing values of the crack deflection angle. Most of the toughening effect occurs at a relatively large deflection angle, however. For example, a 60° angle is required for a 25% increase in the toughness value.

Crack deflection toughening can also be related to the shear ligament toughening identified in both Ti_3Al- and TiAl-base titanium aluminides by Chan [18, 23]. Deflection of the main crack from the mode I path leads to the formation of mismatched microcracks in the grains ahead of the crack tip separated by shear ligaments.

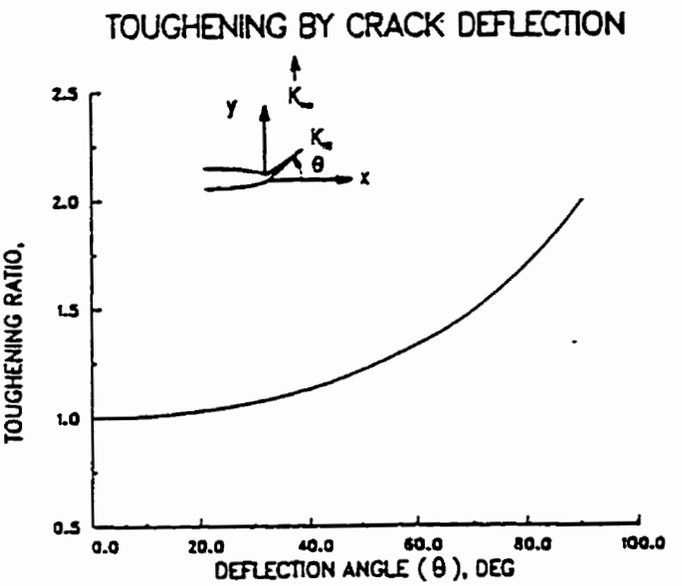

Figure 1.14 Calculated values of the toughening ratio for crack deflection [18].

Microcrack Shielding

Microcracks are generally, widely separated and located either ahead of or in wake of the tip of the main crack as shown in **Figure 1.1i.** One approach to assess microcrack shielding given by Chan [18] follows the one proposed by Rose [58]

$$K_I^P = \sigma_I^P (2\pi R)^{1/2} f_1(S, R, \theta, \alpha, \sigma_I^P) \qquad (1.23)$$

where σ_i^P is a shear traction. S is half of a single microcrack length located at a distance R and angle θ from the tip of the main crack. α is the orientation of the microcrack with respect to the stress axis and $f_I(s, R, \theta, \alpha, \sigma^p)$ are complicated mathematics expressions that are given in Rose's article [58].

Further more, microcrack interaction with the main crack generally leads a toughening ratio, λ_{ms}, as following expression [18]:

$$\lambda_{ms} = \frac{K_i}{K_{ms}} = \frac{K_i}{[(K_i + K_1^P)^2 + (K_2^P)^2]^{1/2}} \qquad (1.24)$$

but this is correct only if the shielding effect is from a single or two symmetrically disposed secondary cracks in the vicinity of the principal crack tip.

Second approach is given by Evans and Cannon [48] in the following form,

$$K_r = 1.12(1+\nu)\sigma_R V_{ms} h^{1/2} \qquad (1.25)$$

where ν is Poisson's ratio, σ_R is the residual stress, V_{ms} is the volume fraction of microcracked grains in the micro shielding zone and h is the height of microcrack shielding zone as shown in **Figure 1.1i**.

Figure 1.15 shows the formation of microcracks in Ti-24Al-11Nb in-situ composites [18]. It is interesting to be noted that the number and length increase with increasing K levels and crack extension.

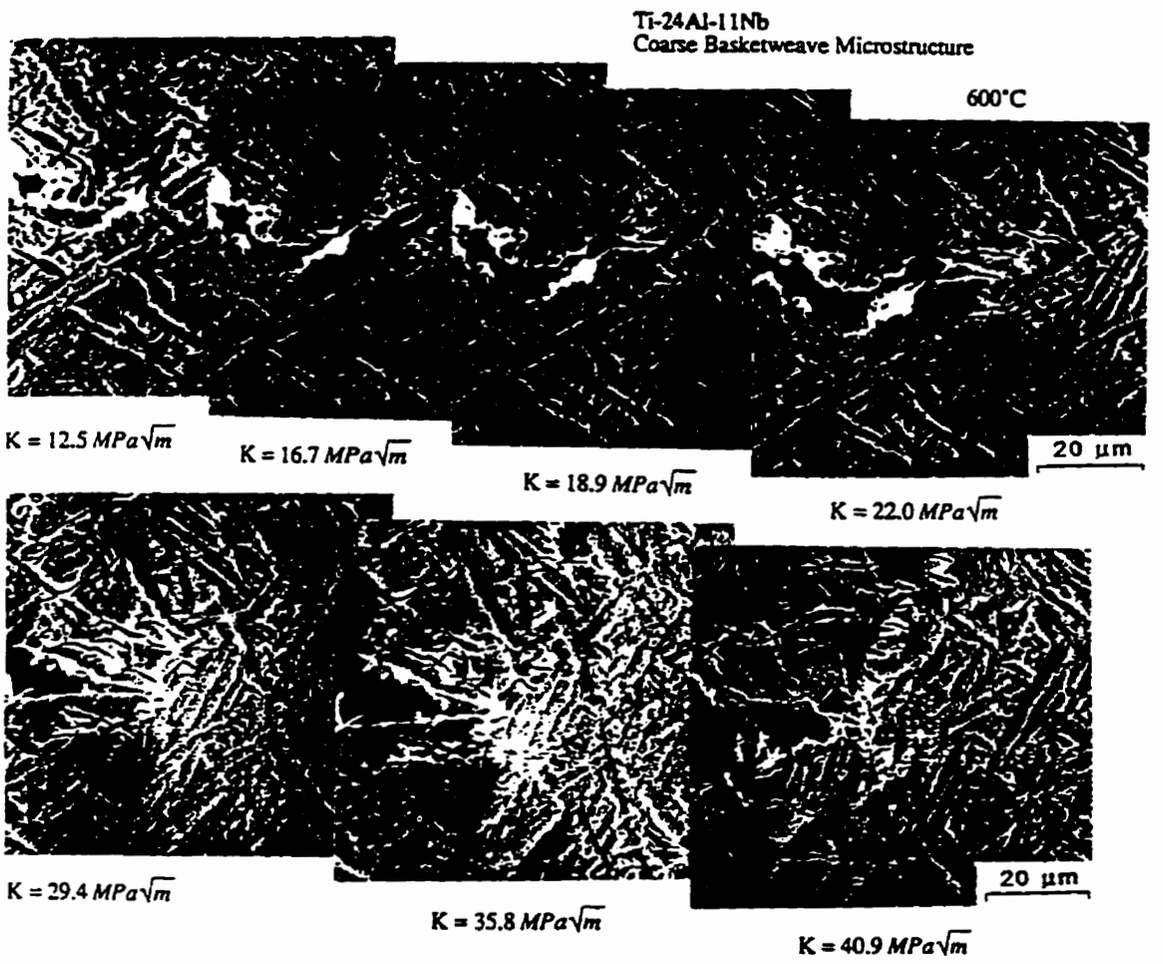

Figure 1.15 Composite in situ SEM micrographs show that the near-tip fracture process in the coarse basketweave microstructure at 600°C is characterized by the formation of the microcracks whose number and length increase with increasing K levels and crack extension [18].

1.1.4 Rule of Mixtures (ROM)

Recently, the rule of mixtures for fracture toughness in a composite has been proposed by Davidson et al. [61-62], Krstic [59], Budiansky et al. [39], Flinn et al. [43], Ravichandran [60] and Soboyejo et al. [7, 54].

By analogy with the upper bound of elastic modulus of a composite as shown in **Figure 1.16b**, Davidson et al. [61-62] suggested a rule of mixtures (ROM) as a straight line (**Figure**

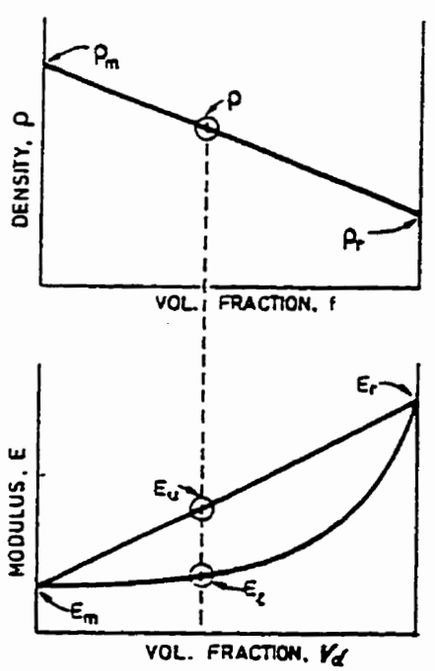

Figure 1.16 For a given density, there exist two values of modulus: an upper bound and a lower bound [63].

1.17) to connect the two points of $(K_{Ic})_m$ and $(K_{Ic})_d$, which were obtained from the experimental results of the Cr_2Nb-containing the Nb-Cr_2Nb in-situ composites. The straight line is simply mathematically expressed as:

$$K_{Ic} = (1 - V_d) K_m + V_d K_d \qquad (1.26)$$

where V_d is volume fraction of ductile phase. As shown in **Figure 1.16**, all the experimental fracture toughness values of the in-situ composites are lower than the straight line. This fact indicates that the presence of brittle Cr_2Nb in the Nb-Cr_2Nb in-situ composites reduces the fracture toughness of the in-situ composite significantly.

Krstic [59], Budiansky et al. [39], Flinn et al. [43], Ravichandran [60] and Soboyejo et al. [7, 54] used an E-modified rule of mixtures (*E-ROM*) for fracture toughness of an in-situ composite. They [7, 39, 43, 54, 59, 60] proposed that fracture energy G_{Ic}, i.e., critical strain energy release rate of an in-situ composite can be expressed as:

$$G_{Ic} = (1 - V_d) G_m + V_d G_d \qquad (1.27)$$

where G_m and G_d are fracture energies (critical strain energy release rates) of the matrix and ductile reinforcing phase, respectively.

Recalling $K_{Ic}^2 = E'G_{Ic}$ (where $E'=E$ for plane stress, $E'=E/(1-\nu^2)$ for plane strain), the E-*ROM* for fracture toughness K_{Ic} in an in-situ composite is given in the following form:

$$K_{Ic} = \{ E'_c [\frac{(1 - V_d) K_m^2}{E'_m} + \frac{V_d K_d^2}{E'_d}] \}^{1/2} \ [MPa.m^{1/2}] \qquad (1.28)$$

where E'_m and E'_d are plane strain elastic moduli of the matrix and ductile second phase,

respectively. As shown in **Figure 1.17**, *E*-modified ROM is a curve above the straight line of ROM.

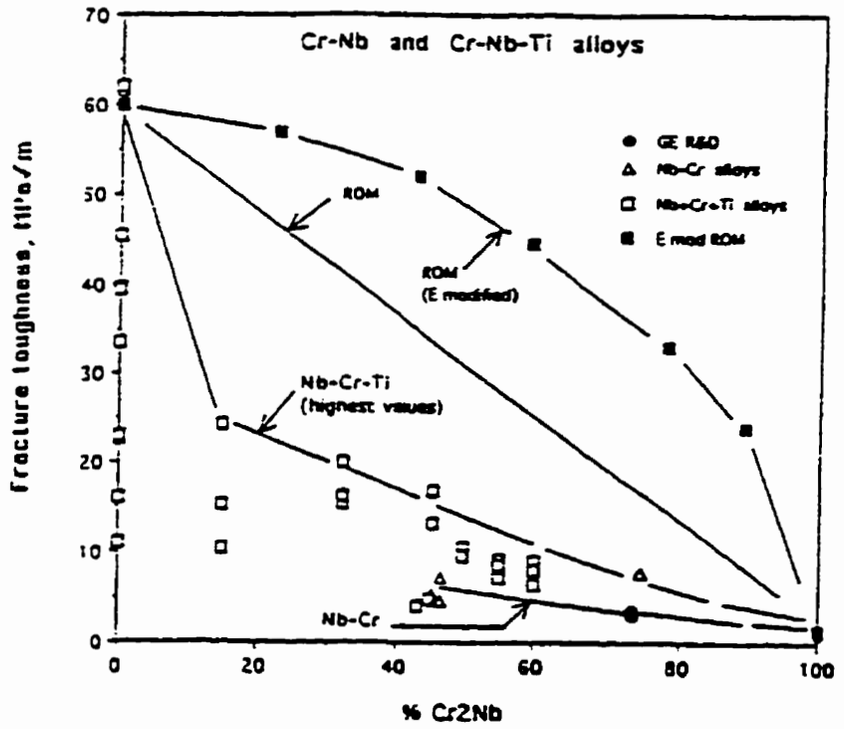

Figure 1.17 Fracture toughness as a function of the vol.% of Cr_2Nb. For comparison with measured values, rule-of-mixtures (ROM) and ROM modified by modulus values are shown [61-62].

However, it has to be pointed out that *Eq.(1.26)* or *Eq.(1.27)* is a simple assumption without any formal justification or derivation.

Ashby [63] pointed out that *Eq.(1.26)* and *Eq.(1.28)* should be treated as the lower and upper limits for fracture toughness, which is similar to a function of the upper and lower bounds for moduli (**Figure 1.16**), respectively, not as precise formulae for calculating K_{Ic} values.

Furthermore, Ashby [63] modified the ROM of *Eqs.(1.26)* and *(1.28)* and considered the worst and best cases for an in-situ composites as shown in **Figures 1.18** and **1.11**, respectively.

Ashby [63] explained that if the less tough component is thought as the matrix, the most damaging situation, leading to a lower bound, only arises when $G_m<G_d$ and $E_m<E_d$, and a crack propagates entirely in the phase of lower toughness avoiding reinforcements (**Figure 1.18a**). In this case a lower limit for a composite toughness can be expressed as [63],

$$(G_{Ic})_{\min} = G_m \frac{(1+2V_d)^{1/2}}{1-V_d^{1/2}}, \quad G_{Ic} < G_d. \tag{1.29}$$

From *Eq.(1.29)*, obviously, even in this case the toughness still increases with increasing reinforcement fraction. This is because the crack, in avoiding the reinforcement, is forced into a path of greater area which increases by a factor of approximately $(1+2V_d)^{1/2}$, and also because the rough crack faces tend to interlock or rub, which contributes a factor $1/(1-V_d)$. It has to be noted that *Eq.(1.29)* is cut off at $G_{Ic}=G_d$ since the crack will then penetrate in the ductile phase of the composite.

Then the lower bound for fracture toughness, $(K_{Ic})_{min}$, of the composite can be given by the following form,

$$(K_{Ic})_{\min} = K_m \left\{ \frac{(1+2V_d)^{1/2}}{1-V_d^{1/2}} \frac{E_c}{E_m} \right\}^{1/2}, \quad K_{Ic} < K_d. \tag{1.30}$$

When $V_d = 0$, the composite toughness has the value K_m of the matrix. Definitely, $(K_{Ic})_{min}$ from *Eq.(1.30)* represents a curve connecting the ends of the straight line but below the straight line marked as *ROM* (**Figure 1.17**).

The upper limit was derived by considering crack bridging [63]. Ashby assumed that the characteristic stress exerted by a bridging ligament, cannot be greater than the theoretical strength of the ligament itself, i.e., $E_d/40$. Based on this assumption, Ashby [63] gave the increment of the stress intensity factor at crack tip, $(K_{ic})=(1-V_d)V_d\sigma(\pi a^*)^{1/2}=(1-V_d)V_d(E_d/40)(\pi a^*)^{1/2}$. Recalling $G_{Ic}=K_{Ic}^2/E'$ and simply adding this term into *Eq.(1.27)*, Ashy [63] derived the following form for the upper limit of a composite,

$$G_{Ic} = (1-V_d)G_m + V_d G_d + \left[\frac{V_d(1-V_d)E'_d}{40} \right]^2 \frac{\pi a^*}{E'_c} \tag{1.31}$$

where a^* is half of the maximum crack length, which can be taken as 5mm in a calculation [63]. Similarly, the upper limit of fracture toughness for a composite can be expressed as,

$$(K_{Ic})_{\max} = \left\{ E'_c \left[\frac{(1-V_d)K_m^2}{E'_m} + \frac{V_d K_d^2}{E'_d} \right] + \left(\frac{V_d(1-V_d)E'_d}{40} \right)^2 \pi a^* \right\}^{1/2} \tag{1.32}$$

where the first two terms on the right describe the rule-of-mixtures (see *Eq.(1.28)*); the last term is the additional energy absorbed by the work done against the bridging forces [63]. Obviously, $(K_{Ic})_{max}$ from *Eq.(1.32)*, is above the *E-ROM* curve as shown in **Figure 1.17**.

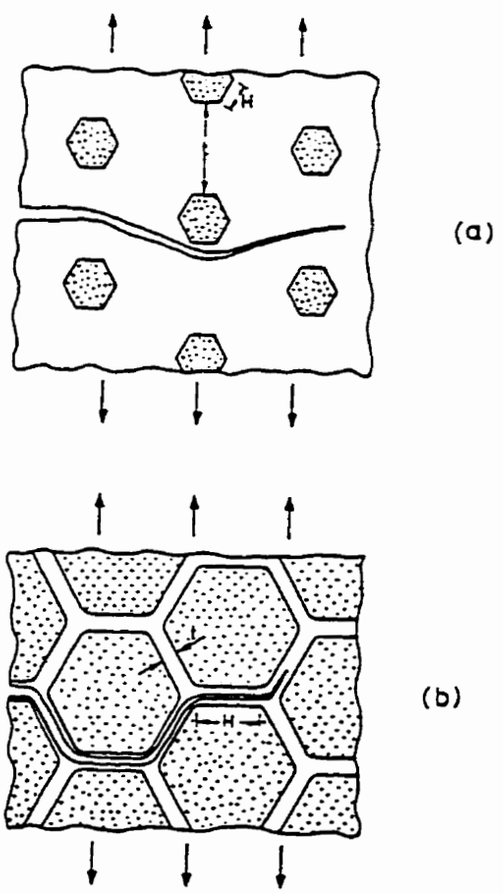

Figure 1.18 The basis of the lower-limit estimate for composite toughness. The crack propagates entirely in the phase of lower toughness. The apparent toughness increases slowly with volume fraction because of increasing area, and because of an increasing mode II component in its loading [63].

As shown in **Figure 1.17** for the Nb-Cr_2Nb in-situ composite, the lower bound, K_{min} model (*Eq.(1.32)*), predicted values approximately along the experimental Nb-Cr line. In addition, almost all of the experimental data exactly fall into the area surrounded by *ROM* from *Eq.(1.28)* and the lower bound $(K_{Ic})_{min}$ from *Eq.(1.32)* (**Figure 1.17**).

1.2 Experimental Observations and Analyses of Fracture Toughness of the In-Situ Intermetallic Composites

As discussed in **Section 1.1**, reasonably good correspondence between predicted and measured particle concentration effects on fracture toughening is insightful. However, the properties of the ductile phase that provide optimum toughness are not apparent, either from models or experimental observations. That is because toughening is sufficiently complex and involves a sufficiently large number of independent variables that microstructure optimization only becomes practical when each of the important models has been described by a rigorous model, validated by experiment.

In this section our discussion will be focused on the in-situ intermetallic composites, which were obtained only through liquid or solid state reactions occurring in the metallurgical systems under consideration. In particular, the emphasis will be placed on the dependence of fracture toughness on volume fraction of second phase. It must be pointed out that in the intermetallic

composites listed in **Table 1.1** the effect of the volume fraction of the second phase was not systematically investigated. In fact, the data on the effect of the volume fraction are rather scarce and confusing.

Strum and Henshall [64] claimed that the fracture toughness K_Q increases linearly with increasing volume fraction of the ductile phase in the V-V_3Si in-situ composites (**Figure 1.19**). In fact, the fit is not that linear. Power-law fit yields (broken line in **Figure 1.19**) the following equation:

$$K_Q = 2.824 + 0.003\,V_d^2 \quad [MPa.m^{1/2}] \tag{1.33}$$

The result can not be expected by any toughening model discussed before.

Bewlay et al. [65] investigated in-situ intermetallic composites in the binary system of Nb-Si. They used directional solidification (DS) to process the alloys. The DS hypoeutectic alloys with compositions less than 18.2% Si were found to contain primary Nb dendrites and the (Nb+Nb_3Si) eutectic. The hypereutectic alloys with compositions of 18.7% Si and greater were found to contain primary Nb_3Si dendrites with the inter-dendritic eutectic. Alloys with compositions between 20 and 22 at.% Si contained additionally primary Nb_5Si_3 dendrites. Bewlay et al. [65] observed the linear increase of fracture toughness with decreasing Si concentration (increasing Nb volume fraction) as shown in **Figure 1.20**.

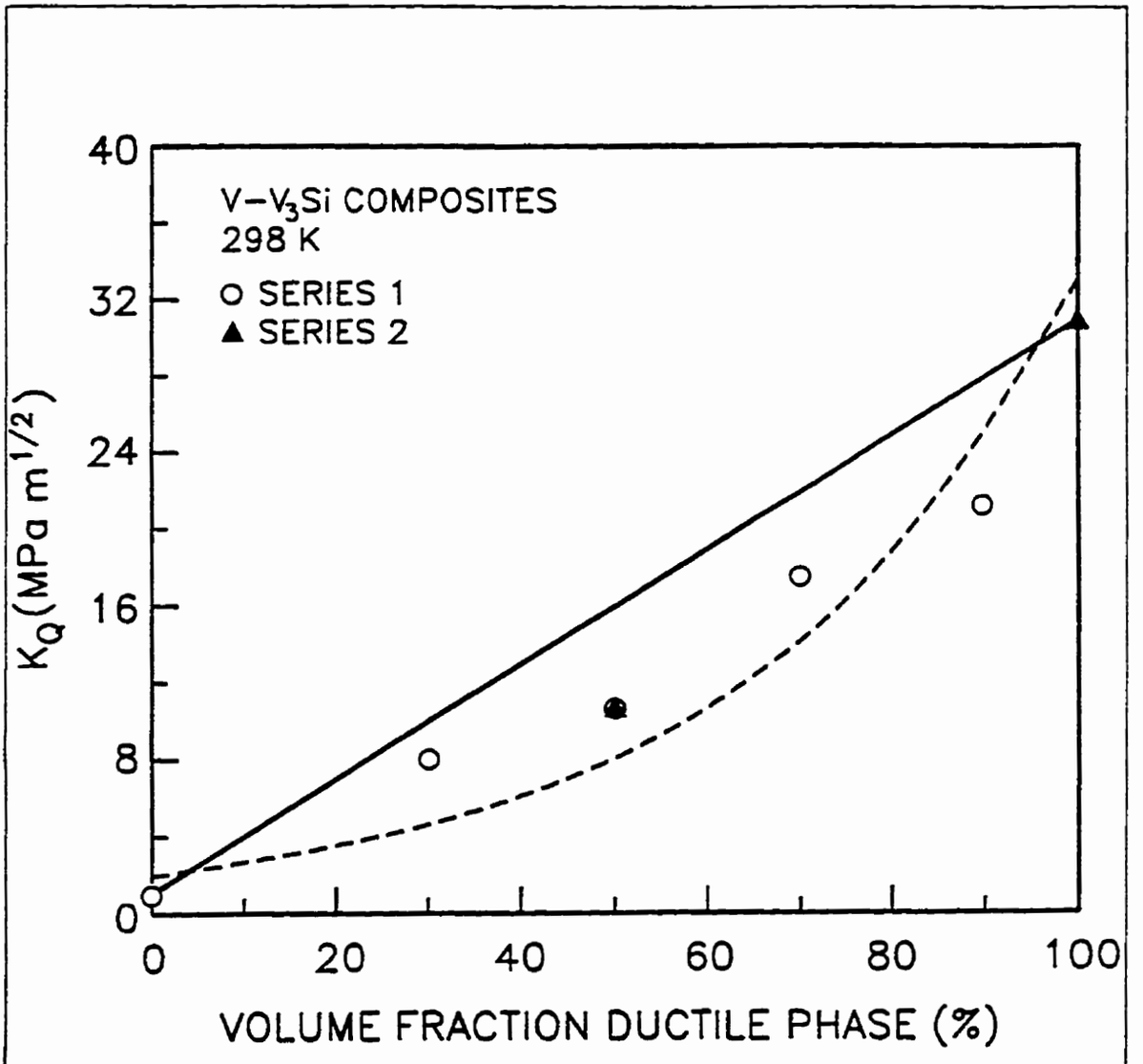

Figure 1.19 The average fracture toughness of V-V_3Si composites as a function of ductile phase fraction (All the castings were arc melted. To minimize hydrogen absorption from requisite acid cleaning and to attempt further minimization of interstitial levels from the melt stock, high-purity vanadium chips were substituted for melting stock in the series-2 castings) [64].

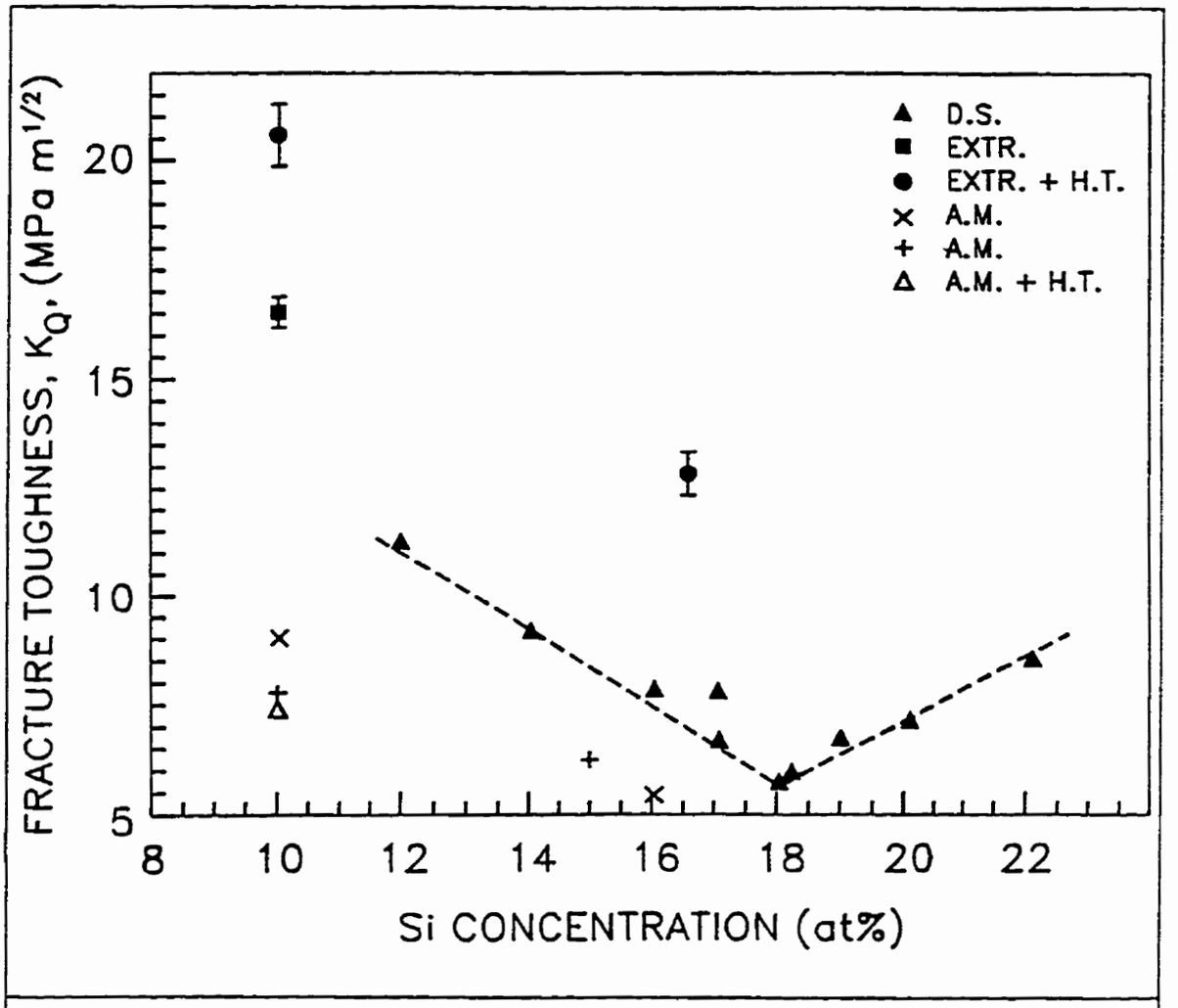

Figure 1.20 The effect of Si concentration on the fracture toughness of binary DS Nb-Si alloys with composition from 12 to 22% Si (D.S.: directly solidified; Extr. :extrusion; A.M.: arc melting; H.T.: heat treatment) [65].

To explain the linear rather than proportional to $V_d^{1/2}$ (*Eq.1.16*) increase of K_Q with increasing Nb volume fraction, Bewlay et al. [65] put forward several possible factors for this behaviour. The first is that crack bridging by the ductile phase is not the predominant

toughening mechanism and that other mechanisms, such as micro-cracking, crack deflection and crack blunting are playing more significant roles. The second factor is that not all the Nb contributes the same specific work of fracture, since the latter is dependent on the scale of the Nb. In attempting to correlate the above ductile phase toughening theory with fracture toughness, it is assumed that all the Nb fails in a ductile manner. This is true for the eutectic and some of dendritic Nb, but much of the dendritic Nb failed by cleavage. Third, the degrees of constraint of the different types of Nb may be different. For example the shape of the high aspect ratio DS eutectic Nb may lend itself to interface decohesion more readily than the DS dendrites; in addition, the relative volume fractions of the eutectic and dendritic Nb change with Si concentration. Measurements of the eutectic alloy made by Bewlay et al. [65] indicate that the toughening increment that the eutectic possesses over the single phase Nb_5Si_3 is ≈3 MPa$\sqrt{m}$, assuming that the contributions from the individual toughening mechanisms are additive. Because of its fine scale, the eutectic Nb cannot be expected to contribute a much larger toughening increment [65].

In the hypereutectic region, where the eutectic matrix is reinforced by the brittle Nb_3Si, the fracture toughness increases linearly with increasing Si content, i.e., with increasing volume fraction of Nb_3Si and Nb_5Si_3 (**Figure 1.20**), which is quite surprising because both the Nb_3Si and Nb_5Si_3 are rather brittle phases. So far, the reason for such a behaviour is still not clear. A major improvement in the fracture toughness of the extruded alloys is also clearly seen in **Figure 1.20**. Extrusion makes several major modifications to the microstructure including phase alignment, reduced grain size, Nb hardness, Nb-Nb_5Si_3 interface orientation relationship

and the reduction of flaws, such as pores and cracks. It is also to be pointed out that the arc-melted (A.M.) alloys exhibit noticeably lower fracture toughness than the directionally solidified (D.S.) ones (**Figure 1.20**).

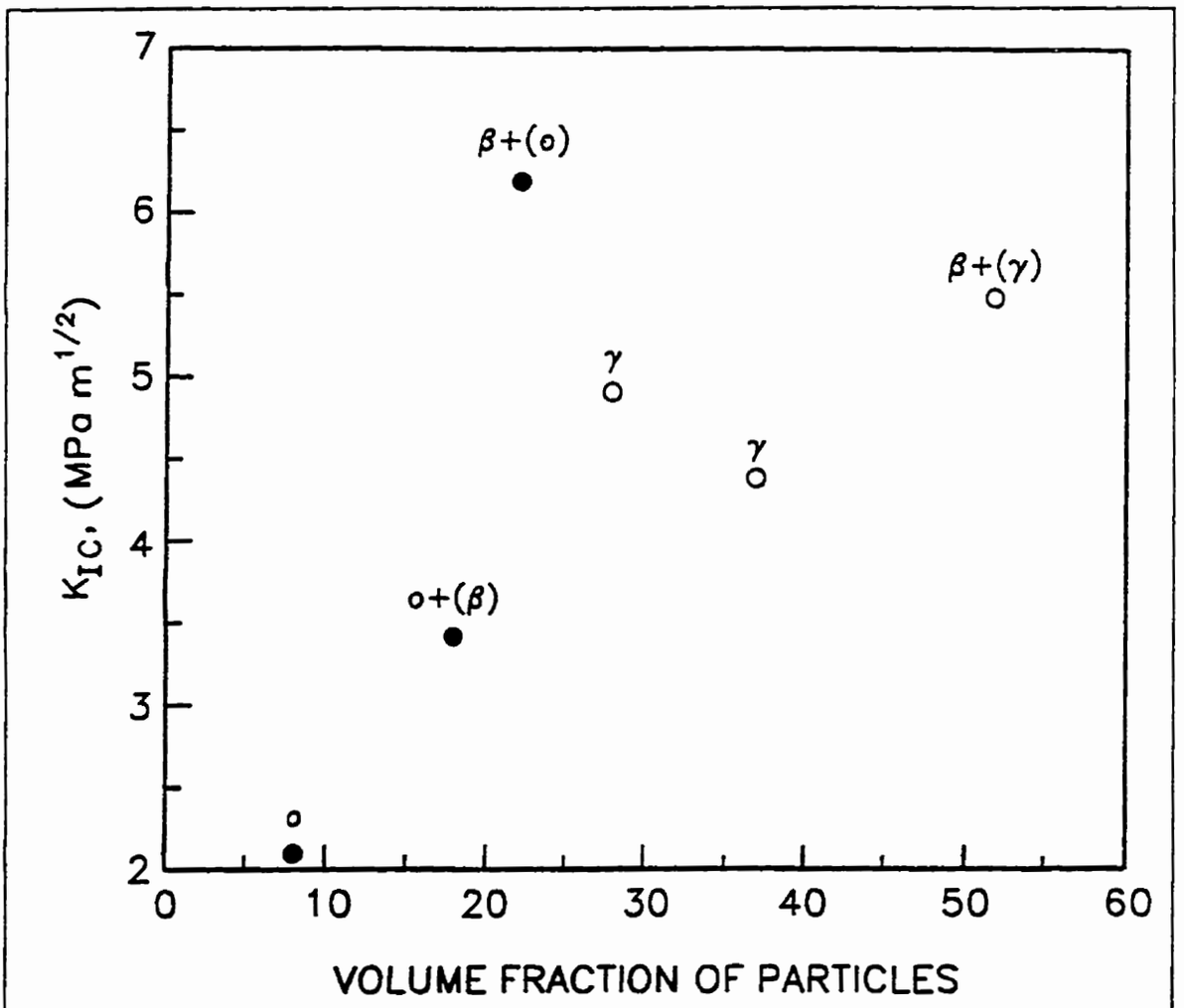

Figure 1.21 Fracture toughness as a function of volume fraction of particles in σ+*X* microstructures, where *X* designates each phase such as β, γ and *σ* phase [66].

Ebrahimi et al. [66] observed approximately the linear increase of fracture toughness, K_{Ic}, of σ phase ($Nb_2Al(Ti)$) in the Nb-Ti-Al ternary system, with increasing volume fraction of β (Ti-Nb BCC disordered solid solution), γ (TiAl(Nb)) and orthorhombic (Ti_2NbAl) (*o*) phases (**Figure 1.21**). Based on the fractographic studies various toughening mechanisms were proposed by Ebrahimi et al. [66]. In the case of the β and orthorhombic phases the particle-matrix interface was strong and toughening was achieved by crack tip trapping in the particle (crack blunting), crack front impediment, reinitiation of the crack ahead of the impeded crack front, crack bridging and separation of the crack surfaces by cleavage of the particle. The γ phase was associated with large tensile internal stresses and perhaps a low interfacial energy allowing for the crack deflection and following the σ-γ interface. The latter mechanism results in a lower level of toughening (**Figure 1.21**).

The fracture toughness of the NiAl-Ni_3Al in-situ intermetallic composite seems to increase linearly with increasing content of Ni (**Figure 1.22**). This suggests that fracture toughness could increase with the volume fraction of Ni_3Al (γ') because the latter increases with increasing Ni content. However, fracture toughness of the alloys in the region from about 62 to 75 at.% Ni is not well researched. As seen in **Figure 1.22** only several data points exist, mostly grouped at around 62 at.% Ni and the broken line up to 75 at.% Ni in **Figure 1.22** is essentially an extrapolation [67].

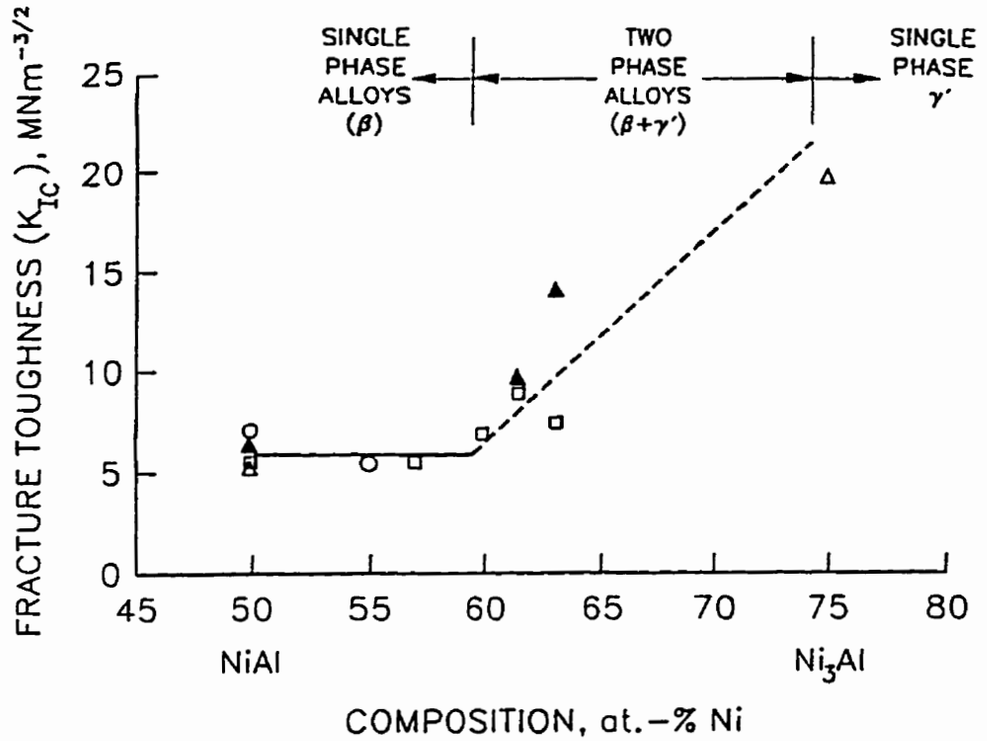

Figure 1.22 Room temperature fracture toughness of Ni-Al alloys as a function of stoichiometry: an increase in toughness occurs as a percentage of γ′ increases in two phase β+γ′ alloys [67].

Varin and Li [68] also obtained a linear increase of K_{Ic} with increasing volume fraction of minority phases, such as Ni (Si), $MgNi_2$ and Ni_5Si_2 formed in the brittle $Mg_6Ni_{16}Si_7$ (η phase) [69] intermetallic matrix of the in-situ intermetallic composites based on the Ni-Mg-Si ternary system (**Figure 1.23**). Interestingly, Ni_5Si_2, which is a rather brittle intermetallic phase, gives approximately the same amount of toughening as Ni(Si) which by its nature is a more ductile

phase (compare alloy 4 and 5 in **Figure 1.23**). Such a result is unexpected and difficult to explain by the existing models discussed in **Section 1.1**. Such a behaviour is similar to the one discussed for the DS hypereutectic Nb-Si composite alloys by Bewlay et al. [65]. Again, an apparently brittle intermetallic phase embedded in the intermetallic (rather brittle) matrix provides a respectable amount of toughening.

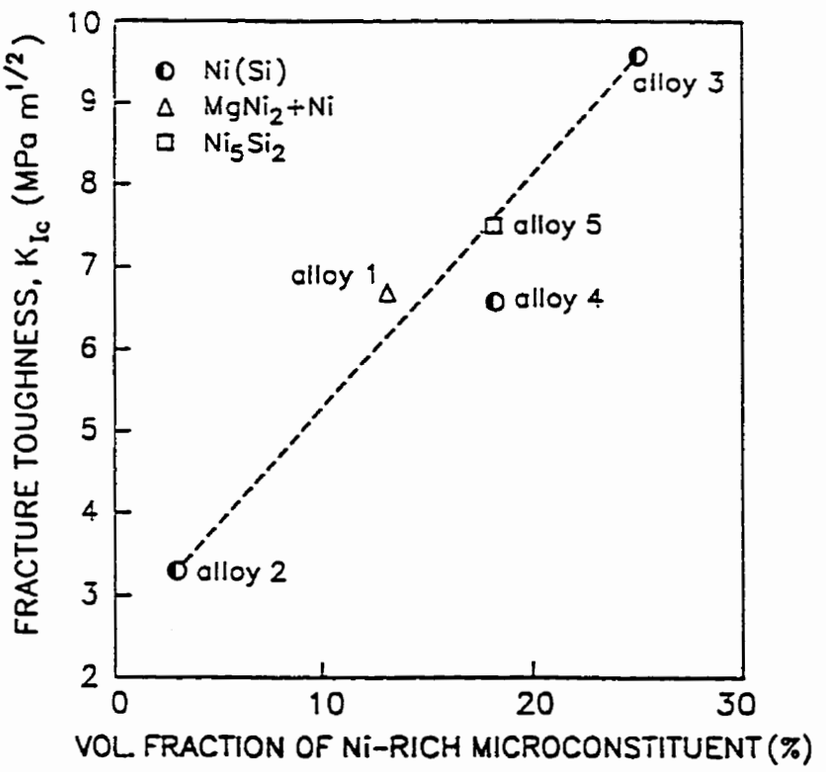

Figure 1.23 Dependence of K_{Ic} on the volume fraction of Ni-rich microconstituent; matrix is a brittle intermetallic of the $Mg_6Ni_{16}Si_7$-type ($Mn_{23}Th_6$ structure type) [68, 69].

It can be speculated that a weak interface between the matrix and reinforcing material aids the bridging mechanism. When a matrix crack encounters such an interface, this interface experiences Mode II loading; debonding occurs if the fracture energy of the interface is low [38].

So far the only case of the dependence of fracture toughness on the $V_d^{1/2}$ (*Eq.1.16*) is the result obtained by Rao et al. [70] on the intermetallic γ-TiAl reinforced with TiNb particles (**Figure 1.24**). This is not an in-situ intermetallic system because the composite was obtained

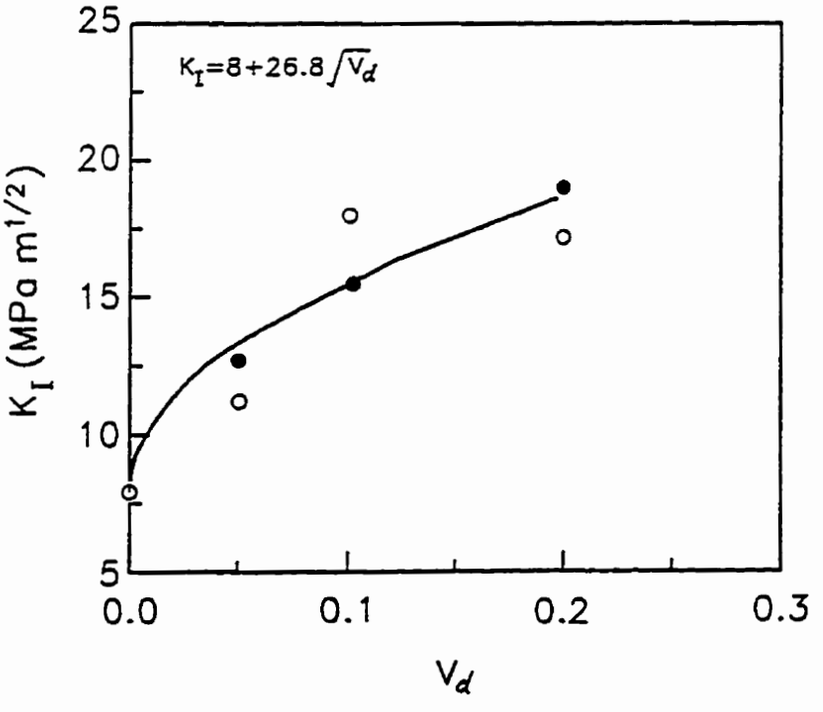

Figure 1.24 Variation in crack-initiation toughness, K_I, with volume fraction, V_d, for both Nb/TiAl and TiNb/TiAl composites (open and filled symbols are separately face and edge of the pancakes-shaped particles) [70].

artificially by blending the γ-TiAl powder with TiNb particles, and consolidated under vacuum at high temperature followed by high temperature forging [70]. As a result the TiNb particles were shaped in a pan-cake form. With respect to volume fraction of TiNb, power-law fit yielded

$$K_I = 8 + 26.8\, V_d^{1/2} \qquad [MPa.\, m^{1/2}] \qquad (1.34)$$

However, it must be pointed out that the scatter of data points in **Figure 1.24**, would probably give a reasonable fit to V_d.

Chan [23] tried to correlate experimental values of K_{Ic} in Ti_3Al-base alloys with his crack-tip blunting model expressed by *Eq.(1.5)*. The value of K_m=12.5 $MPa\sqrt{m}$, for a single phase α_2 alloy [71], was used in *Eq.(1.5)*. Chan [18] used n=18 because most of the alloys exhibited relatively low strain breaking at 25°C. Varying the n value from 8 to 18 resulted in insignificant changes in λ_b ratio. The comparison is shown in **Figure 1.25**. As seen, the scatter of experimental K_{Ic} values is quite substantial which precludes any firm statement about the predictability of *Eq.(1.5)* with respect to fracture toughness. The only conclusion that can be drawn from **Figure 1.25** is that the initiation fracture toughness shows a trend to increase with increasing volume fraction of the ductile phase.

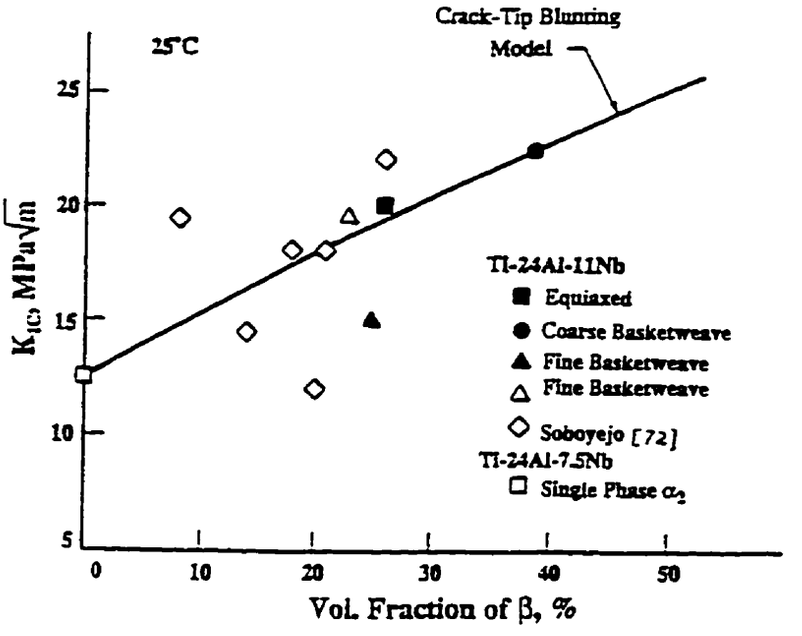

Figure 1.25 Comparison of the crack-tip ductile-phase blunting model with measured K_{Ic} values [18, 23].

Li and Schulson [73] used the model (*Eq.(1.16)*) to check whether the increment of fracture toughness (ΔK_{Ic}) is proportional to the square root of the product of the particle strength, volume fraction and size of particles ($L=a_0$, as shown schematically in **Figure 1.26**) for boron-free and boron-doped Ni-23 at.% Si alloys. However, no effect is apparent as shown in **Figure 1.27**. They stated that possibly, it can be explained in terms of an attendant reduction in the strength of the composite particles, for as the product $(V_d L)^{1/2}$ increased, the volume fraction of the harder Ni_3Si rim decreased, correspondingly, σ_y should have decreased, because hardness and strength are related.

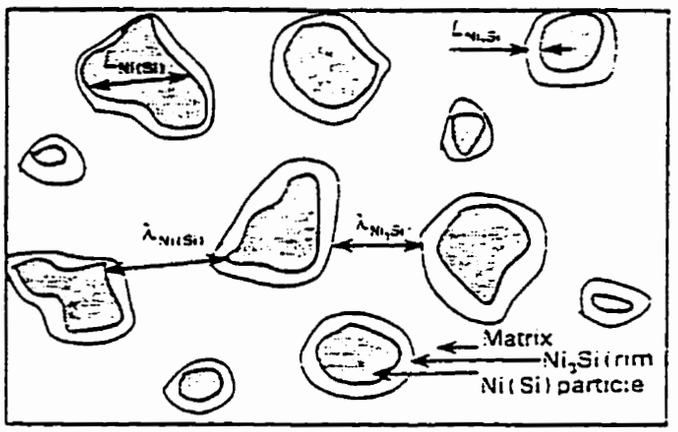

Figure 1.26 Schematic sketch defining the microstructural parameters for a complex nickel silicide containing particles of a ductile phase [73].

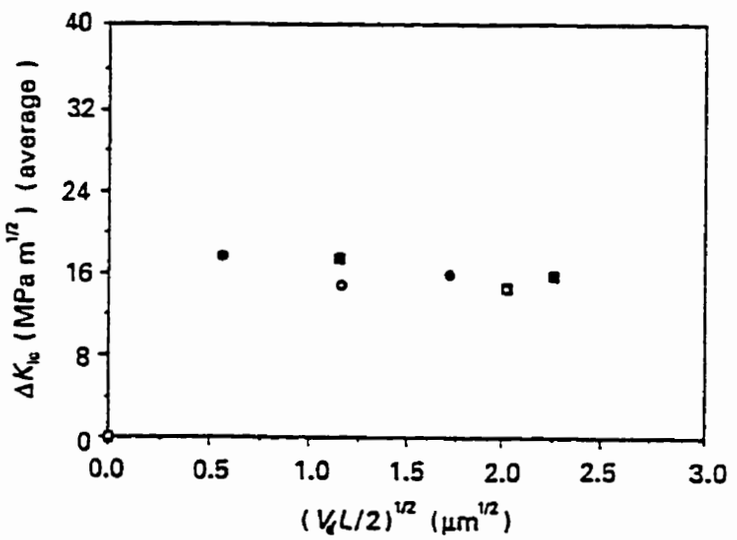

Figure 1.27 Fracture toughness increment as a function of $(V_d L)^{1/2}$. (○, □) Boron-free and (●, ■) boron-doped alloys. Points were obtained using (○, ●), $L=L_{Ni(Si)}$ and (□, ■), $L=L_{Ni(Si)}+L_{Ni3Si}$ [73].

Bencher et al. [44] also used *Eq.(1.16)* to calculate the increase in toughness of the Nb/Nb_3Al composite. Using $V_d \approx 0.4$, $\sigma_y = 90$ MPa, $E = 123$ GPa, Nb lamellar thickness $a_o \approx 1$ μm and $\chi \approx 2.7$ (assuming a well bonded interface), the predicted elevation in toughness from bridging is ≈3.5 MPa√m. Taking K_{Ic} for monolithic Nb_3Al as 1.1 MPa√m [10] and $K_{Ic} = K_m + \Delta K_{Ic}$, the toughness of the Nb/Nb_3Al in-situ composite is ≈4.6 MPa√m, which is slightly lower than the experimental value (5.5 MPa√m). However, it must be noted that according to Chan's rule for extrinsic toughening mechanism [17-18, 23], crack bridging of *Eq.(1.16)* cannot effect the K_{Ic} value of the composite. Obviously, Bencher et al. [44] did not take into account of the Chan's rule [17-18, 23].

Kumar et al. [13] investigated the role of brittle TiB_2 particulates and/or Al_2O_3 whiskers in affecting the toughness of stoichiometric and Ni-rich NiAl as shown in **Figure 1.28**, in which fracture toughness of about 10 vol.% TiB_2 composite is less than that of the matrix (**Figure 1.28a**) but additions of up to 25 vol.% Al_2O_3 whiskers improved the K_{Ic} of stoichiometric NiAl (**Figure 1.28b**).

Enoki and Kishi [57] also found another example in an arc-melted Ti-48 at.% Al composite with a duplex microstructure consisting of equiaxed γ grains and γ/α_2 (TiAl/Ti_3Al) lamellar grains, in which the static fracture toughness decreased with increasing volume fraction of equiaxed γ as shown in **Figure 1.29**. In other words, the toughness of the in-situ composite decreases with increasing volume fraction of brittle γ reinforcement.

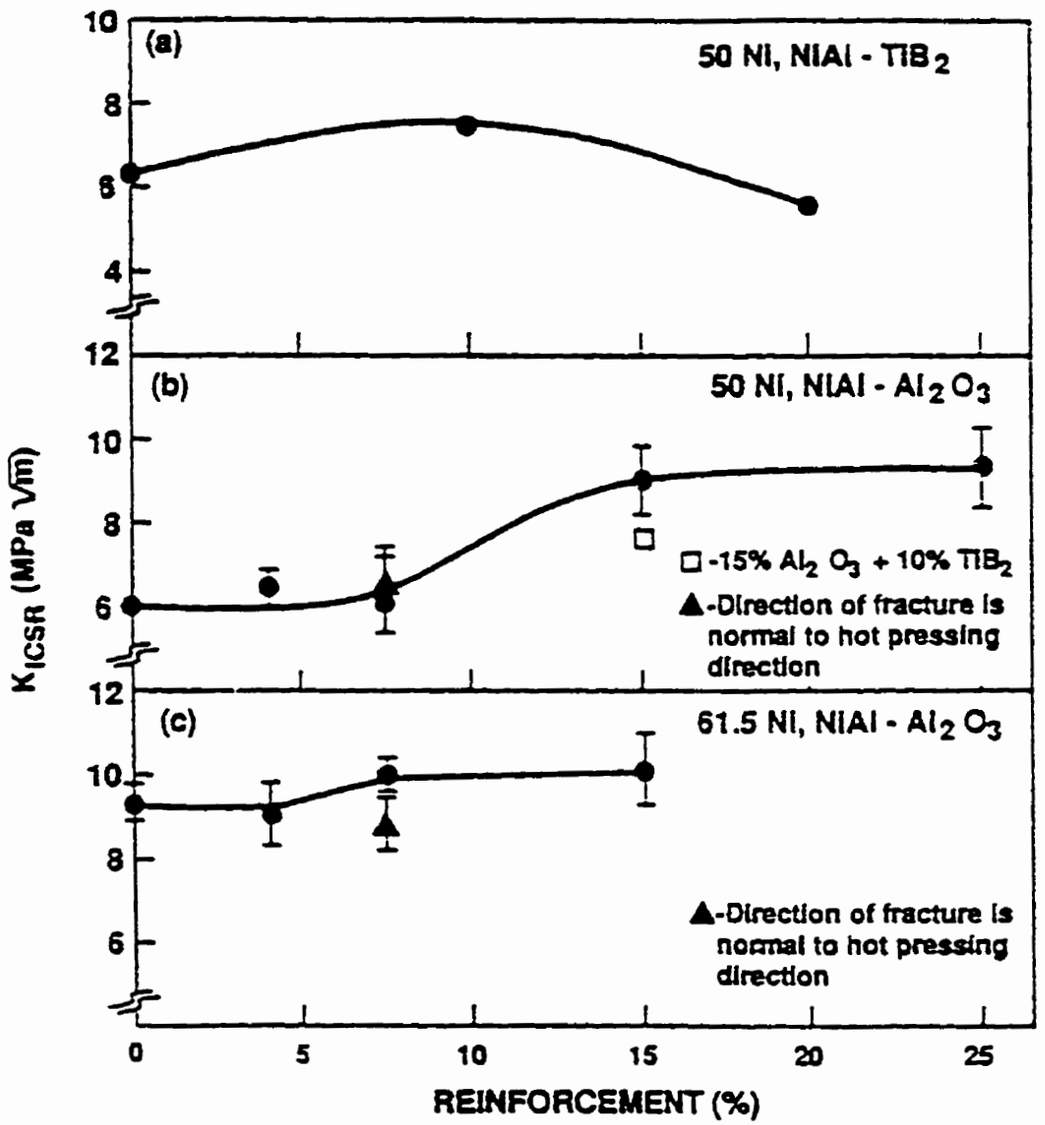

Figure 1.28 Effect of reinforcement type and volume fraction on fracture toughness. (a) Stoichiometric NiAl-TiB_2 particulate composites, (b) stoichiometric NiAl-Al_2O_3 whisker composites, (c) Ni-rich (61.5 at.% Ni) NiAl-Al_2O_3 whisker composites [13].

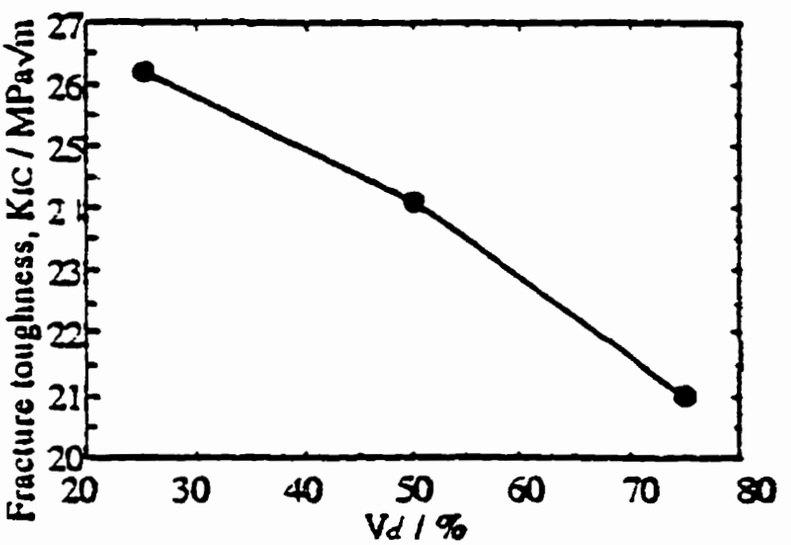

Figure 1.29 Effect of volume fraction of equiaxed γ phase in a duplex TiAl on (a) static fracture toughness [57].

Chan [51] used *Eq.(1.21)* to calculated the crack growth toughness, K_r, in the K-resistance curve (**Figure 1.2**) for the TiAl-base alloys. Comparison of the calculated and observed K_r values is presented in **Figure 1.30**, which shows good overall agreement between theory and experiment. In other words, the crack growth toughness, K_r, also depends on volume fraction as predicted by shear ligament toughening.

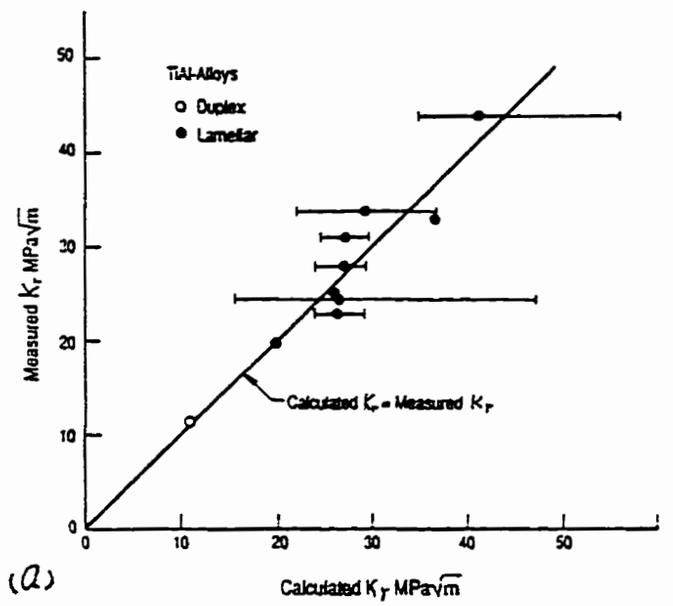

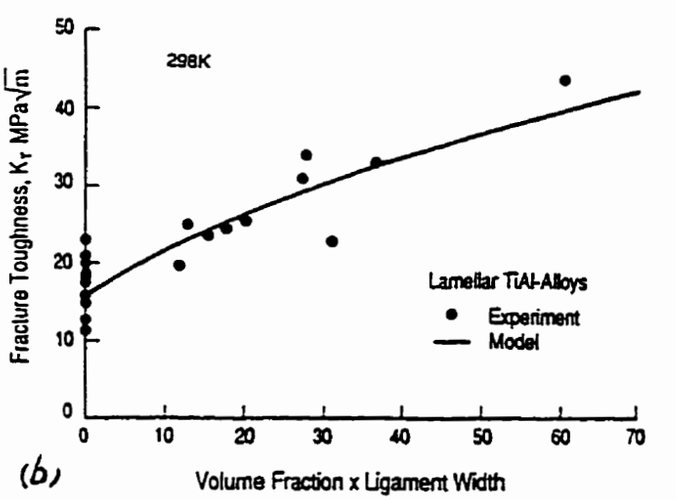

Figure 1.30 (a) Comparison of model calculation and experimental data of crack growth toughness, K_r. (b) Dependence of K_r on the product of volume fraction and width of the crack-wake ligament in TiAl-base alloys [51].

1.3 Alloy System Selection and Statement of Objectives

To meet the demand for new structural materials to be employed in advanced jet engines and other high performance applications, alloys based on several intermetallic systems have been targeted for research [74-76]. One of the most important intermetallics is NiAl which has been targeted for an extensive research over the last five years because the NiAl-based intermetallic composites have a great potential for commercial applications. Fracture toughness evaluations of the NiAl-based materials have been a major topic of recent emphasis [67]. The fracture toughness of polycrystalline NiAl seems to increase by going to Ni-rich composition, within the two phase $\beta+\gamma'$ ($NiAl+Ni_3Al$) field as shown in **Figure 1.22**. The behaviour in **Figure 1.22** suggests a certain relationship between fracture toughness and the volume fraction of a more ductile Ni_3Al (γ') phase embedded in the more brittle NiAl (β) matrix. However, fracture toughness of the alloys in the region from about 62 to 75 at.% Ni is not well researched. As seen in **Figure 1.22** only limited data are available, mostly grouped at around 62 at.% Ni and as mentioned previously the broken line up to 75 at.% Ni in **Figure 1.22** is essentially an extrapolation.

Another problem pertinent to the $NiAl-Ni_3Al$ system is the transformation of β NiAl into martensite upon cooling and formation of the Ni_5Al_3 phase upon subsequent annealing in the Ni-Al system, in the composition range from about 62 to 74 at.% Ni [71-79]. **Figure 1.31** shows a portion of recently evaluated Ni-Al binary system. In this system the nickel-rich NiAl

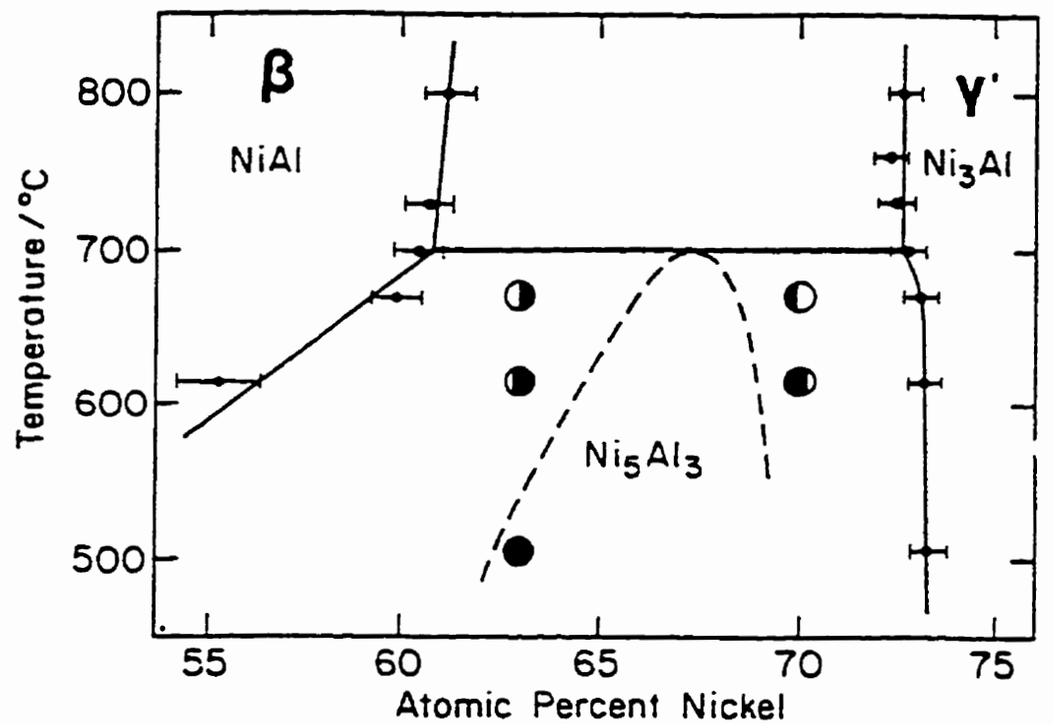

Figure 1.31 Approximate positions of boundaries in the nickel-aluminum phase diagram involving the Ni_5Al_3 [77].

phase existing in the range greater than about 61 at.% Ni, transforms martensitically upon cooling from elevated temperatures [77-79]. As seen, the field of the existence of Ni_5Al_3 is indicated by a broken line. This phase is formed in both 63 and 70 at.% nickel-aluminum alloys on annealing below about 700°C from the martensitically transformed NiAl [77]. In view of the above, the in-situ intermetallic composite alloys existing in the approximate range from 60 to

=65 at.% [77] in **Figure 1.22** could be in reality the mixture of martensitic NiAl and Ni_5Al_3 or regular NiAl and Ni_5Al_3, rather than NiAl and Ni_3Al. Similarly, the alloys in the range from 65 to 74 at.% Ni (**Figure 1.31**) could be the mixture of martensitic NiAl and Ni_3Al or Ni_5Al_3+Ni_3Al rather than NiAl and Ni_3Al.

The third problem is that polycrystalline Ni_3Al is extremely brittle in tension and apt to fail along grain boundaries at room temperature [80-81]. The low ductility of monolithic Ni_3Al, however, has been improved dramatically by microalloying with a small amount of boron. Subsequent studies [82-83] suggested that the role of boron, which was observed to segregate along the grain boundaries, is to enhance the bonding between nickel atoms and result in improvement of grain-boundary cohesion and reduction of the tendency toward brittle intergranular fracture. This is because boron alleviates the effects of moisture in air which in reaction with Al releases atomic hydrogen with, in turn, penetrates the crack tip embrittling it [83]. The boron-doped Ni_3Al exhibited a fracture toughness exceeding 30 MPa.$\sqrt{m}$ [81], however, the toughening mechanisms are still not clear so far.

Therefore, the two phase region NiAl or Ni_5Al_3 + Ni_3Al in **Figure 1.31** was selected as a model in-situ composite system for preliminary investigations of the processing and resulting microstructures. The principal objective of this research is to understand the relations of microstructures, fracture toughness and fracture mechanisms in view of the toughening mechanisms discussed in **Sections 1.1** and **1.2** on the selected system with or without boron doping. In particular, the focus will be on establishing the effect of volume fraction of Ni_3Al on the fracture toughness of the in-situ NiAl/Ni_3Al composites.

1.4 Ni-Rich Part of The Ni-Al Binary System

1.4.1. Phase Diagram

The generally-accepted Al-Ni phase diagram is shown in **Figure 1.32**, in which the Ni rich

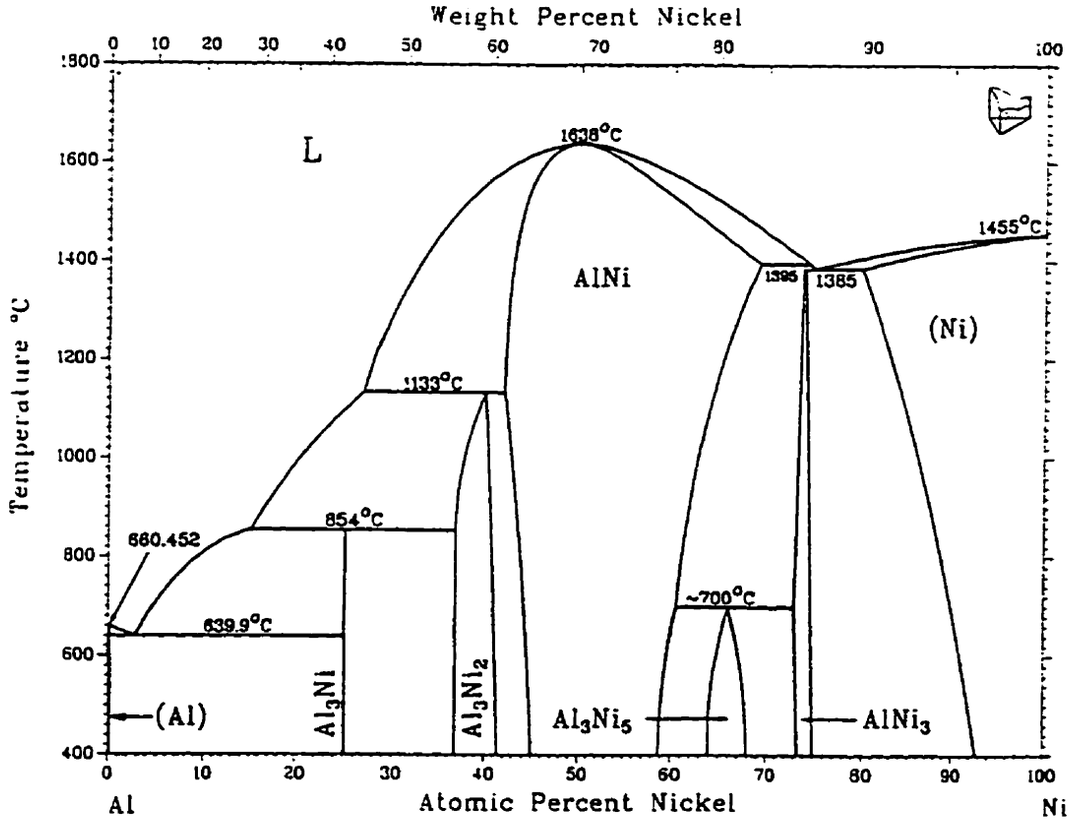

Figure 1.32 Al-Ni phase diagram taken from Massalski (after Singleton et al.) [84].

part has been given the conventional names used in the superalloy literature, β (NiAl), γ′ ($AlNi_3$), Al_3Ni_5 and γ (Ni). The equilibria between these phases involve the following three reactions,

1. peritectic: **$L + \beta\ (AlNi) \leftrightarrow \gamma'\ (AlNi_3)$** **at 1395°C;**

2. eutectic: **$L \leftrightarrow \gamma\ (Ni) + \gamma'\ (AlNi_3)$** **at 1385°C;**

3. peritectoid: $\beta\ (AlNi) + \gamma'\ (AlNi_3) \leftrightarrow Al_3Ni_5$ at 700°C.

The compositions of phase boundaries between these phases are approximately 58.8 at.% Ni at $\beta/(\beta+Al_3Ni_5)$, 63.9 at.% Ni at $(\beta+Al_3Ni_5)/Al_3Ni_5$, 67.9 at.% Ni at $Al_3Ni_5/(Al_3Ni_5+\gamma')$, and 73.3 at.% Ni at $(Al_3Ni_5+\gamma')/\gamma'$, in **Figure 1.32.** However, some recent studies [85-87] agree with the older Ni-rich portion of the diagram due to Schramm [88], which show

1. peritectic: **$L + \beta\ (AlNi) \leftrightarrow \gamma'\ (AlNi_3)$** **at 1362°C;**

2. eutectic: **$L \leftrightarrow \gamma\ (Ni) + \gamma'\ (AlNi_3)$** **at 1360°C;**

3. peritectoid: $\beta\ (AlNi) + \gamma'\ (AlNi_3) \leftrightarrow Al_3Ni_5$ at 700°C.

Along the increasing of Ni at.% content, the eutectic reaction occurs first instead of the peritectic one as shown in **Figure 1.33.**

In 1991, Verhoeven et al. [87] proposed a portion of the Ni-Al phase diagram (**Figure 1.34**), which supports the result in **Figure 1.33.** However, as shown in **Figure 1.34**, the eutectic and peritectic temperatures are higher than those in **Figure 1.33**, but lower than those in **Figure 1.32.**

In 1994, Lee et al. [89] estimated the position of the γ'/β eutectic in the Ni-Al system. It is

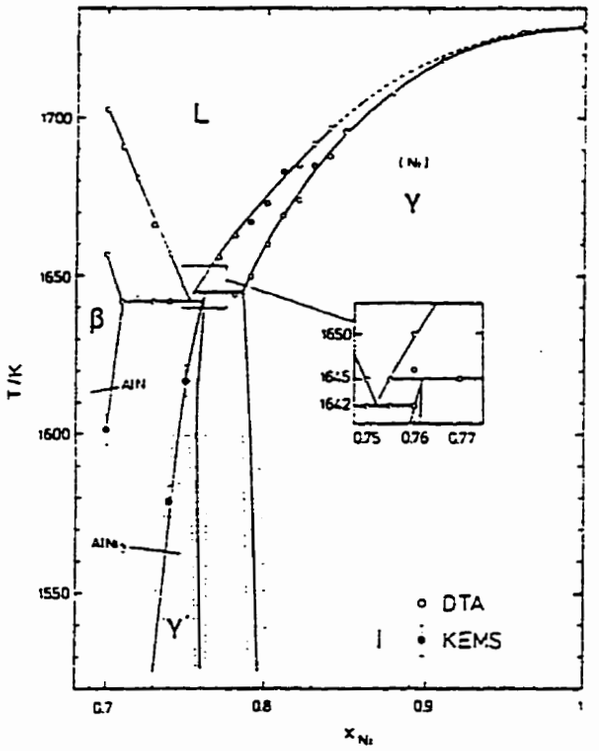

Figure 1.33 Ni rich part of the Al-Ni phase diagram taken from Hilpert et al. [85].

found that the equilibrium β/γ' eutectic is located at 75.4% Ni (24.6% Al) and the metastable β/γ' eutectic is at 75.5% Ni (24.5% Al) as shown in **Figure 1.35.**

Khadkikar et al. [90] also carried out a quantitative phase analysis to establish the (NiAl + Ni_5Al_3)/Ni_5Al_3 phase boundary location as shown in **Figure 1.36.** The composition of the phase boundary is around 59.5 at.% Ni at (NiAl + Ni_5Al_3)/Al_5Ni_3. Obviously, the established

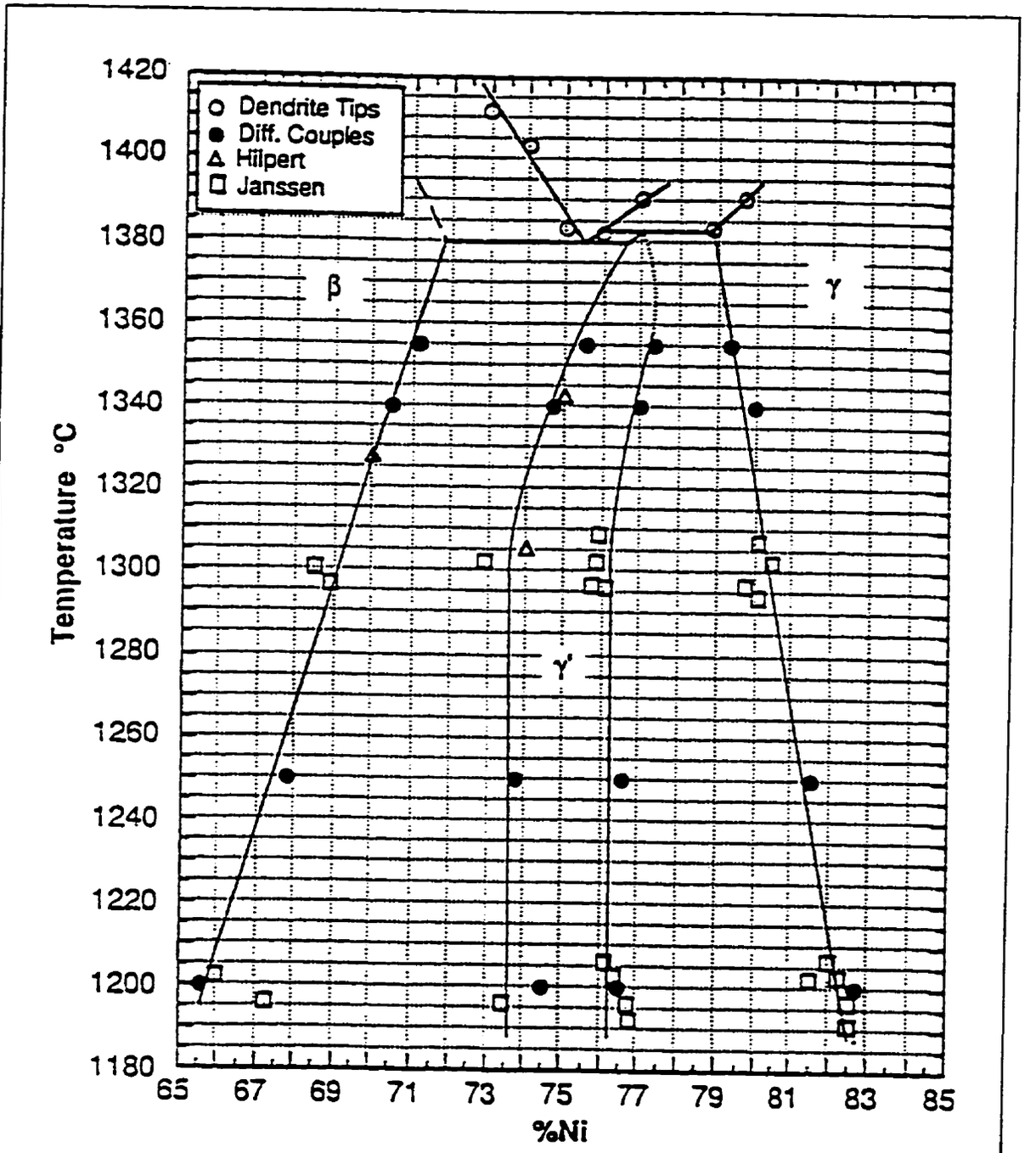

Figure 1.34 Ni-rich portion of the Al-Ni phase program taken from Verhoeven et al. [87].

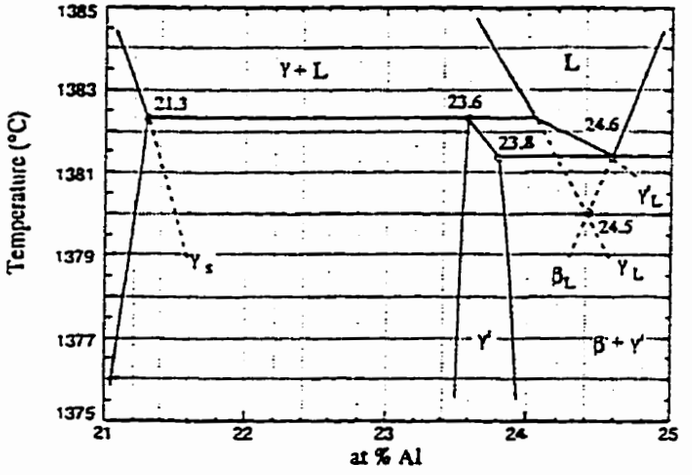

Figure 1.35 Estimated position of the metastable γ'/β eutectic in the Ni-Al system [89].

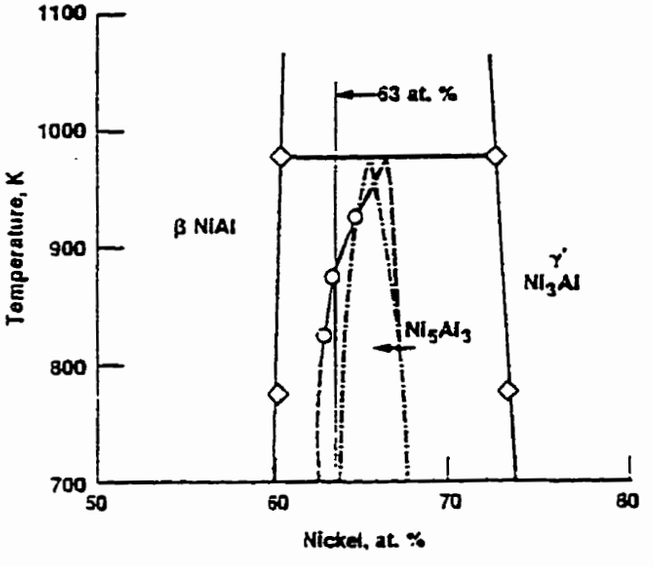

Figure 1.36 Portion of the Al-Ni phase program established by Khadkikar et al. [90].

phase boundary is on the nickel-rich side compared to **Figure 1.32.** It must be mentioned that the alloys used by Khadkikar et al. [90] were produced by a powder metallurgy process.

As mentioned above, the more recent proposition for the complete Al-Ni phase diagram is shown in **Figure 1.37.** This is essentially the same one as developed by Singleton et al. [84] with the following modifications. Comparing **Figure 1.37** and **Figure 1.32,** we could see that the melting point of stoichiometric NiAl, while still assumed to be congruent, is approximately 44K greater than previously reported [91]. This higher liquidus temperature also has been confirmed by Noebe [24] on both single crystal and prealloyed powder NiAl materials. The peritectoid reaction, resulting in the formation of Ni_5Al_3, is approximately 25K higher in temperature [92] (725°C vs 700°C as in Refs. [86, 90]) and the boundary for the Al-rich side of the Ni_5Al_3 phase has been modified based on the result by Khadkikar [90] (**Figure 1.36**). The most significant changes in this version of the phase diagram, however, concern the Ni_3Al region. The position of the eutectic and peritectic reactions are reversed. The changes to the Ni_3Al portion of the phase diagram are based on significant experimental work by Bremmer et al. [86] and are in agreement with previous work by Schramm [88].

So far, however, the exact equilibrium positions of $\beta/(\beta+Al_3Ni_5)$, $(\beta+Al_3Ni_5)/Al_3Ni_5$, $Al_3Ni_5/(Al_3Ni_5+\gamma')$, and $(Al_3Ni_5+\gamma')/\gamma'$ boundaries are still uncertain.

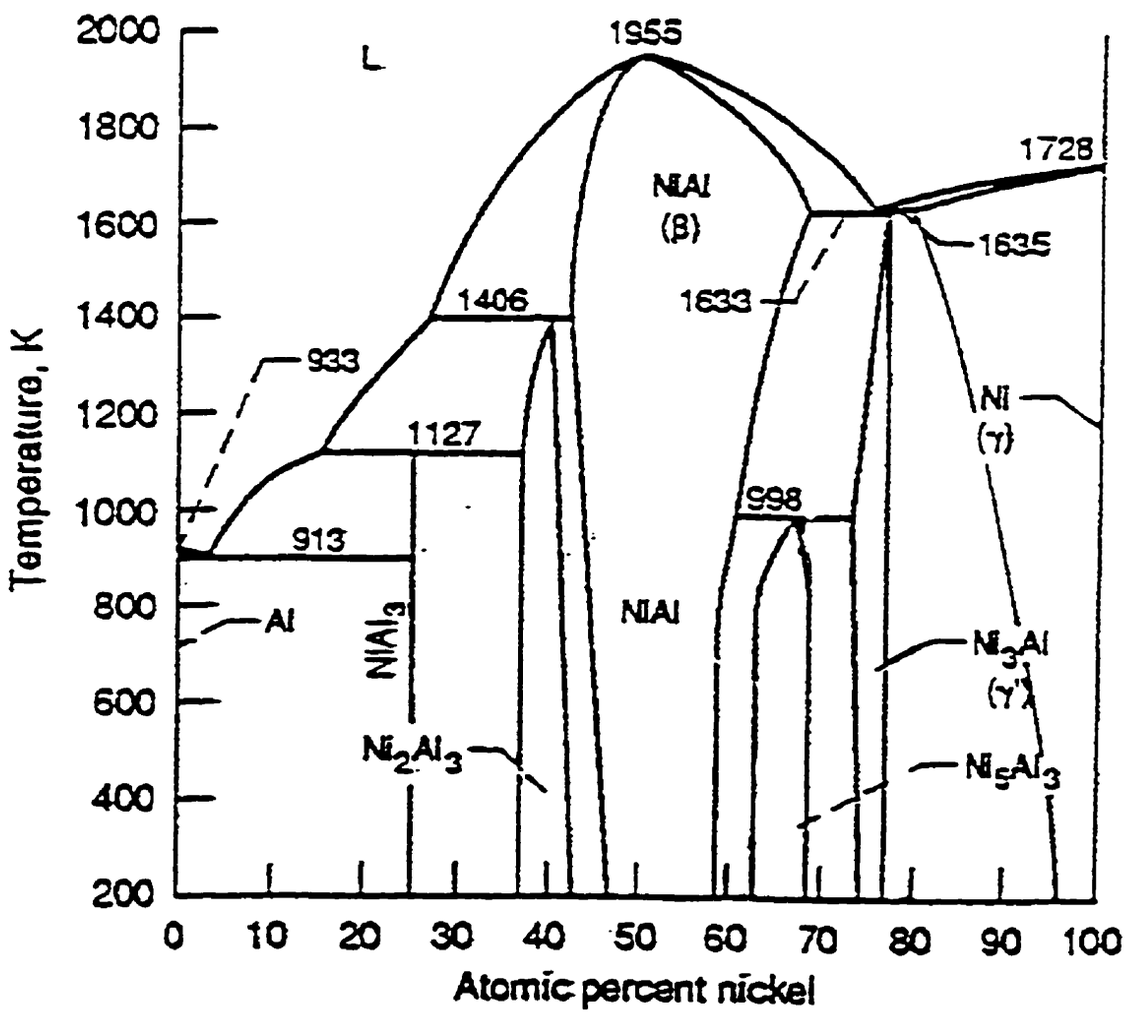

Figure 1.37 Al-Ni phase diagram taken from Noebe [24].

1.4.2. Transformations and Microstructures in the Ni-Rich Ni-Al System

Martensitic Transformation on Cooling

The martensitic transformation upon cooling results in the formation of $L1_0$ martensite with either ABC (*3R*) stacking or ABCABAC (*7R*) stacking [86, 90]. The β and *3R* structures are the same except for the c/a ratio (f.c.t. indexing) [90]. The transformation sequence from NiAl to Ni_5Al_3 is depicted in **Figure 1.38**. The Ni-rich B2 NiAl, with excess nickel atoms on aluminum sites, undergoes Bain distortion and transforms to $L1_0$ martensite upon quenching. A simple ordering of the nickel atoms on the aluminum sublattice (which can take place at low temperatures) is required to transform the martensitic structure to Ni_5Al_3. A summary of the available data for the dependence of the measured M_s temperatures on NiAl alloy composition is shown in **Figure 1.39**. A compilation of the literature data on transformation temperature as a function of composition indicates large discrepancies (120K) in the measured M_s temperatures in NiAl alloys. A rather steep dependence of the M_s temperature on alloy composition exacerbates the error in measurement of both the M_s temperature and the alloy composition [90].

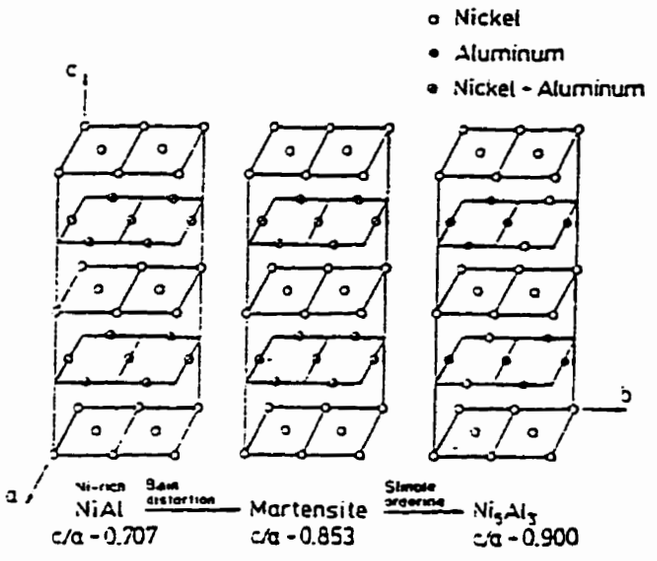

Figure 1.38 Transformation sequence from NiAl to Ni_5Al_3 [93].

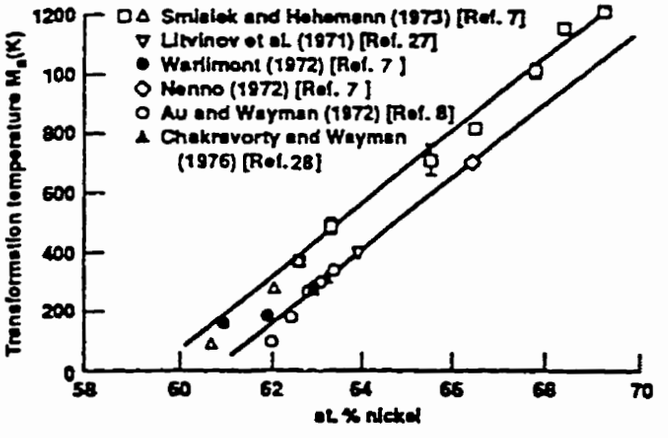

Figure 1.39 Summary of available data on the dependence of M_s temperature on alloy composition [90].

Annealing and Aging

A typical example of the microstructure that results from annealing of an arc-melted alloy ($Ni_{64}Al_{36}$) for 10 hours at 727°C to increase the amount of γ' present (the method of cooling, i.e., furnace or air cooling is not given in Ref.[24]), is shown in **Figure 1.40**. It is evident that γ' preferentially nucleates at the grain boundaries forming a continuous film around the β grains, a microstructure that is now commonly referred to as a "necklace microstructure" [94].

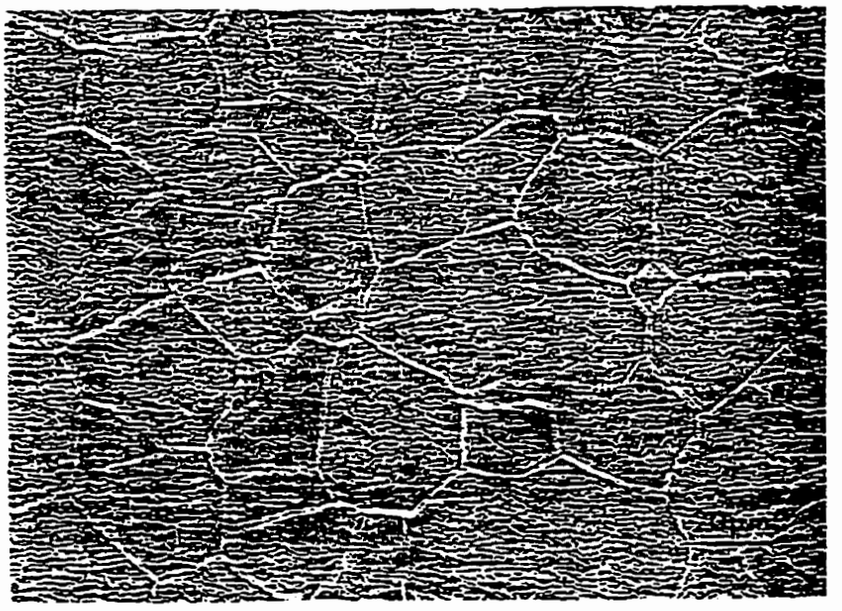

Figure 1.40 Backscatter SEM micrograph of an extruded alloy $Ni_{64}Al_{36}$ annealed at 727°C for 10 hours resulting in a necklace microstructure of γ'. The alloy was processed by directional solidification or extrusion (927°C) of prealloyed metal powders [24].

The particles within the NiAl grains are Ni_3Al. This result is consistent with the NiAl portion of the Ni-Al diagram in **Figures 1.22** and **1.40**. However, peritectoid temperature is 725°C in **Figure 1.37**. It means that the annealing at 727°C would occur almost at peritectoid temperature and it is not clear why it might not have led to the formation of Ni_5Al_3.

Robertson and Wayman [93, 95, 96] investigated the $Ni_{63}Al_{37}$ and $Ni_{70}Al_{30}$ alloys (at.%) which were obtained in the form of cast rods [95]. After annealing at temperatures of 1100°C for the 63% Ni alloy and 1300°C for the 70% Ni alloy and water-quenching, as pointed out by the authors [96], the former was entirely β phase, while the latter contained both β and γ' phases. Then, according to the authors [96], the 63% Ni sample aged at 505°C became single-phase Ni_5Al_3, which was found to be stable below about 700°C.

Khadkikar et al. [78-79] investigated microstructures in $Ni_{70.3}Al_{28.8}$ and $Ni_{64.4}Al_{34.7}$ (at.%) alloys, also containing less than 0.9 at.% of Hf and 0.1 at.% of boron, as well as $Ni_{63.05}Al_{36.93}$ (with major impurity of 0.045 wt.% oxygen) alloy, produced by a powder metallurgy process. These hot-extruded microstructures can be modified dramatically by suitable heat treatments. **Figure 1.41** shows the microstructures of the alloy A ($Ni_{70.3}Al_{28.8}$) and alloy B ($Ni_{64.4}Al_{34.7}$) after various heat treatments. At the homogenization temperature of 1250°C, according to phase diagrams in **Figure 1.32** and **Figure 1.37**, the alloy A transforms to a mixture of Ni_3Al plus NiAl phases with the compositions of the respective phase boundaries and the alloy B completely transforms to Ni-rich NiAl. Upon rapid cooling from this temperature, the alloy A transforms to a two phase mixture of NiAl martensite (*3R*-type) plus NiAl (**Figure 1.41a**) whereas the Ni-rich ß-phase in alloy B transforms completely to *3R* martensite (**Figure 1.41d**).

After the above heat treatments and upon additional aging at 850°C (above the peritectoid temperature, see **Figures 1.32** and **1.37**), both of alloys A and B should be transformed to Ni_3Al plus NiAl phase mixtures (**Figures 1.41b** and **e**) as one would expect from the phase diagrams presented in **Figures 1.32** and **1.37**. Unfortunately, it is not clear in **Figure 1.41e** where the Ni_3Al phase is located. However, aging at 600°C (below the peritectoid temperature in **Figure 1.37**) after quenching will result in the formation of Ni_5Al_3 phase. Hence, the alloy A transforms to Ni_5Al_3 plus Ni_3Al (**Figure 1.41c**) whereas, the alloy B transforms to Ni_5Al_3 plus NiAl (**Figure 1.41f**). The proportions of the two phases vary and approach equilibrium with aging time. All of the above resultant microstructural phases were detected by X-ray diffraction [78]. However, the exact volume fractions of each of the phases and the compositions of the Ni_5Al_3 phase are in question since the phase boundaries between $\beta/(\beta+Al_3Ni_5)$, $(\beta+Al_3Ni_5)/Al_3Ni_5$, $Al_3Ni_5/(Al_3Ni_5+\gamma')$, and $(Al_3Ni_5+\gamma')/\gamma'$ in **Figures 1.32** and **1.41** are not exactly known and are based on only a few data points [96].

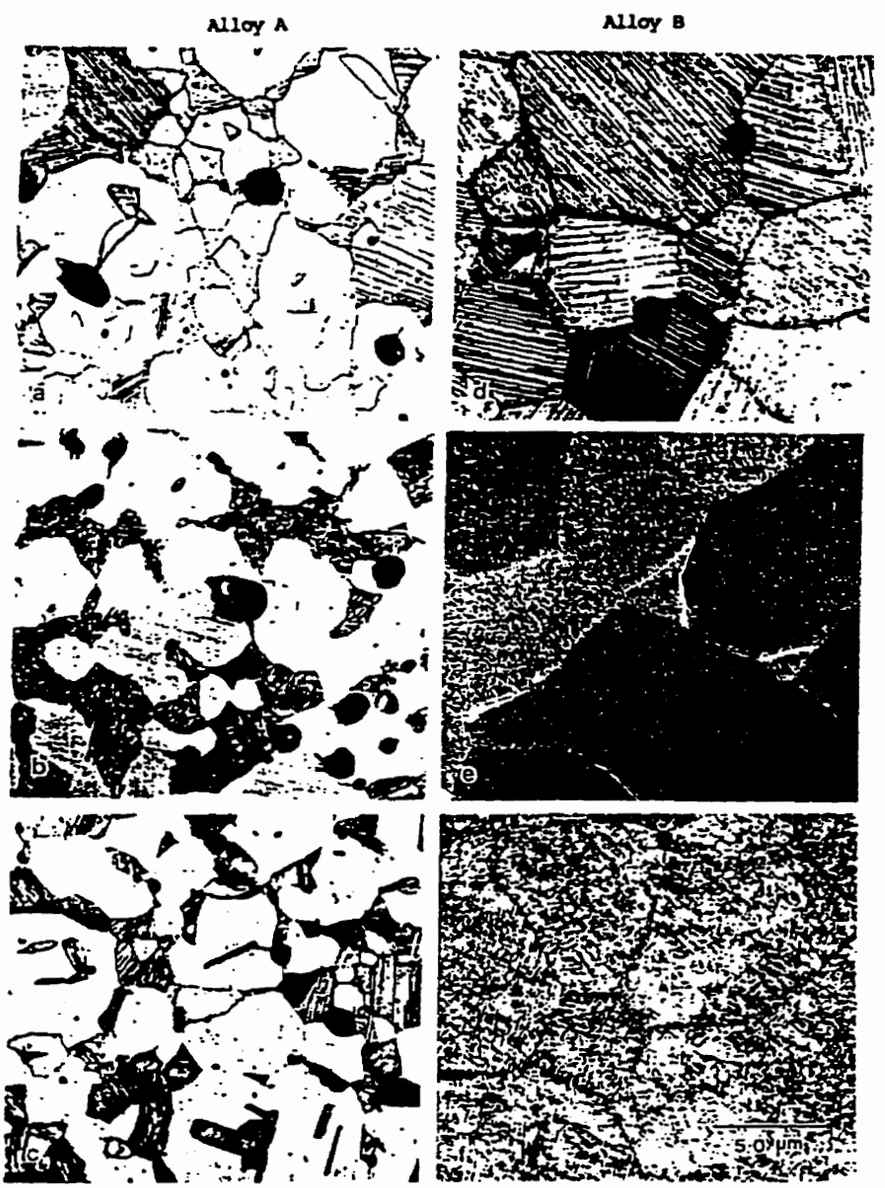

Figure 1.41 Microstructures of alloys A ($Ni_{70.3}Al_{28.8}$) and B ($Ni_{64.4}Al_{34.7}$) after various heat treatments. (a) and (d) 1250°C/24 hr, water quenched, (b) and (e) 1250°C/24 hr, water quenched plus 850°C/24 hr, (c) and (f) 1250°C/24 hr, water quenched plus 600°C/24 hr [78]. However, the method of cooling after aging was not mentioned in ref.[78].

Figure 1.42 illustrates typical microstructures in alloy B ($Ni_{64.4}Al_{34.7}$), which was annealed at 1250°C for 4h, water-quenched (**Figure 1.42a**) and aged at 550°C for 15 days (**Figure 1.42b**) [79]. The NiAl martensite is heavily twinned (**Figure 1.42a**) and the Ni_5Al_3 has a very distinct needle-like microstructure (**Figure 1.42b**). This sequence of transformation can be

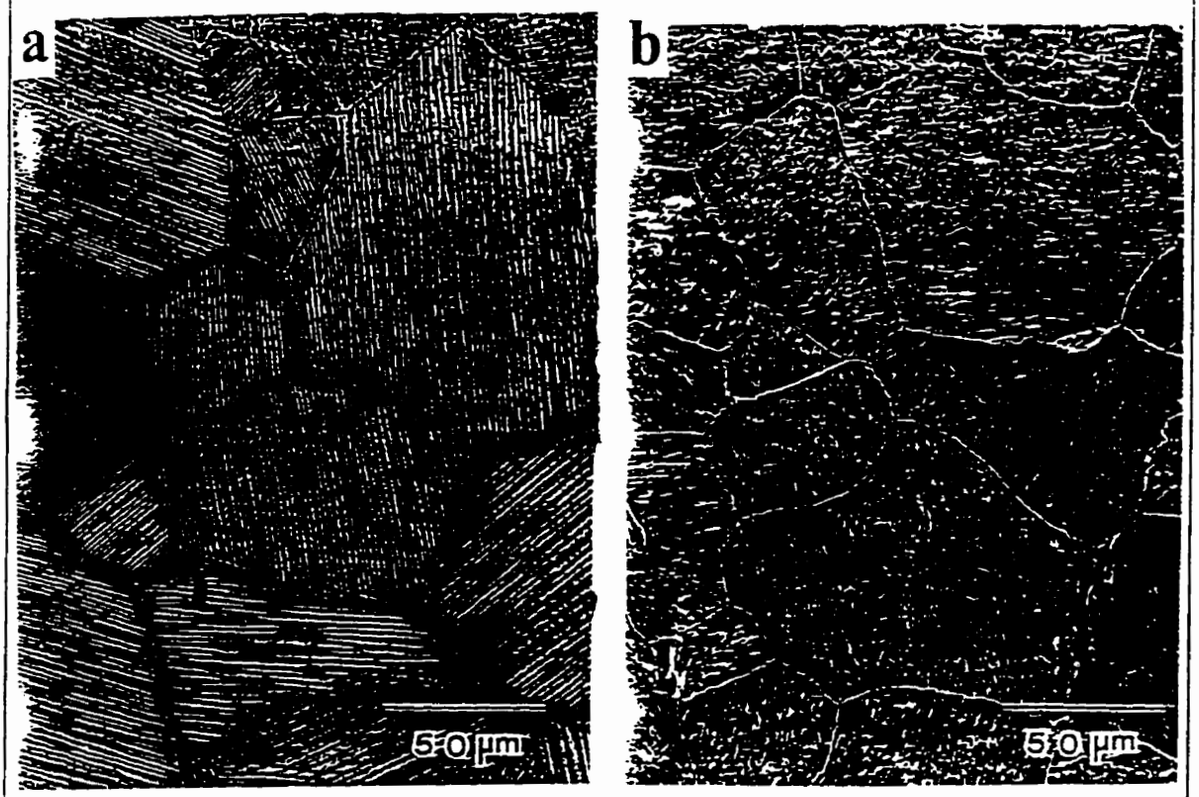

Figure 1.42 Optical microstructure of the $Ni_{64.4}Al_{34.7}$ alloy for (a) specimen homogenized at 1250°C for 4h and probably water quenched according to the text; (b) specimen homogenized at 1250°C for 4h and probably water quenched according to the text, and aged at 550°C for 15 days [79].

described in such a manner that the Ni_5Al_3 phase results from a transformation of $L1_0$ martensite upon aging at lower temperatures (up to approximately 700°C) whereas the martensite was formed by water-quenching the Ni-rich NiAl alloy that is stable at high temperature. The interesting point is that a small amount of NiAl was found to retain in equilibrium with Ni_5Al_3 even after aging for 15 days at 550°C. According to the phase diagrams in **Figures 1.32** and **1.37**, no NiAl should exist at equilibrium at the composition of 64.4 at.% nickel after aging at 550°C only single phase Ni_5Al_3. These observations indicate that the position of the $Ni_5Al_3/(Ni_5Al_3 + NiAl)$ phase boundary is uncertain. This is no surprise since the phase boundary indicated in **Figures 1.32** and **1.37** is actually based on only a few data points for the Ni_5Al_3 phase from the original study [96]. Also the transformation to Ni_5Al_3 might be very sluggish and aging time at 550°C was insufficient.

The microstructures of $Ni_{63.05}Al_{36.93}$ alloy in water-quenched (after homogenizing at 1250°C for 4h) and aged (550°C, 600°C and 650°C for 720h; 550°C for 1 to 360h) conditions are shown in **Figures 1.43-1.45**. The presence of parent B2-NiAl phase in the optical micrograph shows that the martensitic transformation has not been completed at room temperature (**Figure 1.43a**). Of particular interest are the clean (i.e., no grain boundary phase) grain boundaries seen in the *SEM* micrograph of **Figure 1.43b**.

The *SEM* micrographs show that mat-like microstructures are observed in the specimens aged at both 600°C and 650°C (**Figure 1.44**), the aging at the higher temperature results in a coarser microstructure. X-ray diffraction traces showed that a nearly complete transformation

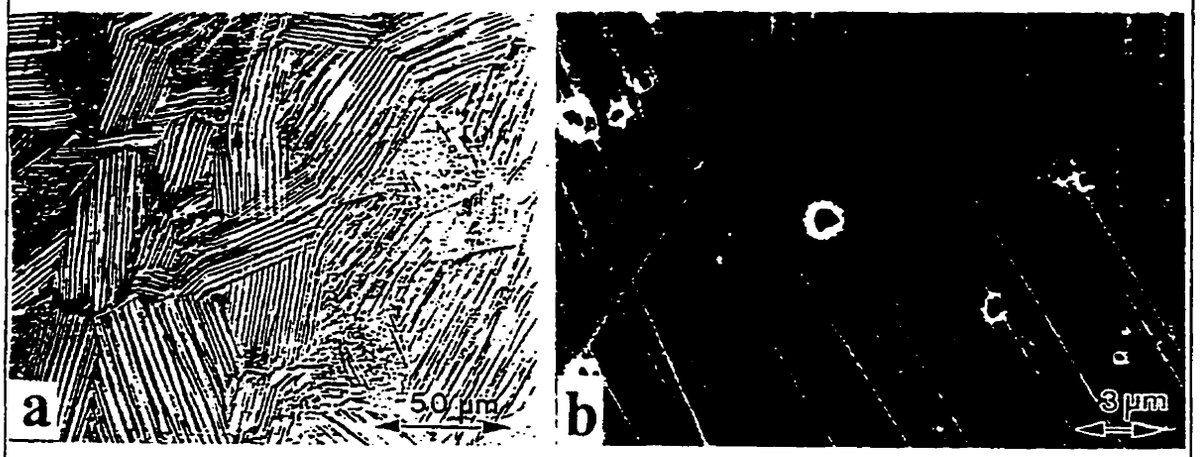

Figure 1.43 (a) Optical micrograph and (b) SEM images showing the microstructure of the $Ni_{63.05}Al_{36.93}$ alloy in the as-quenched condition after 1250°C/4h) [90].

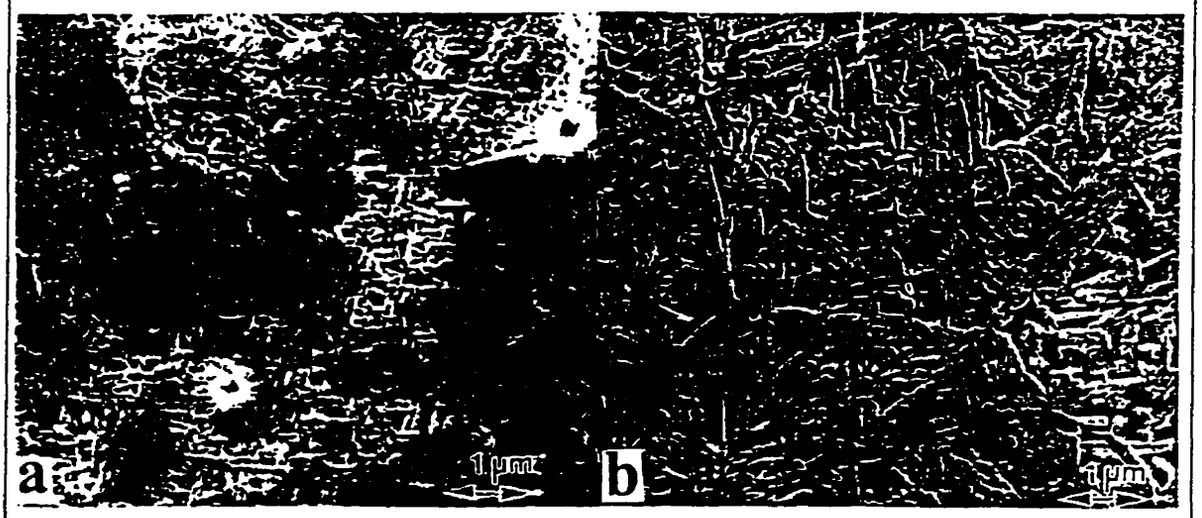

Figure 1.44 SEM images showing the microstructure of the $Ni_{63.05}Al_{36.93}$ alloy in the as-aged conditions (720h), (a) 550°C and (b) 650°C after homogenizing at 1250°C/4h and water-quenching [90].

to Ni_5Al_3 occurred with only a minor amount of NiAl but a two-phase microstructure consisting of most probably Ni_5Al_3 and NiAl is still observed upon aging at 600°C and 650°C (**Figure 1.44**). The short-time aging was carried out in order to understand the microstructural evolution of transformation to Ni_5Al_3. The short-time aging produced a very complex microstructure due to the presence of multiple phases (**Figure 1.45**). Two distinct phases, a blocky grain boundary phase and a platelet-like grain interior phase, appear to grow with aging time. According to the authors [90], these platelet-like precipitates in the grain interior were identified from electron diffraction patterns to be new variants of the *3R* martensite. The *3R* martensite increased in number as a function of aging time. The matrix surrounding the platelet 3R precipitate was identified as *7R* martensite, as shown in the BF image of **Figure 1.46** with its corresponding diffraction pattern [90].

The blocky grain boundary phase were identified as to Ni_5Al_3. The volume fraction of NiAl transformed to the Ni_5Al_3 phase plotted versus aging time at 550°C is shown in **Figure 1.47**. The transformation curve generated has an S shape indicating cellular transformation kinetics [90].

As discussed above, transformation to Ni_5Al_3 can occur either from B2-NiAl or $L1_0$ martensite as the parent phase aging below 700°C for the alloy of 63-70 at.% Ni content. In addition, simultaneous hot-stage microscopy experiments indicated that the nucleation of Ni_5Al_3 occurs at the NiAl grain boundaries after 2 hours of exposure at 600°C [90].

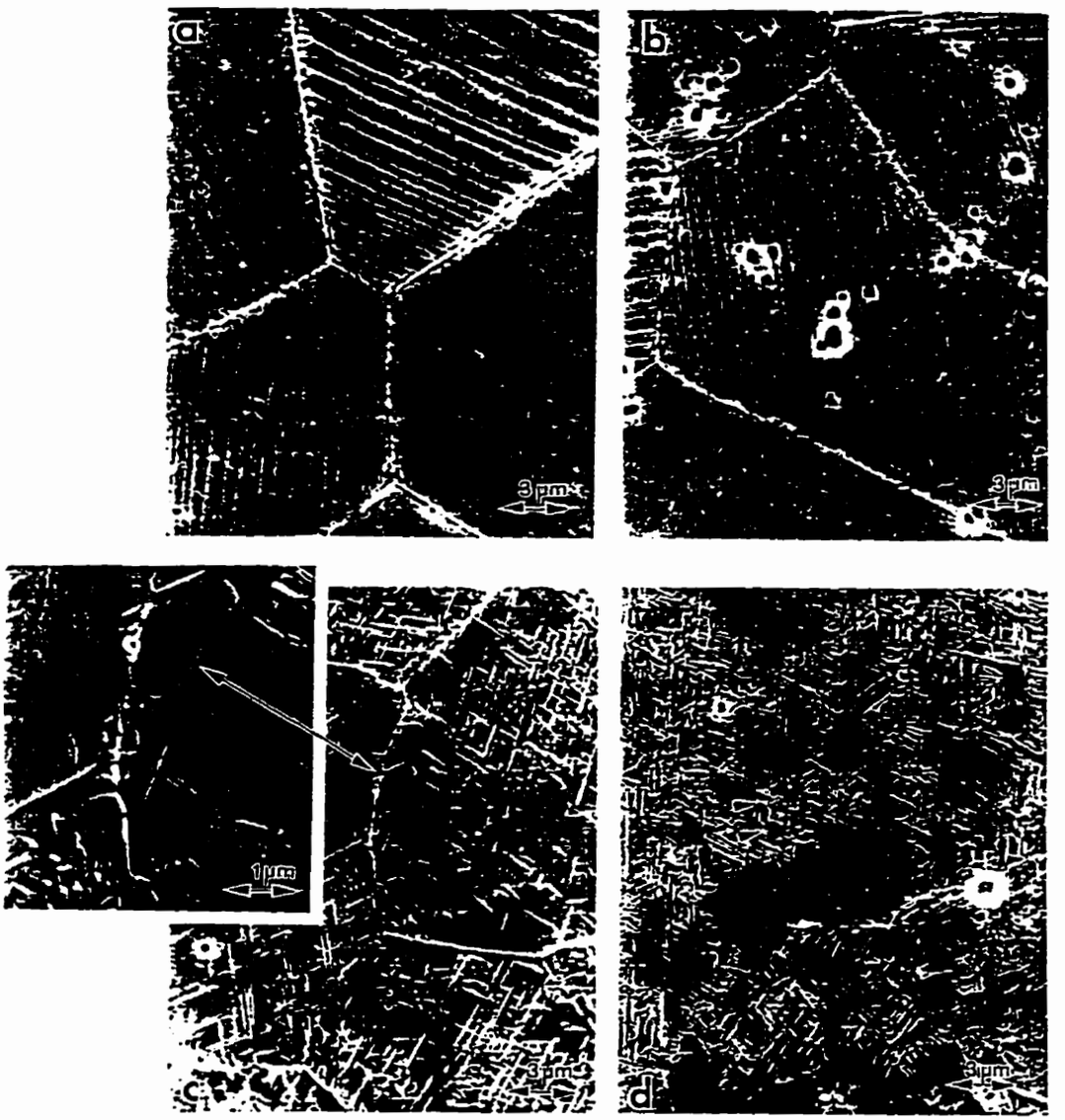

Figure 1.45 SEM images showing the microstructure of the $Ni_{63.05}Al_{36.93}$ alloy in the short-time, as-aged conditions (550°C), (a) 1h, (b) 4h, (c) 12h, and (d) 72h. Note the mat-like structure in (c) and (d) and grain boundary precipitation [90].

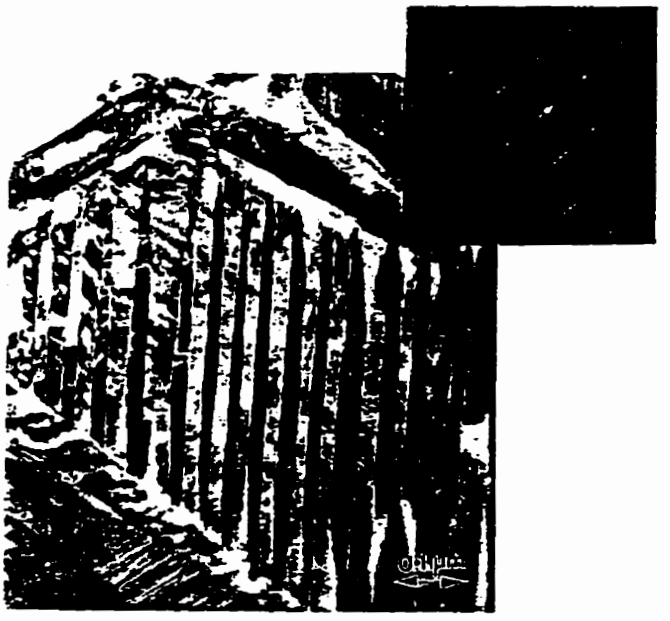

Figure 1.46 BF TEM image showing the 7R martensite matrix observed in the specimen aged for 12h at 550°C. A selected area diffraction pattern of the 7R martensite is also shown [90].

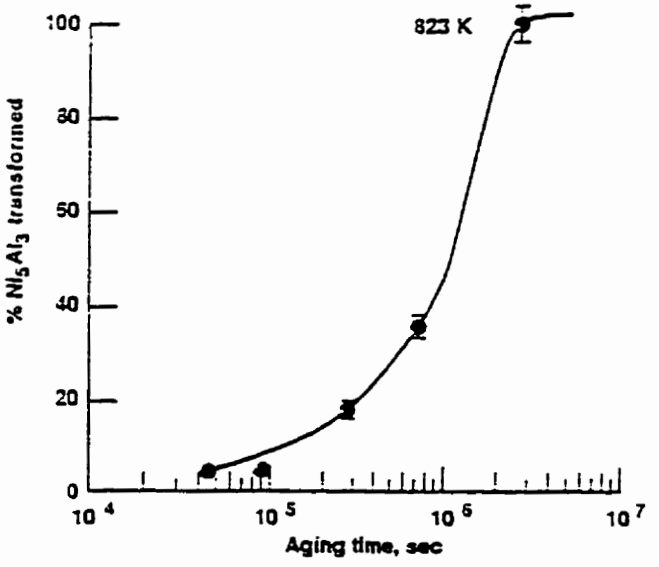

Figure 1.47 (111) peak area as a function of aging time at 550°C indicative of the increase in volume fraction of the Ni_5Al_3 phase [90].

CHAPTER 2

EXPERIMENTAL PROCEDURE

2.1 The Specimen-Dimension Design for a Bending Test

According to the existing *ASTM* standards *E 399-90* [97], *E 1304* [98] and *E 813-89* [99], a small-size notch-bend test as shown in **Figure 2.1** will be prepared for the investigation of the fracture toughness of the in-situ composites. The reason is that this specimen configuration is much simpler to fabricate and test, the least amount of material required and more flexible with respect to size compared to other specimen configurations [97-99].

The bend specimen can be loaded in three-point or four-point loading. In four-point loading the specimen alignment is not very critical because of the constant moment between the inner loading points (**Figures 2.1b** and **d**). Also, additional interaction between the load roller stress field and the crack stress field, which can happen in three-point loading (**Figure 2.1a**), is avoided [38, 100, 101]. However, more material will be needed because of the additional span (S_2) and the diameter of the rollers. A three-point loading is preferred for this test as will be discussed further.

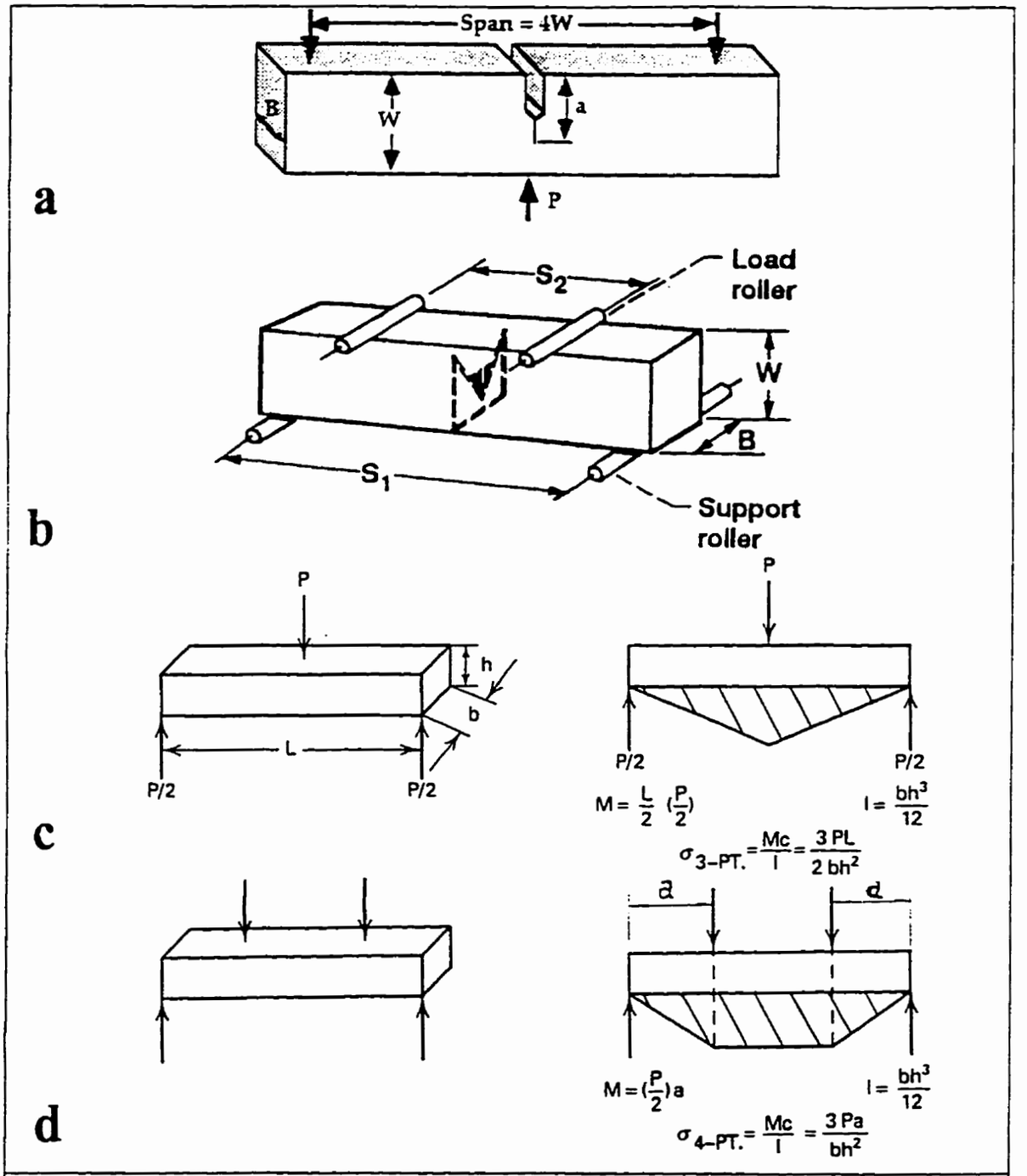

Figure 2.1 The profiles of the two specimen types: (a) single-edge-precrack-beam (SEPB) by three-point loading [38] (b) chevron-notch-beam (CNB) by four-point loading [101]. Bending and tensile stress formulae and distribution: (c) three-point loading (d) four-point bending [100].

2.1.1 The Validity Requirements for a K_{Ic} test

The concept of plane-strain fracture toughness K_{Ic} of materials has been widely used since it was first formulated by Irwin in 1958 [102-103]. So far, for small-size notch-bend specimen tests to measure K_{Ic} directly, there are two different notch-producing fracture testing methods more popular recently such as (1) Single-Edge Precracked Beam (SEPB) [38, 104] as shown in **Figure 2.2**, (2) Chevron-Notch Beam (CNB) (**Figure 2.1b**), since for both specimens costly fatigue precracking could be avoided [104-106].

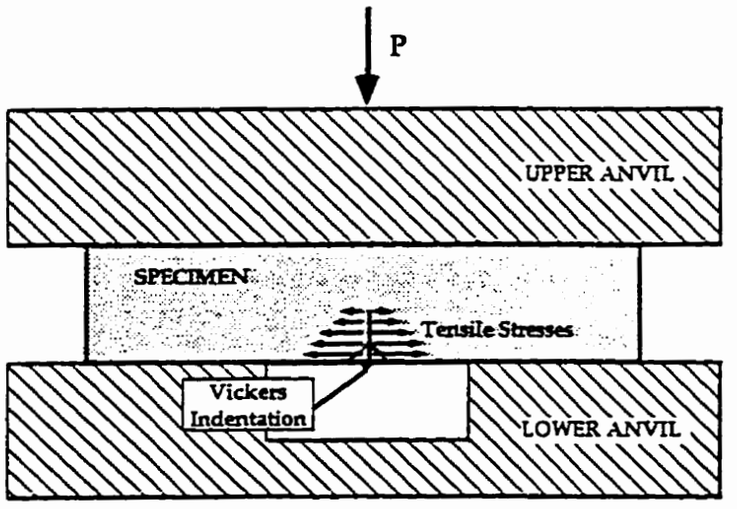

Figure 2.2 Schematic of single-edge-precracked-beam (SEPB) [38, 104]. A crack starter, i.e., a Vickers indentation or a straight-through notch [104].

Plastic Zone Size in an Elastic-Plastic Material

There seems to be general agreement that properly designed and tested bend specimens should provide good measurements of K_{Ic}, provided the specimen conforms sufficiently well to the assumptions of linear elastic fracture mechanics (*LEFM*). For the in-situ composites, the most important *LEFM* assumption is that there is negligible plasticity in the specimen. In other words, the *LEFM* criterion is satisfied only when the specimen size is very large compared to that of crack-tip plastic zone size which is characteristic of the material of which the specimen is made. Then it is essential to know the plastic zone size in a real material before designing a fracture toughness test.

Based on the theory of linear-elasticity, the stress field caused by tension loading (opening mode I), near the crack tip in a linear-elastic, isotropic and infinite plate as shown in **Figure 2.3**, can be shown as the following equations [38, 107-108]:

$$\sigma_x = \frac{K_I}{(2\pi r)^{1/2}} \cos\frac{\theta}{2}\left[1 - \sin\frac{\theta}{2}\sin\frac{3\theta}{2}\right] + \ldots \tag{2.1}$$

$$\sigma_y = \frac{K_I}{(2\pi r)^{1/2}} \cos\frac{\theta}{2}\left[1 + \sin\frac{\theta}{2}\sin\frac{3\theta}{2}\right] + \ldots \tag{2.2}$$

$$\tau_{xy} = \frac{K_I}{(2\pi r)^{1/2}} \cos\frac{\theta}{2}\sin\frac{\theta}{2}\sin\frac{3\theta}{2} + \ldots \tag{2.3}$$

$$\sigma_z = 0 \quad \textit{(plane stress)} \tag{2.4}$$

$$\sigma_z = \nu(\sigma_x + \sigma_y) \quad \textit{(plane strain; } \varepsilon_z = 0) \tag{2.5}$$

$$\tau_{yz} = \tau_{zx} = 0 \tag{2.6}$$

However, it was noted that real materials cannot support the theoretically infinite stresses at the tip of a sharp crack. Upon loading the crack tip becomes blunted and a region of yielding, crazing, or microcracking forms as shown in **Figure 2.4.**

For such an elastic, perfectly plastic, isotropic and infinite plate, Tresca predicts yielding to occur if the maximum yield stress τ_{max} exceeds the yield stress in shear, $\sigma_{YS}/2$. The Von Mises criterion, in terms of the principal stresses, follows from [108]

$$(\sigma_1-\sigma_2)^2+(\sigma_2-\sigma_3)^2+(\sigma_3-\sigma_1)^2 = 2\sigma_{YS}^2 \qquad (2.7)$$

where, σ_{YS} is the uniaxial yield strength of the material. In the crack plane ($\theta = 0$), the size of the crack tip yielding zone r_y (**Figure 2.4**) as a function of θ follows from substitution of *Eqs.(2.1-2.6)* to into *Eq.(2.7)*:

$$r_{y\sigma} = \frac{1}{2\pi}\frac{K_I^2}{\sigma_{YS}^2} \qquad \textit{(plane stress)} \qquad (2.8)$$

$$r_{y\varepsilon} = \frac{1}{6\pi}\frac{K_I^2}{\sigma_{YS}^2} \qquad \textit{(plane strain)} \qquad (2.9)$$

where $\nu = 0.3$; the subscripts σ and ε designate plane stress and plane strain conditions, respectively. It is clear that the crack tip yielding zone size $r_{y\varepsilon}$ for plane strain is only one third of that $r_{y\sigma}$ for plane stress. The yielding zone r_y can be called a first order estimate of plastic zone r_p because it was based on an elastic crack tip solution. For a real elastic-plastic material, the stresses are lower than the values from the elastic stress field equations because of yielding within the plastic zone.

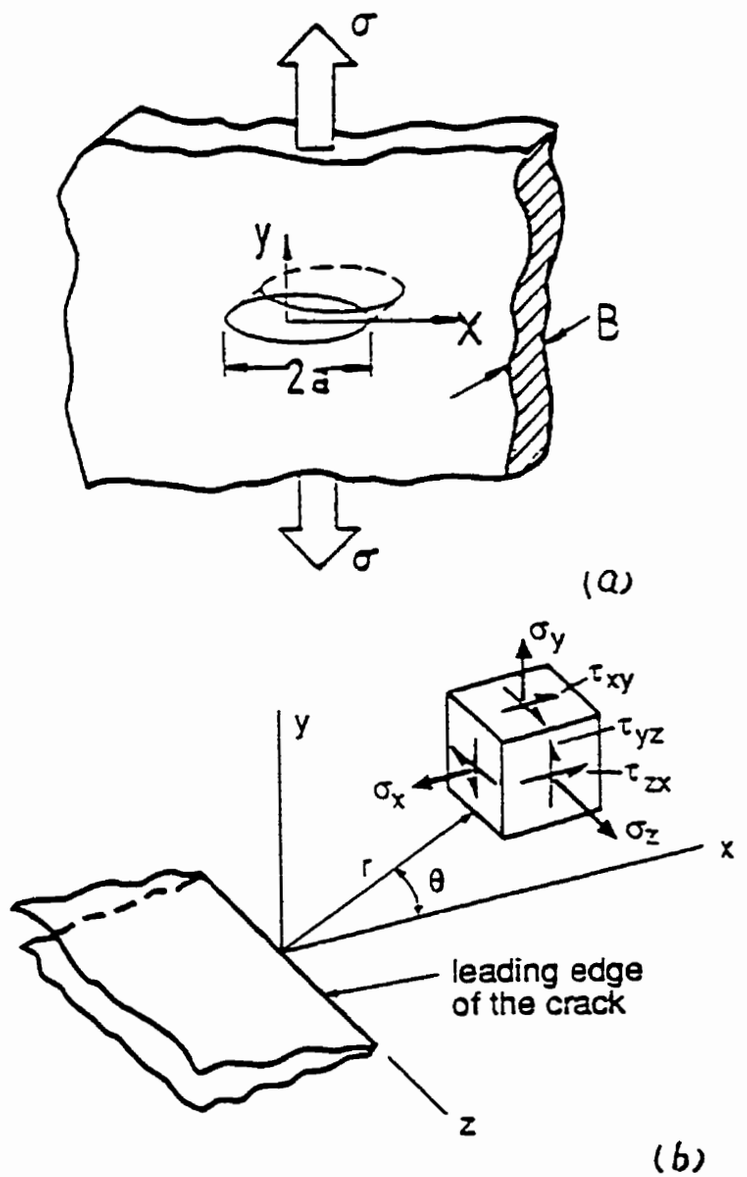

Figure 2.3 (a) An infinite plate containing a through-thickness central crack, (b) three-dimensional coordinate system for the region of a crack tip [107].

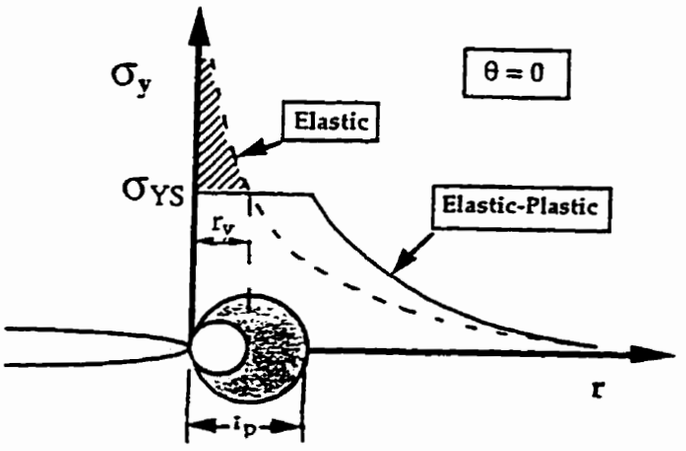

Figure 2.4 First-order and second-order estimates of plastic zone size (r_y and r_p, respectively). The cross-hatched area represents load that must be redistributed, resulting in a larger plastic zone r_p [38].

The yielded material thus offers resistance that expected, and large deformation occurs, which in turn causes yielding to extend even farther than r_y, as illustrated in **Figure 2.4**. A simple force balance leads to a second order estimate of the plastic zone size, r_p [38]:

$$\sigma_{YS} r_p = \int_0^{r_y} \sigma_{yy} dr = \int_0^{r_y} \frac{K_I}{(2\pi r)^{1/2}} dr \qquad (2.10)$$

Integrating and solving for r_p gives that yielding actually extends to about $2r_y$, called real plastic-zone size r_p in this thesis,

$$r_{p\sigma} = 2 r_{y\sigma} = \frac{1}{\pi} \frac{K_I^2}{\sigma_{YS}^2} \quad (plane\ stress) \qquad (2.11)$$

$$r_{p\varepsilon} = 2\,r_{y\varepsilon} = \frac{1}{3\pi}\frac{K_I^2}{\sigma_{YS}^2} \quad (plane\ strain) \tag{2.12}$$

where $r_{p\sigma}$ and $r_{p\varepsilon}$ represent the real plastic zone sizes in an elastic-plastic material under plane stress and plane strain, respectively.

The Validity Requirements in ASTM Standard E 399-90

If the plastic zone is sufficiently small, there will be a region outside of it where the elastic stress field *Eqs.(2.1) to (2.6)* still apply, called *K*-field as shown in **Figure 2.5a**. The existence of such a region is essential for linear elastic fracture mechanics (*LEFM*) theory to be applicable because the *K*-field surrounds and controls the behaviour of the plastic zone and crack tip area.

As a practical matter, it is necessary that the plastic zone be small compared to the distance from the crack tip to any boundary of the member, such as distance (a), (W-a), and (h) for a cracked plate as in **Figure 2.5b**. Generally, a distance larger than twelve times the plastic zone size $r_{p\varepsilon}$ is sufficient. Hence, an overall limit on the use of *LEFM* applicable for opening mode is [107]

$$a, (W-a), h \geq \frac{4}{\pi}\left(\frac{K_I}{\sigma_{YS}}\right)^2 \quad (LEFM\ applicable) \tag{2.13}$$

From *Eqs.(2.12)* and *(2.13)*, it is clear that $(K_I/\sigma_{YS})^2$ is a characteristic dimension of the

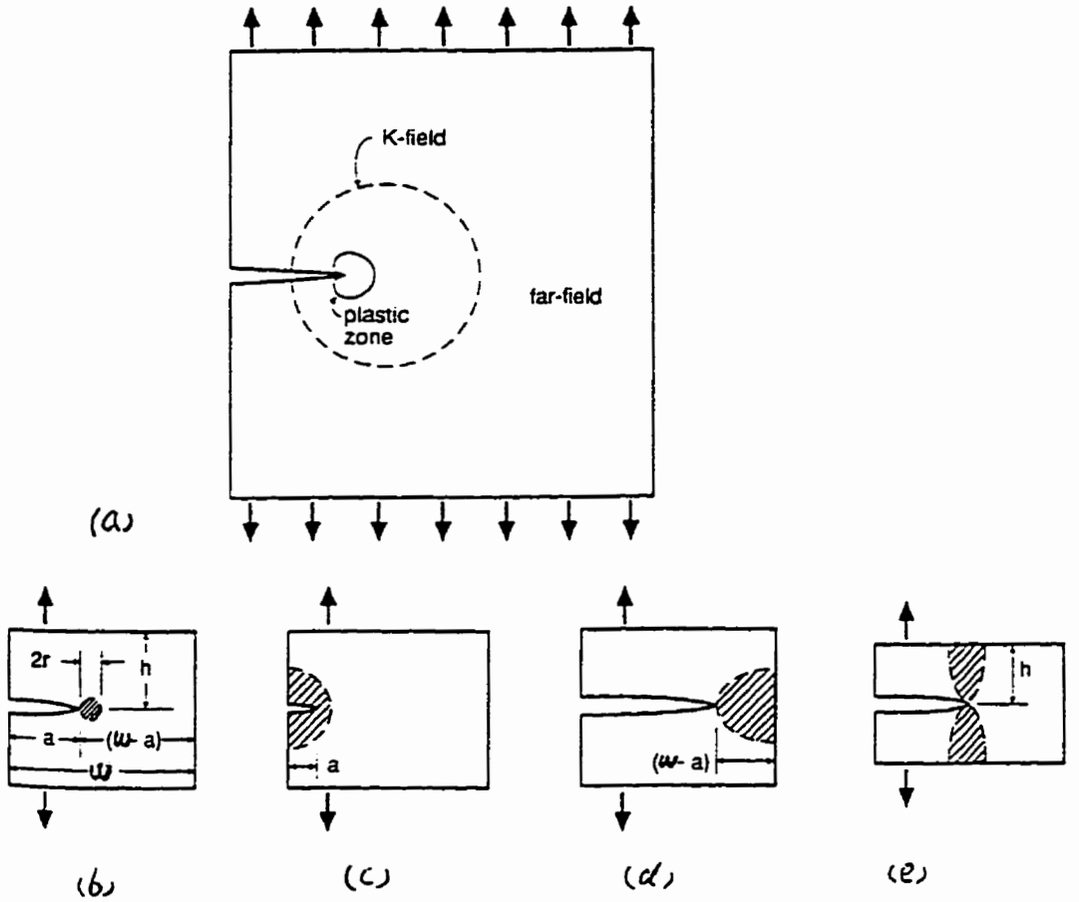

Figure 2.5 (a) A crack and its plastic zone, and the larger K-field that must exist for LEFM to be applicable. Small plastic zone compared to planar dimensions (b), and situations where LEFM is invalid due to the plastic zones being too large compared to (c) crack length, (d) uncracked ligament, and (e) member height [107].

plastic zone that should be useful in estimating specimen dimensions. The pertinent dimensions of plate specimens for K_{Ic} bend-testing are crack length (a), thickness (B), and ligament length (uncracked length: W-a, W is the width of the specimen as shown in **Figure 2.1**). For a critical fracture toughness K_{Ic} which is independent on size parameters, these parameters must be greater than a certain multiple (α) of $(K_{Ic}/\sigma_{YS})^2$ (**Figure 2.6**), these multiples to be determined by an adequate number of trial K_{Ic} tests [109].

Figure 2.6 showed effects of thickness and crack size on measured K_{Ic} of a maraging steel [108, 109]. According to **Figure 2.6** consistent K_{Ic} values are obtained if $\alpha \geq 2.5$, the value adopted in the *ASTM* size requirement [97]

$$B, a, (W - a), h \geq 2.5\left(\frac{K_{IC}}{\sigma_{YS}}\right)^2 \quad (plane\ strain) \tag{2.14}$$

Comparing *Eq.(2.12)* to *Eq.(2.14)* indicates that specimen dimension must be $2.5 \times 3\pi \approx 24$ times larger than the plastic zone size $r_{p\varepsilon}$ for plane strain in order to obtain a size-independent critical K_{Ic} value. In addition, the requirements on the in-plane dimensions of *Eq.(2.13)* are less stringent than *Eq.(2.14)*, so that the limits on the use of *LEFM* are automatically satisfied if plane strain is satisfied.

Although plane strain as shown in *Eq.(2.14)* is necessary condition for a valid K_{Ic} test, it is not sufficient. The validity requirements in *ASTM* Standard *E 399-90* [97] are very stringent because it is possible that a fracture-toughness test displays considerable plastic deformation prior to failure as shown in **Figure 2.7**. A K_Q value computed from P_Q [97] may just barely

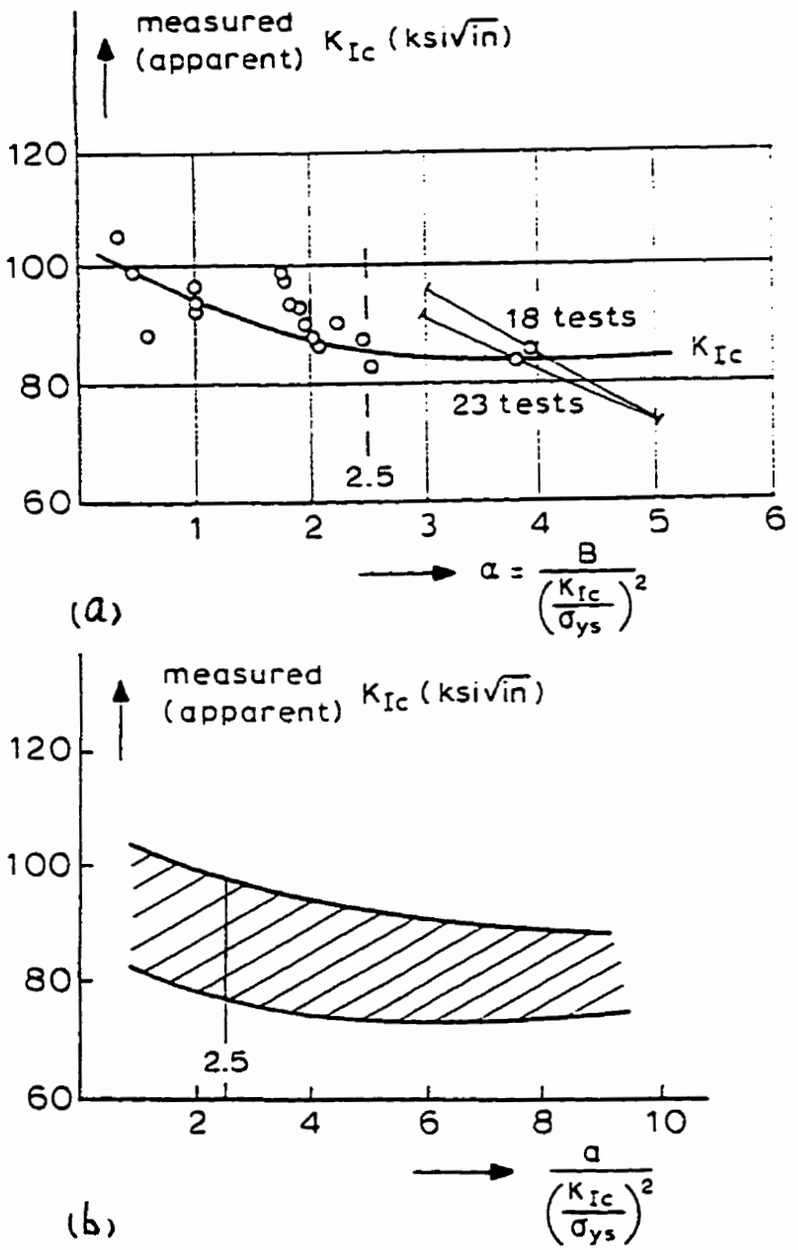

Figure 2.6 Effects of (a) thickness, (b) crack size on measured K_{Ic} of a maraging steel [108, 109].

satisfy the size requirements of *Eq.(2.14)*, however, such a quantity would have little relevance to the fracture toughness of the material. Since the specimen fails well beyond P_Q, the K_Q value in this case would grossly underestimate the true toughness of the materials. Therefore, another requirement is essential to a K_{Ic} test as described in *E 399-90* [97]:

$$P_{\max} \leq 1.10 P_Q \tag{2.15}$$

The meaning of P_Q can be explained by **Figure 2.8**.

As shown in **Figure 2.8**, three types of the load-displacement curves could be obtained during K_{Ic} testing. The critical load, P_Q, is defined in one of several ways, depending on the type of curve. A smooth curve as in Type I can be caused by a steady tearing type of fracture called slow-stable crack growth, plastic zone effects, or both. In other cases, the crack may suddenly grow a short distance, which is called pop-in (II), or it may suddenly grow to complete failure (III). A line from origin with a slope equal to 95% of the initial elastic loading slope must be constructed to determine P_5 (**Figure 2.8**) because it corresponds to crack growth through approximately 2% of the ligament in test specimens with $a/W \approx 0.5$ [38]. In the case of Type I behaviour, $P_Q = P_5$. With a Type II curve, a small amount of unstable crack growth occurs before the curve deviates from linearity by 5%. In this case, P_Q is defined at the pop-in. For Type III behaviour, a specimen fails completely before achieving 5% nonlinearity. In this case, $P_Q = P_{max}$.

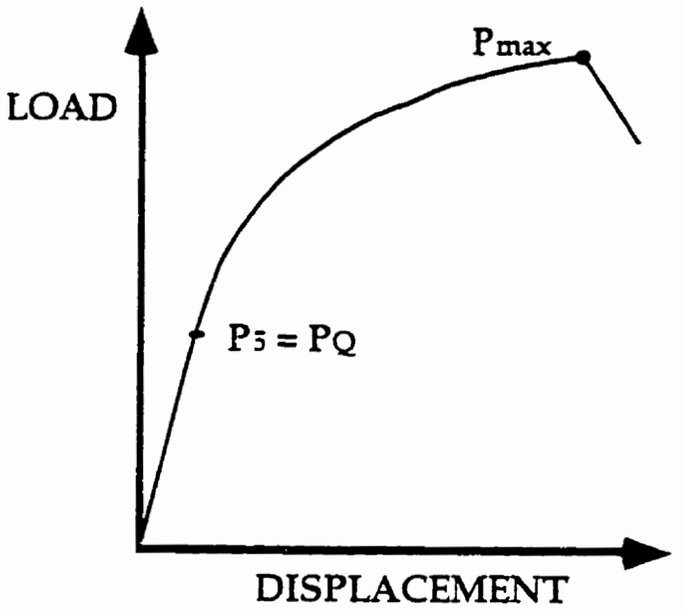

Figure 2.7 A schematic load-displacement curve for an invalid K_{Ic} test, where ultimate failure occurs well beyond P_Q [38].

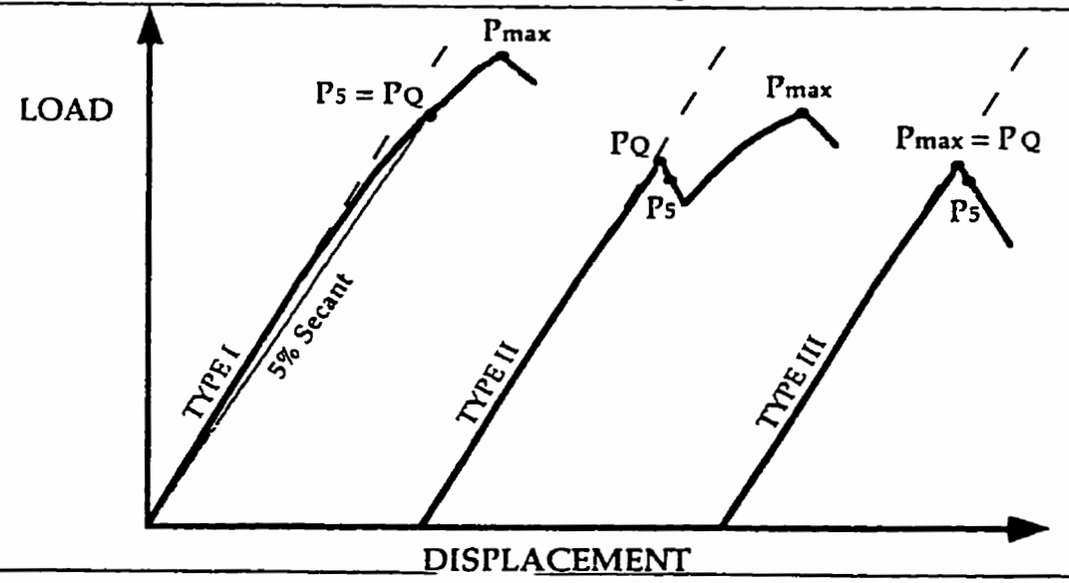

Figure 2.8 Major types of load-displacement records during K_{Ic} testing. For the valid test, $P_{max} \leq 1.10\ P_Q$ [97].

2.1.2 Preliminary Estimation of the Bend-Specimen-Size of the Selected System

The values of yield strength σ_{YS}, elastic modulus E, Poisson's ratio v and fracture toughness K_{Ic} of polycrystalline NiAl, monolithic Ni_3Al and boron-doped Ni_3Al at room temperature are listed in **Table 2.1**. The alloy processing method (*APM*) and alloy grain size are also shown in **Table 2.1** if they are available in references because the values of σ_{YS} and K_{Ic} are different depending on various alloy processing method (*APM*) and alloy grain size as shown in **Table 2.1**.

For example, Rigney et al. [81] explained that the compressive yield strengths of NiAl were significantly higher than expected, resulting from possible interstitial contamination during hot pressing. That is the only case that the values are not considered in the following specimen-size design. Taking the average values of σ_{YS} and K_{Ic}, the specimen sizes for polycrystalline NiAl, boron-free and boron-doped monolithic Ni_3Al should be:

$$NiAl: \quad B, a, (W-a) \geq 2.5(\frac{6}{244})^2 x\, 10^3 = 1.5mm \qquad (2.16)$$

$$Ni_3Al: \quad B, a, (W-a) \geq 2.5(\frac{20}{294})^2 x\, 10^3 = 11.6mm \qquad (2.17)$$

$$Ni_3Al + B: \quad B, a, (W-a) \geq 2.5(\frac{30.5}{304})^2 x\, 10^3 = 25.2mm \qquad (2.18)$$

For the specimens containing 50 vol.% NiAl + 50 vol.% Ni_3Al with assumption of the averages of σ_{YS} and K_{Ic} for each phase, the specimen size could be:

Table 2.1 The values of E, ν, σ_{ys} and K_{Ic} of polycrystalline NiAl and monolithic Ni_3Al (with and without boron doping) at room temperature.

Alloys	E (GPa)	σ_{ys} (MPa)	K_{Ic} ($MPa\sqrt{m}$)	Grain Size (μm) and *APM*	Poisson's Ratio ν [119]
NiAl	294 [110] 189 [115]	360 [111] 70↔270 [115] 154↔275 [116] 250↔342 [117] 180 [118] 762↔902 [81]	5.4 [111] 6↔9 [13] 4↔7 [114] 4.1↔6.6 [81]	20, *HPP** [111] =28, *HPP** [13] 19 *CP+AE** [116] 11↔22 *PE** [117] 18, *CP** [118] 20↔2000 *HPP** [81]	0.315
Ni_3Al	179 [110]	100↔450 [112] 236↔389 [81]	20 [111] 18.7↔20.9 [81]	9, *HPP** [111] 8↔69, [112] 9↔25, *HPP** [81]	0.305
Ni_3Al+B	-	280 [113] 283↔374 [81]	>28.1 [111] 28 ↔ 33 [81]	9, *HPP** [111] 9↔150 *HPP** [81]	-

Note: Alloy processing method (*APM*) are marked by references. *HPP*: hot-pressed powders; *CP+AE*: conventional purity induction melted casting + as-extruded; *PE*: powder extruded.

$$B, a, (W - a) \geq 2.5\left(\frac{(6+20)/2}{(244+294)/2}\right)^2 x\, 10^3 = 5.8mm \quad (2.19)$$

Obviously, in order to get valid K_{Ic} values the size of the bend specimens can be designed as very small, e.g. from 1.5 to 6 mm, only for polycrystalline NiAl to the polycrystalline NiAl containing less than 50 vol.% Ni_3Al (not sure how much less than 50 vol.% now) in the in-situ composites. However, for the polycrystalline NiAl with more than vol.50% Ni_3Al to approximately 100% Ni_3Al which shows higher K_{Ic} values and almost the same σ_{YS} values, the size of the bend specimens could be very large, from 5.8 to 25.2 mm. Therefore, the maximum length of the specimens could be more than 4x25.2=100.8 mm because the standard loading span for the bend specimen should be four times the width (W) [97] (**Figure 2.1**). Such a huge specimen is completely impractical for fabrication in our lab. Definitely, an alternative bending method, J-integral method, for fracture-toughness determination is needed for the selected system.

2.1.3 The specimen-Size Requirements for a Valid J_{Ic}

To determine K_{Ic} indirectly since linear elastic fracture mechanics (*LEFM*) is valid only as long as nonlinear material deformation is confined to a small region surrounding the crack tip, there is only one experimental technique appropriate, i.e., J-integral method [38, 99, 100].

Obviously, the design of the specimen size and geometries for a valid K_{Ic} test needs a thorough understanding of applications of *LEFM* and elastic-plastic fracture mechanics (*EPFM*).

In *ASTM* standard *E 813-89* [99], a provisional $J_Q=J_{Ic}$ as long the following size requirements are satisfied:

$$B,(W-a) \geq \frac{25\,J_Q}{\sigma_{YS}} \tag{2.20}$$

It is instructive to compare specimen size requirements associated with valid K_{Ic} and J_{Ic} test procedures. The upper-bound specimen sizes of NiAl and Ni_3Al can be calculated for a valid J_{Ic} test by substituting data for σ_{YS} from **Table 2.1** into *Eq.(2.20)* and recalling that $J_{Ic}=(1-\nu^2)K_{Ic}^2/E$ [38, 100]:

$$NiAl:\quad B,(W-a) \geq 25\frac{J_{Ic}}{\sigma_{YS}} = \frac{25x6^2}{241.5(1-0.315^2)244} = 0.017mm \tag{2.21}$$

$$Ni_3Al:\quad B,(W-a) \geq 25\frac{J_{Ic}}{\sigma_{YS}} = \frac{25x20^2}{179(1-0.305^2)312.5} = 0.2mm \tag{2.22}$$

$$Ni_3Al+B:\quad B,(W-a) \geq 25\frac{J_{Ic}}{\sigma_{YS}} = \frac{25x30.5^2}{179(1-0.3^2)328.5} = 0.4mm \tag{2.23}$$

Where, E and σ_{YS} are the average values of elastic moduli and yield strengths taken from **Table 2.1**. Obviously, the J_{Ic} size requirements are much more lenient than the K_{Ic} requirements.

2.2 Geometrical Criteria for the Design of Small-Size Bend Specimen

Fracture mechanics theory applies to cracks that are infinitely sharp prior to loading. While laboratory specimens invariably fall short of this ideal, it is possible to introduce cracks that are sufficiently sharp for practical purposes. A fatigue-precracking method is adopted in *ASTM E 399-90* [97], which requires the peak value of stress intensity in a single cycle, K_{max}, should be no larger than 0.8 K_{Ic} during the initial stages of fatigue precracking and less than 0.6 K_{Ic} as the crack approaches its final size [38, 97]. The user must specify fatigue loads based on the anticipated toughness of the material. If one is conservative and selects low loads, precracking could take a very long time. On other hand, if precracking is conducted at high loads, the user risks an invalid result, in which case the specimen and the user's time are wasted. Therefore, people have been trying to develop other techniques in order to replace costly fatigue-precracking method. *SEPB* and *CNB* are such types of fracture specimens developed recently.

2.2.1 Single-Edge-Precracked-Beam (*SEPB*)

As a substitute for the fatigue-precracked-beam method prescribed in *ASTM E399 A2*, this method involves testing of straight through notched specimens that have been precracked in bridge-compression method as shown in **Figure 2.2**. A crack starter, i.e., a Vickers indentation or a straight-through notch (0.1 mm wide by 1.5 mm deep) can be placed at the center of the

bottom surface [104]. The precrack length is varied by changing the groove width in bridge configuration and loading greater than the pop-in load, and can be controlled by a pop-in sound detected by a sonic sensor attached to the pusher framework. A dye penetrant mixed with acetone can be used before the bending test to distinguish the difference between the precrack and the final fracture [104].

However, this method has the following disadvantages: (1) Secondary microcracks in a specimen might be introduced during the precracking by bridge-compression for very brittle material; (2) Cannot easily be used to obtain crack growth data; (3) The length of pre-crack may not be fully reproducible from specimen to specimen due to difficulty with controlling load.

The author has tried several specimens by *SEPB* technique. The problems are (1) it is very hard to introduce precrack for the relatively tougher material in the selected system such as $Ni_{73.2}Al_{26.8}$ in-situ composite, even at the maximum groove width and highest load closed to 500 kg. (2) A dye penetrant mixed with acetone was used for precracked $Ni_{67.3}Al_{32.7}$ specimens but it was hard to distinguish the difference between the precrack and the final fracture. Therefore, the method was abandoned in this research.

2.2.2 Chevron-Notched-Beam (CNB) Test

The geometry of Chevron-notched bending specimens can be seen in **Figure 2.9**. The main advantages of CNB are: (1) no pre-cracking essentially necessary; (2) condition, $a \geq 1.25(K_Q/\sigma_{YS})^2$, is irrelevant. Similar condition $a \geq 2.5(K_Q/\sigma_{YS})^2$, which must be obeyed in SENB and SEPB, makes notching and pre-cracking more time consuming procedure particularly for materials of unknown K_{Ic}; (3) More likely to obtain a load-displacement records as shown in **Figure 2.10**, which can be used to calculate work-of-fracture (γ_{WOF}) and other

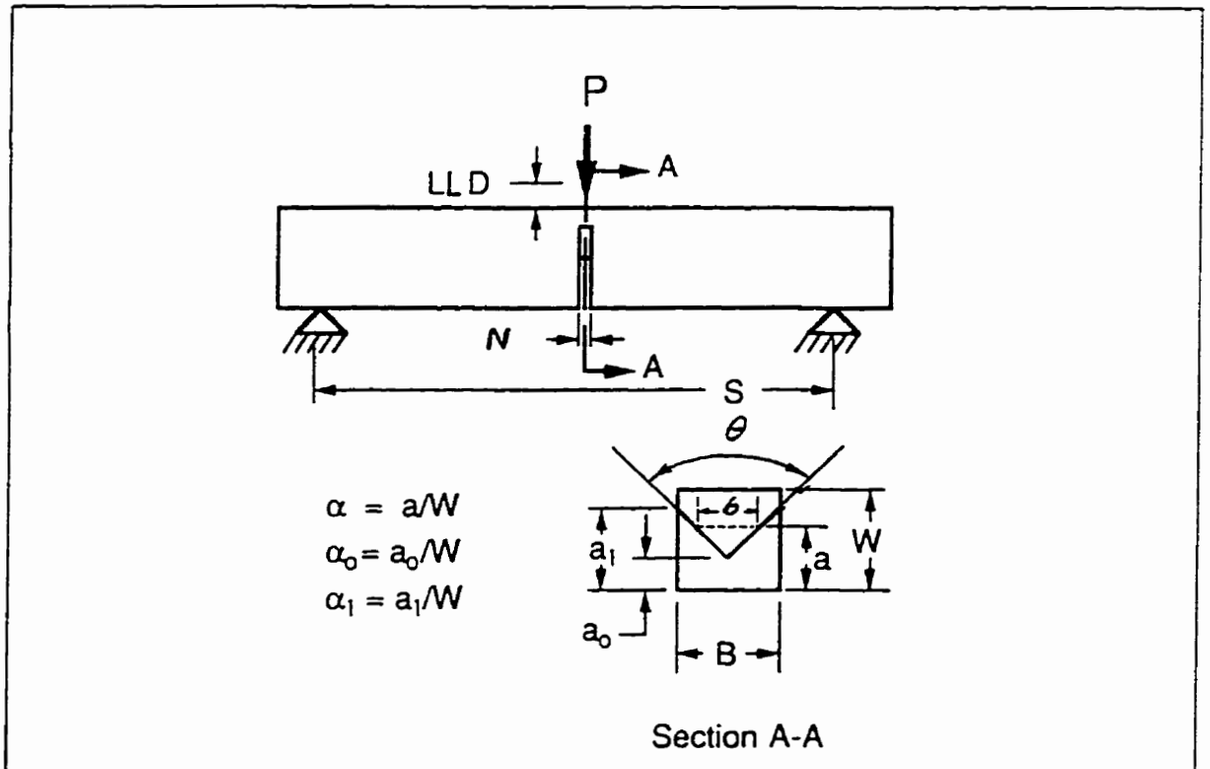

Figure 2.9 Chevron-notched, three-point flexure test geometry [120].

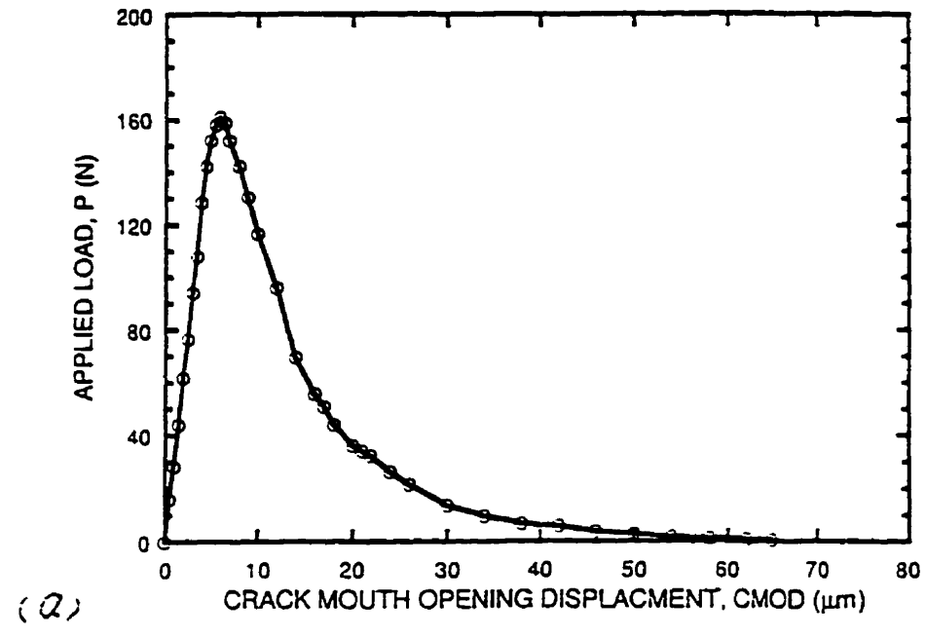

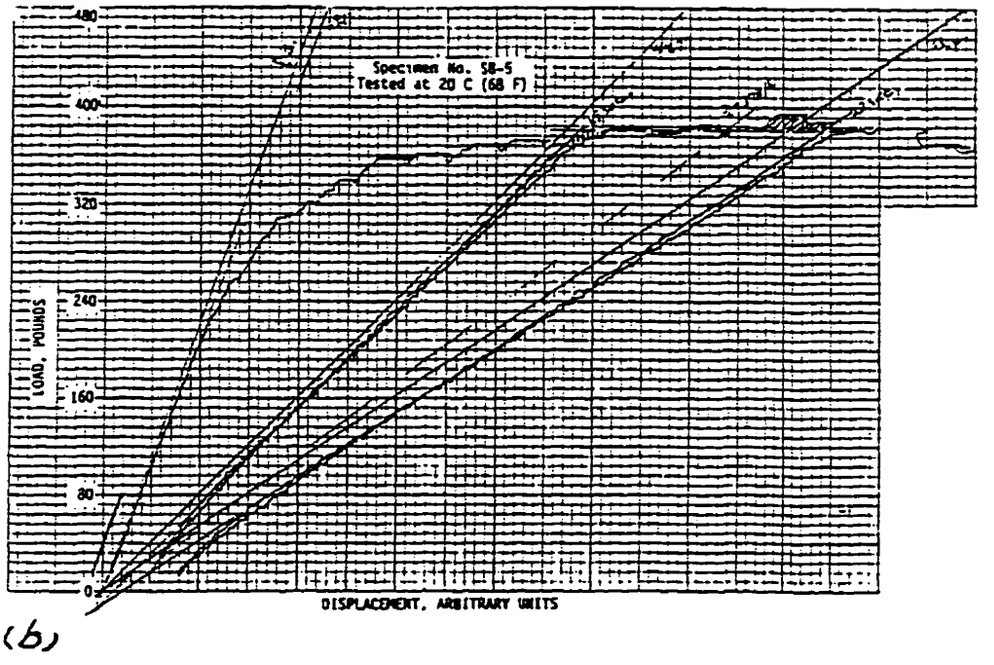

Figure 2.10 Examples of load-displacement curves for CNB specimens, (a) stable crack growth fracture test of silicon nitride at room temperature [120], and (b) stable crack growth fracture test of martensitic stainless steel at room temperature [125].

parameters (*J*-integral); (4) specimen size is much smaller than for a *SENB* (*SEPB*) because for CNB: $B \geq 1.25(K_Q/\sigma_{YS})^2$ [98].

One of the important assumptions of the chevron-notch geometry is that the crack growth occurs in a stable manner prior to the attainment of a peak load. The apex of the chevron-notch gives rise to a high stress concentration and propagation occurs at relatively low loads. Because of the low initiation load, the stored elastic strain energy in the specimen and the test machine (probably negligible if machine is stiff enough) is also low which promotes the stable crack growth. This is also due to the fact that as the crack progresses through the chevron the crack front continually increases promoting stable crack growth [121-123]. Load-displacement curve for such a situation exhibits an initially linear behaviour until the crack propagation commences and then becomes nonlinear just before it reaches P_{max}. This non-linearity is caused by the stable crack propagation. The extent of this non-linearity on the load (P) - displacement curve before P_{max} seems to depend on the material. In materials which can be called "linear elastic" (flat R-curve) or "nonlinear elastic" (rising R-curve) [120], (non-linear elastic behaviour, e.g. in ceramics, is due to the development of nonelastic processes in the crack tip region such as microcracking phase transformations, or grain interlock [124] or fracture mechanisms which develop in the wake of region as the crack propagates [120]), the extent of the non-linearities before P_{max} is rather minimal (**Figure 2.10a**). However, in materials which also develop some plasticity during stable crack growth this extent can be much more substantial (**Figure 2.10b**).

At P_{max}, a balance is achieved between the increasing crack area and the resistance to crack propagation by the material and the crack driving force from the external loading. Once the maximum load for the load-displacement curve is achieved, then in the ideal case the further crack growth is stable where the increasing resistance of the specimen to crack extension is just balanced by the crack driving force so that the crack propagates in a quasistatic, stable manner, instead of catastrophically. This results in a characteristic "tail" on the load-displacement curve (**Figure 2.10a**).

However, there is a strong experimental evidence that on many occasions despite predictions to the contrary, the presence of a chevron notch in a bend or short-bar specimen does not always guarantee the formation of a stably growing crack at low loads. Instead, a sharp drop in the load occurs immediately at the end of a linear portion of the load-displacement record, at P_{max} [106, 124, 125-129].

Usually this kind of behaviour is related to a relatively wide chevron-notch slot width [106, 124]. Chuck et al. [124] argued that the problem with a wide notch is not the difficulty of initiating a crack at the apex of the chevron, but rather of propagating a "proper" chevron crack (that is, a crack that is in the proper plane and not pinned by the notch groove). Barker [130, 131] recommended for chevron-notched short-rod and short-bar specimens the notch width gap less than 0.03B and ideally, the slots forming the chevron should have sharply pointed slot bottoms ($\leq 60°$) to maintain good plane strain constraint along the crack front. However, data listed in **Table 2.2** for specimens exhibiting a fully linear load-displacement record and unstable

crack growth do not convincingly show that a stable crack growth can always be obtained for the slot width *N/B* ratios smaller than 0.03 as suggested by Barker [130, 131]. The Barker's notch width criterion was established for short-bar or short-rod specimens and it is not clear whether or not it applies to a bend specimen (3 or 4 point loading). In trialuminides tested in bending [129] it was impossible to obtain a stable crack growth despite that the chevron slot width ratio was only 0.022 (**Table 2.2**), i.e. much less than that recommended by Barker [130. 131]. However, the fracture toughness values obtained from chevron-notch-beam (*CNB*) specimens were conservative and almost identical as those obtained from single-edge-precracked-beam (*SEPB*) specimens [129]. Similarly, Horton and Schneibel [128] obtained

Table 2.2 Slot widths in chevron-notch testing of various materials at room temperature exhibiting a fully linear load-displacement record and unstable crack growth.

Material	Chevron Slot Width *N* (mm)	Slot Width Ratio *N/B*	Loading Mode	Validity of Test	Refe-rence
Glass	0.50	0.125	4PB	Invalid	[124]
Steel	0.37	0.031	3PB	Invalid	[126]
Glass	2.38	0.170	3PB	Valid	[106]
Steel	0.14	0.005	T (Short Bar)	Invalid	[127]
Trialuminide	0.11	0.022	4PB	Valid	[129]

rather conservative fracture toughness values calculated from the maximum load for a $Nd_2Fe_{14}B$ intermetallic despite that the load-displacement record in three-point bending was fully linear up to P_{max} with the following unstable crack growth. In conclusion, it seems that as long as the chevron slot width in bend specimens is smaller than 0.03B the maximum load at the fully linear load-displacement record indicating unstable crack propagation can be utilized for the calculation of conservative (valid) fracture toughness value. Because of the unique features of *CNB* specimen as discussed above, some of these specimens such as short rod and short bar in tension test have been considered by *ASTM* [98]. Unfortunately there is no *ASTM* standard file available for *CNB* specimen in bending, which obviously can save more material and be tested in easier way than short-bar or rod in tension. But more and more investigators have been working on it recently because it is fairly well based theoretically and has much more attractive advantages than other conventional methods [120-128]. Furthermore, the bending tests on *CNB* can be performed by analogy with the *ASTM* standards *E 1304-89* [98], *E 399-90* [97] and *E 813-89* [99].

Determination of Specimen-Size and Loading Mode

Considering the dimension and cast-quality of the ingot and numbers of specimens for the test, the specimen-dimensions will be designed as follows: B=3.5mm, W=4mm and W/B=1.14, which are decided on the basis of the references (W/B=1.25 [124, 132], W/B=1.5 [126, 133,

134], W/B=1.0 [120], W/B=1.25-2.5 [135], W/B=1.6 [136], W/B=1.8 [106]) and analogy with the requirement in E 399-90: $1 \leq W/B \leq 4$ [97]. A nominal support span will be equal to 16mm for a bending test according to E399-90 (S/W=4) [97] and references [106, 126, 133, 134-136]. The diameter D, of the roller will be 4.8mm, which is close to the requirement of *E399-90*: $W>D>W/2$ [97].

No clear preference is seen for the mode of loading from the references. Most researchers used three-point bending (*3PB*). Munz et al. [132] indicated that in four-point bending (*4PB*) the specimen alignment is not very critical because of the constant moment between the inner loading points as shown in **Figures 2.1 b** and **d**. Additionally interaction between the load roller pins stress field and the crack stress field, which can happen in *3PB* is avoided in *4PB*. Therefore *4PB* might be preferred for a bending test. But in testing small-size specimens the above concerns don't seem to be too important. From references [106, 120, 124, 126, 132-136], the most preferred geometry seems to be S/W = 4 for 3PB and S_1/W = 8 for *4PB*. Therefore, for a four-point loading as shown in **Figure 2.1b**, the major span, S_1, the distance between the support rollers, would be at least 40 mm if considering S_2 = 10 mm and the diameter of the rollers, D = 4.8mm in our case. Thus the total length of the specimen would be approximately 45 mm, which would definitely increase the difficulty to prepare the ingots, and more than twice as much material would be used comparing to the three-point loading. Therefore, the *3PB* flexure loading arrangement will be preferred in this research.

Notch-Parameter Design

There are six parameters (N, θ, a_0, a_1, α_0, and α_1) as shown in **Figure 2.9** that must be considered for chevron-notch-geometry design, but only three of them are independent.

The Slot Width N of the Notch

Notch preparation is critical in the determination of the plane-strain fracture toughness of materials with notched bend specimen. Measured chevron fracture toughness values (K_{Ivm}) decrease with decreasing slot width, N [132]. Below a critical slot width N_c (or notch root radius ρ_c), "K_{Ivm}" is constant and presumably equal to the plane-strain fracture toughness that would be obtained from specimens with sharp cracks. In *E 1304-89* [98], the slot width is recommended as $N \leq 0.03B$. Wu [126, 133] chose N/B=0.013 in a three-point loading *CNB* and obtained a very good result: $K_{Ivm} \approx K_{Ic}$, where K_{Ic} was determined by *ASTM E399* Standard method. However, Wu [126] observed a change to completely linear load-load line displacement (*LLD*) and unstable crack growth with N/B = 0.031. Probably, the best choice would be to have it at $N/B \approx 0.01$ but that might be difficult to machine. In our case, an electric discharge machine (*EDM*) thinner wire of 0.1 mm thickness will be used in this experiment to yield the notch width of $\approx$ 0.11 mm and notch ratio of $N/B \approx 0.031$.

The Slot Angle θ of the Notch

Bar-on et al. [134], Nakamura and Kobayashi [137] suggested the optimum sharpness of the notch because stable crack growth must occur easily when the notch tip angle is relatively sharp. In *E 1304-89* [98], two small slot angles (θ = 54.6° or 34.7°) were used. Wu [126, 133] used θ = 60° and obtained a stable crack growth up to P_{max}. In this research, θ = 60° (**Figure 2.9**) will be chosen as the slot angle of the notch.

The Initial Crack Length a_0

Bar-On et al. [134] pointed out that the larger value of a_0 promotes stable crack propagation after reaching maximum load. Wu [126, 133] also recommended the depth ratio of chevron notch α_0 (a_0/W) ≥ 0.3 because the fracture toughness values K_{Ivm} determined by *CNB* and K_{Ic} from *ASTM E 399* Standard method were in good agreement with one another. However, Munz et al. [132] obtained very good agreement between K_{Ivm} from *CNB* and K_{Ic} determined by *ASTM E 399-90* [97], which appeared to be independent of the initial crack length a_0. Chuck et al. [124], and Merkel and Messerschmidt [136] also obtained pretty good results (K_{Ivm}=K_{Ic}) by choosing a_0=0.2W. In other words, K_{Ivm} seems not to be sensitive to a_0. In this experiment, a_0 will be dependent on other three parameters because of the *EDM* processing. a_0 could vary from 0.4 to 1.6 mm (a_0/W = 0.1 to 0.4) which was measured on broken specimens.

The Slot Length a_1 of the Notch

Bar-On et al. [134] pointed out that interaction of the stress field arising from the loading pin with the stress field of the advancing crack was avoided by locating the base of the triangle far enough away from the loading point. Therefore, $a_1 = 0.75W$ was used in their three-point loading *CNB* test. Jenkins et al. [120] chose $a_1=W$ for their three point *CNB* to investigate work-of-fracture. Merkel and Messerschmidt [136] also used $a_1=W$ for their three-point *CNB* and obtained a lower K_{Ivm} with much better reproducibility than K_{Ic} values obtained from tests using straight-notched specimens [136]. Thereby, $a_1 = 0.8W$ is chosen in this research.

Thus, the dependent ratios of the notch parameters of the *CNB* are as follows: $\alpha_0 = 0.1$-0.4, $\alpha_1 = 0.8$ and $N/B = 0.031$ as shown in **Figure 2.9**.

2.2.3 Evaluation of Fracture Toughness Parameters in *CNB* Bend Testing

Evaluation of Fracture Toughness K_{Ivm}

Munz et al. [132] and Barker [121] developed a basic relation of evaluating K_{Ivm}, which denotes the fracture toughness of *CNB* calculated from the P_{max} and Y_m^*, by use of the energy approach of linear elastic fracture mechanics as follows (**Appendix B**):

$$K_{Qv} = \frac{P_{\max}}{BW^{1/2}} Y_m^* \qquad (2.24)$$

where Y_m^* is the minimum value of the dimensionless stress-intensity-factor coefficient (**Figure 2.11**) when the crack length, a, increases to a critical value, a_m, and the load reaches a maximum P_{max} in the meantime if the crack growth resistance curve of the tested material is flat [126, 133]. The Y^* parameter depends only on the geometry of the specimens [122, 126, 132-133],

$$Y^* = \left\{ \frac{1}{2} \frac{dC_v(\alpha)}{d\alpha} \frac{\alpha_1 - \alpha_0}{\alpha - \alpha_0} \right\}^{1/2} \tag{2.25}$$

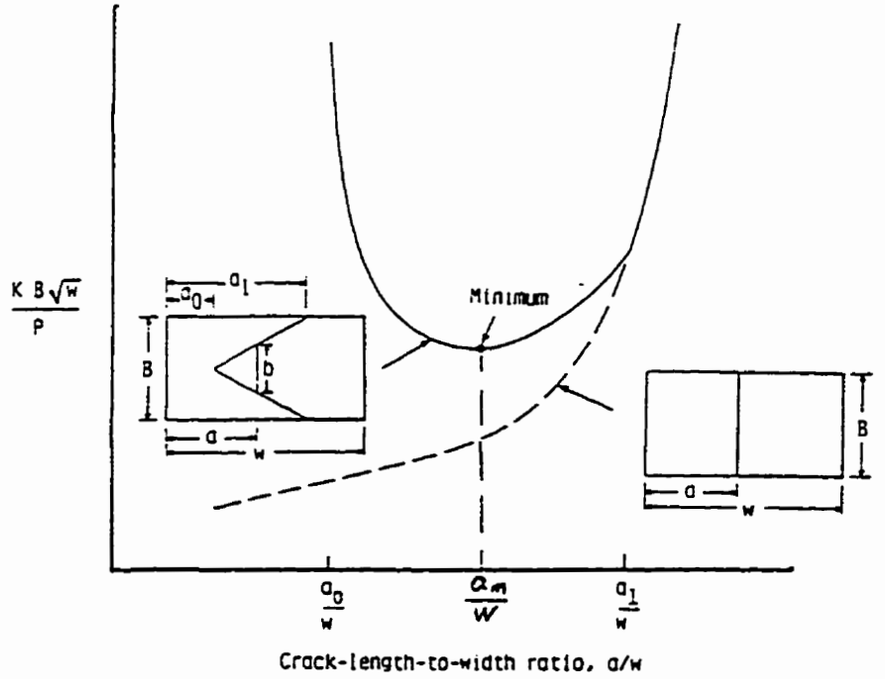

Figure 2.11 Comparison on normalized stress-intensity factor coefficients for chevron-notched and straight-through crack specimens [121].

where $C_v(\alpha)=E'BC$ (C denotes the compliance of the material, $E'=E$ for plane stress and $E'=E/(1-\nu^2)$ for plane strain), is the dimensionless compliance. α, α_0 and α_1 are normalised depths by $\alpha=a/W$, $\alpha_0=a_0/W$ and $\alpha_1=a_1/W$ as shown in **Figure 2.9**, respectively. For the occurrence of P_{max} at approximately a_m for Y^* function it is important that the chevron crack must grow in a stable fashion before the load reaches P_{max}.

There are three methods for determination of Y^* coefficient. The first one is the direct experimental calibration of Y^* with K_{Ic} value obtained by *ASTM E 399-90* [97]. However, the direct calibration is dependent on the behaviour of the calibrated material and is restricted to a single specimen geometry. The second one is the experimental calibration of $C_v(\alpha)$ [138]. The compliance calibration is dependent on the loading device used in the calibration. In addition, the results of Y^* are dependent on the fitting functions of $C_v(\alpha)$. The third method is a calculation of $C_v(\alpha)$ based on the straight-through-crack assumption (*STCA*) proposed by Munz et al. [132, 139]:

$$\frac{dC_v(\alpha)}{d\alpha}=\frac{dC_s(\alpha)}{d\alpha} \tag{2.26}$$

or a more refined "slice model" proposed by Bluhm [140]

$$\frac{1}{C_v(\alpha)}=\frac{\alpha-\alpha_0}{\alpha_1-\alpha_0}\frac{1}{C_s(\alpha)}+\frac{k}{\alpha_1-\alpha_0}\int_{\alpha}^{\alpha_1}\frac{1}{C_s(\xi)}d\xi \tag{2.27}$$

where k is the shear transfer coefficient. $C_s(\alpha)$ is defined as follows:

$$C_s(\alpha) = \gamma + \beta \tan^2(\frac{\pi\alpha}{2}) \tag{2.28}$$

with (Wu [126, 133], hereafter called as "Wu's solution")

$$\gamma = \frac{1}{4}(\frac{S}{W})^3 [1 + 3(1+\nu)(\frac{W}{S})^2] \tag{2.29}$$

$$\beta = \frac{2}{\pi}(\frac{S}{4W})^2 [7.31 + 0.21(\frac{S}{W} - 2.9)^{1/2}]^2 \tag{2.30}$$

or (Bluhm [140], Munz [132], and Withey and Bowen [141], hereafter called as "Bluhm's solution")

$$\gamma = \frac{1}{4}(\frac{S}{W})^3 [1 + 2(1+\nu)(\frac{W}{S})^2] \tag{2.31}$$

$$\beta = 2.7(\frac{S}{W})^2 \tag{2.32}$$

Thus an analytical expression of the dimensionless compliance of *CNB* specimen can be deduced by substituting *Eq.(2.28)* into *Eq.(2.27)*,

$$\frac{1}{C_v(\alpha)} = \frac{\alpha - \alpha_0}{\alpha_1 - \alpha_0} \frac{1}{\gamma + \beta \tan^2 \pi\alpha / 2} + \frac{k}{(\alpha_1 - \alpha_0)(\gamma - \beta)} \{(\alpha_1 - \alpha) - \frac{2}{\pi}$$

$$(\frac{\beta}{\gamma})^{1/2} [\arctan((\frac{\beta}{\gamma})^{1/2} \tan\frac{\pi\alpha_1}{2}) - \arctan((\frac{\beta}{\gamma})^{1/2} \tan\frac{\pi\alpha}{2})]\} \tag{2.33}$$

where the value of k is given as [133],

$$for\ \phi \geq 1:\quad k = 1 + 0.444(\alpha_1)^{3.12} \tag{2.34}$$

$$\phi < 1:\quad k = 1 + \alpha_1^{3.12}(2.236\phi - 4.744\phi^2 + 4.669\phi^3 - 1.77\phi^4) \tag{2.35}$$

where $\phi=0.5(\pi-\theta)$ (for definition of θ see **Figs. 2.9** and **2.12**). It must be pointed out that the expressions provided by *Eqs.(2-34)* and *(2.35)* for the shear coefficient k, are semi-empirical and must be treated with caution.

From the references [126, 132, 133, 140, 141], it is hard to see which solution is correct. Therefore, the two solutions will be used by Maple software to calculate K_{Ivm}. These two solutions will be used for calculation of the fracture toughness values which will be designated K_{Ivm}^{W} (Wu's solution) and K_{Ivm}^{B} (Bluhm's solution), respectively. The experimental results of the two solutions will be compared and analyzed in Chapters 3 and 4.

In addition, the stress-intensity factor coefficient Y^* is very sensitive to the V-notch geometry. The two sides of the V-notch machined by the preceding method may cause a deviation of f from the midthickness plane as shown in **Figure 2.12**. Wu [133] derived a formula to calculate the dimensionless compliance, $C'_v(\alpha)$, of the specimen with a deviation of f by use of the slice model as follows,

$$\frac{1}{C'_v(\alpha)} = \frac{1}{C_v(\alpha)} + \Delta(F) \tag{2.36}$$

where

$$\Delta(F) = \frac{k}{\pi(\alpha_1 - \alpha_0)(\gamma - \beta)}\left(\frac{\beta}{\gamma}\right)^{1/2}\left[2\arctan\left(\left(\frac{\beta}{\gamma}\right)^{1/2}\right.\right.$$

$$-\arctan\left(\left(\frac{\beta}{\gamma}\right)^{1/2}\tan\frac{\pi(\alpha_1+F)}{2}\right)-\arctan\left(\left(\frac{\beta}{\gamma}\right)^{1/2}\tan\frac{\pi(\alpha_1-F)}{2}\right)] \quad (2.37)$$

with
$$F=\frac{f}{W}\cot\frac{\theta}{2} \quad (2.38)$$

$$\alpha_1=\frac{a_1}{W}=\frac{B}{2W}\cot\frac{\theta}{2}+\alpha_0 \quad (2.39)$$

The size requirement for a valid K_{Ivm} in a *CNB* bending test is [98, 122],

$$B \geq 1.25\left(\frac{K_{Qv}}{\sigma_{YS}}\right)^2 \quad (2.40)$$

Here it has to be pointed out that K_{Ivm} values are not necessarily, automatically equivalent to K_{Ic} obtained from *ASTM E 399* [97].

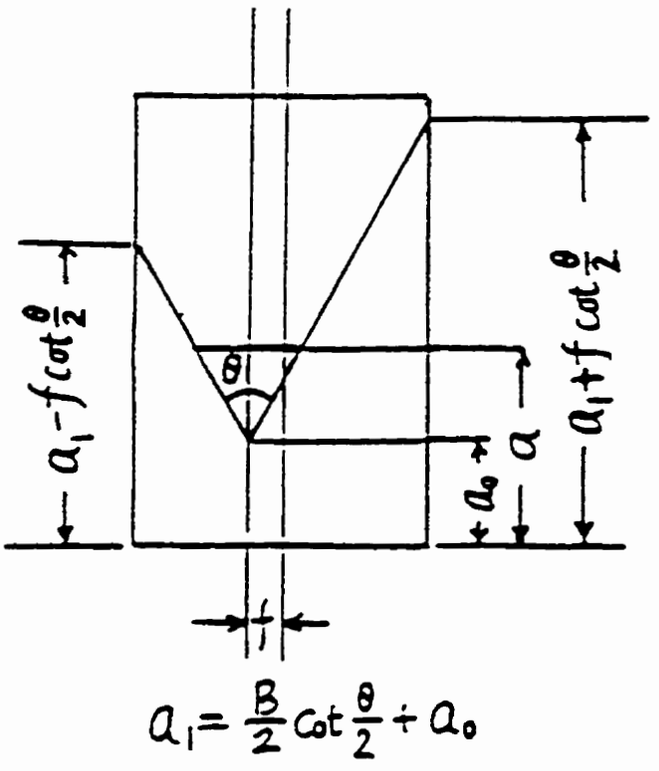

Figure 2.12 Cross section of deviated chevron notch [133].

Evaluation of Apparent Fracture Toughness K_{WOF} in *CNB* Bend Testing

At the point of complete fracture through the chevron section, the work-of-fracture can be determined from the total energy consumed during the entire fracture process divided by the total, projected fracture area, $2A_T$, of the specimen such that [120] (under the condition that the load-displacement curve has the shape as shown in **Figure 2.10a**):

$$\gamma_{WOF} = \frac{\int_0^{LLD} Pd(LLD)}{2A_T} \tag{2.41}$$

where the integral can be calculated directly from the area under the load-displacement curve. γ_{WOF} can be used as an estimate of the fracture energy. Extending the assumption of linear elastic behaviour to *LEFM*, the apparent fracture toughness can be calculated from the γ_{WOF} such that [120],

$$K_{WOF} = [E'(2\gamma_{WOF})]^{1/2} \tag{2.42}$$

where K_{WOF} is the apparent fracture toughness, which can be used to predict fracture toughness of linear or sometimes nonlinear elastic materials. However, if the energy consumed by the nonlinear elastic fracture processes of the composite is too large, total work-of-fracture cannot be used to predict the *LEFM* K_{Ic}.

In addition, because the work-of-fracture is related to nonlinear elastic fracture mechanisms its determination will be dependent upon such conditions as crack velocity (displacement or

loading rate), size of the chevron section, and other testing variables [120]. Despite these limitations in non-*LEFM* materials, γ_{WOF} is still a useful nonlinear elastic fracture parameter for comparative purposes for the same material and test conditions.

2.2.4 *J*-Integral Method in a *CNB* Test

Unfortunately, there is no *ASTM* Standard file available for *J*-integral method for a *CNB* test so far and also not much experimental work on this subject. However, the *J*-integral test for a *CNB* can be performed by analogy with the fundamental concepts and methods as described above in the *ASTM* Standards *E 813-90* [99], *E 1304-89* [98] and *E 399-90* [97]. Besides, this is also the reason why we choose this approach: we are trying to establish a new, maybe not perfect, but reasonable approach for *J*-integral method as applied for a *CNB* test.

Evaluation of *J*-Integral in *ASTM* Standard *E 813-89*

This method is an energy approach and has been developed to define the fracture conditions in a component experiencing both elastic and plastic deformation. *J*-integral is a mathematical expression, a line or surface integral that encloses the crack front from the one crack surface to the other, used to characterize the local stress-strain field around the crack front.

The J-Δa data can be generated by either multiple specimen (at least five) or single specimen techniques.

With the multiple specimen technique, a series of nominally identical specimen are loaded to various levels and then unloaded. These samples should reveal various amounts of crack extension, which is marked by heat tinting to discolour the existing fracture surface after the test. Each specimen is then broken open and the crack extension is measured. Δa is given by the average of nine readings taken across the crack front from one surface to the other (**Figure 2.13b**). The area under the load-displacement plot for each sample is measured, and J_{pl} is computed as shown below.

The *ASTM* Standard *E 813-89* [99] defines the J value at a given measured point i ($1 \leq i \leq n$) on the load-displacement line corresponding to a load P_i and displacement δ_i. For three-point bending with a span/width ratio of four, the elastic and plastic components of J can be estimated from the following expression [99]:

$$J_i = J_{el(i)} + J_{pl(i)} = \frac{K_i^2(1-\nu^2)}{E} + \frac{2A_i}{Bb} \qquad (2.43)$$

where b ($=W-a$) is the initial uncracked ligament and B is thickness of the specimen as shown in **Figure 2.1a**. A_i is the plastic area under the load-displacement curve as shown in **Figure 2.13c**.

The J-integral is determined and plotted against physical crack growth, Δa, using at least four data points within specified limits of crack growth. In *ASTM* Standard *E 813-89* [99], the crack length was not measured directly from the bent specimen but calculated from a

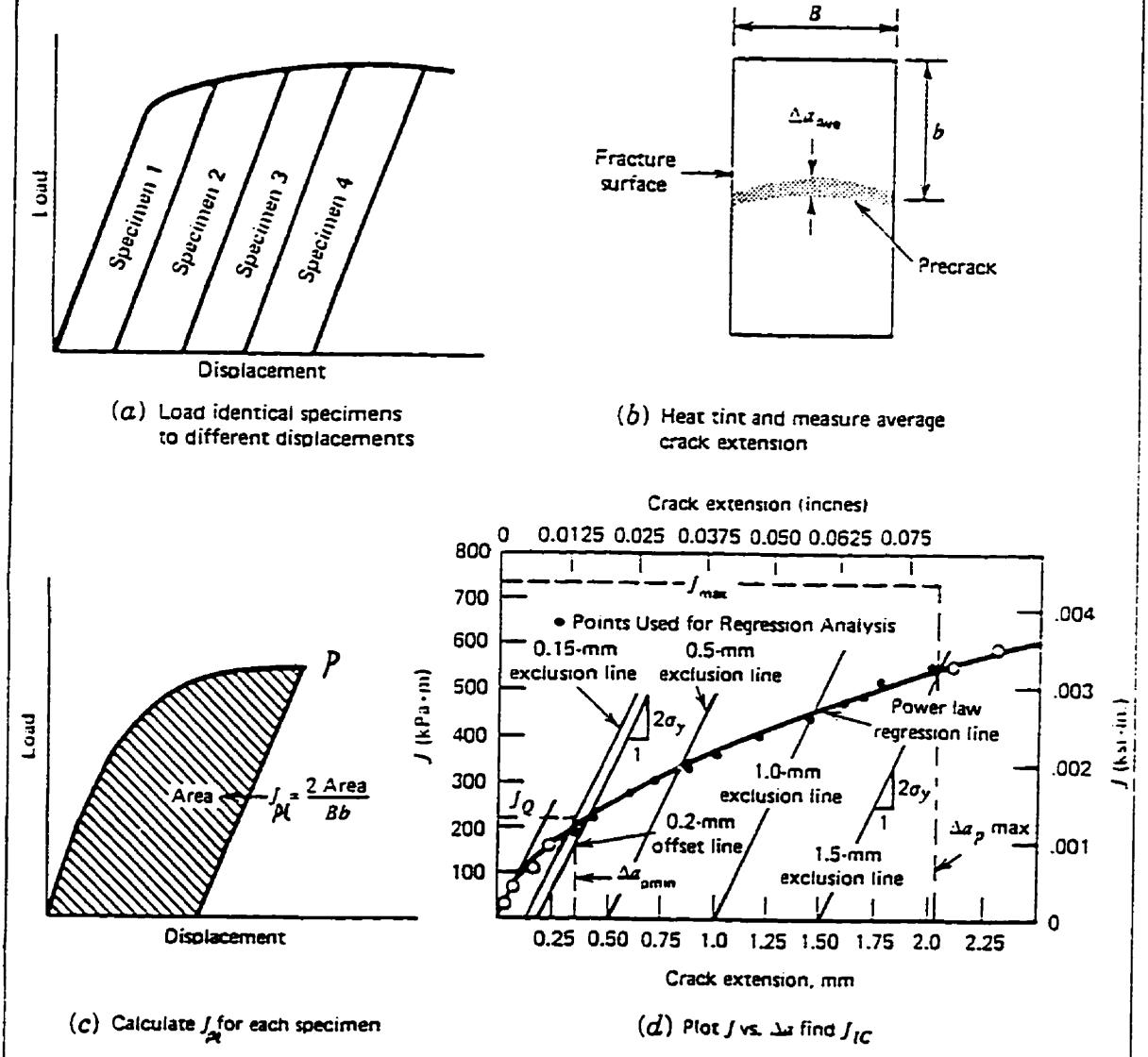

Figure 2.13 Procedures for multi-specimen determination of J_{Ic} [100].

relationship with crack opening displacements, which measured at the notched edge. These data reflect the materials resistance to crack growth.

The J versus crack extension behaviour is approximated with a best-fit power law relationship (**Figure 2.13d**). In **Figure 2.13d**, the blunting line has a slope of $2\sigma_y$ (where effective yield strength $\sigma_y = (\sigma_{YS} + \sigma_{TS})/2$, σ_{TS} denoting the ultimate tensile strength), which takes into account strain hardening in the material. A 0.2 mm offset line parallel to the blunting line is drawn and the intersection of this line and the power law fit defines J_{Ic}, provided the validity requirements of this test method are satisfied.

Obviously, the multiple specimen technique involves the testing of numerous specimens, which makes the procedure both tedious and very expensive. Particularly, it is very difficult to machine several specimens with absolutely identical dimensions. As a substitute of it, another technique has been developed from multiple loadings of a single sample, which is illustrated in **Figure 2.14**. After the sample is loaded to a certain load and displacement level, the load is reduced by approximately 10%. By measuring the specimen compliance during this slight unloading period, the crack length corresponding to this compliance value can be defined [99]. As the crack grows, the specimen becomes more compliant. Relatively deep cracks ($0.50 \leq a/W \leq 0.70$) are required in *E 813-90* [99] because the unloading compliance technique is not sufficiently sensitive to $a/W < 0.5$ [99].

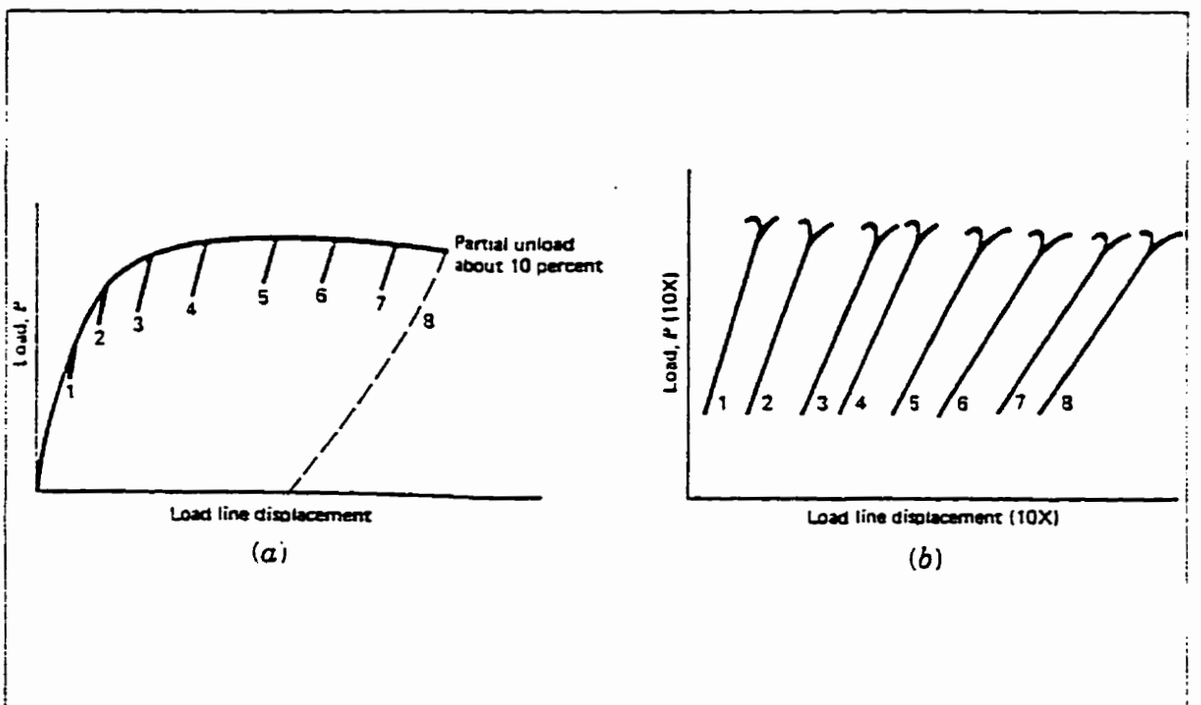

Figure 2.14 Single specimen compliance method for J_{Ic} determination. (a) load versus load-line displacement with several unloadings; (b) amplified segments of (a) revealing change in compliance associated with crack extension [100].

Evaluation of J-Integral for a CNB Test

Before the ASTM standard E 813-89 [99] for J-integral method was available, Sakai et al. [142] successfully used such a similar loading-unloading procedure on polycrystalline graphite by tensile testing of chevron-notched specimens and proved that the energy method for determining nonlinear fracture mechanics parameters from load-displacement diagrams was very effective and feasible in studying the elastic-plastic fractures of various materials.

According to *Eq.(2.24)* and analogy with *Eq.(2.43)*, the elastic and plastic components of *J*-integral in a *CNB* test can be assessed by:

$$J_i = J_{el(i)} + J_{pl(i)} = \frac{P_i^2 Y_i^{2*}(1-\nu^2)}{B^2 W E} + \frac{4 A_i}{B(2W - a_1 - a_0)} \qquad (2.44)$$

For monitoring crack growth and calculating the plastic area A_i, the unloading compliance method for a single specimen can be used as illustrated by **Figure 2.15.**

Figure 2.15a shows the special case of negligible plasticity, which exhibits a load-displacement curve deviating from its initial linear shape because the compliance continuously changes. If the specimen were unloaded prior to fracture, the curve would return to the origin, as the dashed lines indicate [38]. The instantaneous crack length can be inferred from the compliance through relationships given in *Eq.(2.33)* with $\alpha=a/W$ and $C=C_v/E'B$ or from assumed linear relationship between load-line-displacement (*LLD*) and a crack extension as it is calculated in this work (see Section 4.8 and 4.9).

Figure 2.15b illustrates the case where a plastic zone forms ahead of the growing crack. The nonlinearity in the load-displacement curve is caused by a combination of crack growth and plastic deformation. If the specimen is unloaded prior to fracture, the load-displacement curve does not return to the origin; crack tip plasticity produces a finite amount of permanent deformation in the specimen [38]. The stress intensity should be corrected for plasticity effects by substituting C_{eff} into *Eq.(2.33)* to determine an effective crack length.

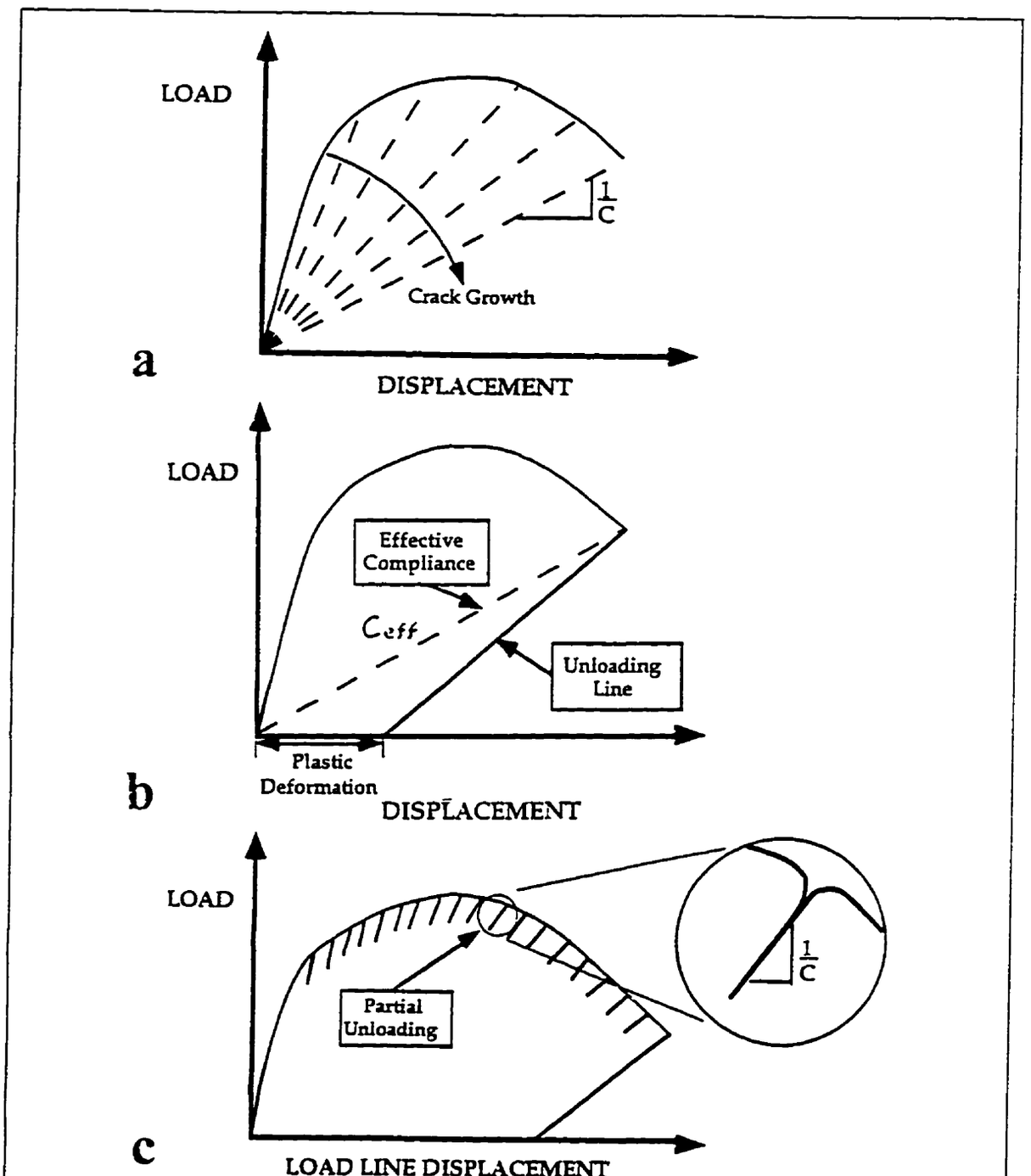

Figure 2.15 Load-displacement curve for crack growth (a) in the absence of plasticity, (b) with plasticity. (c) the unloading compliance method for monitoring crack growth and calculate the plastic area A_i ($1 \le i \le n$) [38].

Figure 2.15c shows the most common case where the crack length is computed at regular intervals during the single specimen test by partially unloading the specimen and measuring the compliance. As the crack grows, the specimen becomes more compliant (less stiff) [38]. The plastic area A_i can be calculated by

$$A_i = A_{i-1} + \frac{P_i(P_iC_i - P_{i-1}C_{i-1})}{2} \tag{2.45}$$

where $1 \leq i \leq n$. When $i = 1$, the A_0 could be measured directly from the load-displacement curve.

Thereafter, according to the *ASTM* Standard *E 813-90* [99] the *J*-integral is determined and plotted against physical crack extension, Δa, using at least four data points. The *J* versus crack extension behaviour can be simulated by a power law curve, which reflect the materials resistance to crack growth. Thereby, a J_{Q} value can be obtained from this curve. After verifying the validity of J_{Q} by *Eq.(2.20)*, a J_{Ivc} value would be obtained and used to calculate the K_{Ivc} [38, 99-100],

$$K_{Ivc} = \left[\frac{J_{Ivc}E}{(1-\nu^2)}\right]^{1/2} \tag{2.46}$$

Obviously, the *J*-integral, unloading-reloading method in a CNB test by three-point bending has more advantages than a customary *CNB* test for K_{Im} because this method needs exceptionally small amount of materials as discussed in Section 2.1.3 and is much more useful for non-elastic materials.

2.3 Alloy Processing and Microstructure Measurement Techniques

The in-situ boron-free and boron-doped composite alloys investigated were prepared from pure elements (nickel (99.98 pct) and aluminum (99.99999 pct)) and a master alloy of Al-3.2 wt.% B, and had a composition of $Ni_{y-x}Al_{100-y}B_x$ x = 0.2 or 0.4 at.% for boron-doped alloys; y = 65, 67, 69, 70, 73, 75 and 77 at.%). The pure elements were melted by a high frequency induction melting method in a graphite crucible coated inside with a boron nitride aerosol lubricoat and then poured into a stainless steel mould under a high-purity argon atmosphere. The details of the melting procedure are given in **Table 2.3.**

In addition, the maximum temperature of the melt was measured by a thermocouple (W-5%Rh and W-26%Rh) inserted into the graphite crucible. Temperature had to be controlled accurately (within ± 5°C) to avoid the reaction between the melting solution and the crucible at elevated temperature.

An additional homogenizing heat treatment was performed at 1000°C/100h (furnace cooling) for all the ingots in a tube furnace. Some additional annealing or quenching was also done for some of the samples to investigate the changes in the microstructure. To reveal the grain-boundaries, the polished surface of the specimen was etched by Nital (4% $HNAl_3$+ alcohol) for 20 to 90 seconds.

Table 2.3 Details of melting and casting processing procedure.

In-situ Composite	Method no.	Description
$Ni_{65}Al_{35}$ $Ni_{67}Al_{33}$	1	(i) Evacuating the chamber of the induction furnace to 0.05 atm. (ii) Heating up to ≈400°C in vacuum (iii) Evacuating again to 0.05 atm. or below (iv) Pressurize the chamber with high purity argon gas ($1.7x10^{-2}$ MPa) (v) Slow heating up to max. temperature ≈1520°C in 10 min. (vi) Holding at ≈1520°C for 6 min. (vii) Pouring into a stainless steel mould (viii) Furnace cooling (20°C)
$Ni_{69}Al_{31}$ $Ni_{71}Al_{29}$	2	Almost the same steps as above except: (v) Slow heating up to max. temperature ≈1500°C in 15 min. (vi) Holding at ≈1500°C for 6 min.
$Ni_{73}Al_{27}$ $Ni_{72.8}Al_{27}B_{0.2}$ $Ni_{75}Al_{25}$ $Ni_{74.8}Al_{25}B_{0.2}$ $Ni_{74.6}Al_{25}B_{0.4}$	3	Almost the same steps as above except: (v) Slow heating up to max. temperature ≈1485°C in 15 min. (vi) Holding at ≈1485°C for 6 min.
$Ni_{77}Al_{23}$ $Ni_{75.6}Al_{24}B_{0.4}$	4	Almost the same steps as above except: (v) Slow heating up to max. temperature ≈1485°C in 15 min. (vi) Holding at ≈1485°C for 6 min.

The microstructure, crystal structure and composition of the alloys were investigated by optical microscopy (Nomarski interference contrast), scanning electron microscopy. X-ray diffraction (*XRD*) patterns carried out in a Siemens D500 diffractometer equipped with a nickel filter and graphite monochromator using Cu-K_α radiation (λ=1.54060 Å) and a fully quantitative X-ray energy dispersive spectroscopy (*EDS*) analysis (QX2000 Link system). The volume fractions of the second phase was measured on the monitor's screen attached to the optical microscope by the linear intercept method [143]. Vickers indentations were made in the proximity of grain boundary under load of 2000g as to induce intergranular cracking at the grain boundaries in the B-free and B-doped Ni_3Al specimens. This in a qualitative manner would test the effect of boron addition on the brittleness of grain boundaries in Ni_3Al. These intergranular microcracks were also measured on some specimens by an automated Java image analysis system [144].

2.4 Preparation and Procedures of the Fracture Toughness Test

This test method involves testing of chevron-notched specimens by three-point loading. The cross head speed was 0.05 mm/min, which was the lowest one of the Instron machine (Model 4206). Load versus load-line displacement (*LLD*) was recorded either digitally by a computer or autographically on an x-y recorder. The K_{Im} value is calculated from the

maximum load by equations that have been established on the basis of elastic stress analysis of CNB specimens described in Chapter 2.

The single specimen technique involves using an elastic compliance technique as discussed in Section 2.2 to obtain the J-Δa curve from a single specimen. At least five specimens for each in-situ composite were tested. The load/reload sequences of a single-specimen technique produce J versus crack extension data points evenly spaced over the prescribed test region. A minimum of six J versus crack-extension data points were obtained.

The validity of the determination of the calculated K_{Ivc} and J_{Ivc} from this test would be discussed in Chapter 4.

2.4.1 Specimen Preparation

The bend specimen is a chevron notched beam with dimensions: (3.5 to 5) x (4 to 5) x 20 mm^3, which is machined by an *EDM*. The ratio *W/B* of the rectangular beam is nominally equal to 1.14↔1.45. The dimensional tolerances and surface roughness satisfied the requirements of *E 399-90 FIG. A3.1* [97] by medium emery paper polishing. The *CNB* was loaded in three-point bending with a support span, S, nominally equal to four times the width, W, as shown in **Figure 2.9.**

The specimen must be installed in the fixture properly. The test fixture was set up so that the line of action of the applied load shall pass midway between the support roller centres within 1% of the distance between these centres. The load point was aligned right in the middle of the specimen using a magnifying glass with light. The span was measured within 0.5% of

nominal length. The specimen was located with the crack tip midway between the rollers to within 1% of the span, and squared to the roller axes within 2°. The specimen was loaded at a rate of $0.0008s^{-1}$ such that the rate of increase of stress intensity is within the range 0.007 to 0.017 MPa.$\sqrt{m}$/s. At least five specimens were tested for each alloy.

2.4.2 Fixture Design and Fabrication

The primary requirements of all alignment devices are that the load is applied axially, uniformly and with negligible "slip-stick" friction [145]. In order to ensure uniaxial loading, a ball-joined fixture was designed and processed by a lathe and a milling machine for a *CNB* test. This fixture is designed to minimize frictional effects by allowing the support rollers to rotate and move apart slightly as the specimen is loaded, thus permitting rolling contact as shown in **Figure 2.16**.

The precise feedings step by step for ball surface was calculated using Matlab software. The fixture was made from Hot Rolled-SPS steel. Before machining, its surface Rockwell "C" hardness was approximately 22, which is easy to machine to any shape. After machining, its surface hardness was increased to 55 HRC when it was heated to 830° for 50 minutes followed by oil quenching in order to avoid its deformation during loading.

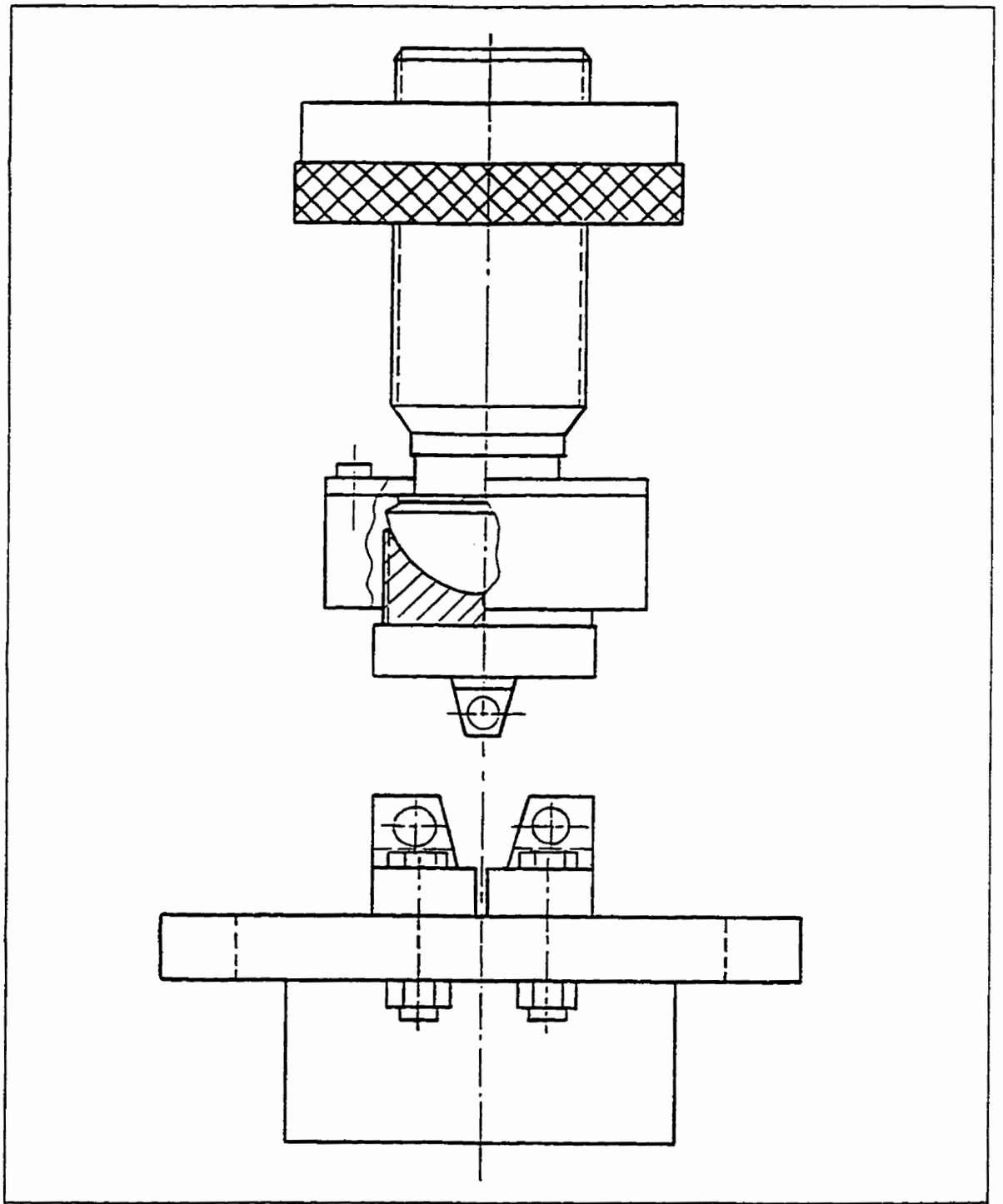

Figure 2.16 Schematically drawings of ball-joined loading parts and span-adjustable support parts, of three-point bending fixture.

This fixture is more adjustable with respect to the size of the specimen because the span can be adjusted continuously to any value that is within its capacity from 8 to 40 mm as shown in **Figure 2.16**. Thus *CNB* specimens with a wide range of thicknesses can be tested with the single fixture.

2.5 Some Additional Tests

2.5.1 Compression Testing

The yield strength σ_{YS} of each broken specimen was obtained by a compression test according to *ASTM* standard *E 9-89a* [145]. The rectangular specimen with 4x4x6.8 mm^3 (the ratio of specimen length over equivalent diameter is 1.5, which is recommended in *E 9-89a* [145) was subjected to an increasing axial compressive load under a constant strain rate of 10^{-4} s^{-1}; both load and strain were monitored and recorded digitally by a computer.

Both ends of the compression specimen shall bear on blocks with surfaces flat and parallel within 0.0002 in/in and with a surface finish less than 1.6 μm by grinding. The two hardened steel blocks with ≈50 HRC after heat treatment 870°C for 30 minutes and brine quenching were carefully centred with respective to the testing machine heads.

To reduce friction, which can effect test results by barrelling, molybdenum disulfide was

applied on the surfaces. The specimens were carefully polished to obtain a surface roughness of 1.6 μm, flatness and parallelism within 0.0005 mm/mm, which was perpendicular to the lateral surface. The specimen was placed in the test fixture and carefully aligned to ensure concentric loading. The strain range was set less than 0.05 because only yield strength was acquired in this test.

2.5.2 Vickers Microhardness Test

The micro-mechanical properties of individual phases were investigated by a Vickers microhardness test. The Shimadzu Micro Hardness Tester HMV-2000 was used to carry out Vickers microhardness test. Its automation of loading, holding of loads, unloading and selection of the test load eliminate individual errors during loading [146]. As well, the additional low weights of 5 gf and 10 gf, and the built-in data processing capability permit the high reliability and controllability of this hardness test.

CHAPTER 3

EXPERIMENTAL RESULTS

3.1.1

3.1.2 As discussed in the previous Chapters, fracture toughness of in-situ composites is very dependent on the microstructural features, which include: morphology of structure, volume fraction of reinforcement, composition and grain size. Therefore, a general investigation and thorough understanding of microstructural features in the as-cast and homogenized, boron-free and boron-doped in-situ NiAl-Ni_3Al composites produced by induction melting method is essential before a discussion of the fracture toughness test results can begin.

3.1 Microstructural Features

3.1.1 The As-Cast, Boron-Free and Boron-Doped In-Situ Composites

Figure 3.1 shows a group of typical photographs obtained from the as-cast, boron-free in-situ composites. A few local twin-structures obviously exist in the NiAl matrix of the as-cast

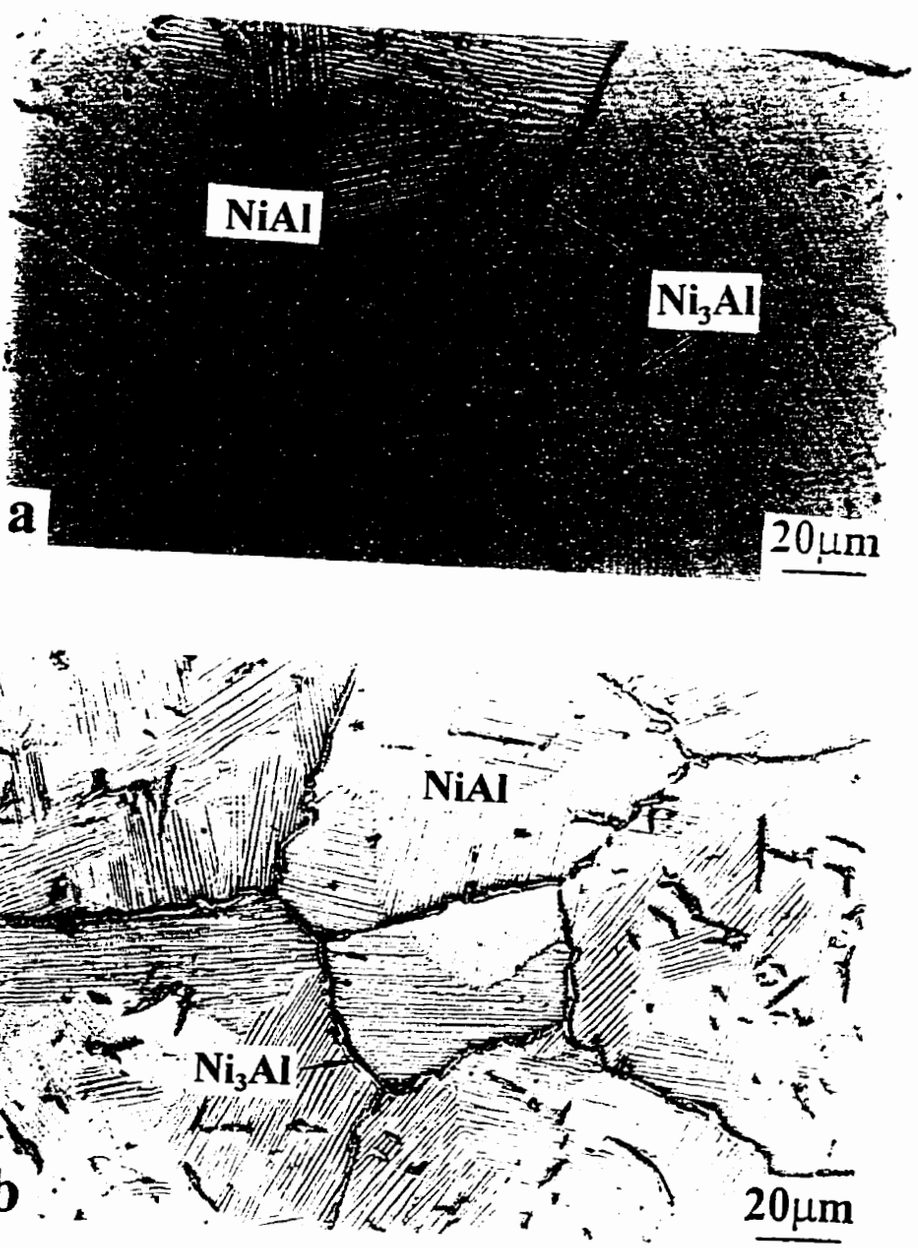

Figure 3.1 Optical micrographs of the etched microstructures of the as-cast, boron-free in-situ composites with Nomarski interference contrast: (a) $Ni_{64.6}Al_{35.4}$ and (b) $Ni_{65.5}Al_{34.5}$.

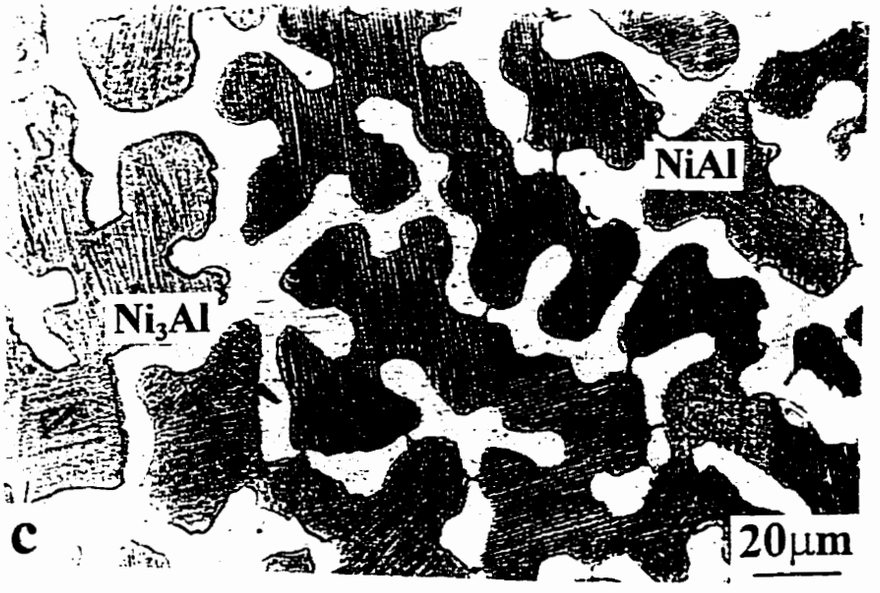

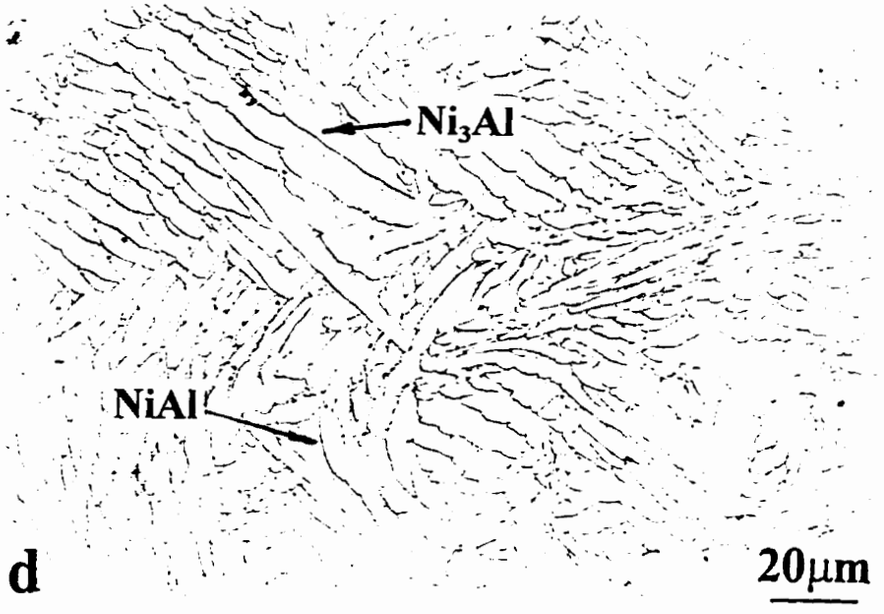

Figure 3.1 Optical micrographs of the etched microstructures in the as-cast, boron-free in-situ composites with Nomarski interference contrast: (c) $Ni_{67.1}Al_{32.9}$ and (d) $Ni_{70.3}Al_{29.7}$.

$Ni_{64.6}Al_{35.4}$ composite alloy as shown in **Figure 3.1a**. The Ni_3Al phase is distributed as an envelope at the grain boundaries and intragranular precipitates. Compared to **Figure 3.1a**, it can be seen that the $Ni_{65.5}Al_{34.5}$ alloy shows almost fully twinned-structures (**Figure 3.1b**) while the overall Ni content in the two composites only differs by 0.9 atomic percent, which demonstrates that the phase morphologies of the Ni-rich in-situ composites are very sensitive to the increase of Ni content. In addition, the volume fraction of Ni_3Al phase in $Ni_{65.5}Al_{34.5}$ distributed as precipitates and at grain boundaries simultaneously increases up to 21%. This is because these structures are in as-cast materials where cooling rates were not in controlled. In other words, these structures are non-equilibrium. The compositions of each phase are shown in **Table 3.1**.

When the overall Ni-content again increases by 1.6 at.% to 67.1 at.% in the in-situ composite $Ni_{67.1}Al_{32.9}$, the microstructure exhibits a round, discontinuous morphology of Ni_3Al phase with a fully twin structure of the NiAl matrix (**Figure 3.1c**). The size of the ductile second phase of Ni_3Al, especially in grain boundaries (as shown in **Figures 3.1a** to **c**), gradually increases from approximately 0.6 to 5 μm with increasing Ni content from 64.6 at.% to 67.1 at.%, respectively. The total volume fraction of the ductile Ni_3Al phase also increases from 5% to 26%, as shown in **Table 3.2**.

Almost equal distribution of Ni_3Al and NiAl, volume fractions of 54% to 46%, respectively is seen in $Ni_{70.3}Al_{29.7}$ as shown in **Figure 3.1d**. It can be seen that the sharp NiAl phase is continuously distributed in the matrix of Ni_3Al (**Figure 3.1d**). Furthermore, increasing the Ni

Table 3.1 Target composition and quantitative EDS results of the as-cast, boron-free and boron-doped in-situ composites (at.%).

Target Ni (at.%)	Element	Overall	Matrix	Grain boundary	Precipitates
63	Ni	64.6±0.5	62.5±0.9	71.0±1.0	71.7±0.8
	Al	35.4±0.5	37.5±0.9	29.0±1.0	29.3±0.8
65	Ni	65.5±0.3	63.6±0.9	73.5±0.4	73.5±0.4
	Al	34.5±0.3	36.4±0.9	26.5±0.4	26.5±0.4
67	Ni	67.1±0.9	65.7±0.5	74.9±0.7	74.8±0.3
	Al	32.9±0.9	34.3±0.5	25.1±0.7	25.2±0.3
69	Ni	70.3±0.6	73.4±0.6	-	64.2±0.7
	Al	29.7±0.6	26.6±0.6	-	35.8±0.7
71	Ni	72.4±0.6	74.9±0.5	-	65.4±0.8
	Al	27.6±0.6	25.1±0.5	-	34.6±0.8
73	Ni	73.1±0.3	76.2±0.4	-	67.6±0.5
	Al	26.9±0.3	23.8±0.4	-	32.4±0.5
77	Ni	77.2±0.5	76.1±0.9	-	94.2±0.7
	Al	22.8±0.5	23.9±0.9	-	5.8±0.7
72.8-0.2B	Ni	73.2±1.1	75.4±0.6	-	65.0±0.6
	Al	26.6±1.1	24.4±0.6	-	34.8±0.6
74.6-0.4B	Ni	74.5±0.7	74.7±0.6	-	-
	Al	25.1±0.7	24.9±0.6	-	-

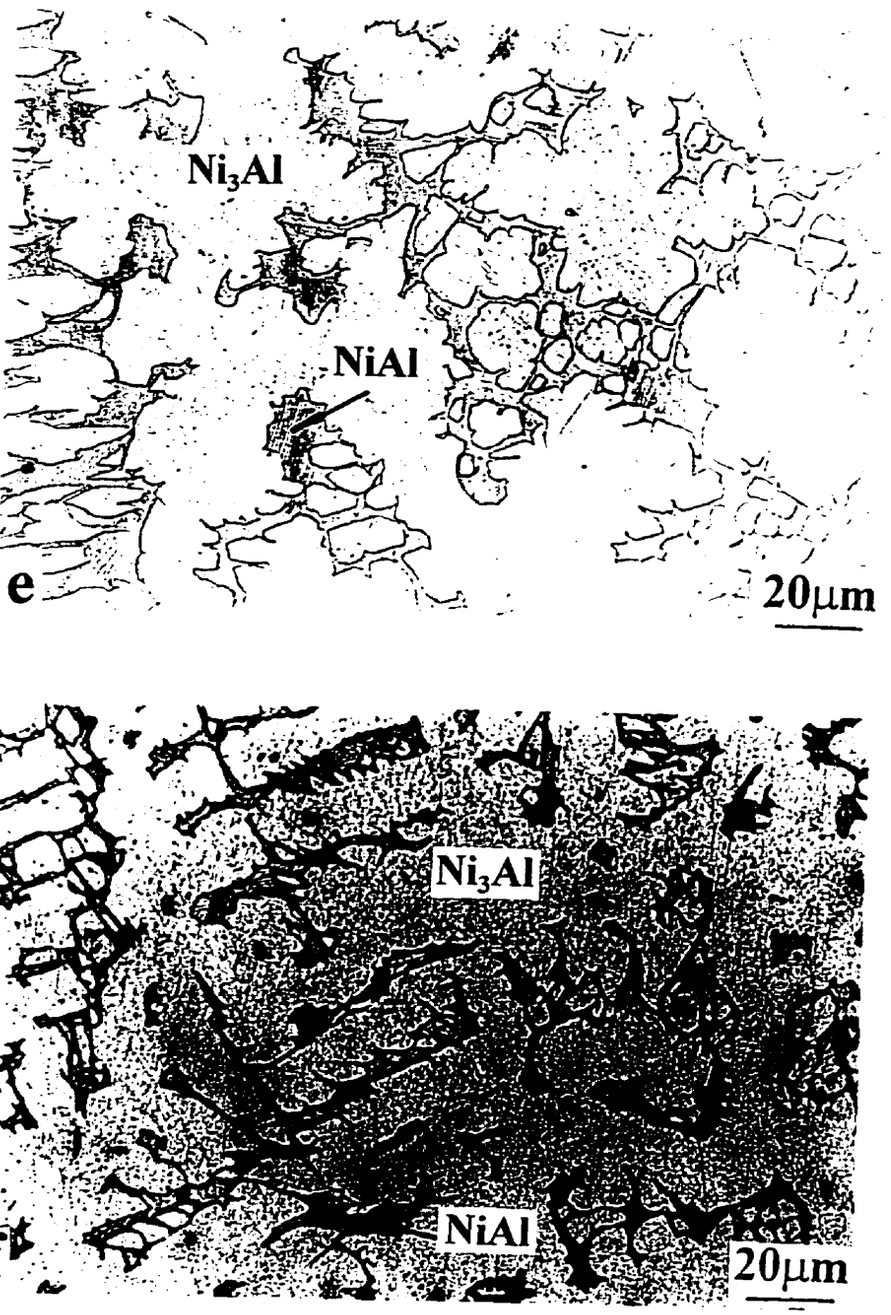

Figure 3.1 Optical micrographs of the etched microstructures in the as-cast, boron-free in-situ composites with Nomarski interference contrast: (e) $Ni_{72.4}Al_{27.6}$ and (f) $Ni_{73.1}Al_{26.9}$.

Table 3.2 The mean grain size of the material and volume fraction of second phase with standard deviations of the as-cast, boron-free and boron-doped in-situ composites.

In-situ compo-sites (at.%)	Type of matrix phase	Matrix grain size (μm)	Type of the second phase	second phase	
				Thickness or size (μm)	Volume fraction (%)
$Ni_{64.6}Al_{35.4}$	NiAl	163 ± 87.4	Ni_3Al	0.8 ± 0.2	5.1 ± 0.7
$Ni_{65.5}Al_{34.5}$	NiAl	121.2 ± 34.7	Ni_3Al	0.9 ± 0.3	20.5 ± 1.2
$Ni_{67.1}Al_{32.9}$	NiAl	-	Ni_3Al	-	25.6 ± 1.0
$Ni_{70.3}Al_{29.7}$	Ni_3Al	-	NiAl	3.5 ± 1.1	46.1 ± 1.1
$Ni_{72.4}Al_{27.6}$	Ni_3Al	-	NiAl	5.2 ± 2.4	35.9 ± 1.2
$Ni_{73.1}Al_{26.9}$	Ni_3Al	-	NiAl	5.1 ± 2.6	32.4 ± 1.3
$Ni_{77.2}Al_{22.8}$	Ni_3Al	168.2 ± 89.4	Ni	-	0.6 ± 0.4
$Ni_{73.2}Al_{26.6}B_{0.2}$	Ni_3Al	-	NiAl	5.5 ± 2.5	29.9 ± 1.1
$Ni_{74.5}Al_{25.1}B_{0.4}$	Ni_3Al	35.6 ± 42.4	NiAl	-	≈ 0.3

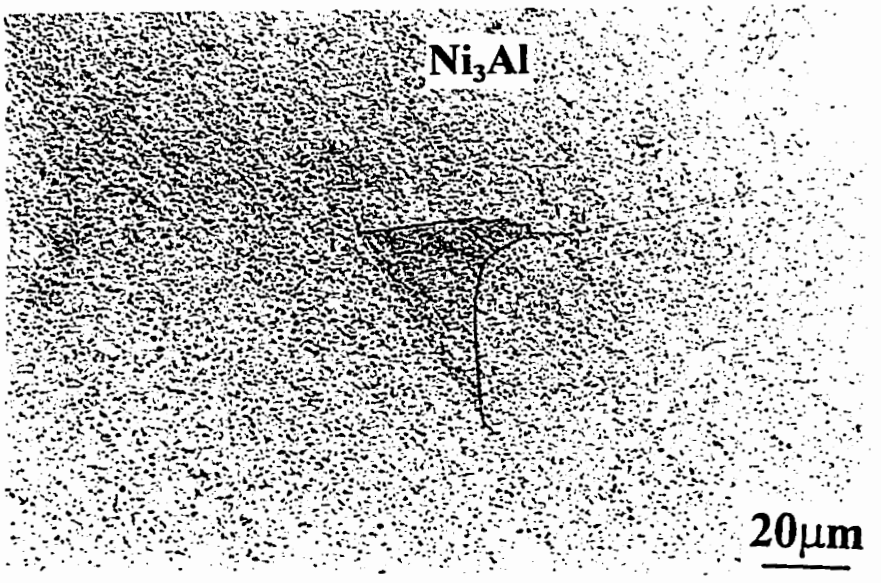

Figure 3.1g Optical micrographs of the etched microstructure of as-cast, boron-free $Ni_{77.2}Al_{22.8}$ in-situ composite (Nomarski interference contrast).

content from 70.3 to 73.1 (**Figures 3.1d** to **f**) results in a gradual decrease of the sharp, locally twinned-structure of the NiAl phase from 46 vol.% to 33 vol.% as indicated in **Table 3.2.**

Figure 3.1g shows the $Ni_{77.2}Al_{22.8}$ alloy which is almost a pure single-phase Ni_3Al (only 0.6 vol.% of Ni found). To check the effect of boron-doping on the investigated in-situ composites, two alloys were produced as shown in **Figures 3.2a** and **b.** The compositions, grain size and volume fraction of each phase are summarised in **Tables 3.1** and **3.2.** It is clear that the $Ni_{73.2}Al_{26.6}B_{0.2}$ in-situ composite shown in **Figure 3.2a** exhibits the same structure as

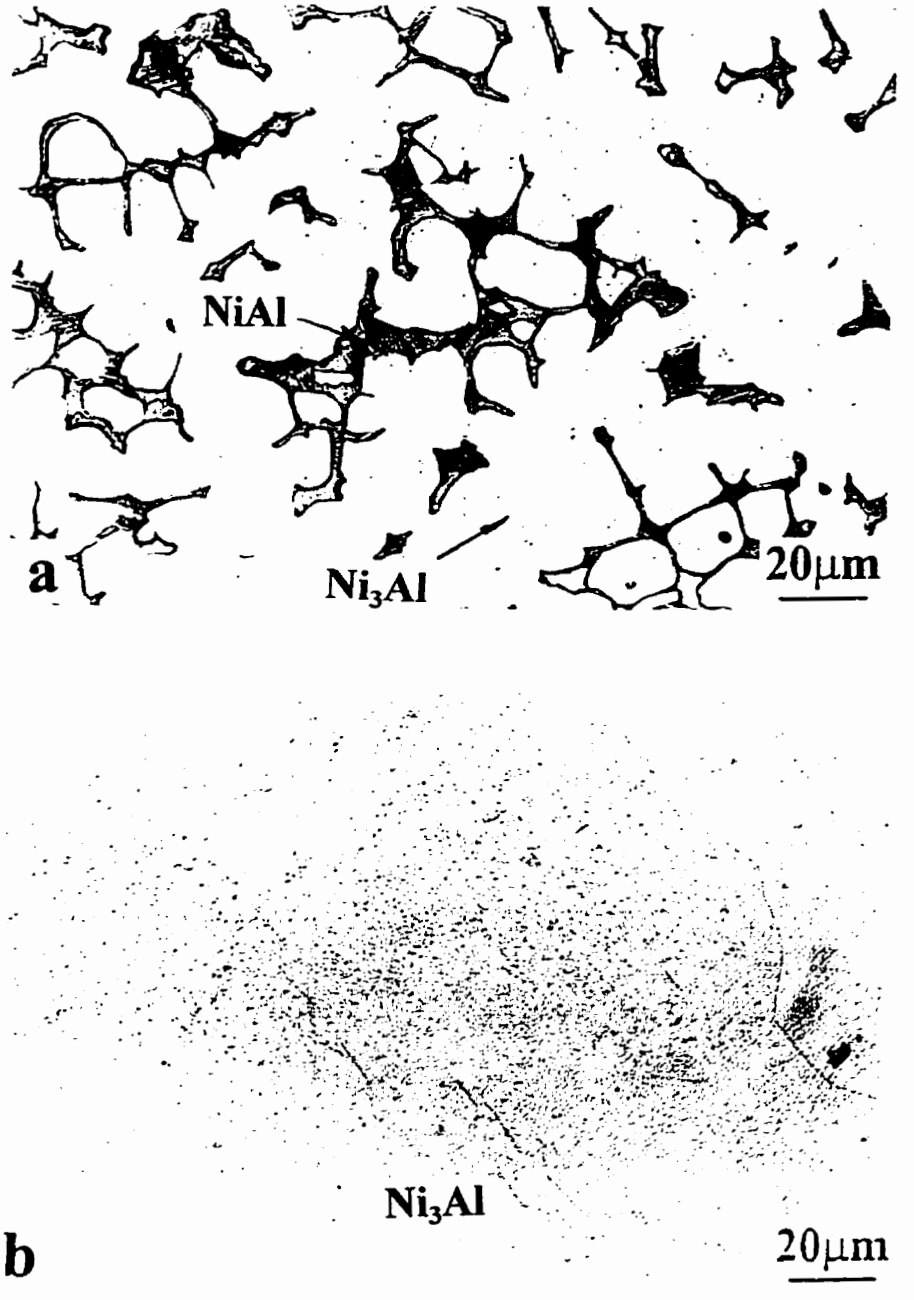

Figure 3.2 Optical micrographs of the etched microstructures in the as-cast, boron-doped in-situ composites with Nomarski interference contrast: (a) $Ni_{73.2}Al_{26.6}B_{0.2}$ and (b) $Ni_{74.5}Al_{25.1}B_{0.4}$.

$Ni_{73.1}Al_{26.9}$ (**Figure 3.1f**). However, the boron-doped $Ni_{74.5}Al_{25.1}B_{0.4}$ alloy is almost pure single-phase Ni_3Al (**Figure 3.1i**), which is similar to the structure of the $Ni_{77.2}Al_{22.8}$ (**Figure 3.1g**).

3.1.2 The Homogenized, Boron-Free and Boron-Doped In-Situ Composites

The as-cast in-situ composites were homogenized at 1000°C for 100h followed by a slow furnace cooling. **Figure 3.3** shows another group of typical, optical micrographs of the as-annealed, boron-free in-situ composites, corresponding to **Figure 3.1**. To show homogenized structure in detail, lower magnification photos are also included for each composite. After the heat-treatment at 1000°C for 100h followed by a slow furnace cooling, the overall Ni-content was the same as that of the as-cast specimens (see **Table 3.3**). The volume fraction of Ni_3Al increased for every in-situ composite (**Table 3.4**). Such an obvious increase of Ni_3Al phase is demonstrated by the coarsening of the intergranular and grain boundary precipitates (**Figures 3.3a** to **f**) or by the larger area of the Ni_3Al matrix (**Figures 3.3g** to **l**). In particular, the $Ni_{73.2}Al_{26.8}$ in-situ composite became almost pure Ni_3Al single phase (91.2%). Obviously, the increase of the volume fraction of relatively more ductile γ' (Ni_3Al) phase after homogenization may lead to fracture toughening of these in-situ composites.

Another obvious change is that the twinned-structure in the NiAl phase decreased dramatically (**Figures 3.3a** to **f**) and the local twin structure in particular almost disappeared in **Figures 3.3g** to **l**. This is probably due to the lower cooling rate.

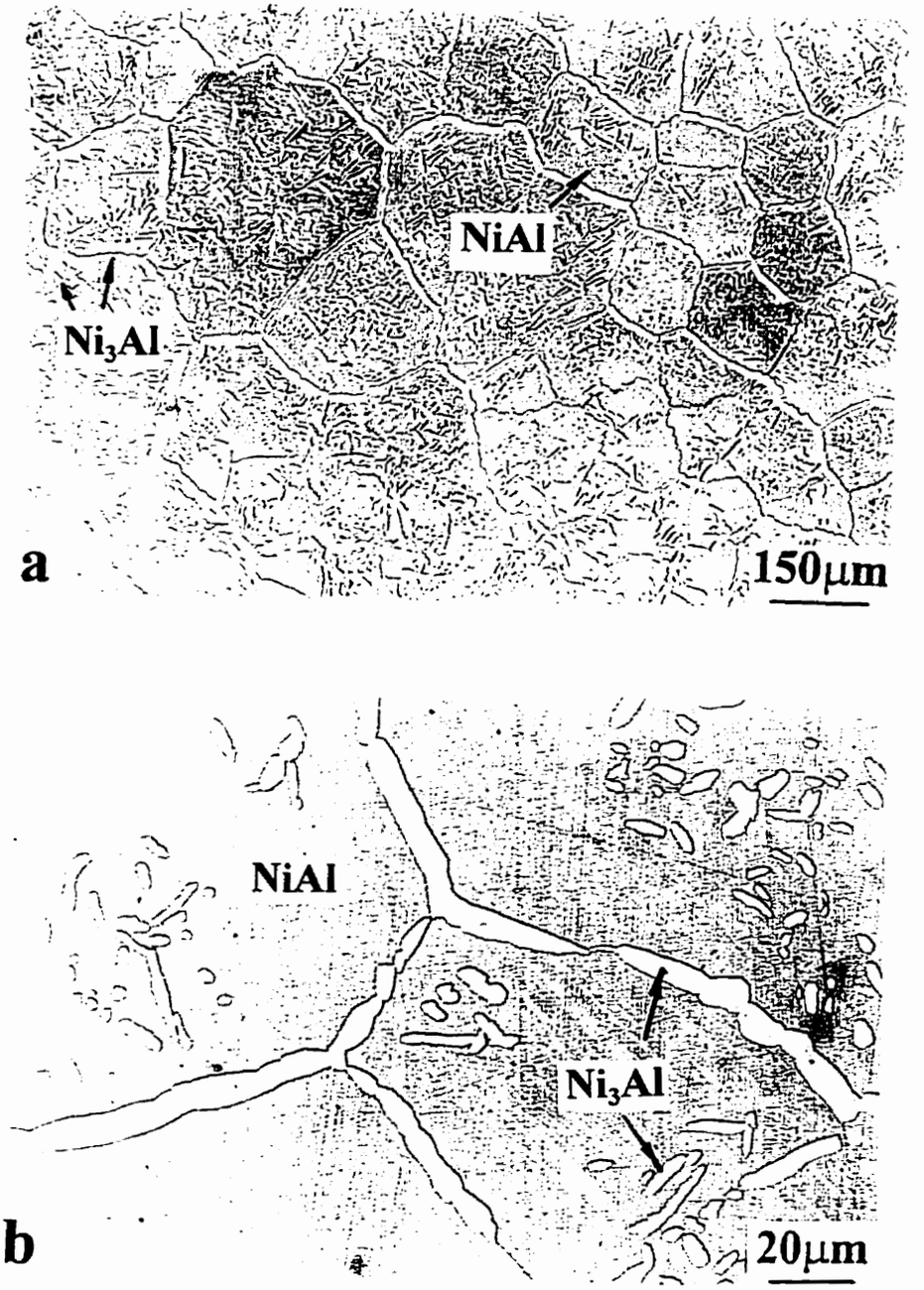

Figure 3.3 Optical micrographs of the etched microstructure of the homogenized $Ni_{63.7}Al_{36.3}$ in-situ composite at: (a) lower and (b) higher magnification with Nomarski interference contrast.

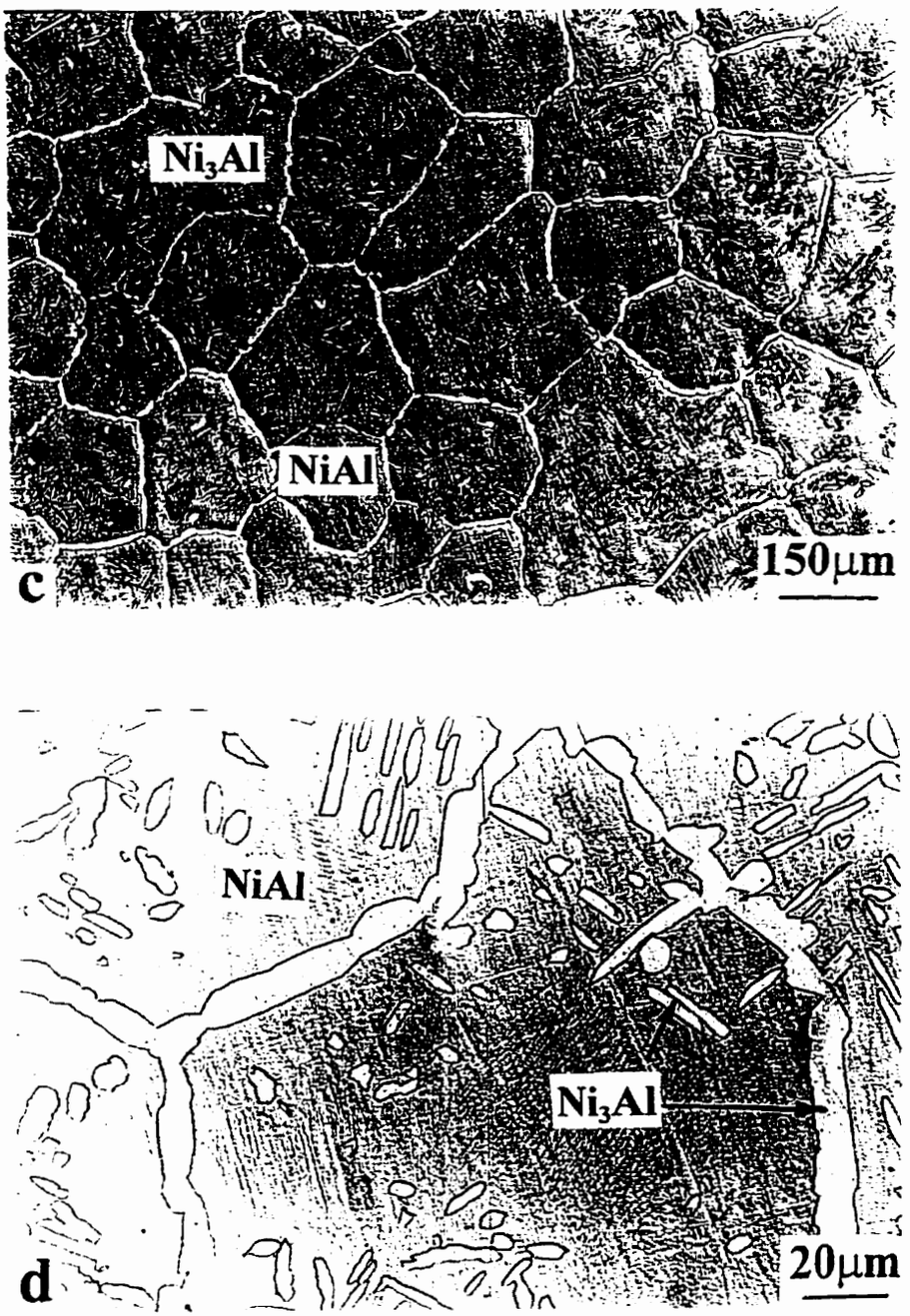

Figure 3.3 Optical micrographs of the etched microstructure of the homogenized $Ni_{65.3}Al_{34.7}$ in-situ composites at: (c) lower and (d) higher magnification with Nomarski interference contrast.

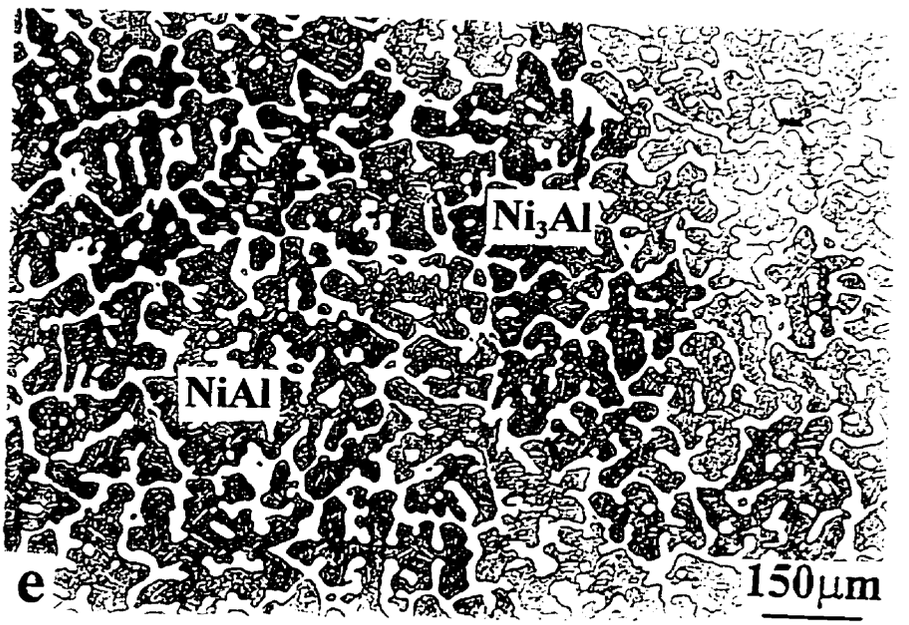

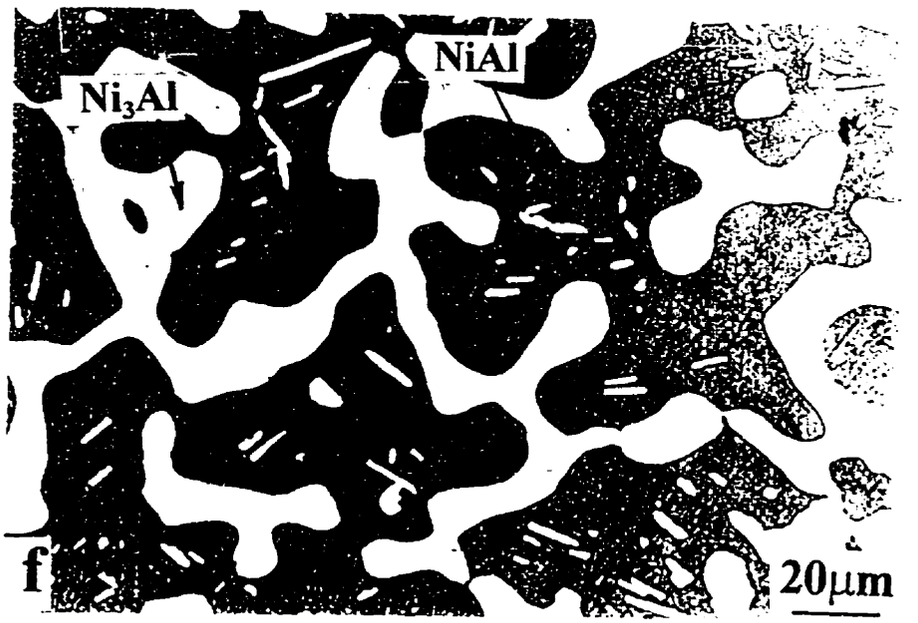

Figure 3.3 Optical micrographs of the etched microstructure of the homogenized $Ni_{67.2}Al_{32.8}$ in-situ composite at: (e) lower and (f) higher magnification with Nomarski interference contrast.

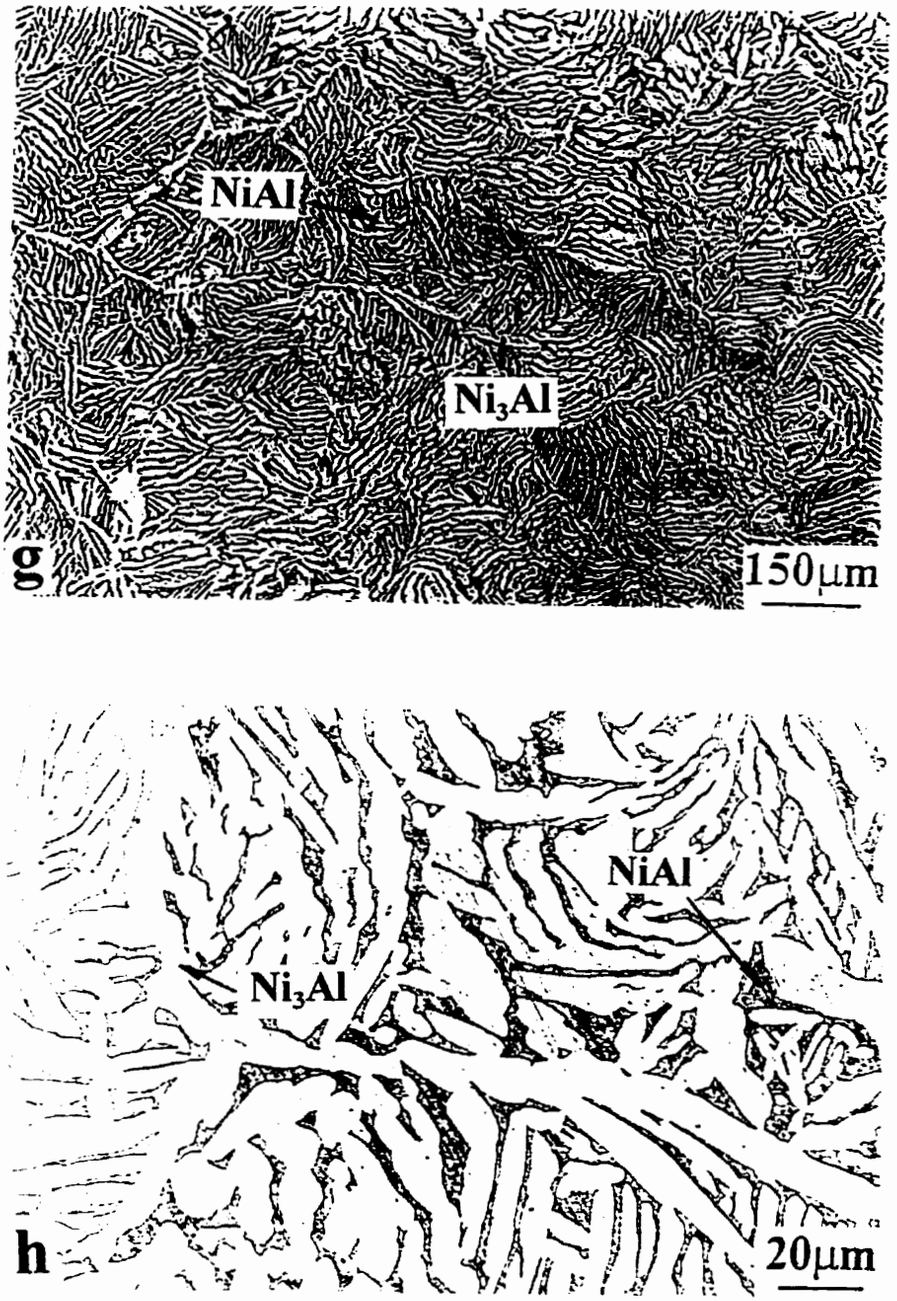

Figure 3.3 Optical micrographs of the etched microstructure of the homogenized $Ni_{70.8}Al_{29.2}$ in-situ composite at: (g) lower and (h) higher magnification (Nomarski interference contrast).

Table 3.3 Target composition and quantitative EDS results of the homogenized, boron-free and boron-doped in-situ composites (at.%).

Target Ni (at.%)	Element	Overall	Matrix	Phase	Grain boundary	Phase	Precipitates	Phase
63	Ni	63.7±0.4	60.7±1.0	NiAl	73.2±0.2	Ni_3Al	72.5±0.3	Ni_3Al
	Al	36.3±0.4	39.3±1.0		26.8±0.2		27.5±0.3	
65	Ni	65.3±0.5	63.9±0.4	NiAl	73.8±0.1	Ni_3Al	73.5±0.4	Ni_3Al
	Al	34.7±0.5	36.1±0.4		26.2±0.1		26.5±0.4	
67	Ni	67.2±0.4	63.3±0.7	NiAl	74.4±0.2	Ni_3Al	74.1±0.5	Ni_3Al
	Al	32.8±0.4	36.7±0.7		25.6±0.2		25.9±0.5	
69	Ni	70.8±0.4	73.2±0.3	Ni_3Al	-	-	62.0±0.5	NiAl
	Al	29.2±0.4	26.8±0.3		-		38.0±0.5	
71	Ni	72.8±0.6	73.7±0.5	Ni_3Al	-	-	63.0±0.7	NiAl
	Al	27.2±0.6	26.3±0.5		-		37.0±0.7	
73	Ni	73.2±0.4	73.7±0.3	Ni_3Al	-	-	62.2±0.5	NiAl
	Al	26.8±0.4	26.3±0.3		-		37.8±0.5	
77	Ni	77.7±0.4	77.6±0.7	Ni_3Al	-	-	95.1±0.6	NiAl
	Al	22.3±0.4	22.4±0.7		-		4.9±0.6	
72.8-0.2B	Ni	73.2±0.5	74.9±1.1	Ni_3Al	-	-	64.2±0.4	NiAl
	Al	26.6±0.5	24.9±1.1		-		35.6±0.4	
74.6-0.4B	Ni	74.8±0.5	75.0±0.4	Ni_3Al	-	-	-	-
	Al	24.8±0.5	24.6±0.4					

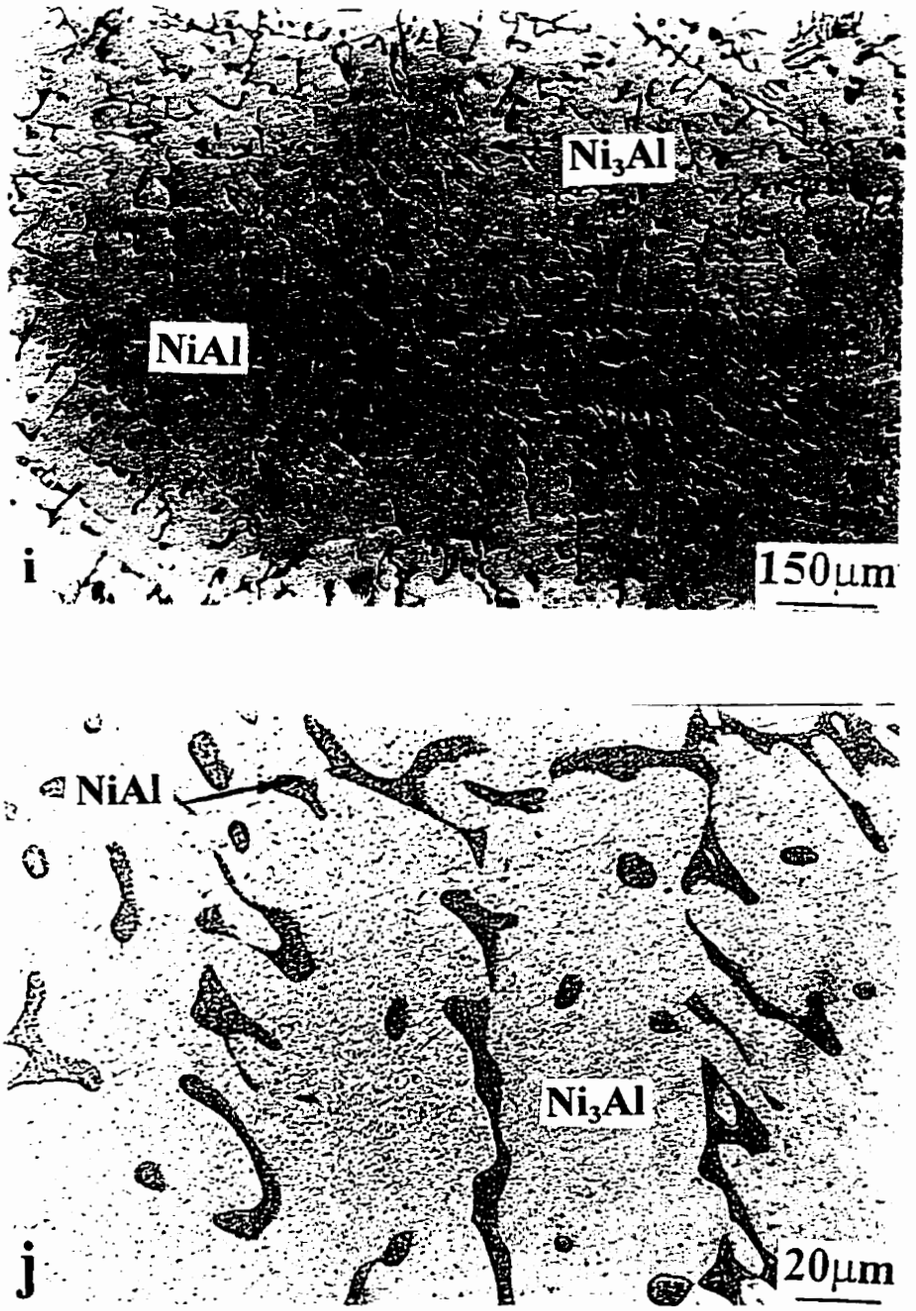

Figure 3.3 Optical micrographs of the etched microstructure of the homogenized $Ni_{72.8}Al_{27.2}$ in-situ composite at: (i) lower and (j) higher magnifications with Nomarski interference contrast.

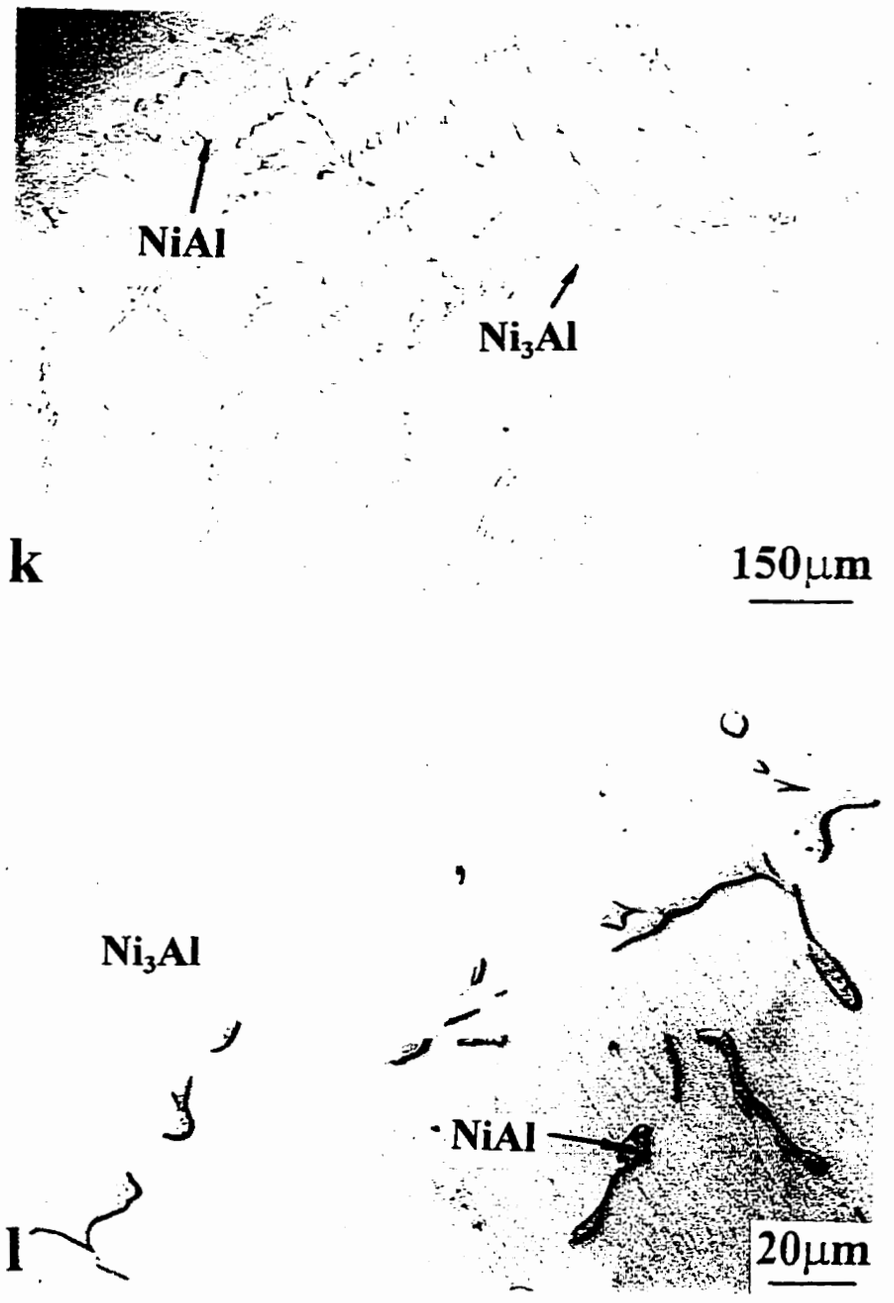

Figure 3.3 Optical micrographs of the etched microstructure of the homogenized $Ni_{73.2}Al_{26.8}$ in-situ composite at: (k) lower and (l) higher magnifications with Nomarski interference contrast.

Table 3.4 The mean grain size of the materials and volume fraction of second phase with standard deviations of the homogenized, aged and boron-free and boron-doped in-situ composites.

In-situ compo-sites (at.%)	Type of matrix phase	Matrix grain size (μm)	Type of the second phase	second phase	
				Thickness or size (μm)	Volume Fraction (%)
$Ni_{63.7}Al_{36.3}$	NiAl	183.8±56.2	Ni_3Al	1.2±0.9	17.4±1.0
$Ni_{65.3}Al_{34.7}$ $Ni_{65.1}Al_{34.9}$ (aged; **Fig. 3.5**)	NiAl	167.5±29.6	Ni_3Al	1.5±0.7	23.5±0.9
$Ni_{67.2}Al_{32.8}$	NiAl	-	Ni_3Al	1.8±0.8	32.2±0.9
$Ni_{70.8}Al_{29.2}$	Ni_3Al	-	NiAl	5.5±2.4	39.8±0.6
$Ni_{72.8}Al_{27.2}$	Ni_3Al	-	NiAl	6.7±1.1	23.1±1.2
$Ni_{73.2}Al_{26.8}$	Ni_3Al	269±82.4	NiAl	3.3±1.5	8.8±1.0
$Ni_{77.7}Al_{22.3}$	Ni_3Al	194±67.2	Ni	-	≈ 0.4
$Ni_{73.2}Al_{26.6}B_{0.2}$	Ni_3Al	275±93.9	NiAl	11.5±7.6	5.4±0.7
$Ni_{74.8}Al_{24.8}B_{0.4}$	Ni_3Al	54.7±39.5	NiAl	-	≈ 0.1

In addition, the grain sizes for all of the in-situ composites are relatively unchanged after homogenization. A group of microstructures of the boron-doped in-situ composites is also shown in **Figure 3.4**. After homogenization, the $Ni_{73.2}Al_{26.6}B_{0.2}$ in-situ composite has only around 5% of the NiAl second phase, which is evenly distributed in the Ni_3Al matrix.

It is also worthy of note that the sharp NiAl phase (shown in **Figures 3.1e** to **f**, and **Figure 3.2a**) has become round (shown in **Figures 3.3i** to **l**, and **Figure 3.4a**), which might also improve the fracture toughness behaviour for the in-situ composites.

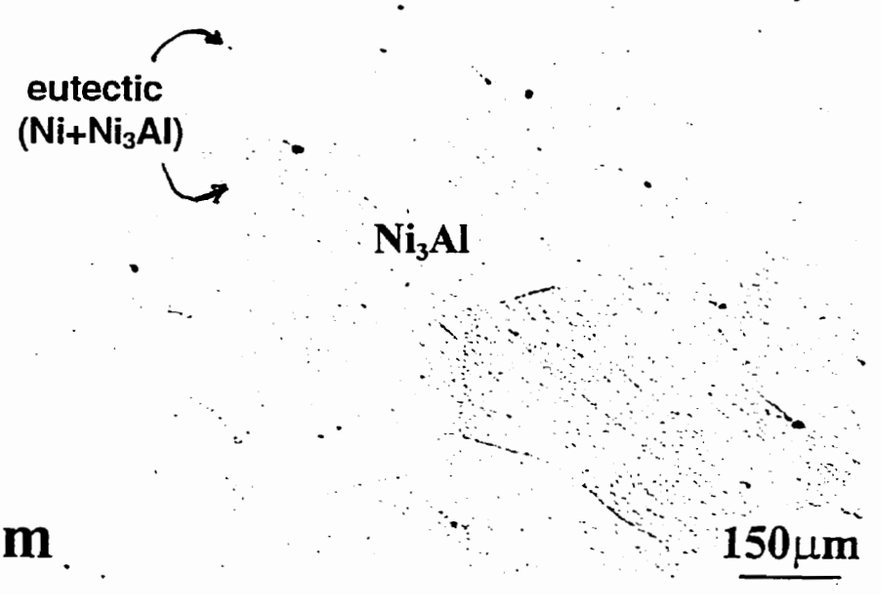

Figure 3.3m A typical micrograph of the etched microstructure of the homogenized, boron-free $Ni_{77.7}Al_{22.3}$ in-situ composite with Nomarski interference contrast.

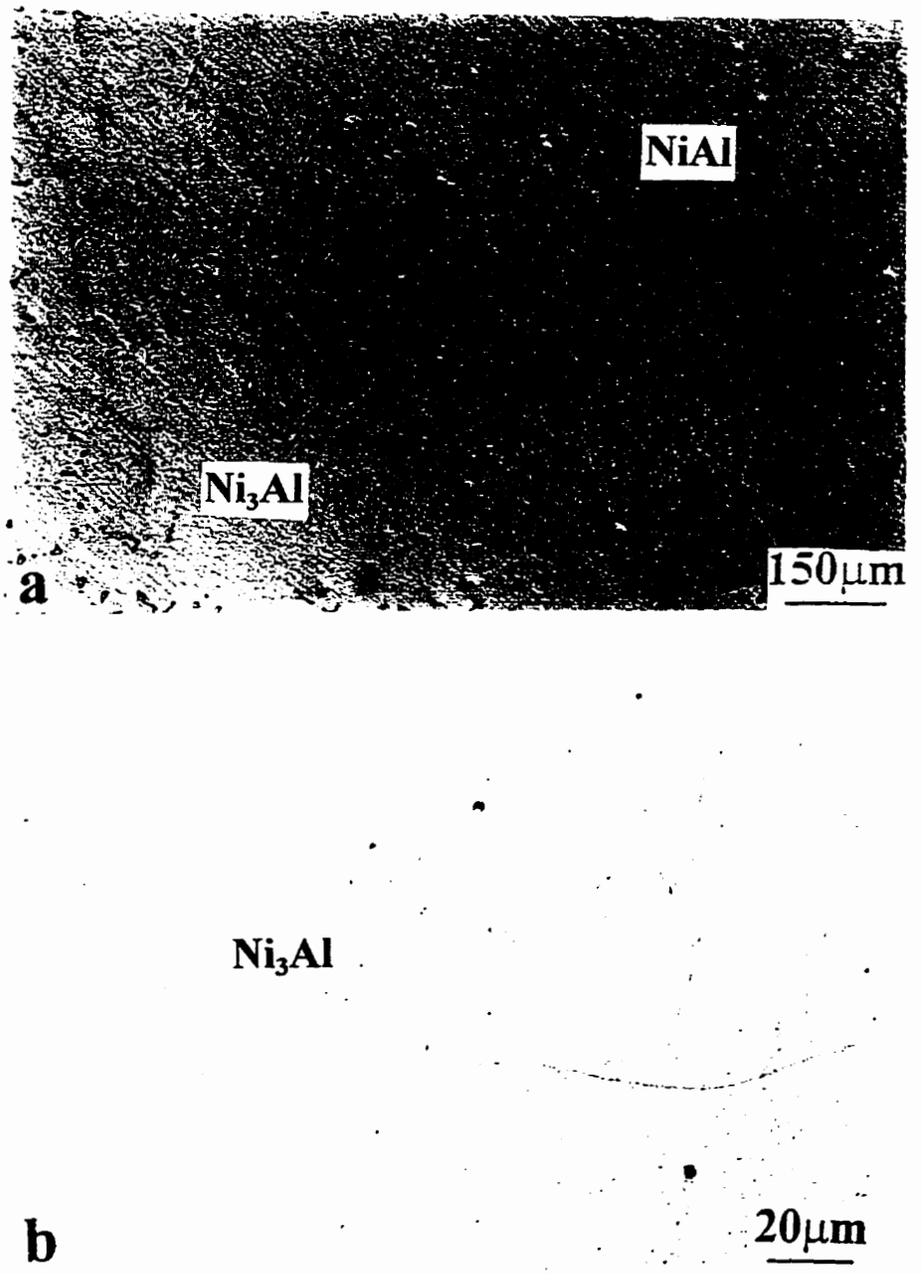

Figure 3.4 Optical micrographs of the etched microstructure of the homogenized, boron-doped in-situ composites (Nomarski interference contrast): (a) $Ni_{73.2}Al_{26.6}B_{0.2}$ and (b) $Ni_{74.8}Al_{24.8}B_{0.4}$.

3.1.3 Some Additional Heat Treatments

In order to form Ni_5Al_3, the homogenized $Ni_{65.3}Al_{34.7}$ in-situ composite (**Figures 3.3c** and **d**) was aged at 550°C for 100h followed by a slow furnace cooling. A typical microstructure of the aged in-situ composite is shown in **Figure 3.5**. A very distinct needle-like, cross-matched structure, called "mat structure", is clearly seen in **Figure 3.5**. However, X-ray analysis must be used to determine whether or not this mat-like structure is the Ni_5Al_3 phase. The overall composition after ageing was measured by *EDS* giving: 65.9 ± 0.5 at.% Ni and 34.1 ± 0.5 at% Al (included in **Table 3.4**).

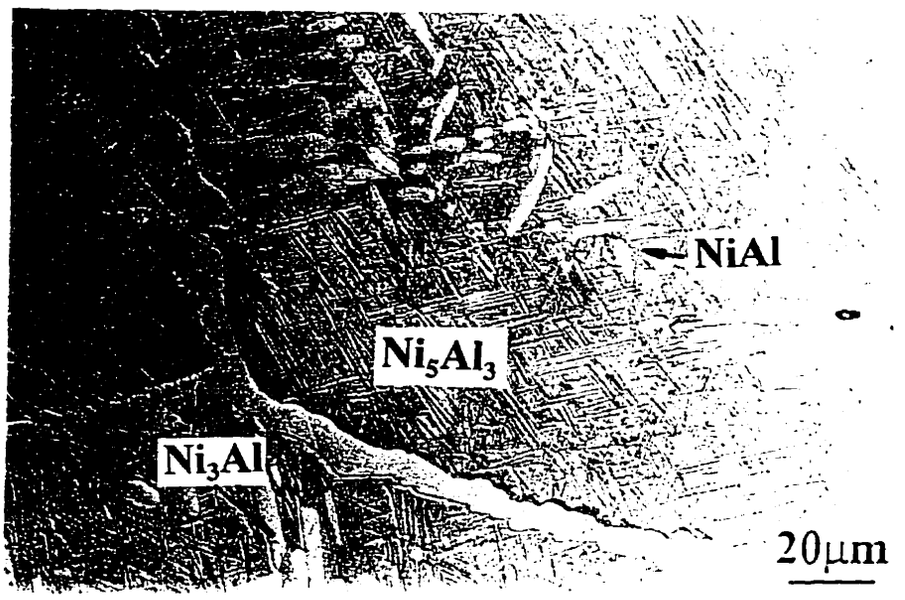

Figure 3.5 An optical micrograph of the etched microstructure of the $Ni_{65.9}Al_{34.1}$ in-situ composite (Nomarski interference contrast) homogenized at 1000°/100h plus aged at 550°/100h followed by furnace cooling.

To check the possible grain-boundary brittleness of the polycrystalline Ni_3Al, the homogenized, boron-free $Ni_{77.7}Al_{22.3}$ in-situ composite was reheated to 1000°C for 15min. followed by water quenching. Local grain-boundary cracking due to quenching (**Figure 3.6a**) was found for this kind of Ni_3Al single-phase alloy. The ratio of the crack length over the total measured area in $Ni_{74.3}Al_{25.7}$ was 0.0055 ± 0.0037 $\mu m/\mu m^2$, as measured by the Java image analysis system [144]. For the water-quenched boron-doped $Ni_{73.2}Al_{26.6}B_{0.2}$ alloy (**Figure 3.6b**) grain-boundary cracking could also be found but seems to be much less pronounced (0.0041±0.0025 $\mu m/\mu m^2$). For the water-quenched boron-doped $Ni_{74.8}Al_{25.8}B_{0.4}$ alloy the ratio of the crack length over the total measured area was 0.0043±0.0019 $\mu m/\mu m^2$, almost the same as that in the 0.2 at.% B alloy. This decrease in the extent of grain boundary cracking might be attributed to the boron segregation effect at grain boundaries.

The water-quenching after homogenization was also used for other in-situ composites. However, no grain boundary cracking was found.

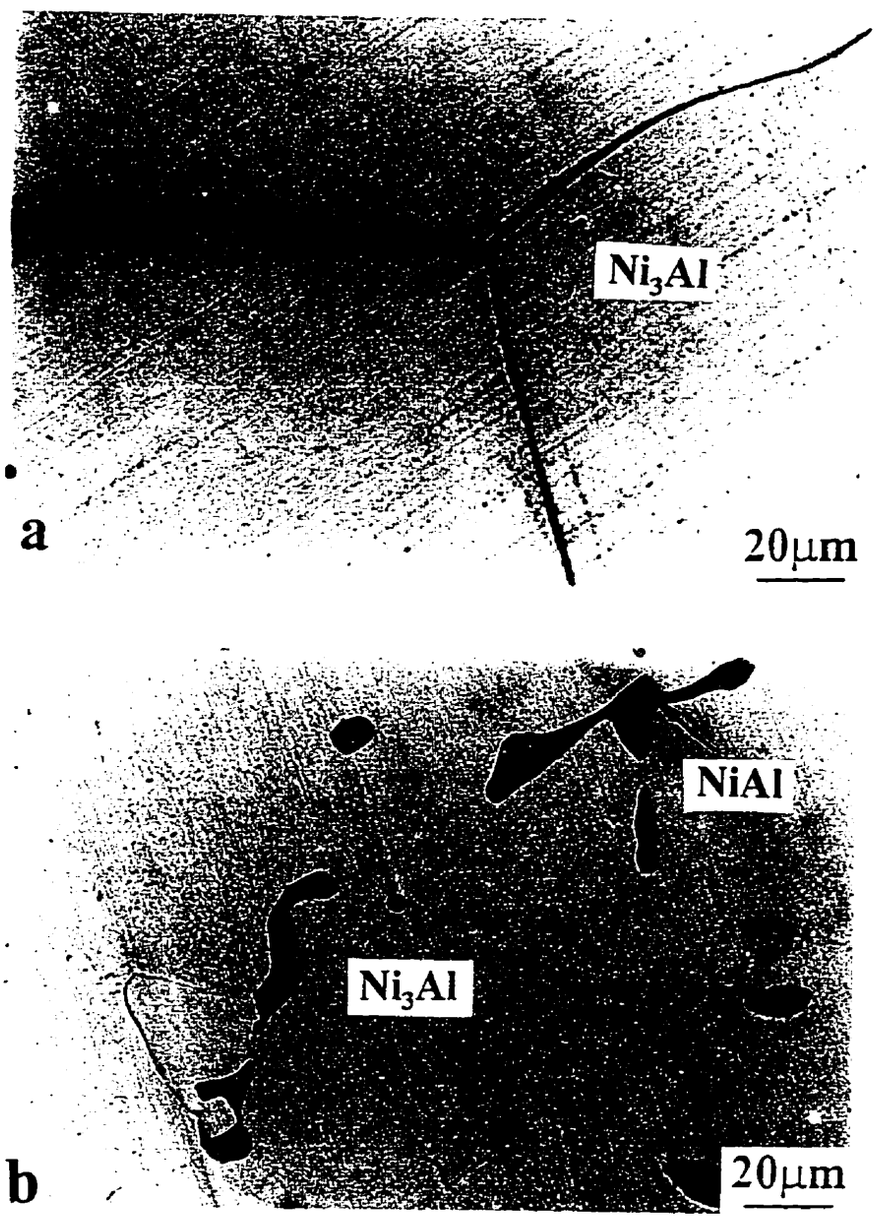

Figure 3.6 The typical micrographs of the grain boundary cracking of (a) the boron-free $Ni_{77.3}Al_{22.7}$ and (b) the boron-doped $Ni_{73.2}Al_{26.6}B_{0.2}$ alloys after re-heat treatment of 1000°C/15min followed by water quenching (Nomarski interference contrast).

3.2 X-Ray Analysis

Typical results of X-ray analysis of the homogenized $Ni_{63.7}Al_{36.3}$ in-situ composite are shown in **Table 3.5**. It is clear that only two phases Ni_3Al ($L1_2$) + NiAl (B2) exist in the $Ni_{63.7}Al_{36.3}$ composite, as expected.

The homogenized (1000°C/100h) plus aged (550°C/100h) $Ni_{65.9}Al_{34.1}$ in-situ composite was also investigated by X-ray analysis and the results are listed in **Table 3.6**. Definitely, the orthorhombic D_{2h}^{19} Ni_5Al_3 [93] exists in the $Ni_{65.9}Al_{34.1}$ in-situ composite.

Table 3.5 A typical X-ray analysis of the homogenized $Ni_{63.7}Al_{36.3}$ in-situ composite.

Position 2θ (deg)	Observed intensity (I/I_0)	Observed d_{hkl} [Å]	Standard d_{hkl} [147] [Å]	Reflection {hkl}	Type of structure
38.146	6.4	2.3573	2.547	110	Superlattice $L1_2$ Ni_3Al
43.668	100.0	2.0712	2.077	111	Fundamental $L1_2$ Ni_3Al
44.472	62.2	2.0355	2.074	110	Fundamental B2 NiAl
50.750	17.8	1.7975	2.020	200	Superlattice $L1_2$ Ni_3Al
63.726	9.9	1.4592	1.461	211	Superlattice $L1_2$ Ni_3Al
64.817	18.7	1.4373	1.434	200	Fundamental B2 NiAl
74.950	16.6	1.2661	1.285	210	Superlattice B2 NiAl

Table 3.6 A typical X-ray analysis of the aged, boron-free $Ni_{65.9}Al_{34.1}$ in-situ composite.

Position 2θ (deg)	Observed intensity (I/I_0)	Observed d_{hkl} [Å]	Standard d_{hkl} [147] [Å]	Reflection {hkl}	Type of structure
24.796	6.1	3.5916	3.6	100	Superlattice $L1_2$ Ni_3Al
33.183	6.8	2.6976	2.641	100	Superlattice B2 NiAl
35.650	5.7	2.5164	2.500	220, 021	Orthorhombic D_{2h}^{19}
43.777	100.0	2.0662	2.074	111	Fundamental $L1_2$ Ni_3Al
44.700	39.8	2.0257	2.02	110	Fundamental B2 NiAl
47.736	15.1	1.9037	1.869	200	Orthorhombic D_{2h}^{19}
65.000	10.7	1.4336	1.434	200	Fundamental D_{2h}^{19}
69.850	7.4	1.3455	1.320	402	Orthorhombic D_{2h}^{19}
74.983	10.5	1.2656	1.250	422	Orthorhombic D_{2h}^{19}
78.140	17.5	1.2222	1.229	440	Superlattice $L1_2$ Ni_3Al

3.3 Micro-Mechanical Properties

After Vickers microhardness tests, no cracks in the matrix were found for all the as-cast and homogenized in-situ composites under the maximum load of 2000g. However, some serious grain boundary cracking under various indentations were observed for a water-quenched, near-Ni_3Al single-phase in-situ composite as shown in **Figure 3.7a.** In contrast, no cracks were found for boron-doped in-situ composites under various indentations (**Figure 3.7b**). Obviously, boron is shown again to have some positive effect on the room temperature grain boundary cohesiveness of polycrystalline Ni_3Al.

It is worth noting that the mat-like Al_5Ni_3 structure obtained from aging at 550°C/100h exhibits a much higher hardness value (**Table 3.7**) than that of any other structures, as shown in **Figure 3.8a** by the difference in the size of indentation for aged and homogenized alloys. The Vickers hardness values of Ni_3Al and NiAl are almost the same (≈350 kg/mm^2) for all of the homogenized, boron-free in-situ composites (**Table 3.7**). The boron-doped composites, however, show slightly lower Vickers hardness values of ≈290 kg/mm^2 than the boron-free in-situ composites (**Table 3.7**). Vickers hardness of both Ni_3Al and NiAl is almost independent of the load (**Figure 3.9**).

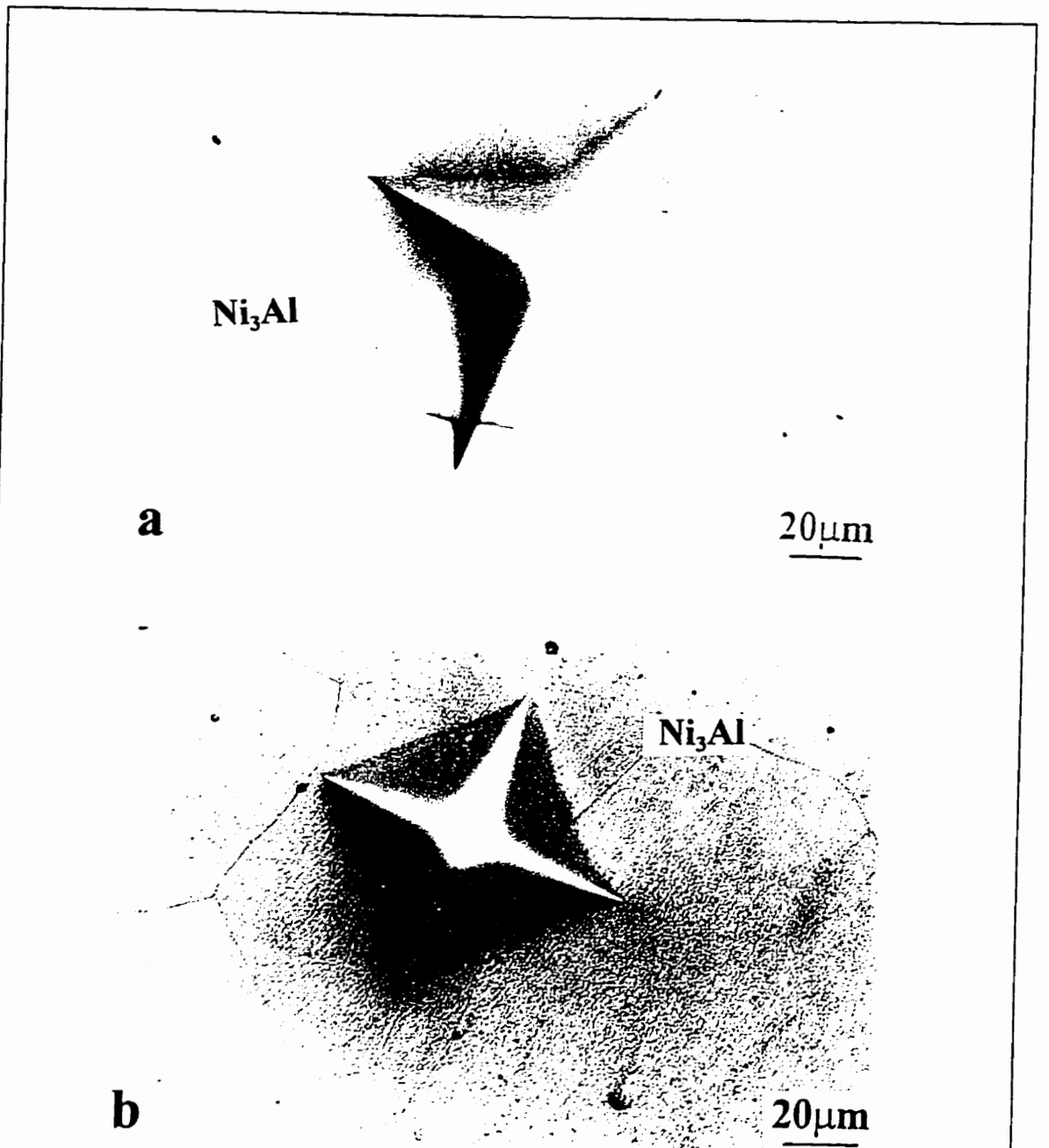

Figure 3.7 Typical micrographs of (a) a grain boundary cracking under 2000g load for the boron-free $Ni_{77.7}Al_{22.3}$ alloy, and (b) no grain-boundary cracking under 2000g load for the boron-doped $Ni_{74.8}Al_{25.8}B_{0.4}$ alloy (Nomarski interference contrast). Both were re-heated at 1000°C/15min followed by water quenching before the microhardness testing.

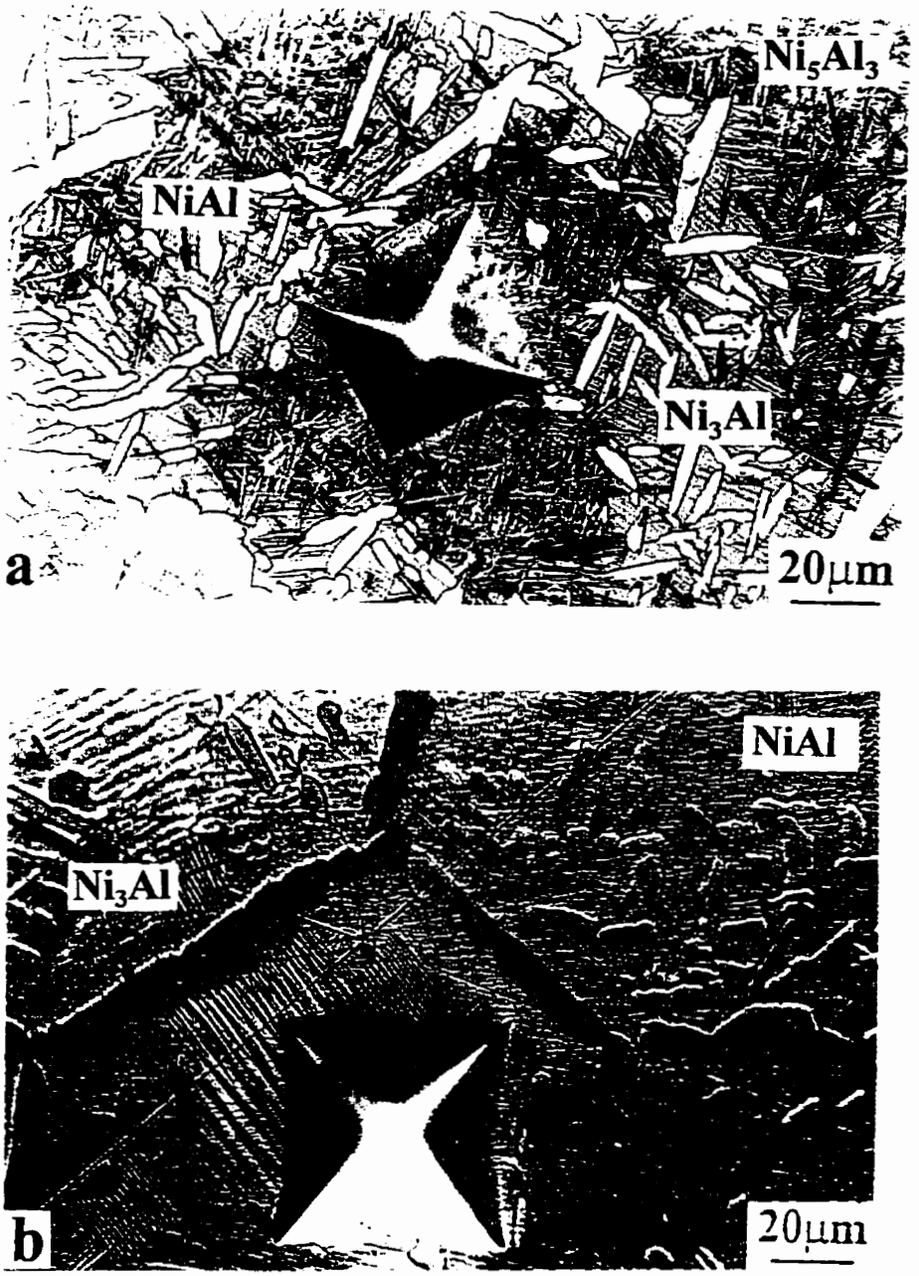

Figure 3.8 Typical micrographs of Vickers microhardness testing on (a) the "mat-structure" of the aged $Ni_{65.9}Al_{34.1}$ (1000°/100h + 500°C/100h both followed by a slow furnace cooling), and (b) the twin-structure of the homogenized $Ni_{63.7}Al_{36.3}$ (1000°/100h followed by a slow furnace cooling) in-situ composites under 2000g load.

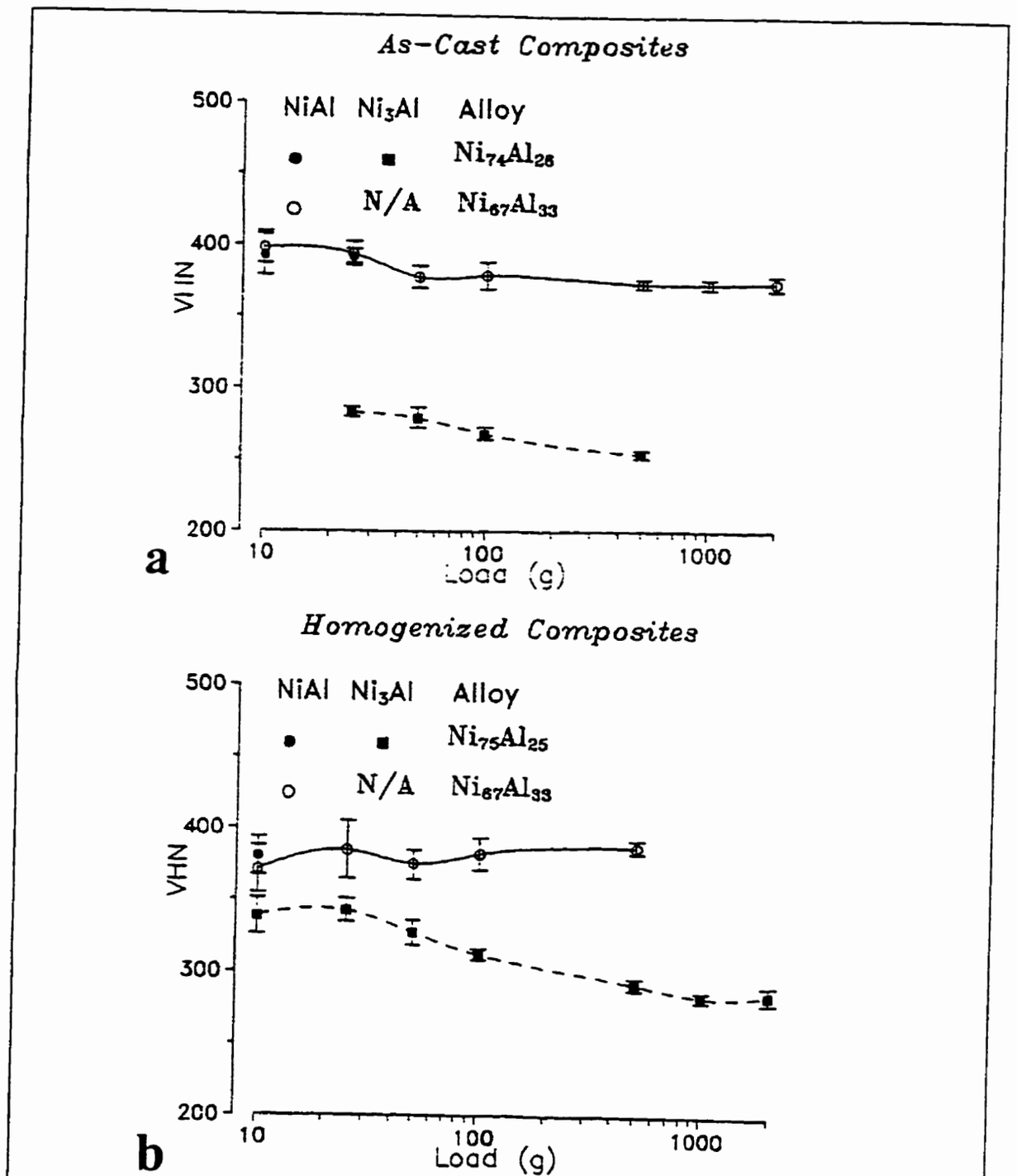

Figure 3.9 Vickers microhardness on the phases of NiAl and Ni_3Al for (a) as-cast and (b) as-homogenized composites.

Table 3.7 Vickers microhardness values with standard deviations of the homogenized and aged*, in-situ composites under 10g load (kg/mm^2).

In-situ composites (at.%)	Ni_3Al	NiAl
$Ni_{63.7}Al_{36.3}$	386 ± 10	359 ± 6
$Ni_{65.3}Al_{34.7}$	378 ± 9	370 ± 10
$Ni_{65.9}Al_{34.1}$*	337 ± 19	**690 ± 15**[1)]
$Ni_{67.2}Al_{32.8}$	384 ± 9	351 ± 10
$Ni_{70.8}Al_{29.2}$	364 ± 7	355 ± 8
$Ni_{72.8}Al_{27.2}$	362 ± 10	384 ± 11
$Ni_{73.2}Al_{26.8}$	344 ± 7	373 ± 8
$Ni_{77.7}Al_{22.3}$	323 ± 9	316 ± 9
$Ni_{73.2}Al_{26.6}B_{0.2}$	278 ± 11	-
$Ni_{74.8}Al_{24.8}B_{0.4}$	297 ± 7	-

1) Ni_5Al_3 precipitates in the NiAl matrix (**Figure 3.8a**).

3.4 Compression Testing

After fracture toughness testing, half of the tested specimens were cut by EDM into a parallelepiped beam (4x4x6.8mm), which was polished properly and compressed by a hydraulic compression machine. The average yield strength and standard deviations for each in-situ composite are listed in **Table 3.8**.

Table 3.8 The average yield strength with standard deviations of the homogenized and aged in-situ composites.

In-situ composites (at.%)	Yield strength (MPa)
$Ni_{63.7}Al_{36.3}$	423 ± 35
$Ni_{65.9}Al_{34.1}$ *)	**1151 ± 148**
$Ni_{67.2}Al_{32.8}$	819 ± 66
$Ni_{70.8}Al_{29.2}$	539 ± 139
$Ni_{72.8}Al_{27.2}$	431 ± 51
$Ni_{73.2}Al_{26.8}$	374 ± 55
$Ni_{77.7}Al_{22.3}$	222 ± 93
$Ni_{73.2}Al_{26.6}B_{0.2}$	535 ± 14
$Ni_{74.8}Al_{24.8}B_{0.4}$	382 ± 72

*) Aged at 550°C for 100h followed by a slow furnace cooling.

3.5 Fracture Toughness Testing

3.5.1 Fractography

Fracture surfaces broken in three-point bend test, were studied by scanning electron microscopy (SEM). A typical group of SEM fractographs is shown in **Figures 3.10** to **3.18**.

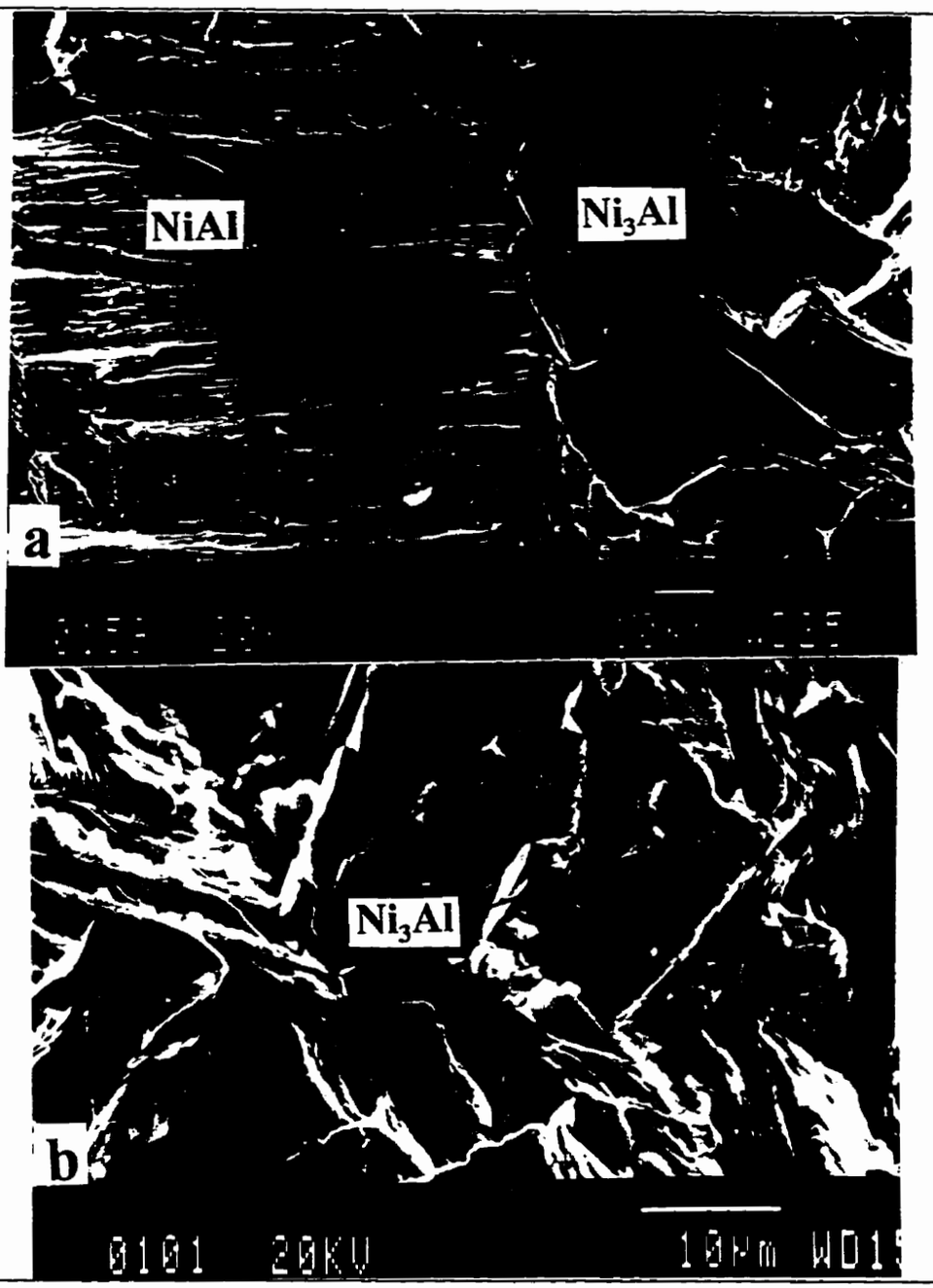

Figure 3.10 Typical scanning electron microscope (SEM) fractographs of the homogenized $Ni_{63.7}Al_{36.3}$ specimens (1000°/100h followed by a slow furnace cooling). (a) transgranular fracture in the NiAl phase and intergranular Ni_3Al grain facets, and (b) two elongated envelops and precipitates of Ni_3Al in the NiAl grains, which shows a river-pattern cleavage fracture.

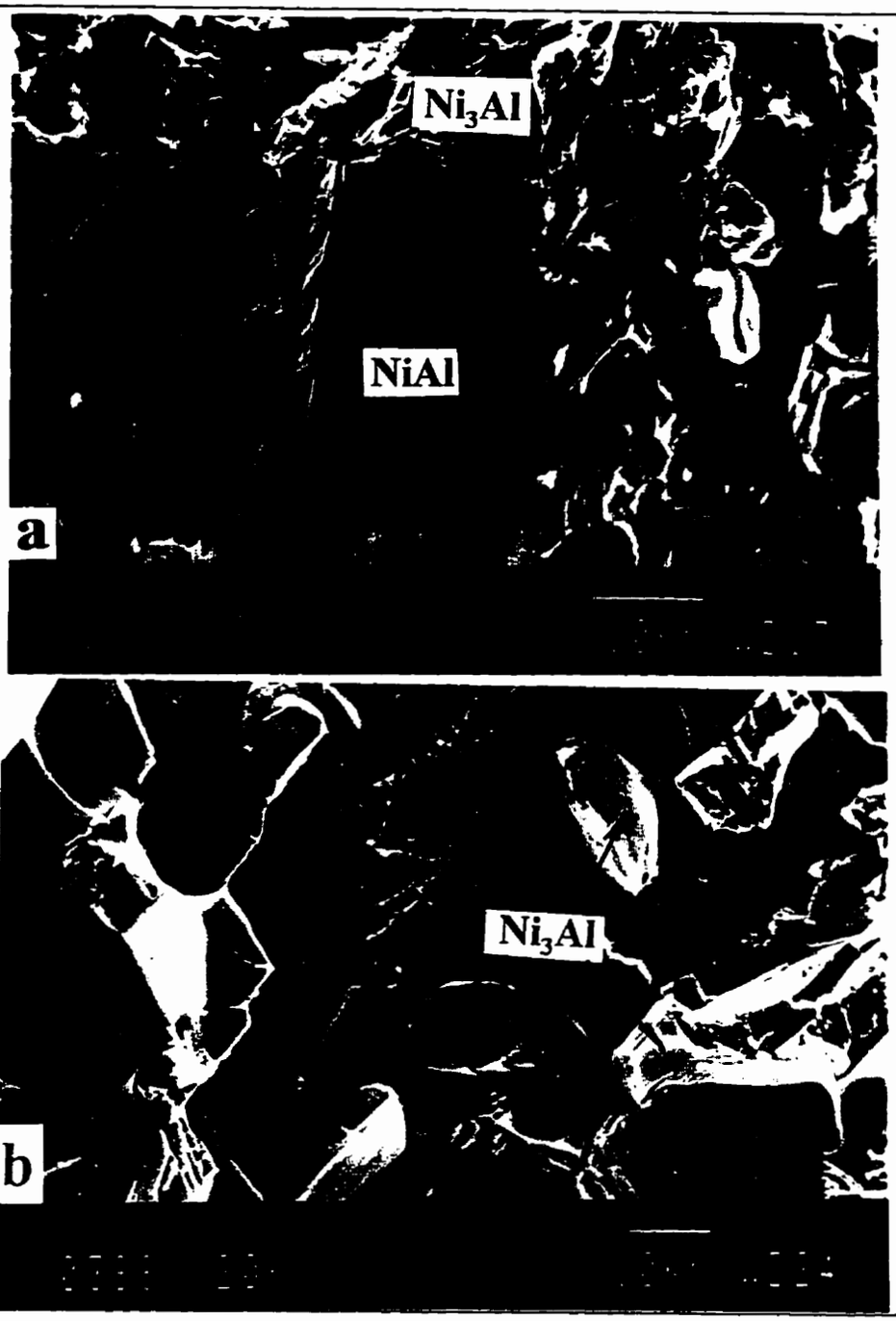

Figure 3.11 Typical scanning electron microscope (SEM) fractographs of the homogenized and aged $Ni_{65.9}Al_{34.1}$ in-situ composite (1000°/100h + 500°C/100h both followed by a slow furnace cooling): (a) local cleavage fracture in the grains, and (b) elongated and broken Ni_3Al reinforcements.

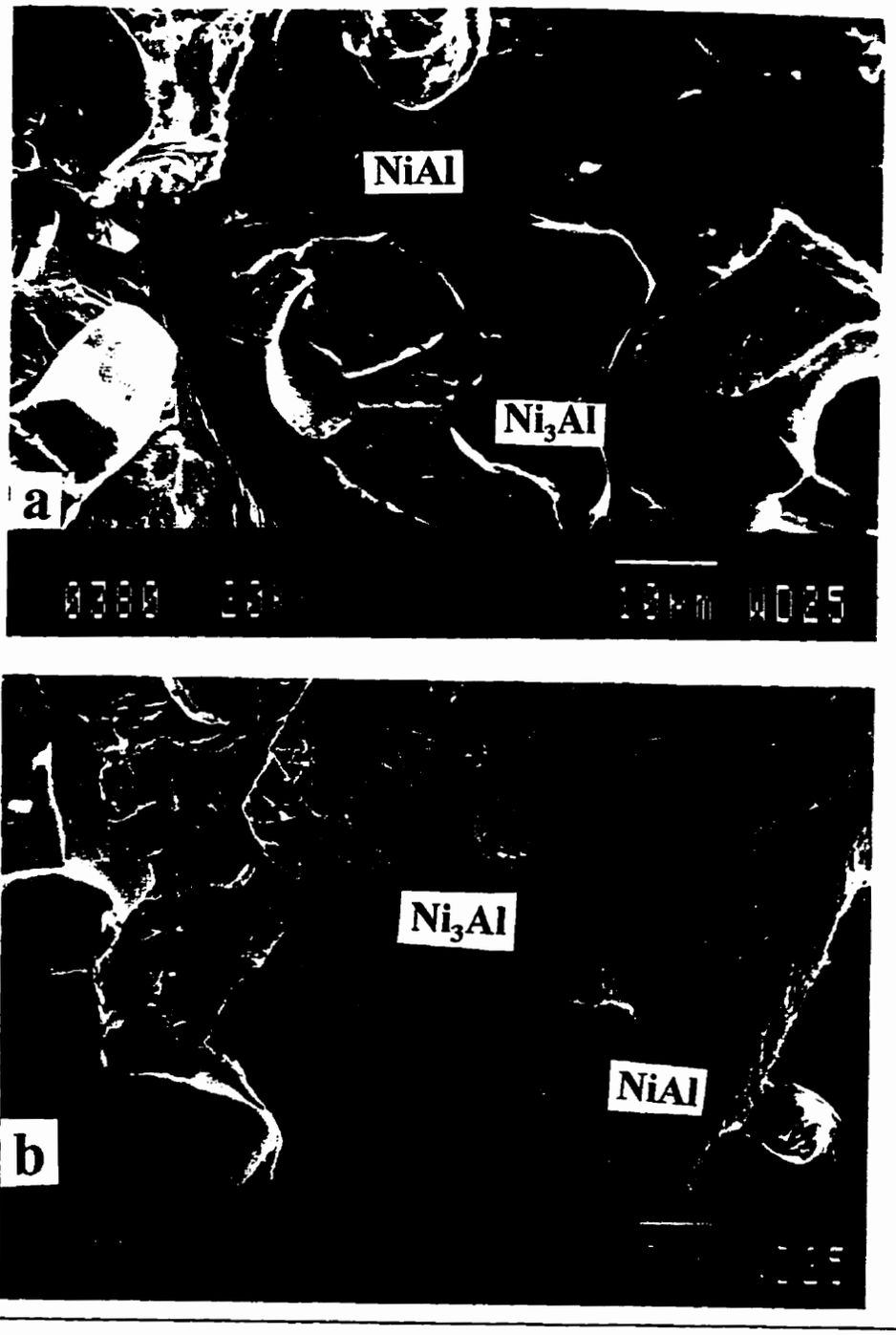

Figure 3.12 Typical scanning electron microscope (SEM) fractographs of the homogenized $Ni_{67.2}Al_{32.8}$ specimens (1000°/100h followed by a slow furnace cooling). (a) stretched ductile second phases, and (b) delamination at interfaces.

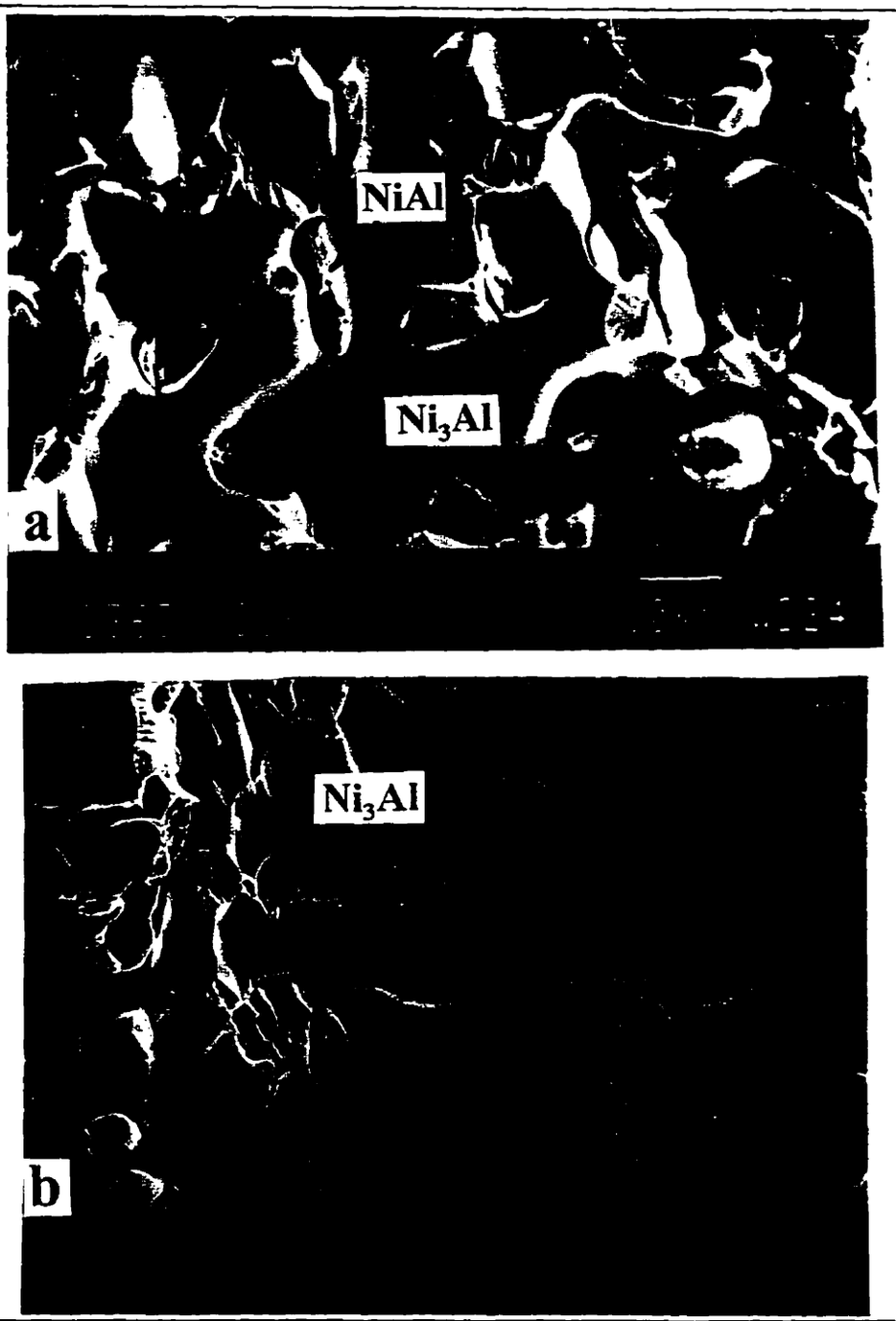

Figure 3.13 Typical scanning electron microscope (SEM) fractographs of the homogenized $Ni_{70.8}Al_{29.2}$ specimens (1000°/100h followed by a slow furnace cooling). (a) debonding at interfaces of NiAl and Ni_3Al (b) intergranular fracture of Ni_3Al.

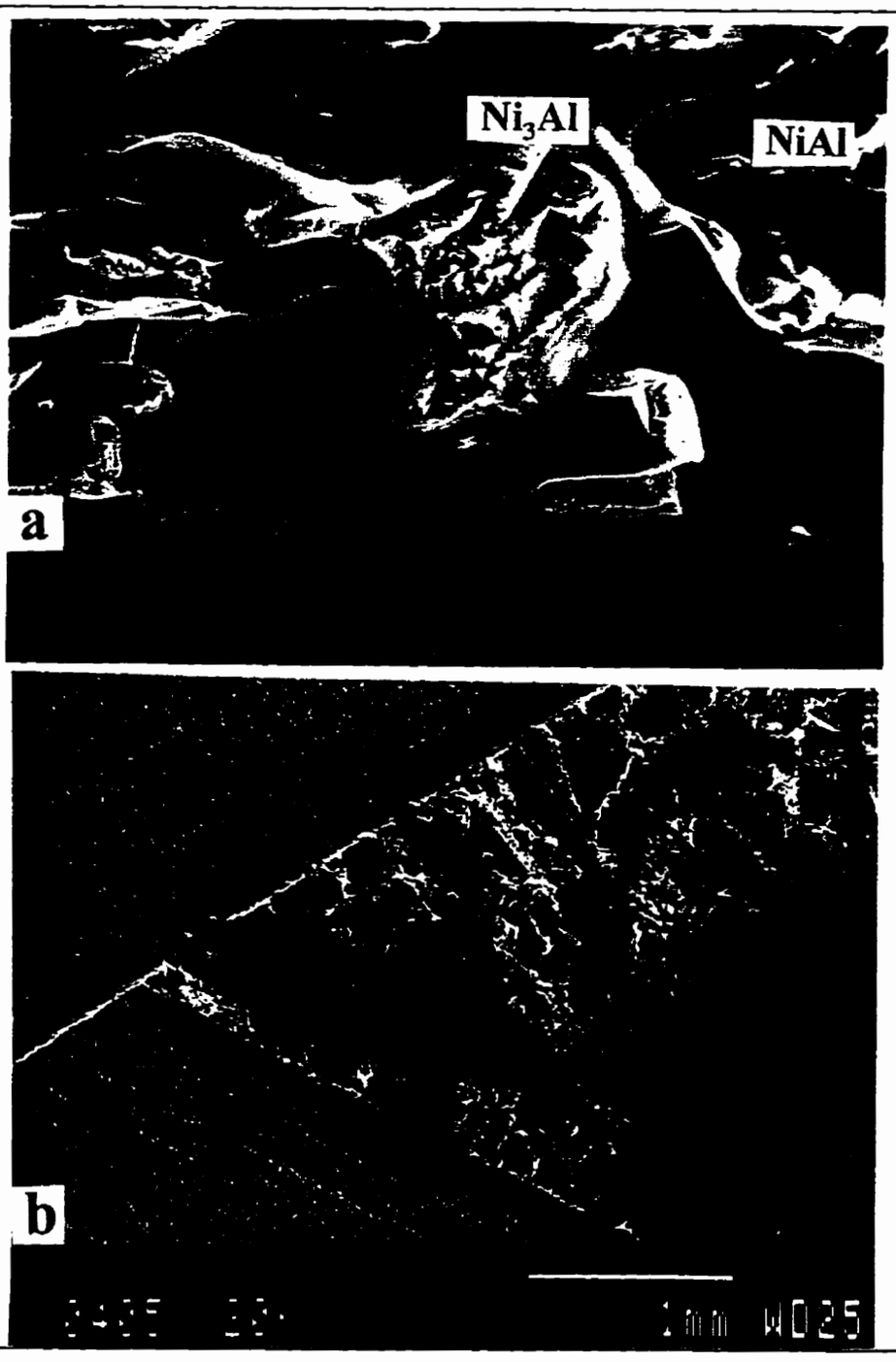

Figure 3.14 Typical scanning electron microscope (SEM) fractographs of the homogenized $Ni_{72.8}Al_{27.2}$ specimens (1000°/100h followed by a slow furnace cooling). (a) delamination at grain boundary of Ni_3Al and at interfaces of Ni_3Al and NiAl, and (b) a whole fracture surface of a bent specimen.

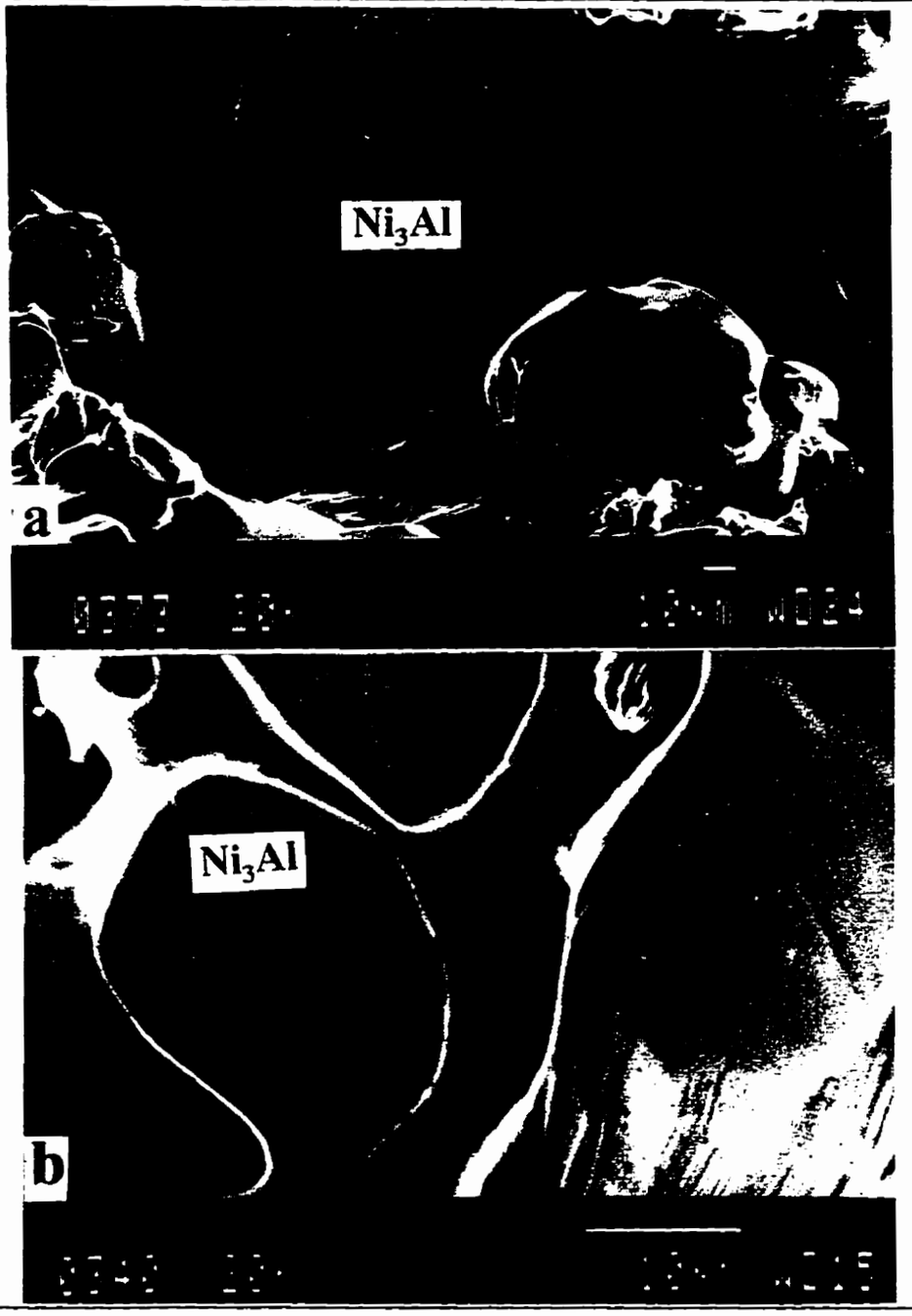

Figure 3.15 Typical scanning electron microscope (SEM) fractographs of the homogenized $Ni_{73.2}Al_{26.8}$ specimens (1000°/100h followed by a slow furnace cooling). (a) intergranular fracture with clear secondary cracks along the grain boundaries, and (b) twin structures clearly marked in the Ni_3Al grains.

A mixed transgranular-intergranular fracture (TIF) mode in NiAl phase was observed in the $Ni_{63.7}Al_{36.3}$ specimens (**Figure 3.10a**). The NiAl matrix exhibits typical river-patterns on each facet (corresponding to a single grain) of cleavage fracture as shown in **Figure 3.10b**. Delamination can be observed at grain boundaries of NiAl and also at Ni_3Al/NiAl interfaces (**Figure 3.10b**).

Figure 3.11a shows primarily transgranular fracture of aged Ni_3Al in $Ni_{65.9}Al_{34.1}$ alloy. In addition, **Figure 3.11a** clearly shows that two propagating cleavage facets of NiAl phase stop at the grain boundaries of Ni_3Al phases in the aged $Ni_{65.9}Al_{34.1}$ in-situ composite. Delamination can be clearly seen at the Ni_3Al/NiAl interfaces as shown in **Figure 3.11b**. It is interesting to note that the ductile Ni_3Al reinforcements embedded in the NiAl grains were elongated and broken after fracture toughness testing (**Figure 3.11b**). Since this process consumes more energy than crack propagation without precipitates, the effects of Ni_3Al reinforcements are evident. In the $Ni_{67.2}Al_{32.8}$ in-situ composite, a precipitate of Ni_3Al was stretched into a tip (see arrow in **Figure 3.12a**). This definitely demonstrates the crack bridging effect of the relatively ductile second phase of Ni_3Al. Debonding at the Ni_3Al/NiAl interface can also be more clearly observed in this alloy. A different direction of alignment of Ni_3Al phase is shown in **Figure 3.12b**, which is a typical example of how complex a composite is. From **Figures 3.10** to **3.12**, it is clear that the NiAl matrix shows a mixed mode of transgranular/intragranular fracture and that the second phase and grain boundary of Ni_3Al phase show partly intergranular fracture with smooth facets.

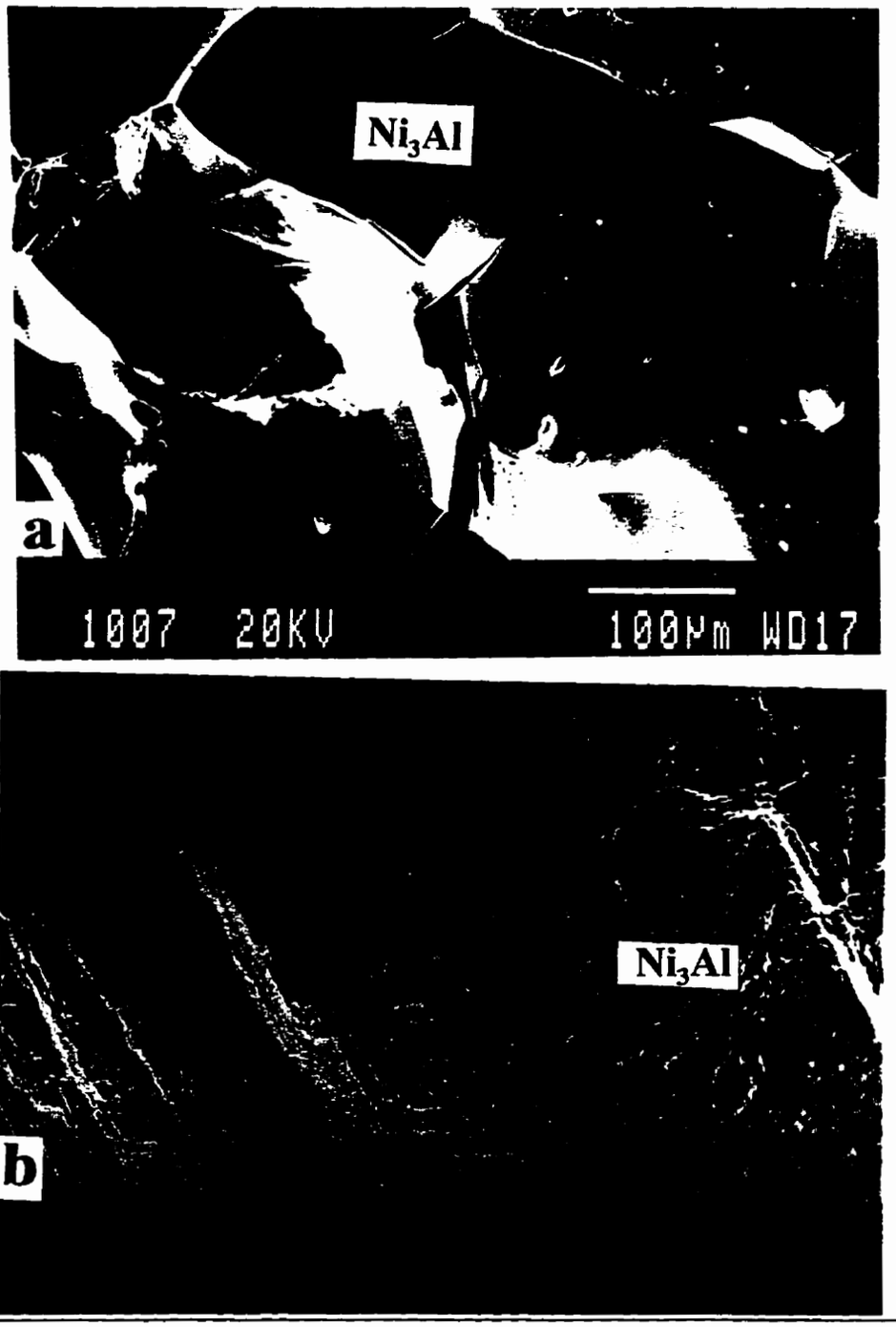

Figure 3.16 Typical scanning electron microscope (SEM) fractographs of the homogenized $Ni_{77.7}Al_{22.3}$ specimens (1000°/100h followed by a slow furnace cooling). (a) smooth intergranular fracture with grain-boundary cracks, and (b) a lot of tiny dimples on the fracture surfaces.

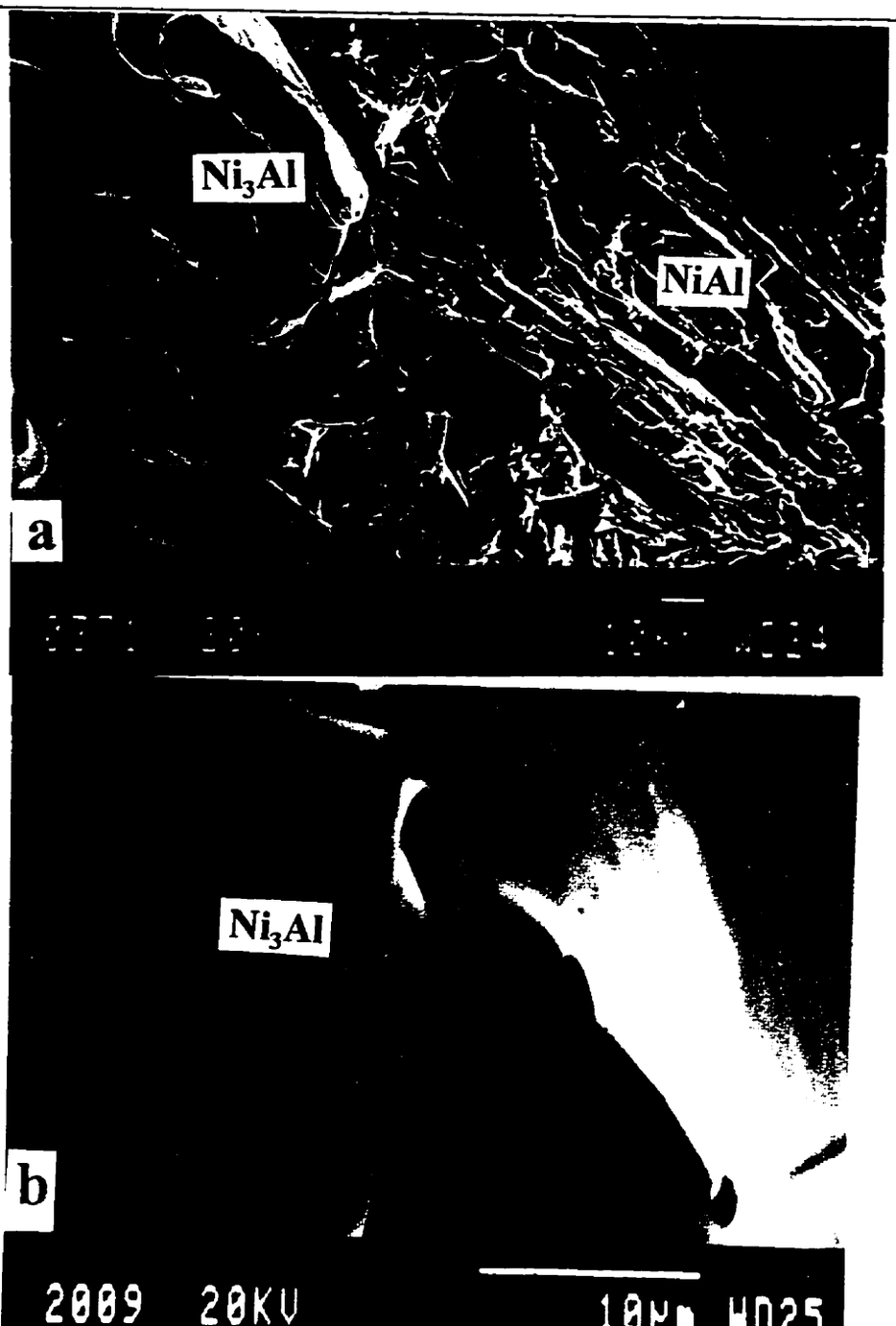

Figure 3.17 Typical scanning electron microscope (SEM) fractographs of the homogenized $Ni_{73.2}Al_{26.6}B_{0.2}$ in-situ composite (1000°/100h followed by a slow furnace cooling): (a) delamination at the Ni_3Al/NiAl interface, and (b) some voids at the grain boundaries.

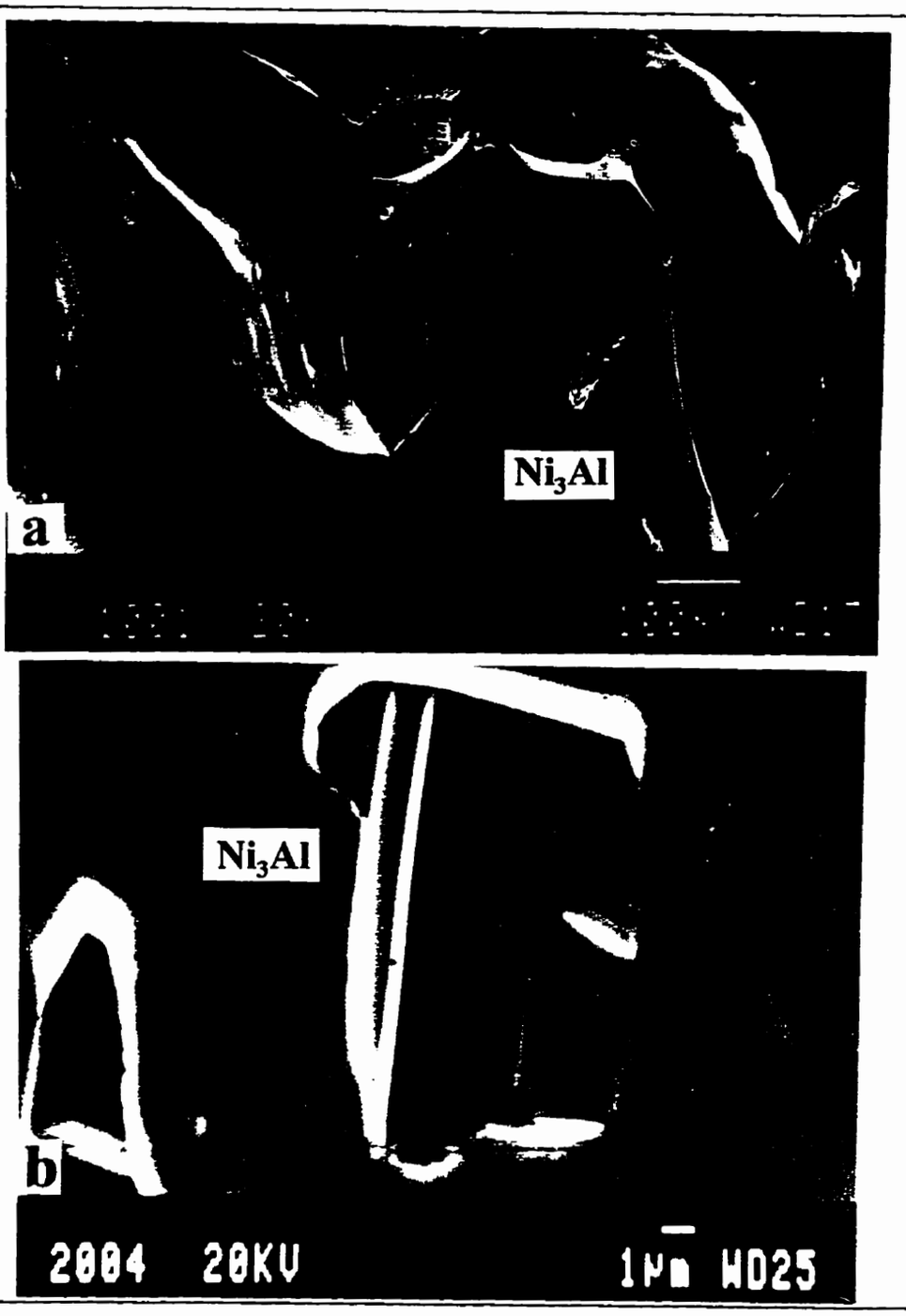

Figure 3.18 Typical scanning electron microscope (SEM) fractographs of the homogenized $Ni_{74.8}Al_{24.8}B_{0.4}$ specimens (1000°/100h followed by a slow furnace cooling). (a) cracks extended along grain boundaries, and (b) square stair-dimple in the grain.

From **Figures 3.13** to **3.18**, it is easy to distinguish that the matrix of Ni_3Al showing intergranular fracture with very smooth grain facets will become dominant in the fracture surfaces of the specimens. A large amount of relatively brittle reinforcements of NiAl in the $Ni_{70.8}Al_{29.2}$ in-situ composite were cleavage fractured during the bend testing (**Figure 3.13b**). A high magnification fractograph in **Figure 3.14a** shows delamination at grain boundary of Ni_3Al and at interfaces of Ni_3Al and NiAl in the $Ni_{72.8}Al_{27.2}$ in-situ composite. A whole fracture surface of a bent specimen was also given by a lower magnification fractograph as shown in **Figure 3.14b**. It will be very helpful to analyze the whole process of crack initiation, growth and termination behaviour during the bending test for this composite. The two symmetric sides of the surfaces cut by the electronic discharge machine (*EDM*) can be clearly seen in **Figure 3.14b**.

The grain boundary brittleness of the Ni_3Al phase in the $Ni_{73.2}Al_{26.8}$ in-situ composite can be clearly seen in **Figure 3.15a**. The distinct plastic deformation markings can also be clearly seen in the Ni_3Al grain facets at a higher magnification fractograph (**Figure 3.15b**).

The fracture behaviour of the boron-free polycrystalline Ni_3Al in the $Ni_{77.7}Al_{22.3}$ bent specimens is seen in **Figure 3.16.** The grain facets are extremely smooth and free from any deformation marks, indicating the brittleness of the boundaries (**Figure 3.16a**). However, the SEM fractograph of the $Ni_{77.7}Al_{22.3}$ bent specimens in **Figure 3.16b** also shows some tearing type fracture regions, indicating potential for some plasticity at room temperature.

The fracture behaviour of the boron-doped polycrystalline Ni_3Al in the $Ni_{73.2}Al_{26.6}B_{0.2}$ and

$Ni_{74.8}Al_{24.8}B_{0.4}$ in-situ composite can be seen in **Figures 3.17** and **3.18**, respectively. A delamination at the Ni_3Al/NiAl interface can be seen in **Figure 3.17a. Figure 3.17b** shows some secondary cracks and pre-existing voids appeared at the grain boundary in the $Ni_{73.2}Al_{26.6}B_{0.2}$ in-situ composite. Serious secondary cracks along grain boundaries can still be seen in the $Ni_{74.8}Al_{24.8}B_{0.4}$ surface fractured by bending (**Figure 3.18a**).

Some square stair-dimples seems to show some ductile potential in the $Ni_{74.8}Al_{24.8}B_{0.4}$ alloy. Further discussion on the fracture behaviour of the investigated in-situ composite will be given in the next Chapter. More examples of fractographs for the investigated in-situ composites are shown in **Appendix C**.

3.5.2 Fracture Toughness of the Investigated In-Situ Composites

Shapes of Load-Load line Displacement (P-LLD) and Y^*-a Curves

In general, according to Munz [101] four possible and principal types of load-displacement records could be observed during a bending test (**Figure 3.19**), which can be related to unstable and stable crack extension.

Type I in **Figure 3.19** shows a linearity up to the maximum load without any stable crack extension. In this case, fracture toughness K_{Ivm} could be calculated from maximum load, P_{max}. However, a delicate problem arises here because *Eq.(2.24)* requires that stable crack growth

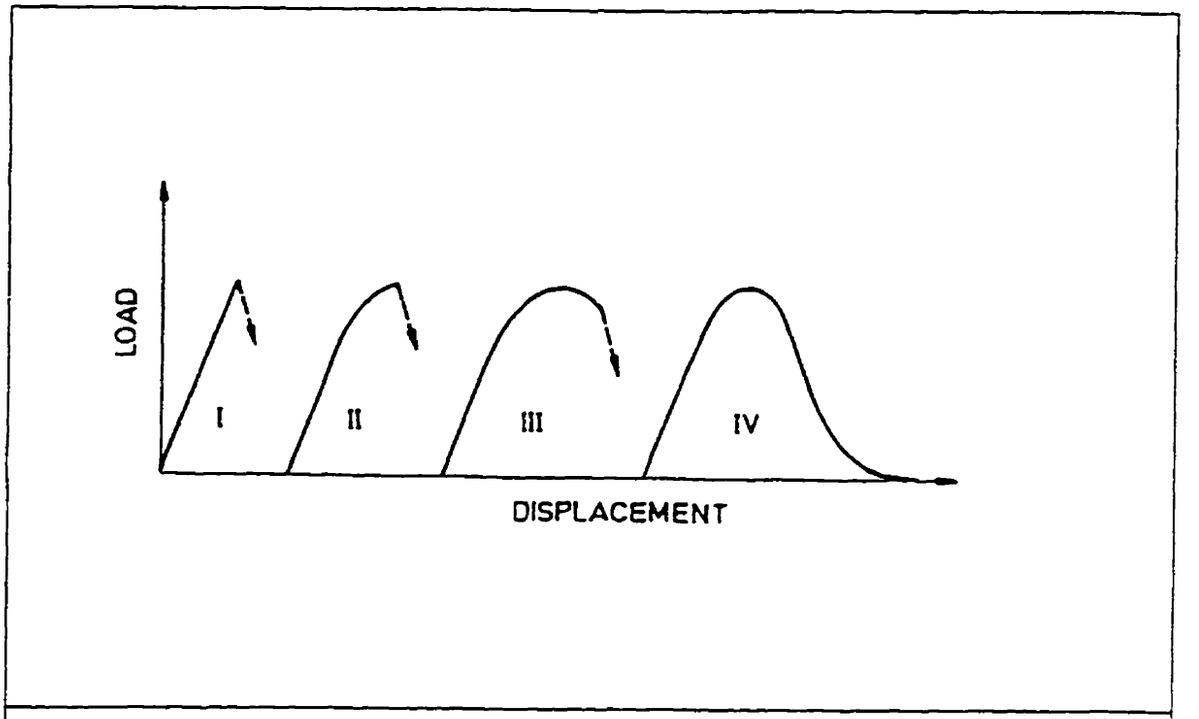

Figure 3.19 Possible load-displacement curves [101].

must precede P_{max} and then Y_m^* in *Eq.(2.24)* corresponds to a certain finite crack length, a_m (or α_m). If load-load line displacement is linear up to P_{max} then obviously the crack length is a_0 at P_{max} rather then a_m. From the formal point of view the Y^* function has almost an infinite value at a_0. It seems, however, that one would be on the rather safe side by still using *Eq.(2.24)* with a calculated Y_m^* which would give quite a conservative value of K_{Ivm}. This might be particularly true if the $Y^*=f(a)$ curve would have a "flat bottom" as shown in **Figure 3.20**.

In the case in **Figure 3.20**, even a minimal crack growth from a_0, sometimes unrecognizable on the load-load line displacement curve, leads to the value of $Y^*=Y_m^*$. It is to be pointed out that Withey and Bowen [2] showed that for relatively brittle materials tested by

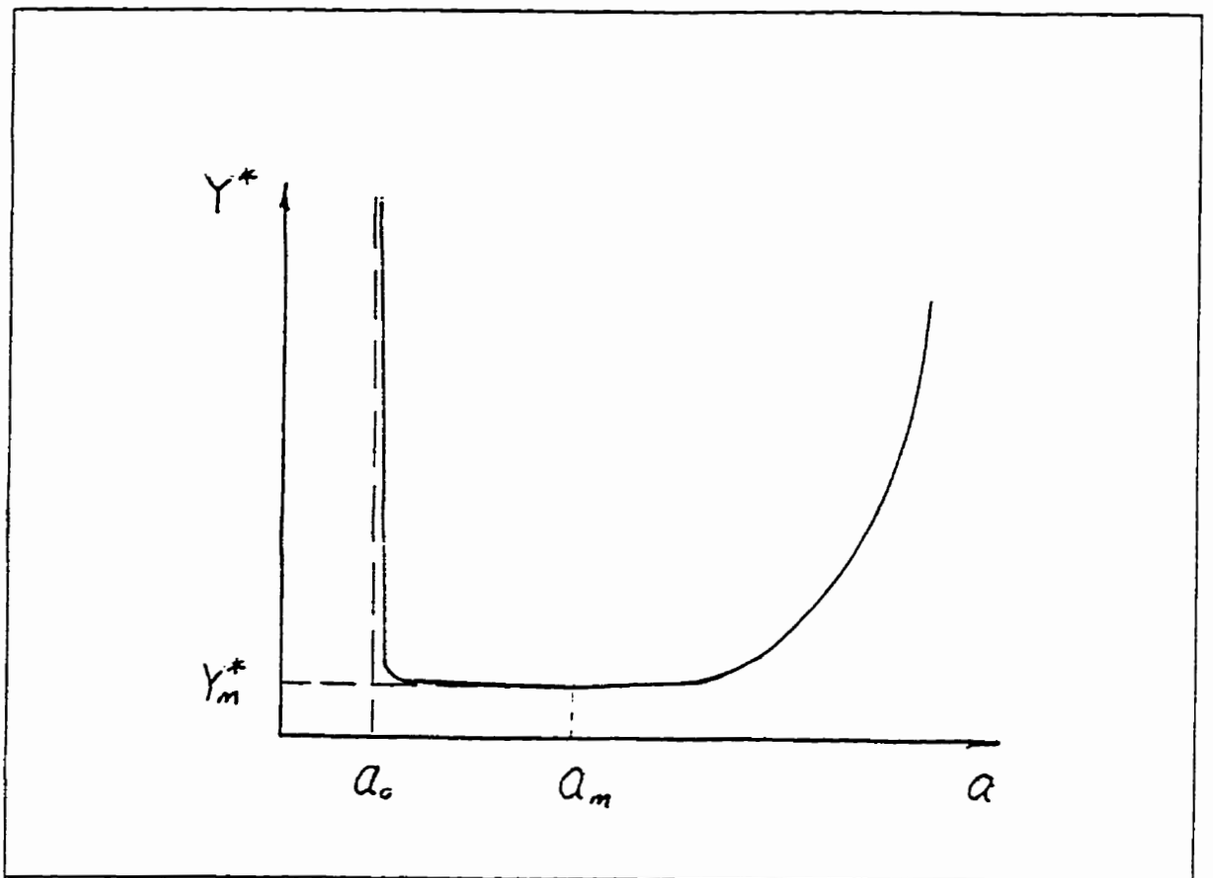

Figure 3.20 A schematic of a $Y^*=f(a)$ curve with a "flat bottom".

CNB (K_{ivm} = 4 MPa$\sqrt{m}$) valid toughness values were obtained even without any indication of non-linear compliance changes prior to failure.

A near-type I curve was observed in the present work for a $Ni_{65.9}Al_{34.1}$ alloy (**Figure 3.21a**) which was aged at 550°C for 100h and contained needle-like precipitates of the Ni_5Al_3 phase in the NiAl matrix (**Figure 3.5**). It was also observed for $Ni_{67.2}Al_{32.8}$, which was a homogenized alloy (**Figure 3.21b**). However, as seen in **Figures 3.21a** and **3.21b**, the curves exhibit a minimal non-linearity just prior to P_{max}. Also, the homogenized $Ni_{63.7}Al_{36.3}$ and $Ni_{73.2}Al_{26.8}$ alloys

showed near-type I behaviour with the modification that the stable crack growth occurred after P_{max} (**Figure 3.22**). Similarly, boron-doped $Ni_{73.2}Al_{26.6}B_{0.2}$ and $Ni_{74.8}Al_{24.8}B_{0.4}$ alloys showed near-type I behaviour with the modification that small pop-ins occurred only prior to the maximum load, and stable crack growth occurred after the maximum load (**Figure 3.23**). Type IV behaviour was exhibited by homogenized alloys $Ni_{70.8}Al_{29.3}$, $Ni_{72.8}Al_{27.2}$ and $Ni_{77.7}Al_{22.3}$ (**Figure 3.24**).

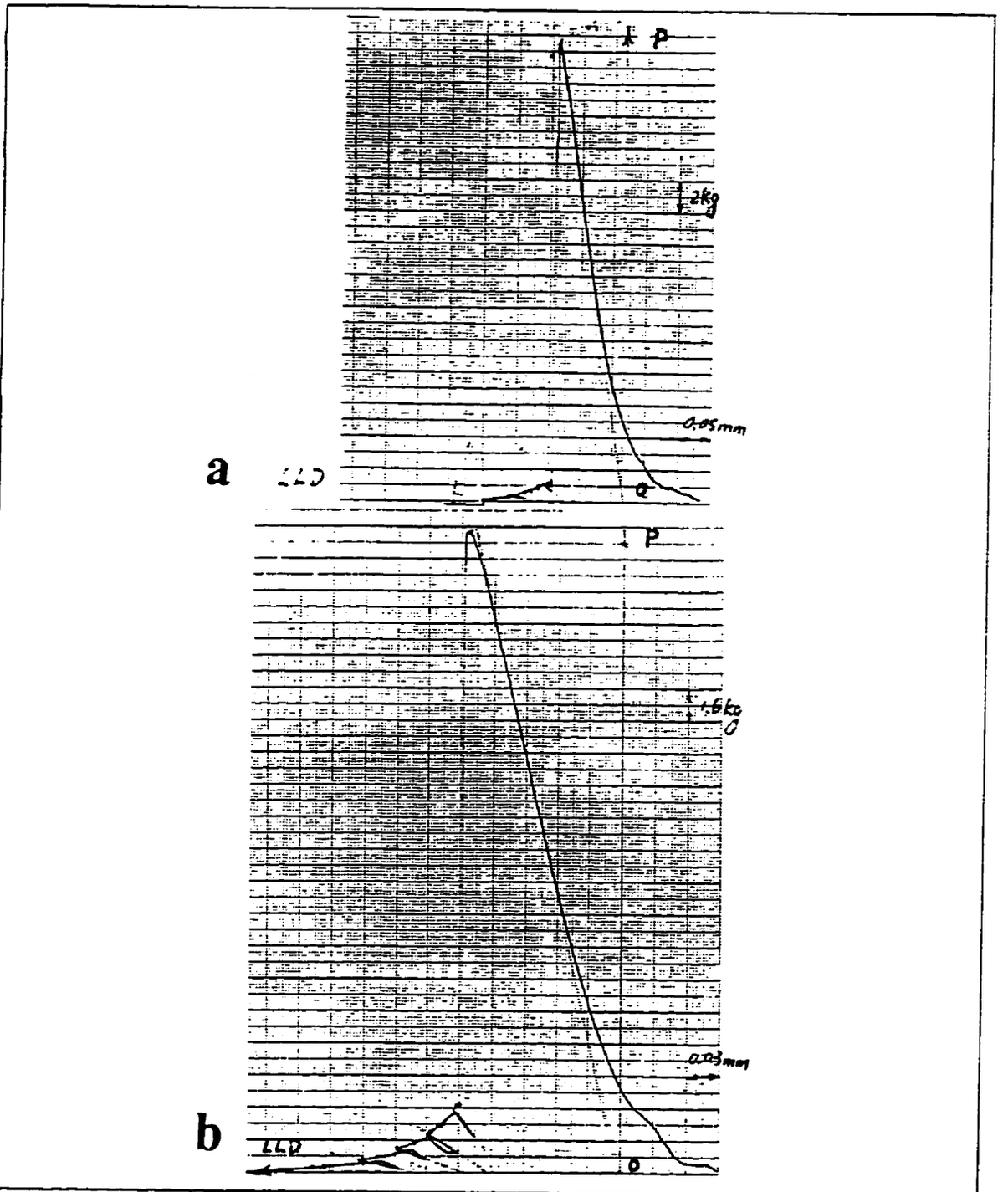

Figure 3.21 A group of near-type I curves was observed in the present work for (a) the aged $Ni_{65.9}Al_{34.1}$ and, (b) the homogenized $Ni_{67.2}Al_{32.8}$ alloys, exhibiting a minimal non-linearity just prior to P_{max}.

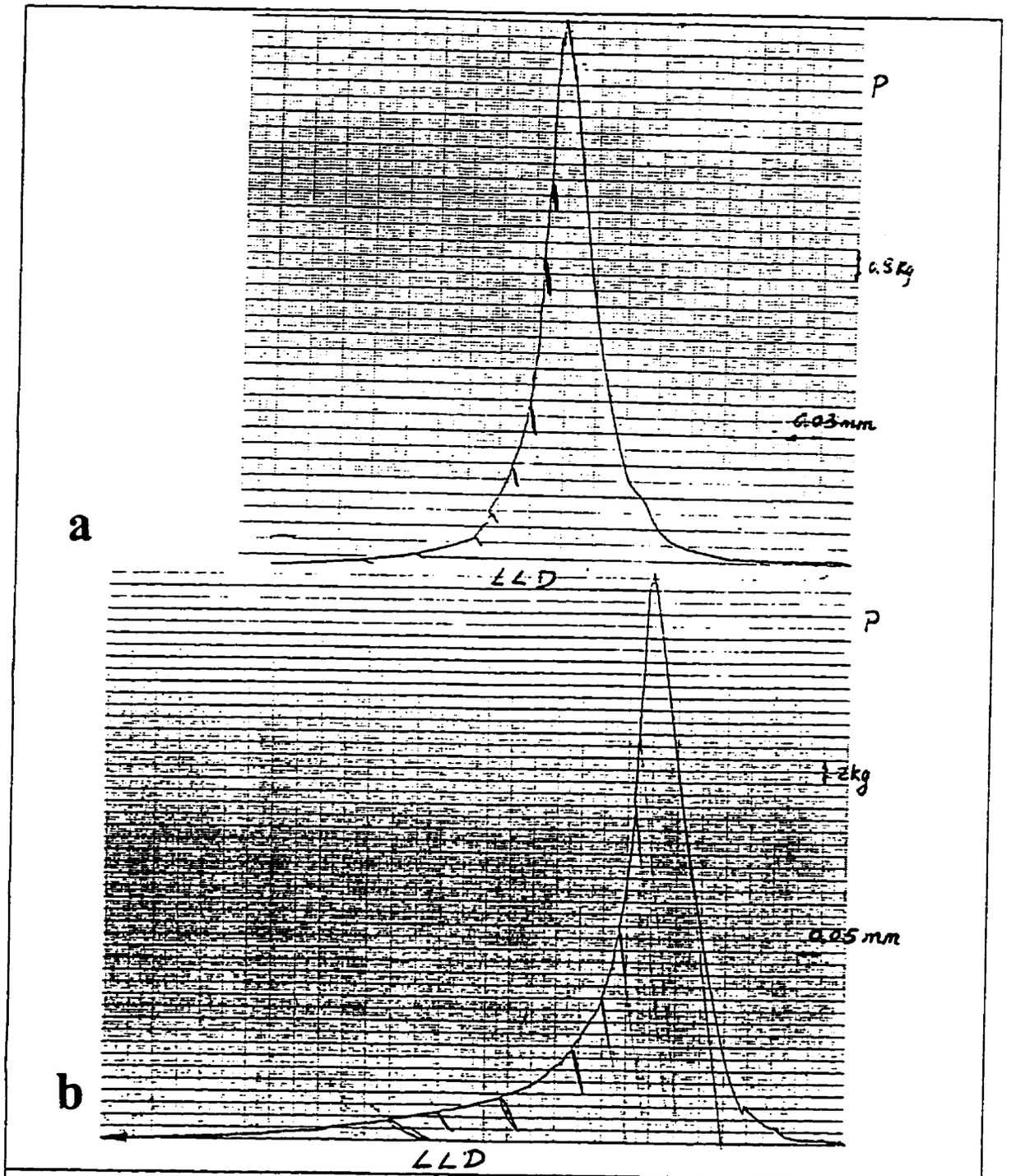

Figure 3.22 A group of near-type I curves was observed in the present work for the homogenized (a) $Ni_{63.7}Al_{36.3}$ and, (b) $Ni_{73.2}Al_{26.8}$ alloys, showing the modification that the stable crack growth occurred after P_{max}.

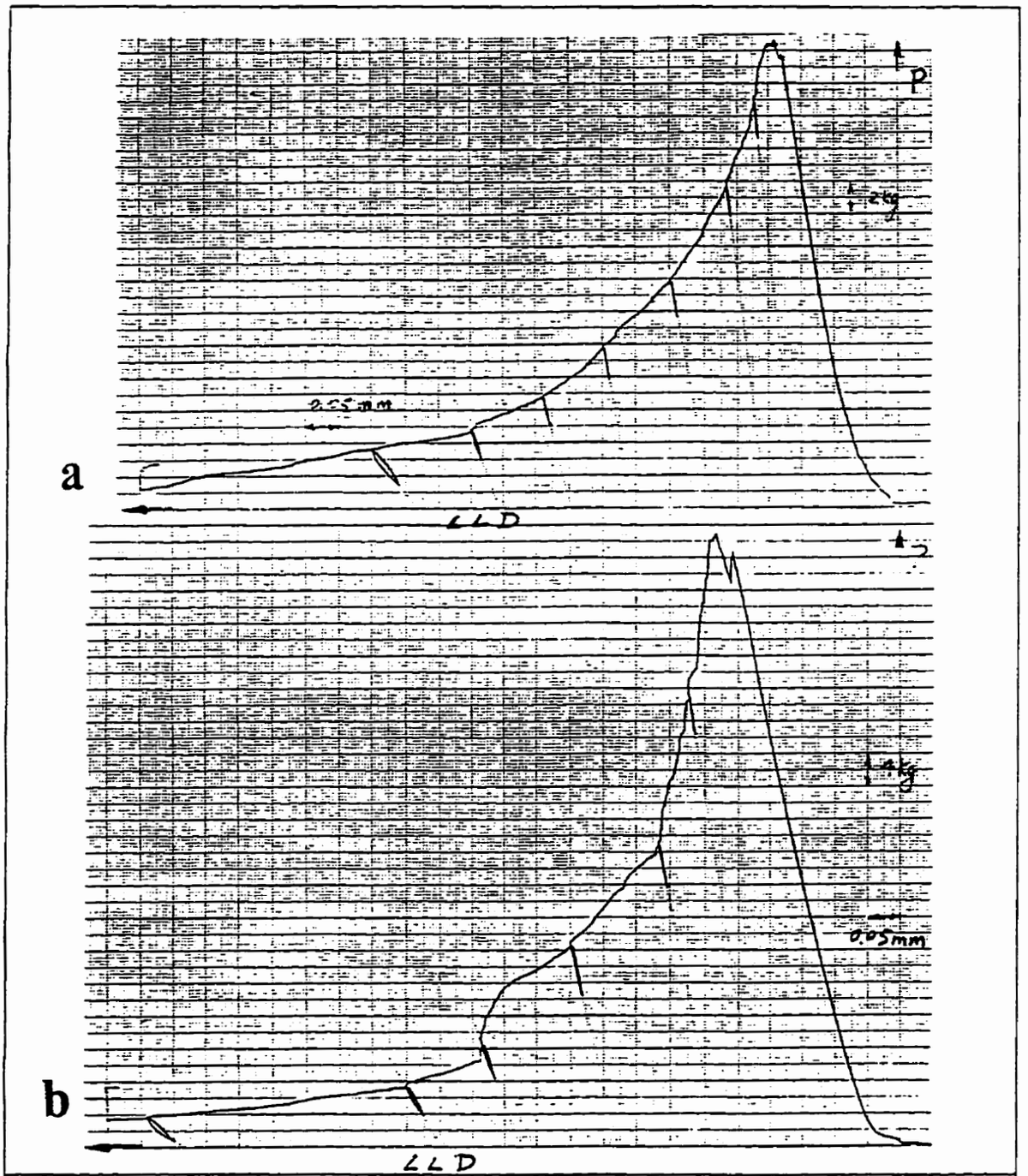

Figure 3.23 A group of near-type I curves was observed in the present work for boron-doped (a) $Ni_{73.2}Al_{26.6}B_{0.2}$ and $Ni_{74.8}Al_{24.8}B_{0.4}$ alloys, exhibiting the modification that small pop-ins occurred only prior to the maximum load and a stable crack growth after the maximum load.

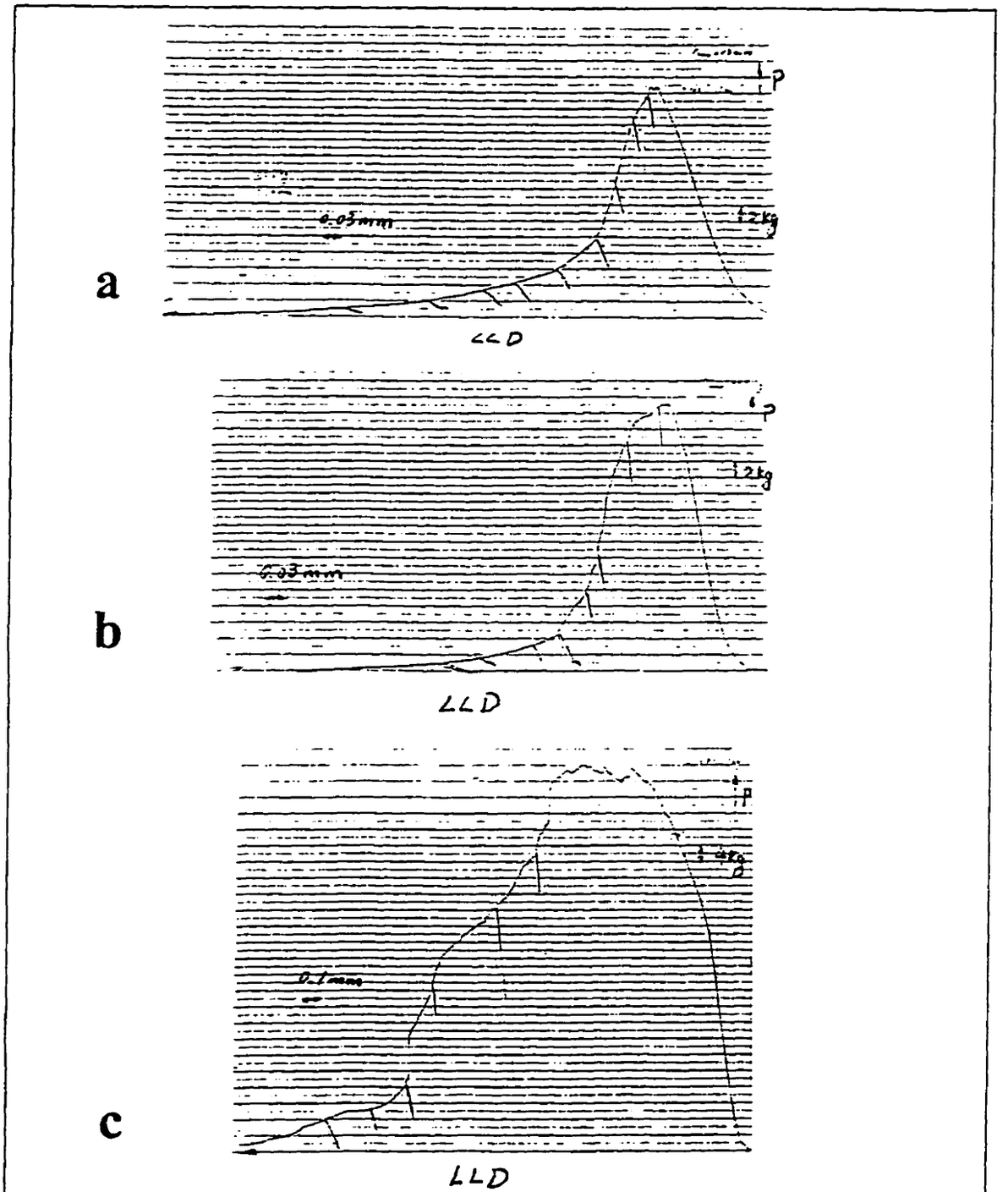

Figure 3.24 Type IV behaviour was exhibited by homogenized alloys (a) $Ni_{70.8}Al_{29.3}$, (b) $Ni_{72.8}Al_{27.2}$ and (c) $Ni_{77.7}Al_{22.3}$.

It must be pointed out that the shapes of the load-load line displacement curves were the same for each group of alloys (**Figures 3.21** to **3.24**) with a specified composition, despite that individual specimens in this group could contain slightly different volume fractions of Ni_3Al (**Appendix D**).

Evaluation of Fracture Toughness Values K_{Ivm}^{W} and K_{Ivm}^{B}, K_{WOF}

The measured (B, W, a_0 and a_1 from each specimen) and calculated (Δa_m and Y^*_m) geometrical parameters and volume fraction of Ni_3Al for each *CNB* specimen of the investigated in-situ composites are listed in **Appendix D**. The Δa_m parameter was calculated from *Eq.(2.25)* taking the first derivative of Y^* as equal to zero ($dY^*/d\alpha = 0$) and taking for calculation the measured geometrical parameters of each individual specimen. Elastic moduli for calculation of $C_i(\alpha)$ were taken from **Table 2.1**.

The mechanical properties such as E_c and σ_{YS}, and the experimental results of K_{Ivm}, work of fracture γ_{WOF} and K_{WOF} values from each *CNB* bend specimen are summarized in **Appendix E**.

To obtain a conservative estimate, the elastic modulus E_c of each *CNB* bend specimen is calculated from the lower bound of the rule of mixtures for composites [63, 100]:

$$E_c = \frac{1}{\frac{V_d}{E_d} + \frac{1 - V_d}{E_m}} \tag{3.1}$$

where the moduli of monolithic alloys are: E_d = 179 GPa for Ni_3Al and E_m = 294 GPa for NiAl.

These values are taken from Ref.[110] (see **Table 2.1**).

The yield strength σ_{YS} (offset = 0.2%) is determined by the compression test (see sections 2.5.1 and 3.4).

The values of $K_{Ivm}{}^{W}$ and $K_{Ivm}{}^{B}$ were calculated from *Eqs.(2.29)* to *(2.32)* from Wu's solution [126, 133] and Bluhm's solution [132, 140, 141], respectively, as mentioned in Chapter 2. It is clear that Wu's solution [126, 133] is more conservative than Bluhm's solution [126, 140, 141] because almost all of the $K_{Ivm}{}^{W}$ values are greater than the $K_{Ivm}{}^{B}$.

The values of γ_{WOF} and K_{WOF} were calculated from *Eqs.(2.41)* and *(2.42)*, respectively. Obviously, the values of the apparent fracture toughness K_{WOF} are greater than those of K_{Ivm}.

The invalid values of $K_{Ivm}{}^{W}$ and $K_{Ivm}{}^{B}$ were also distinguished according to the validity requirements in Chapter 2. The invalid values are marked in bold face in **Appendix E.**

Effects of Slot Geometries of *CNB* Bend Specimens on the Values of $K_{Ivm}{}^{W}$

As indicated in *Eqs.(3.25)*, *(3.27)* and *(3.33)*, stress intensity factor coefficient Y^{*} is a function of the slot geometries of *CNB*. The values of Y_m^{*} increase with the increasing of the initial crack length a_0, as shown in **Figure 3.25a**, which is in agreement with the results calculated by Wu [133]. However, Y_m^{*} seems not to be sensitive to the slot length a_1 (**Figure 3.25b**). The independence of $K_{Ivm}{}^{W}$ values on the slot geometries of a_0 and a_1 can be seen in **Figure 3.26.**

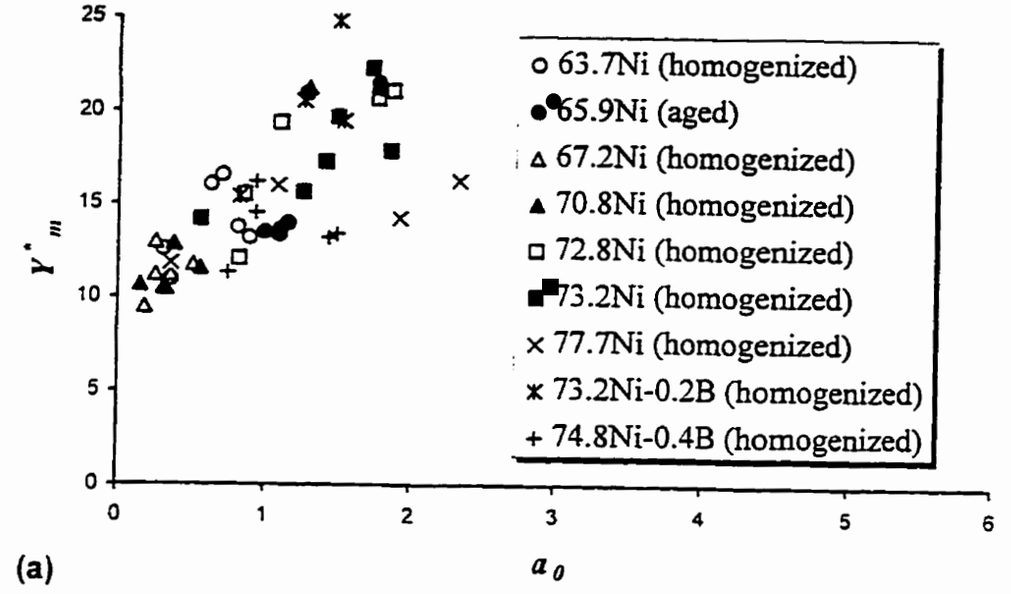

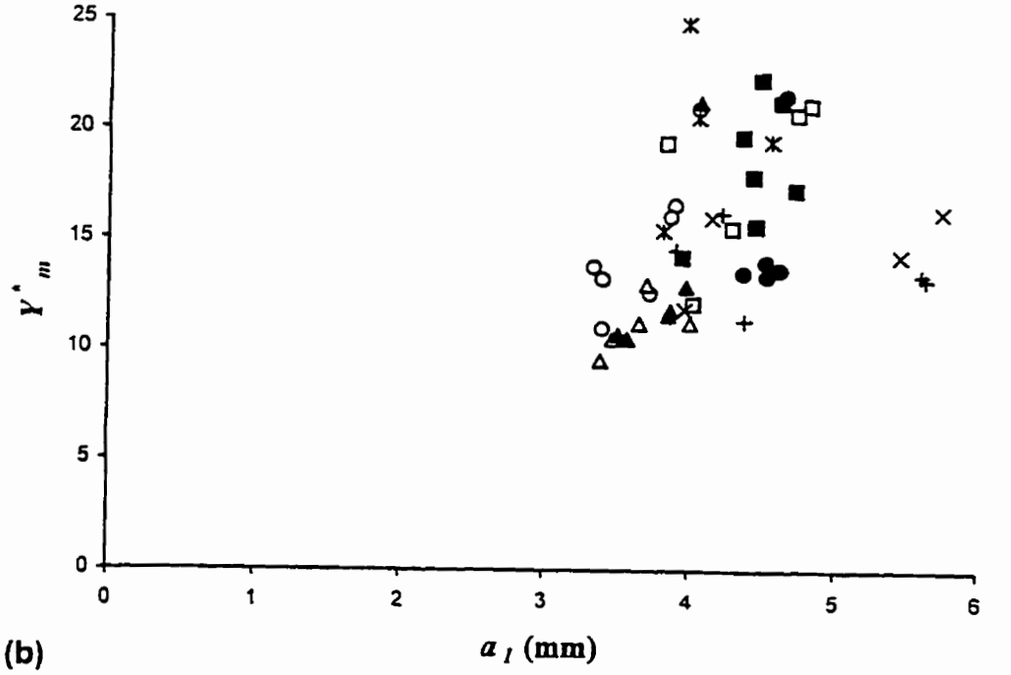

Figure 3.25 The relationship of the stress intensity factor coefficient, Y_m^* with (a) the initial crack length, a_0, and (b) the slot length, a_1, of the CNB bend specimens produced by the investigated in-situ composites.

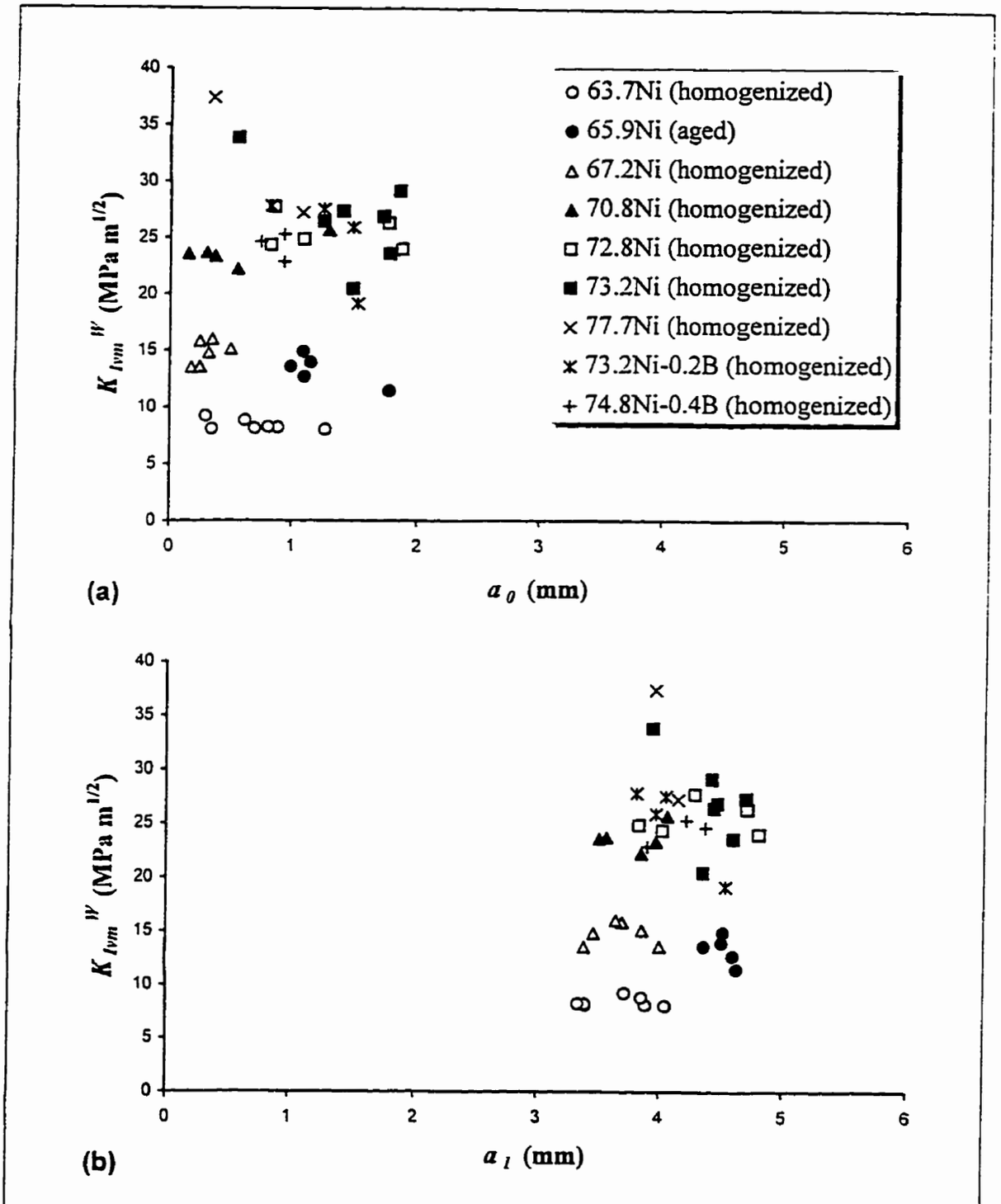

Figure 3.26 The independence of the $K_{Ivm}{}^{W}$ values on (a) the initial crack length, a_0, and (b) the slot length a_1 of the CNB bend specimens produced by the investigated in-situ composites.

The Relationship between *LLD* and Δa in a *CNB* Test

As described in Chapter 2, the partial unloading compliance method was used for monitoring crack extension (Δa) (**Figure 2.15c**) and calculating the plastic area Ai ($1 \le i \le n$) (see *Eq.(2.45)*).

However, the compliance (C_{LLD}) obtained from each load-load line displacement (*LLD*) curve (**Figures 3.21** to **3.24**) is almost ten times greater than the that compliance ($C_{\Delta a}$) calculated from *Eq.(2.33)*. This result indicates that instantaneous crack extension of each bend specimen cannot be monitored by this method in a *CNB* bend test because values of C_{LLD} and $C_{\Delta a}$ did not simultaneously correspond to each other at the unloading points. The reason is not clear.

Therefore, an alternative method to estimate crack extension was used in this research. The alternative method is to assume that a linear relationship exists between *LLD* and Δa prior to and after the maximum load P_{max}. As shown in **Figures 3.27a** and **3.27b**, this method is very reliable for type IV (see **Figures 3.19** and **3.24**, including $Ni_{70.8}Al_{29.2}$, $Ni_{72.8}Al_{27.2}$ and $Ni_{77.7}Al_{22.3}$ alloys), and most of the near-type I *P- LLD* curves (see **Figures 3.22** and **3.23**) because stable crack growth happened both prior to and after P_{max}. The method is also accurate enough for the near-type I curves as shown in **Figure 3.21** because a small stable crack growth always exists prior to P_{max} for all the *CNB* specimens and the experimental values of J_{Ivc} and K_{Ivc} would be calculated in this section (prior to P_{max}) as explained in the following section.

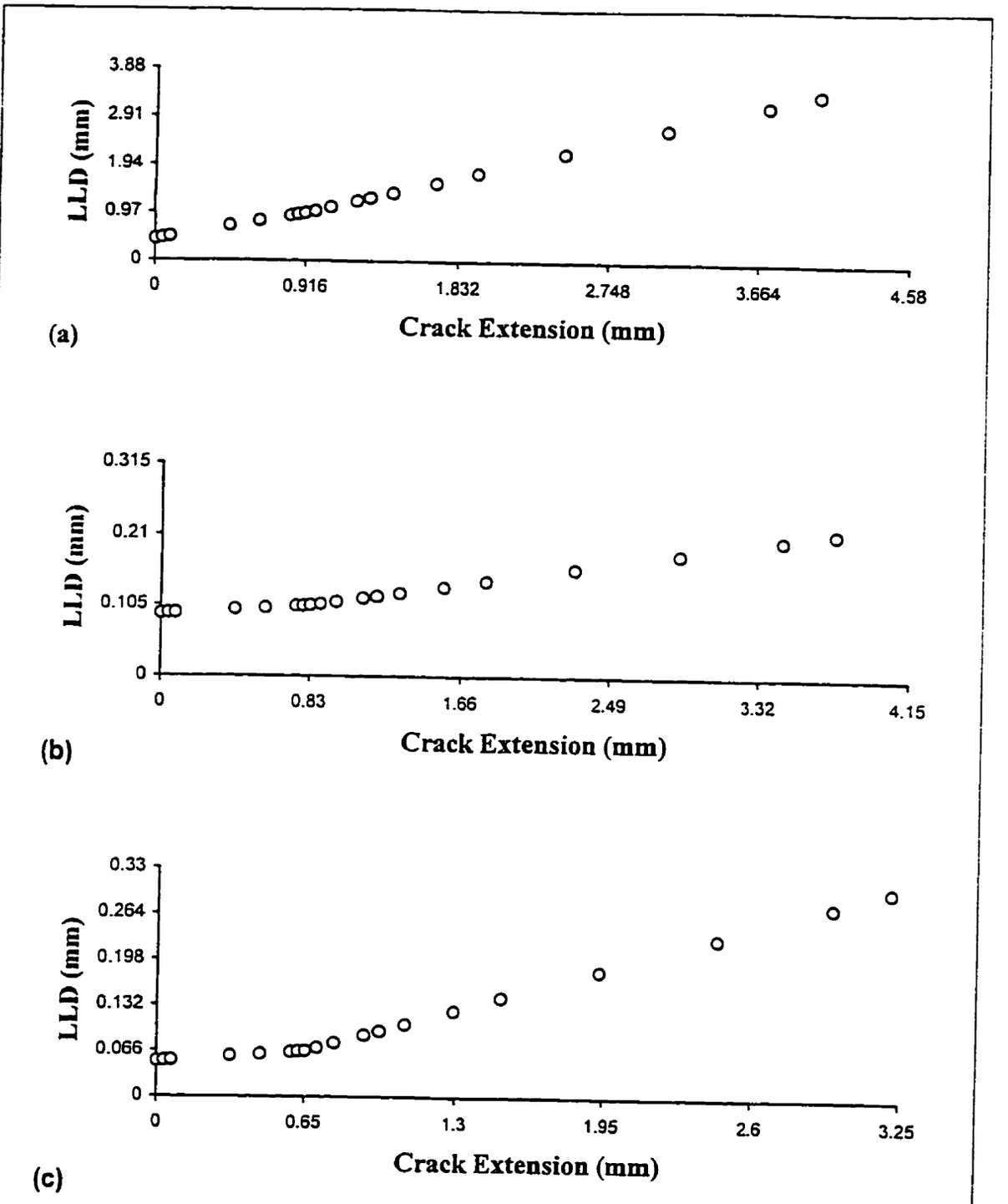

Figure 3.27 The typical linear relationships between load-load line displacement (*LLD*) and crack extension (Δa) for (a) $Ni_{77.7}Al_{22.3}$, (b) $Ni_{65.9}Al_{34.1}$, and (c) $Ni_{63.7}Al_{26.3}$ alloys.

Evaluation of Fracture Toughness Values J_{Ivc} and K_{Ivc}

Figure 3.28 shows a typical relationship between the parameters Y^*, P_{max}, $K_{Ivm}{}^{W}$ and the crack extension (Δa) for the homogenized $Ni_{63.7}Al_{36.3}$ in-situ composite. This figure is a typical example to show all the features in a *CNB* bend test of this research: crack initiates before P_{max} (**Figure 3.28a**), flat-bottom part of Y^* (**Figure 3.28b**) and a decreasing parameter K_{I} with a plateau of K_{Ivm} at Δa_m (**Figure 3.28c**). As a comparison, more examples of such features for each in-situ composite are summarized in **Appendix G.**

The energy parameters of the CNB bend specimens, J_{el}, J_{pl} and J are calculated by *Eq.(2.44)*. A typical group of shapes of J_{el}, J_{pl} and J, versus crack extension is shown in **Figure 3.29a**, **3.29b** and **3.29c**, respectively. As expected, J_{el} is predominant only up to Δa_m while J_{pl} will take over after Δa_m and show a much greater values than J_{el}. However, the shape of J-Δa seems surprising but very reasonable if one checks the procedure carefully. It is very interesting to note that the J-Δa fracture resistance curves showed a "hook" shape for all the CNB bend specimens (**Appendix F**). Therefore, to determine the J_{Ivc} of each specimen, a "minimum-line method", instead of "blunting-line method" [99], was used for the determination of J_{Ivc}. Thereafter, K_{Ivc} can be calculated by *Eq.(2.46)*. The values of J_{Ivc}, K_{Ivc} for each CNB bend specimen of the investigated in-situ composite were calculated and summarized in **Appendix G**. For purely comparative purposes the parameters Δa_c Y^*_c, P_c, and LLD_c and (where c - means "critical") were also calculated from the J-Δa curve at the minimum point of J, and are

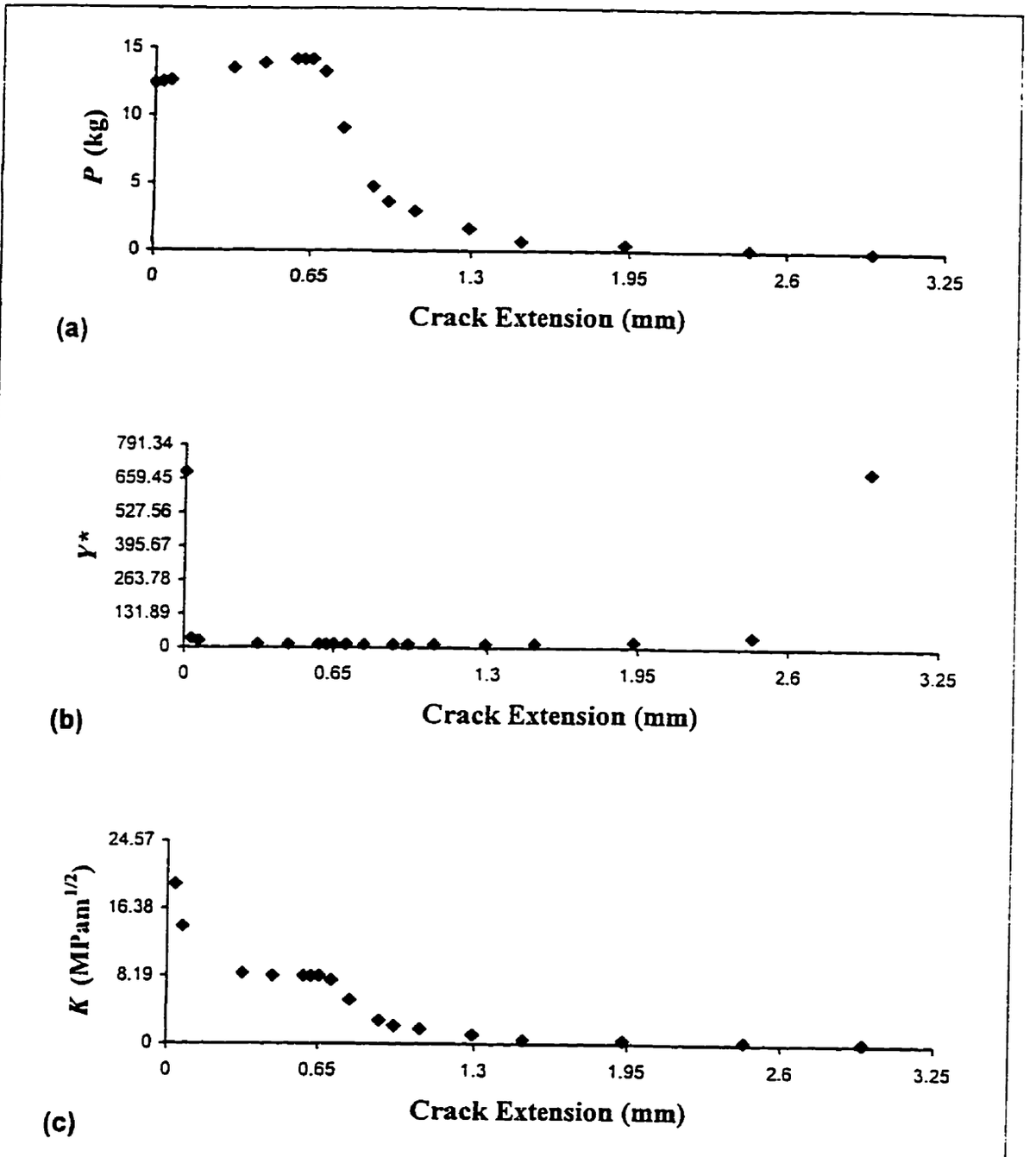

Figure 3.28 A typical relationship between the parameters (a) P_{max}, (b) Y^* and (c) K, and the crack extension (Δa_m=0.65mm) for the homogenized $Ni_{63.7}Al_{36.3}$ in-situ composite.

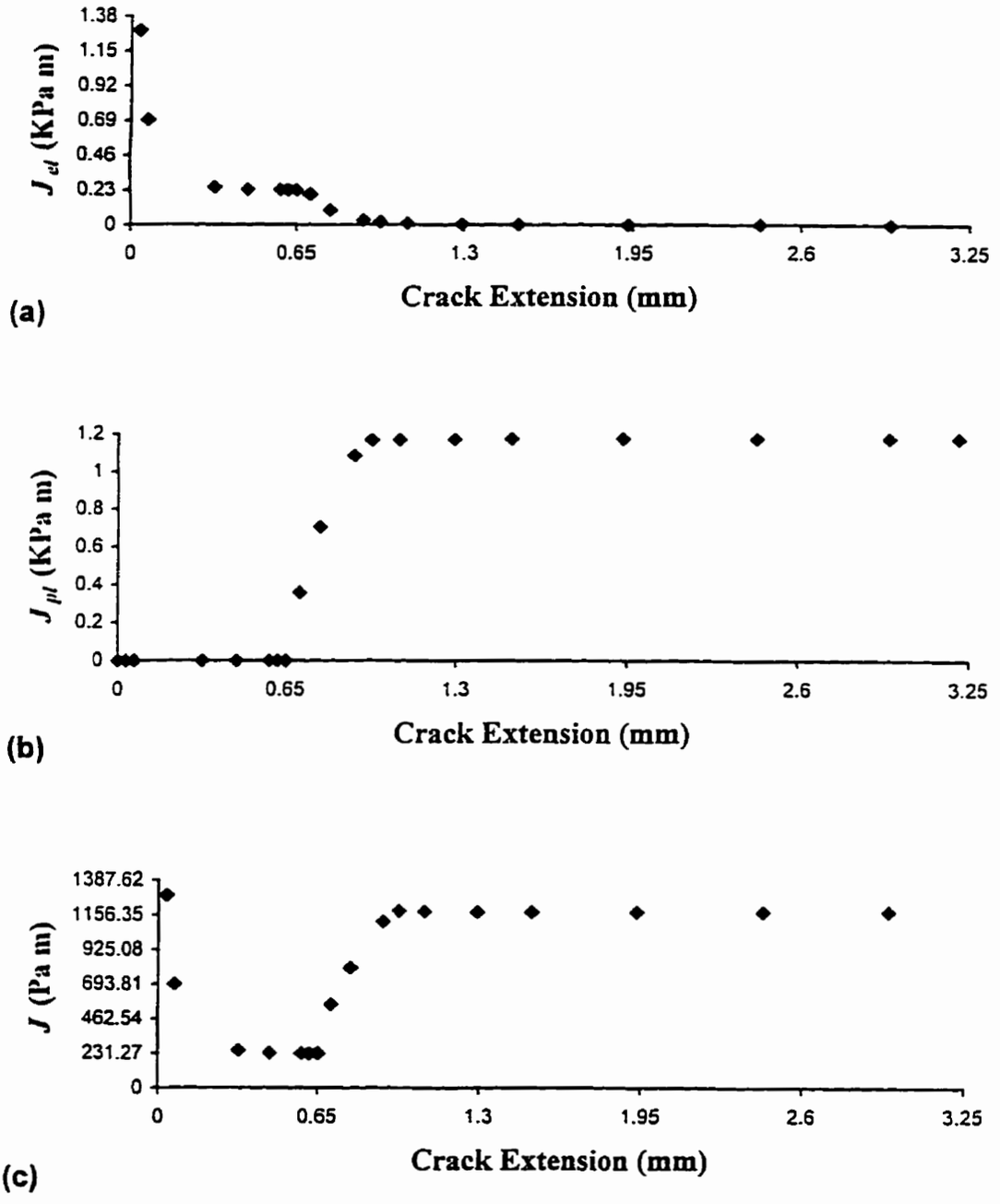

Figure 3.29 A typical group of shapes of the parameters, (a) J_{el}, (b) J_{pl} and (c) J, versus the crack extension (Δa_m=0.65mm).

listed in **Appendix G**. Most of the values of "critical" parameters are exactly equal to the same parameters calculated purely from the geometry of *CNB* specimens and listed in **Appendix D**. The only exceptions are found for some of the 70.8, 72.8, 77.7, 73.2-0.2B and 74.8-0.4B alloys. The validity of experimental values of J_{Ivc} and K_{Ivc} (K_{Ivm}) were verified using *Eqs.(2.20)* and *(2.40)*, respectively.

The "hook" shape of the J-Δa fracture resistance curve shows an exceptionally important feature of a *CNB* bend specimen. This feature make it much easier to determine the values of J_{Ivc}. In addition, the values of J_{Ivc} and K_{Ivc} are more reasonable because this method can automatically avoid either overestimating fracture toughness (see **Appendix F3**) or underestimating fracture toughness (**Appendix F6**).

It is important to note that the Y^* versus Δa curves show a wide, flat range at the bottom (approximately 0.3mm to 1.2 mm as shown in **Figure 3.28b**) for all the investigated in-situ composites (**Appendices F1 (b)** thro **F8 (b)**). In this section of the curve Y^* changes very little as Δa changes. This stability will result in more reliable values when using *Eq.(2.24)* to calculate K_{Ivm}.

CHAPTER 4

DISCUSSION

4.1 Microstructural Characterization

In this study, the overall composition of the as-cast, homogenized and aged in-situ composites ranges from $Ni_{63.7}Al_{36.3}$ to $Ni_{77.7}Al_{22.3}$, which covers the two phase ($\beta+\gamma'$) ($NiAl/Ni_3Al$) field in the Al-Ni phase diagrams (**Figures 1.32** and **1.37**). Due to fast cooling rate the as-cast alloys show non-equilibrium structures (**Figures 3.1** and **3.2**), which are not suitable for a fracture toughness test. The homogenized and aged microstructures conform in general to the phase diagrams as shown in **Figures 1.32** and **1.37**. The fracture toughness values of the homogenized and aged in-situ composites are highly sensitive to their microstructures. Therefore, the toughening mechanisms of the in-situ composites can be explored by analysing their microstructure and fracture surface characterizations. The effects of homogenization at 1000°C for 100h as well as ageing at 550°C for 100h (both followed by a slow furnace cooling), can be summarized as follows:

(1) It is evident that the relatively ductile phase of Ni_3Al preferentially nucleates at the grain boundaries forming a continuous film around the NiAl grains as shown in **Figures 3.1** and **3.3a** to **d**. These results are in agreement with the results from Kumar et al. [13] and Noebe [24]. In addition, the thickness of Ni_3Al phase increases after homogenization from approximately 0.8 μm to 1.5 μm. Such an existence and thickness increment of "necklace microstructure" may toughen the grain boundaries of brittle NiAl phase and thereafter may increase the fracture resistance of the alloys. This is because NiAl does not have enough slip systems to satisfy grain boundary compatibility and the continuous film of γ'-Ni_3Al has multiple independent <110>{111} slip systems, which may enable grain-to-grain compatibility to be restored [114]. Therefore, the continuous, ductile grain boundary film would thus act as a compliant layer between NiAl grain facets.

(2) After homogenization the thickness or size of the Ni_3Al precipitates also increases greatly (**Tables 3.2** and **3.4**), which benefits crack blunting (**Figure 1.1a**) or crack front trapping (**Figure 1.1b**) toughening mechanisms and thereafter increases the fracture toughness of the in-situ composites.

(3) The fully twinned-structure in the NiAl grains, which is most probably a result of martensitic transformation, only appears in the non-equilibrium, as-cast alloys. This is because of the fast cooling rate (≈300°C/h) for the as-cast alloys. After homogenization with much slower cooling rate of approximately 50°C/h (furnace cooling), the occurrence of this twinned-structure (martensitic) of NiAl is reduced but still noticeable (**Figures 3.3b**, **3.3d**, and **3.8b**). This observation might indicate that the NiAl phase is still in a slight non-equilibrium even after furnace cooling from the homogenization temperature.

(4) The most important phenomenon from comparison of morphologies in **Figure 3.1** with **Figure 3.3**, or data in **Table 3.2** with **Table 3.4** is that the volume fraction of ductile Ni_3Al phase increased greatly after homogenization for all the alloys, which may potentially benefit both ductility and toughness of the material.

(5) The morphologies of the in-situ composites are highly sensitive to composition. As shown in **Figure 3.3**, the morphologies after homogenization change greatly when the overall Ni-content increases only a little. After homogenization at 1000°C for 100h followed by a slow furnace cooling, the main distinct structures of the selected system include:

- locally twinned NiAl matrix grains (≈180 μm) with embedded rod-like particles and "necklace" of Ni_3Al (≈17 vol.%) at grain boundaries (**Figures 3.3a** and **b**), for the 63.7-Ni content alloy;
- continuous NiAl matrix (without twinned-structure) surrounded by fine and round semi-continuous Ni_3Al particles (≈32 vol.%) as shown in **Figures 3.3e** and **f**, for the 67.2-Ni content alloy;
- continuous Ni_3Al matrix containing approximately 40 volume percent of *sharp* NiAl particles (**Figures 3.3g** and **h**), for the 70.8-Ni content alloy;
- continuous Ni_3Al matrix containing 23 volume percent of *round* NiAl phase (**Figures 3.3i** and **j**), for the 72.8-Ni content alloy;
- continuous Ni_3Al matrix containing only 8.8 volume percent of *round* or *rod-like* NiAl phase (**Figures 3.3k** and **l**), for the 73.2-Ni content alloy.

(6) Of particular interest is the *aged*, in-situ composite $Ni_{65.9}Al_{34.1}$ which was heated at 1000°C for 100h and aged at 550°C for 100h followed by a slow furnace cooling (**Figure 3.5**).

In this alloy, a partial mat-like structure of Ni_3Al_5 [77] rather than 3-R martensite [78, 79, 90] was confirmed by X-ray analysis (**Table 3.6**). The obtained result is in agreement with the work done by Robertson and Wayman [77] but contrary to the result by Khadkikar et al. [78, 79, 90]. They reported (see **Figure 1.46**) that the plate-like precipitates in the grain interior were identified from electron diffraction patterns to be new variants of the 3R martensite [90].

(7) For the boron-doped in-situ composites, it can be observed that there is a very little microstructural change for the $Ni_{73.2}Al_{26.6}B_{0.2}$ and $Ni_{73.2}Al_{26.8}$ alloys by comparing **Figure 3.4a** with **Figure 3.3k** and data in **Table 3.4**. The $Ni_{74.8}Al_{24.8}B_{0.4}$ alloy is almost a monolithic Ni_3Al with only 0.1 vol.% of NiAl phase as shown in **Figure 3.4b**.

(8) Very little compositional change for overall composition and the composition of each phase in all the in-situ composites was found after homogenization (as shown by comparing **Table 3.1** with **Table 3.3**), which also indicates the reproducibility of EDS measurements.

(9) Compositions of the Ni_3Al phase as listed in **Table 3.3** approximately conform to the most accurate equilibrium Ni-Al binary phase diagram in **Figure 1.34**, although some small discrepancies should be noted. The maximum nickel content in Ni_3Al reported in **Table 3.3** is at 77.6 at.%. However, the data points for the maximum Ni content in Ni_3Al from **Figure 1.34** are no greater than 77 at.%. This is quite satisfactory agreement taking into account that the error in the EDS measurements is not smaller than 0.5 at.%. The minimum nickel content in Ni_3Al in **Table 3.3** is 72.5 at.%. which can be compared to about 73.5 at.% in **Figure 1.34**. The discrepancy is now slightly greater but still within 1 at.%. Less satisfactory agreement between data in the present work and those reported in the literature occurs for the NiAl phase. The maximum nickel content in this phase measured in the present work and listed in **Table 3.3**

is 64.2 at.%. From **Figure 1.36** the maximum nickel content in NiAl is given as approximately 60 at.% and in **Figure 1.32** and **1.37** the maximum nickel solubility content line is drawn at slightly less than 60 at.%. Such a discrepancy between the results obtained in the present work and the literature connot be simply accounted for by the relative inaccuracy of the EDS method used in this work. It is possible that the NiAl phase which is a microconstituent of the investigated in-situ composites still has a slightly non-equilibrium composition most probably owing to a furnace cooling after homogenization (≈50°C/h) which was still too high to allow full compositional equilibration. The highest nickel content of 64.2 at.% found in NiAl in the present work almost corresponds to the nickel content in NiAl at about 1000°C (**Figures 1.32** and **1.37**). Also, another argument supporting the notion about a non-equilibrium furnace cooling rate after homogenization is the occurrence of a twinned martensite in NiAl (martensitic transformation) (e.g. **Figure 3.8**).

4.2 Microhardness and Compressive Mechanical Properties

It is interesting to note that the mat-like structure of Ni_5Al_3 phase showed a significant microhardness value of 690 kg/mm^2 (**Table 3.7**), which shows an obvious smaller indentation area as shown in **Figure 3.8a.** This value is almost twice as much as those of any other structures in the in-situ composites. This behaviour is in agreement with Vickers microhardness measurements by Khadkikar et al. [90]. It is reasonable to assume that the extremely high yield strength of σ_{YS}≈1150 MPa (all σ_{YS} values are tabulated in **Appendix E**) in $Ni_{65.9}Al_{34.1}$ in-situ

composite also results from this special mat-like structure of Ni_3Al_5 phase because very high values of neither yield strength (**Table 3.8**) nor Vickers microhardness (**Table 3.7**) can be found for any other in-situ composites without Ni_5Al_3 phase. It is worth of pointing out that a very high yield strength ($\sigma_{YS} \approx 1150$MPa) and a reasonable value of fracture toughness (≈ 13 MPa$\sqrt{m}$) (**Appendix E**) of the aged $Ni_{65.9}Al_{34.1}$ alloy indicate that such a new promising alloy can be yielded by an economic and simple casting method followed by a proper heat treatment as shown in this research.

4.3 Dependence of Fracture Toughness on Microstructure

4.3.1 Grain Size Effects

It has to be pointed out that the grain sizes of the matrix for all the in-situ composites as shown in **Table 3.4** are approximately one forth of the critical crack length of the chevron-notch specimens as shown in **Appendix D**. This fact seems to indicate that the fracture toughness values obtained from the critical crack length of the in-situ composites might be affected by only a very few matrix grains in the materials. In other words, the small size of bend specimens might be unsuitable from the stand point of the size of matrix grains and should not be used to test the fracture toughness of the in-situ composites when the matrix grain size is relatively large. On the other hand, the linear elastic fracture mechanics (*LEFM*) assumes that

fracture toughness should be obtained from only a continuous material (i.e. many grains in the crack front). However, it might not necessarily be limiting factor for the real materials. In fact, there is no such a grain-size limitation in any *ASTM* Standard document such as *E 399-90* [97], *E 1304-89* [98] or *E 813-89* [99]. Furthermore, a lot of small-size bending tests were performed without any grain-size limitation. For example, the grain size of NiAl in Rigney and Lewandowski's work [81] was approximately 2000 μm and the single-edge-notched, three-point-bend specimen size was also small with dimensions: 6mm x 6mm x 50mm [81], which satisfies the size requirements of *ASTM* Standard *E 399* [97] for plane strain. Rigney and Lewandowski [81] obtained a very reasonable toughness of 6.6 MPa$\sqrt{m}$ for NiAl. Therefore, the toughness values obtained in this research might not necessarily be affected by the relative sizes of the matrix grains and the critical crack lengths of the bend specimens.

4.3.2 The Effect of the Volume Fraction of Ni_3Al on the Fracture Toughness of the Boron-Free, In-Situ Composites

Figures 4.1 and **4.2** shows that both valid $K_{Ivm}{}^{W}$ and K_{Ivc} values of homogenized alloys increase with increasing volume fraction of ductile Ni_3Al phase in the boron-free in-situ composites. The best fit curves in **Figures 4.1** and **4.2** describe exactly the relationship of $K_{Ivc}= A+BV_d^n$ type which is similar to the results for both Ni/TiAl and TiNb/TiAl in-situ composites obtained by Rao et al. [70] (**Figure 1.24**).

Furthermore, comparing **Figure 4.1** with **Figure 4.2**, it also can be seen that valid fracture

toughness values of $K_{Ivm}{}^{W}$ calculated from *Eq.(2.24)* give very consistent results with K_{Ivc} obtained from the *J*-integral method of *Eq.(2.46)*. The best fit curves establishing the precise relationship between fracture toughness and volume fraction of Ni_3Al for the in-situ, boron-free composites, can be given as follows:

$$K_{Ivm}{}^{W} = 6.12 + 0.7\ V_d{}^{0.74} \qquad (MPa\sqrt{m}) \qquad (4.1)$$

$$K_{Ivc} = 6.05 + 0.714\ V_d{}^{0.749} \qquad (MPa\sqrt{m}) \qquad (4.2)$$

where, V_d is in (%) and the residual mean-square correlation coefficients of R^2 are 0.95 and 0.92, for *Eq.(4.1)* and *Eq.(4.2)*, respectively, and are pretty close to 1, showing that the best fit curves give a very good fit to the experimental data for the boron-free, in-situ composites. When $V_d = 0$, the fracture toughness values of $K_{Ivm}{}^{W}$ or K_{Ivc} represent the fracture toughness of NiAl phase, = 6.1 MPa$\sqrt{m}$, which is in a very good agreement with the results obtained by Kumar et al. [13].

In **Figures 4.1** and **4.2**, the solid symbols, representing the fracture toughness values obtained from the aged $Ni_{65.9}Al_{34.1}$ alloy, are very close to the best fit curves, which are yielded by homogenized in-situ composites (half-solid symbols). This fact actually indicates that ageing does not adversely affect the fracture toughness of the in-situ composites because Ni_5Al_3 phase only exists in the grains and does not embrittle the Ni_3Al/NiAl interfaces in the aged $Ni_{65.9}Al_{34.1}$ in-situ composite.

It has to be pointed out that the validity of $K_{Ivm}{}^{W}$ values (see the bold values of $K_{Ivm}{}^{W}$ as shown in **Appendix E**) is definitely limited for higher volume fraction of Ni_3Al (only one valid point for volume fraction higher than 80% of Ni_3Al as shown in the right part of **Figure 4.1**)

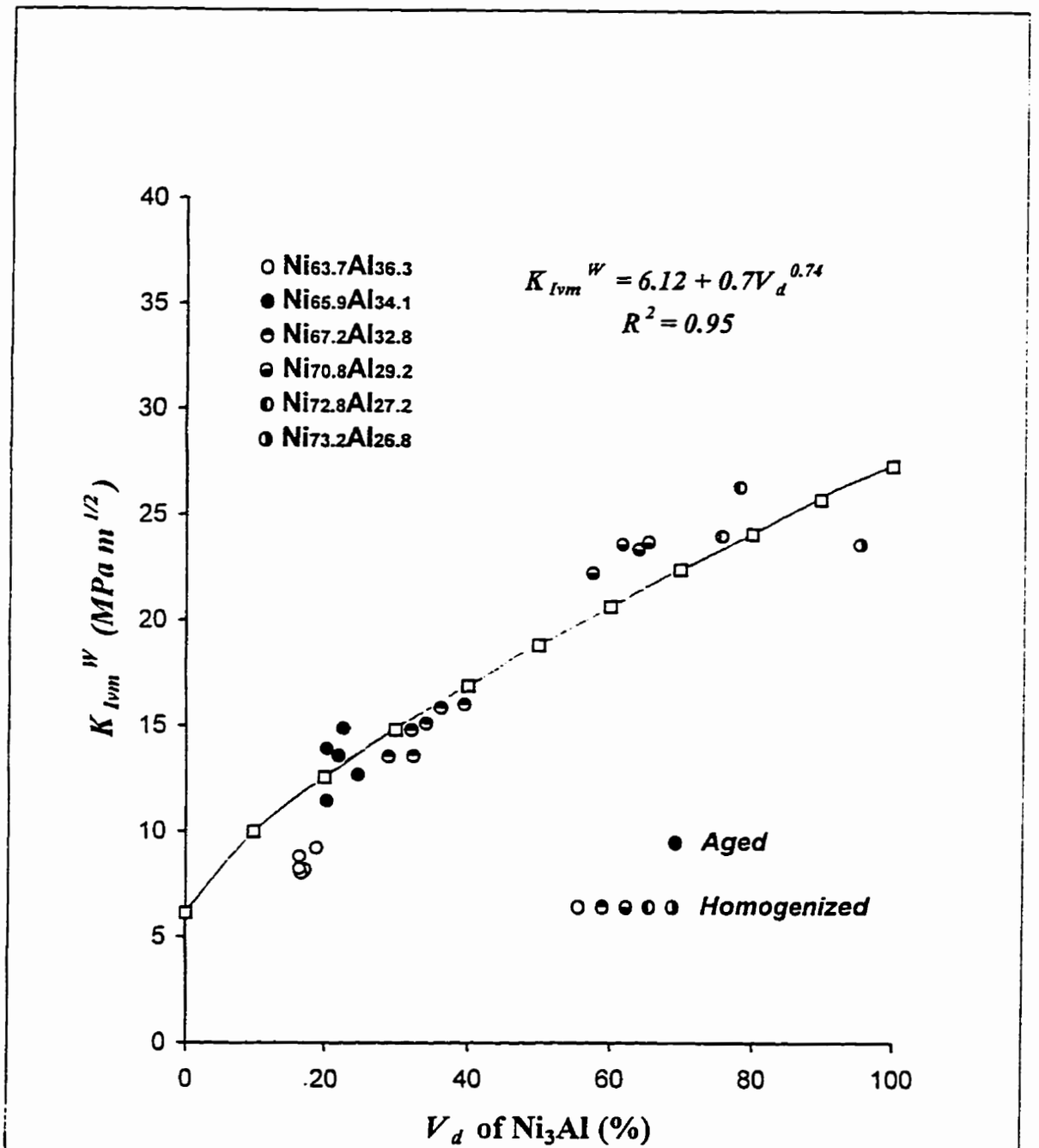

Figure 4.1 The dependence of valid $K_{Ivm}{}^{W}$ values on the volume fraction of Ni_3Al phase in the boron-free, in-situ composites. The solid symbols show the aged alloy of $Ni_{65.9}Al_{34.1}$ and the open ones designate the homogenized alloys. The best fit line is labelled by squares.

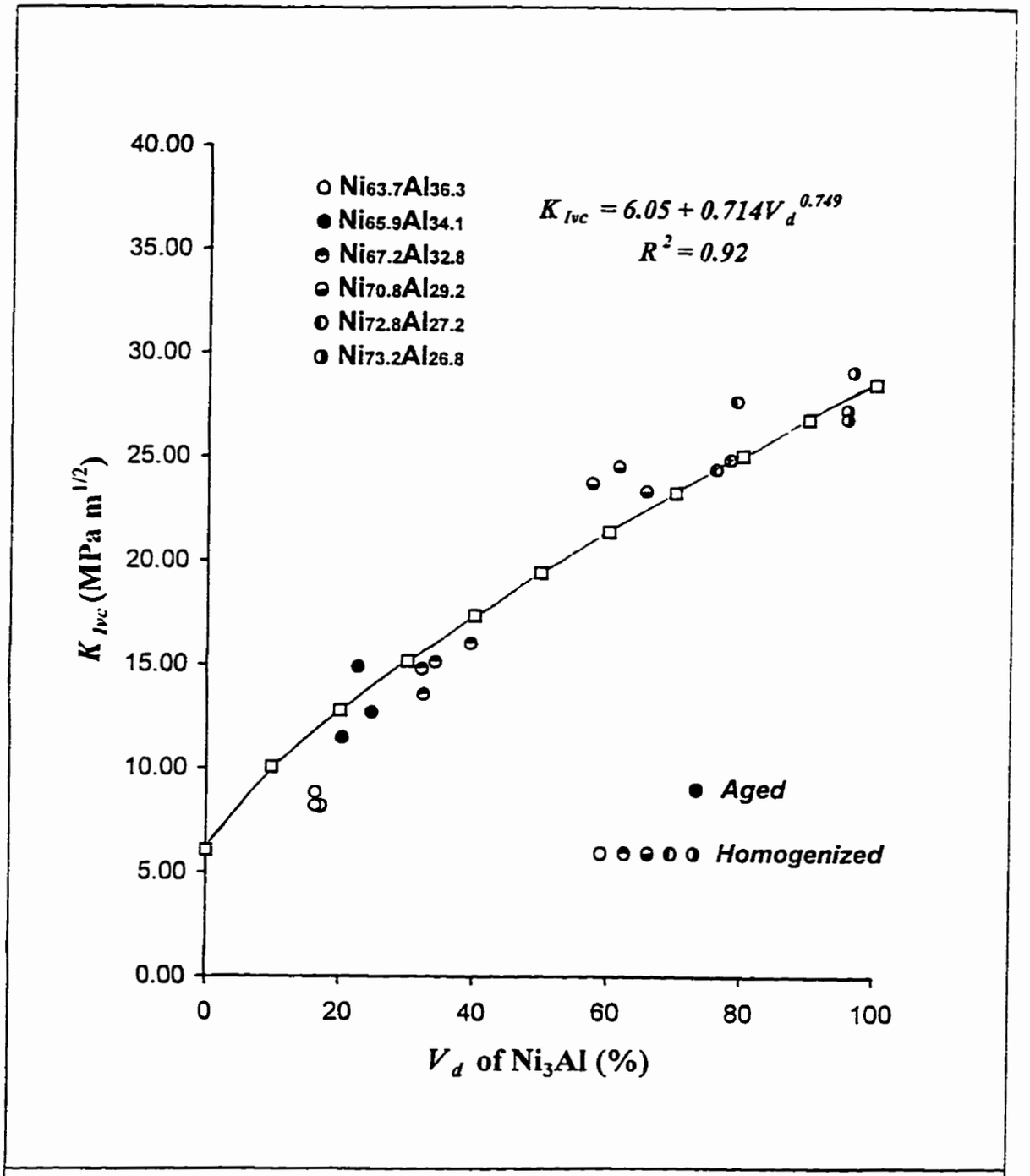

Figure 4.2 The dependence of valid K_{Ivc} values on the volume fraction of Ni_3Al phase in the boron-free, in-situ composites. The solid symbols show the aged alloy of $Ni_{65.9}Al_{34.1}$ and the open ones designate the homogenized alloys. The best fit line is labelled by squares.

while the K_{Ivc} values are all valid as shown in **Appendix G** and more points of K_{Ivc} values are shown in the right part of **Figure 4.2.** This arises from the limitation imposed by the *CNB* specimen-thickness ($B \geq 1.25(K_Q/\sigma_{YS})^2$ for a conventional K_{Ivm} bending test. In other words, the *J*-integral unloading-reloading method for a single specimen of a *CNB* bend test is a much more convenient and useful tool to obtain valid fracture toughness values for the more ductile in-situ composites because the size requirement ($B \geq 25(J_Q/\sigma_{YS})$ as shown in *Eq.2.20*) for valid-J_{Ic} of the *J*-integral unloading-reloading method is much more lenient than the conventional K_{Ic} requirements as discussed in Section 2.1.2.

Dependence of fracture toughness of the "in-situ" NiAl/Ni_3Al composite on volume fraction of toughening phase (Ni_3Al) can also be analysed in terms of the rule of mixtures (*ROM*) as reported by Davidson and Chan [61-62] for the Nb-Cr_2Nb system.

For comparison with the experimental results, the calculated rule of mixtures (*ROM*), both with and without considering the differences in modulus between NiAl (E_m = 294 GPa [110]) and Ni_3Al (E_d = 179 GPa [110]), are represented by dashed lines and designated "*E-ROM*" and "*ROM*", respectively. The lower bound, K_{min}, and upper bound, K_{max}, of the modified *ROM* by Ashby [63] are also shown as solid lines in **Figure 4.3.** The typical points on the *E-ROM*, *ROM*, K_{min} and K_{max} lines are calculated by *Eqs.(1.26), (1.28), (1.30)* and *(1.32),* respectively. The parameters for calculating *E-ROM*, *ROM*, K_{min} and K_{max}, are summarized in **Table 4.1.**

Table 4.1 The parameters used for calculating *E-ROM*, *ROM*, K_{max} and K_{min}.

	V_d	E_d	E_m	E_c	E'_d	E'_m	E'_c	a^*	K_m	K_d	K_{Ic}
	(vol.%)	(GPa)	(GPa)	(GPa)	(GPa)	(GPa)	(GPa)	(mm)	(MPa $m^{1/2}$)		
ROM	0	179	294	294	196.70	323.1	323.08		6	28	6
	100	179	294	179	196.70	323.1	196.70		6	28	28
E-ROM	0	179	294	294	196.70	323.1	323.08		6	28	6
	20	179	294	271	196.70	323.1	297.80		6	28	16.25
	40	179	294	248	196.70	323.1	272.53		6	28	21.28
	60	179	294	225	196.70	323.1	247.25		6	28	24.54
	80	179	294	202	196.70	323.1	221.98		6	28	26.7
	100	179	294	179	196.70	323.1	196.70		6	28	27.96
K_{min}	0	179	294	294	196.70	323.1	323.08		6	28	6
	20	179	294	271	196.70	323.1	297.80		6	28	8.51
	40	179	294	248	196.70	323.1	272.53		6	28	10.18
	60	179	294	225	196.70	323.1	247.25		6	28	11.45
	80	179	294	202	196.70	323.1	221.98		6	28	12.27
	100	179	294	179	196.70	323.1	196.70		6	28	12.63
K_{max}	0	179	294	294	196.70	323.1	323.08	5	6	28	6
	20	179	294	271	196.70	323.1	297.80	5	6	28	16.73
	40	179	294	248	196.70	323.1	272.53	5	6	28	22.11
	60	179	294	225	196.70	323.1	247.25	5	6	28	25.27
	80	179	294	202	196.70	323.1	221.98	5	6	28	27.1
	100	179	294	179	196.70	323.1	196.70	5	6	28	28.04

Note: Poisson's ratio, v, taken for calculations of E'_m (NiAl) is equal to 0.315 [119] and for E'_d (Ni_3Al) is equal to 0.305 [119]. Values of E_d and E_m are taken from **Table 2.1.**

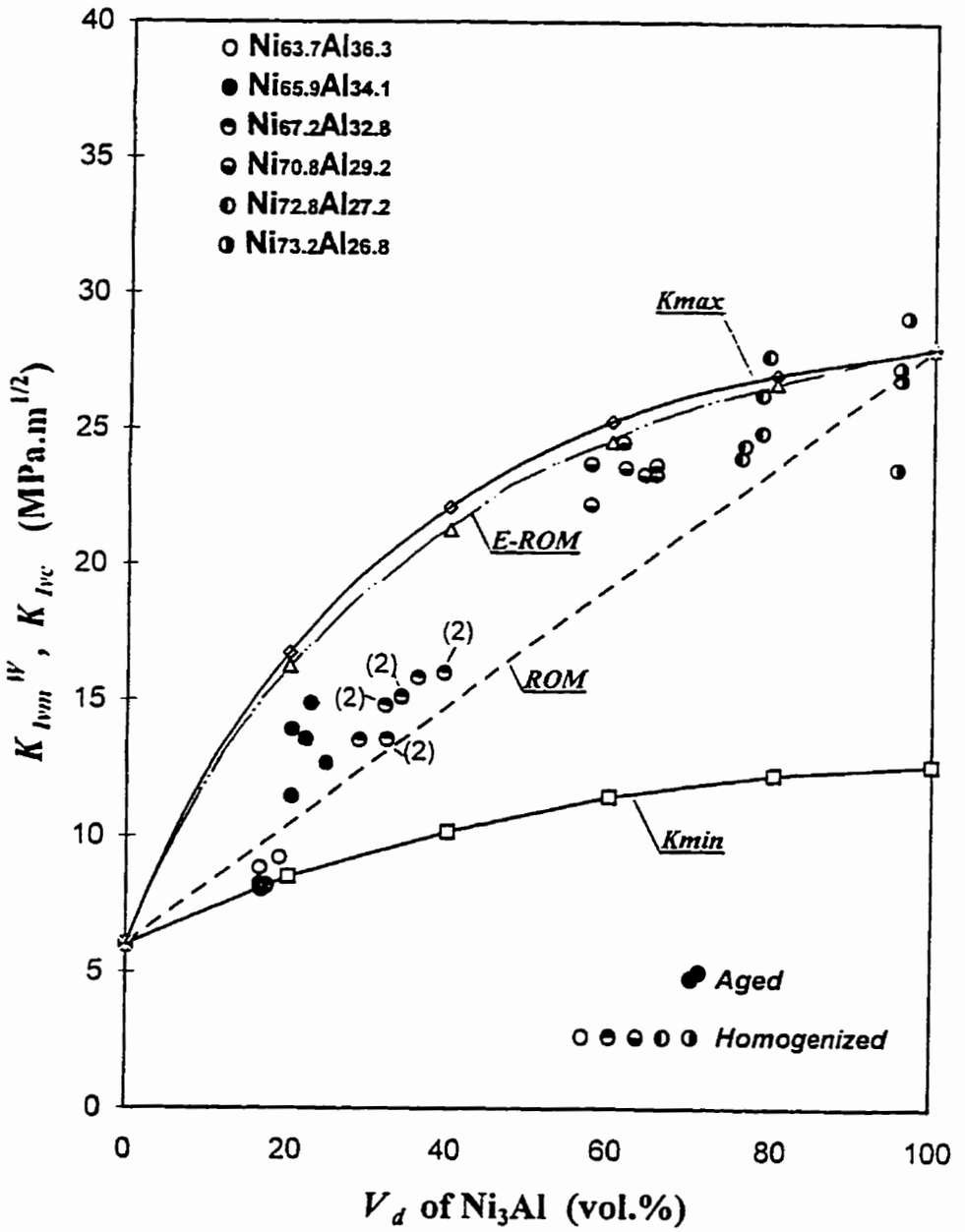

Figure 4.3 The valid K_{Ivm}^{W} and K_{Ivc} fracture toughness of the boron-free in-situ composites as a function of volume fraction of Ni_3Al. A regular *ROM* (straight broken line), modulus-modified (*E-ROM*) as well as upper bound (K_{max}) and lower bound (K_{min}) of Ashby's modified *ROM* [63] are shown. The solid symbols designate the aged alloy of $Ni_{65.9}Al_{34.1}$ and the unsolid ones represent the homogenized alloys. The numbers in parentheses indicate overlapping data points.

In either case, the values of the fracture toughness of the investigated in-situ composites are almost within the *ROM* and K_{max} (or *E-ROM*) lines. In particular, this behaviour experimentally confirms the validity of either *E-ROM* or K_{max} by Ashby' approach [63]. Furthermore, all the data from the NiAl-Ni_3Al are close to the upper bound, which is contrary to the results from the Nb-Cr_2Nb in-situ composites obtained by Davidson and Chan [61-62]. In their results [61-62], all the data from the Nb-Cr_2Nb in-situ composites were close to the K_{min} lower bound line (**Figure 1.17**).

4.3.3 Comparison with Existing Toughening Models

The Alloys Containing a Continuous NiAl Matrix and a Discontinuous Ni_3Al Phase

Crack bridging is probably one of the pronounced toughening mechanisms for the in-situ composites containing a continuous NiAl matrix and a discontinuous Ni_3Al phase (**Figures 3.3a** thro **f**, and **Figure 3.5**) because the stretched ductile Ni_3Al particles could be clearly observed from the typical fractographs of these alloys as shown in **Figures 3.10b**, **3.11b**, **3.12a** and **b**. This is because when they are intercepted by a crack, the ductile Ni_3Al particles could undergo extensive plastic stretching in the crack wake and contribute to the toughness of the in-situ composites by inhibiting or making further crack opening very difficult.

A quantitative analysis of crack bridging mechanism can be given by *Eq.(1.16)* although according to Chan's rule for extrinsic toughening mechanism [17-18, 23], crack bridging model described by *Eq.(1.16)* cannot effect the K_{Ic} value of the composite, as discussed in Chapter 1.

Disregarding the Chan's rule [17-18, 23] one can try to use simple addition rule: $K_{Ic} = K_m + \Delta K_r$, where ΔK_r designates the toughness contribution by crack-bridging toughening mechanism as shown in *Eq.(1.16)*. This rule has been applied several times by other researchers for an in-situ Nb-reinforced Nb_3Al intermetallic composite [44] and both fully lamellar and duplex TiAl system [57]. The quantitative analysis of crack-bridging toughening mechanism can be given as follows.

The parameters to calculate crack-bridging toughening mechanism for the in-situ composites containing a continuous NiAl matrix and a discontinuous Ni_3Al phase (**Figures 3.3a** thro **f**, and **Figure 3.5**) are listed in **Table 4.2**. The elastic modulus of the in-situ composites, E, as shown in *Eq.(1.16)*, is calculated from the lower bound of the rule of mixtures for composites as *Eq.(3.1)* [63, 100] and listed in **Appendix E** (this is a conservative estimate of the elastic modulus of a composite).

Table 4.2 The parameters for quantitative analysis of crack-bridging toughening mechanism in the alloys containing the NiAl matrix and a discontinuous Ni_3Al phase.

Ni	V_d	E	σ_{YS}	χ	a_0	ΔK_r	K_m	K_{Ic}	K_{Ivm}^{W}
at.%	vol.%	GPa	MPa		μm	MPa $m^{1/2}$	MPa $m^{1/2}$	MPa $m^{1/2}$	MPa $m^{1/2}$
63.7	16.53	261.97	395.2	0.4	1.2	2.8661	6.2	9.0661	8.09
63.7	17.16	264.81	377.8	0.4	1.2	2.870631	6.2	9.070631	8.13
63.7	17.27	264.51	461.7	0.4	1.2	3.181763	6.2	9.381763	8.19
63.7	18.86	262.23	421.1	0.4	1.2	3.161734	6.2	9.361734	8.22
63.7	16.7	265.51	400	0.4	1.2	2.917758	6.2	9.117758	8.02
63.7	16.48	265.85	434.4	0.4	1.2	3.022473	6.2	9.222473	8.25
63.7	16.48	265.85	471.4	0.4	1.2	3.148563	6.2	9.348563	8.82
65.9	22	257.59	1051	0.6	1.5	7.321473	6.2	13.52147	13.57
65.9	24.7	253.74	1000	0.6	1.5	7.51042	6.2	13.71042	12.68
65.9	20.3	260.08		0.6	1.5				13.91
65.9	22.6	256.72	1241	0.6	1.5	8.049914	6.2	14.24991	14.87
65.9	20.3	260.08	1311	0.6	1.5	7.892673	6.2	14.09267	11.45
67.2	36.14	238.6	895.2	1.1	1.8	12.36294	6.2	18.56294	15.83
67.2	34.09	241.18	770.7	1.1	1.8	11.20107	6.2	17.40107	15.1
67.2	39.43	234.58	756.4	1.1	1.8	11.76975	6.2	17.96975	15.99
67.2	28.98	247.85	753.9	1.1	1.8	10.3546	6.2	16.5546	13.53
67.2	32.33	243.44	889.2	1.1	1.8	11.77148	6.2	17.97148	13.56
67.2	32.1	243.73	847.4	1.1	1.8	11.45734	6.2	17.65734	14.8

Note: 1. $K_{Ic} = K_m + \Delta K_r$;

2. K_{Ivm}^{W} is experimental.

The work-of-fracture parameter χ can vary from the interface debonding of the two phases, e.g., Ni_3Al/NiAl in the in-situ composites. For a well-bonded interface (debonding length, $d \approx 0$) and for ductile ligaments that fail by necking to a point, the resultant χ is in the range 0.3 to 1 [45]. For various extents of debonding at the interface of the cylindrical specimens of Pb in glass, experiments show that χ can vary from 0.5 to 6 (**Figure 4.4**) For the network structure of Al_2O_3/Al composites, χ is in the range of 2 to 3.5 [43]. For the particulate ductile phase toughened brittle materials, since the maximum debonding that can be achieved is appreciably smaller than that of the other two microstructures, the χ value is comparatively small [45]. Therefore, by analogy with references [43-45] and according to the typical fractographs as shown in **Figures 3.10**, **3.11** and **3.12**, the χ values of 0.4, 0.6, and 1.1 for the homogenized $Ni_{63.7}Al_{36.3}$ alloy, the aged $Ni_{65.9}Al_{34.1}$ alloy and the homogenized $Ni_{67.2}Al_{32.8}$ (**Table 4.2**), respectively, can be arbitrarily assumed as reasonable approximations for χ.

The average values of thickness of Ni_3Al, a_0, are taken from **Table 3.4**. The K_{Ic} value of the matrix, K_m = 6.2 MPa$\sqrt{m}$ for monolithic NiAl in **Table 4.1**, is taken from *Eqs.(4.1)* and *(4.2)* when $V_d = 0$.

The results by simple addition rule ($K_{Ic} = K_m + \Delta K_r$) as shown in **Table 4.2**, seem to fit well to the $Ni_{63.7}Al_{36.3}$ ($K_{Ic} \approx 9.22 \pm 0.14$ MPa$\sqrt{m}$ vs. $K_{Ivm}^{W} \approx 8.25 \pm 0.27$ MPa$\sqrt{m}$) and $Ni_{65.9}Al_{34.1}$ ($K_{Ic} \approx 13.89 \pm 0.34$ MPa$\sqrt{m}$ vs. $K_{Ivm}^{W} \approx 13.30 \pm 1.30$ MPa$\sqrt{m}$) alloys but overestimate the fracture toughness of the $Ni_{67.2}Al_{32.8}$ in-situ composite ($K_{Ic} \approx 17.69 \pm 0.68$ MPa$\sqrt{m}$ vs. $K_{Ivm}^{W} \approx 14.80 \pm 1.07$ MPa$\sqrt{m}$). These results might indicate that the crack bridging model of *Eq.(1.16)* be only suitable for the homogenized $Ni_{63.7}Al_{36.3}$ and aged $Ni_{65.9}Al_{34.1}$ in-situ composites, but not for

the $Ni_{67.2}Al_{32.8}$ in-situ composite. This is most probably because the interfacial/grain boundary fracture of Ni_3Al becomes more (dominant) in the $Ni_{67.2}Al_{32.8}$ alloy over crack bridging by the Ni_3Al particles. Such a scenario seems to agree with the fractographs of the $Ni_{67.2}Al_{32.8}$ alloys in **Figure 3.12.**

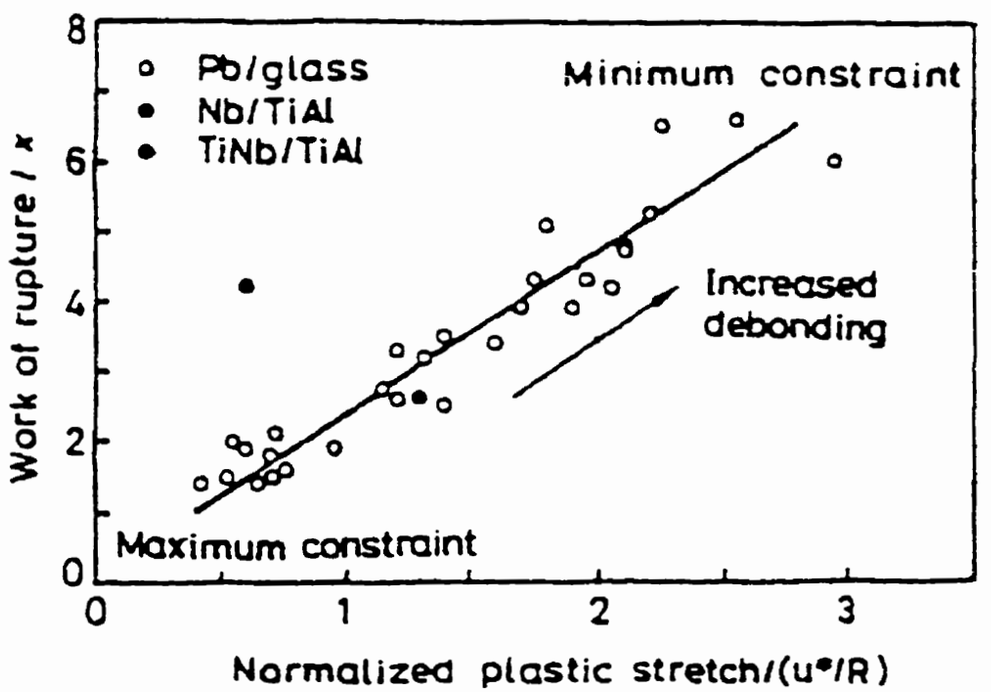

Figure 4.4 χ "work of rupture" parameter against maximum normalized displacement [41].

Crack blunting could be another evident toughening mechanism for the in-situ composites containing the continuous NiAl matrix and a discontinuous Ni_3Al phase (**Figures 3.3a** thro **f**, and **Figure 3.5**) since the impeded "river-pattern" crack at the grain boundaries could be observed in the typical fractographs of **Figures 3.10b**, **3.11** and **3.12**. This is due to the

impediment of the propagation of cleavage crack forming river-pattern in the NiAl grains as they intersected the "necklace", i.e., ductile γ'-Ni_3Al at the grain boundaries. The extensive localized plastic deformation of the second γ' phase may cause the stresses at the crack front to relax sufficiently to blunt the crack in the ideal case, and therefore would prevent the crack from propagating further. As indicated in crack blunting model *Eq.(1.5)*, the fracture toughness caused by this mechanism would be more significant when the volume fraction of ductile Ni_3Al phase increases. Unfortunately, since the effective fracture strain values of matrix and ductile phase (ε_{fm} and ε_{fd} in *Eq.(1.7)*) as required in this model are hard to measure for the in-situ composites, the quantitative analysis of this toughening mechanism on the in-situ composites could not be given in this work.

The Alloys Containing a Continuous Ni_3Al Matrix and a Discontinuous NiAl Phase

As shown in **Appendices E** and **G**, the in-situ composites containing a continuous Ni_3Al matrix and a discontinuous NiAl phase (**Figures 3.3j** thro **m**, and **Figures 3.4a**, **b**) showed higher fracture toughness values of $K_{Ivm}{}^{W}$ and K_{Ivc} than the ones for the in-situ composites containing a continuous NiAl matrix and a discontinuous Ni_3Al phase (**Figures 3.3a** thro **h**, and **Figure 3.5**).

It can also be seen that the Ni_3Al grain facets show intergranular fracture mode in all the in-situ composites with the Ni_3Al matrix (**Figures 3.13** to **3.16**) as well as in the boron-doped in-situ composites (**Figures 3.17** to **3.18**). Although the Ni_3Al matrix was shown to fail by brittle intergranular fracture, toughness values in excess of 20 MPa$\sqrt{m}$ (**Appendices E** and **G**) were still obtained from the in-situ composites containing a continuous Ni_3Al matrix and a

discontinuous NiAl phase (**Figures 3.3h** thro **m**, and **Figures 3.4a** and **b**). These results are consistent with Rigney and Lewandowski' earlier work [81]. This is because of several factors, including interfacial delamination, crack tip blunting or plastic deformation on the grain facets and in the specimen bulk. As indicated by Rigney and Lewandowski' earlier work [81], the intergranular cracks of Ni_3Al phase are clearly stable and significant plasticity develops at the crack tip, which may result in the observed high toughness values as shown in **Appendices E** and **G**. In addition, with increase in load, dislocation motion is promoted in the Ni_3Al grains contained within the plastic zone at the crack tip, and owing to high stresses and strains attained ahead of the chevron notch, the blunting of the crack tip causes further yielding along the grain facets neighbouring the crack faces.

The reason that the in-situ composites with higher volume fraction of γ'-Ni_3Al phase shows higher potential ductility, can be explained by comparing the slip systems of NiAl phase and Ni_3Al phase.

It is well known that only three independent slip systems are available for polycrystalline NiAl deformation by <110> slip, regardless of the operative slip planes [24, 67, 82-83, 111-115]. Because this is less than the five independent deformation modes considered necessary for extensive, uniform, crack free deformation of a polycrystalline aggregate, NiAl is considered to have little potential for exhibiting substantial room temperature tensile ductility and fracture toughness. This view is supported by experimental evidence (only zero to a maximum of about 4% room-temperature tensile ductility [24, 114] and 4 to 7 MPa$\sqrt{m}$ of fracture toughness of polycrystalline NiAl [81, 111]). Therefore, simply speaking, monolithic NiAl is a slip system limited material.

In contrast to NiAl, the ordered fcc Ni_3Al phase has enough independent slip system to accommodate plastic deformation in polycrystalline form since its low temperature deformation occurs by <110>{111} slip [82-83, 113]. γ'-Ni_3Al has inherent tensile ductility at room temperature as demonstrated by single crystal behaviour (over 98% elongation) and even with intrinsic grain-boundary brittleness, monolithic Ni_3Al has superior toughness of 20 $MPa\sqrt{m}$ [81]. This makes higher volume fraction of γ'-Ni_3Al phase a higher contributor of fracture toughness in the in-situ composites. Besides, the effect of volume fraction of Ni_3Al ductile phase on fracture toughness on the in-situ composites would be discussed in detail in the following sections because of its exceptional importance.

Figure 4.5 schematically show the toughening mechanism proposed to be responsible for the high toughness in Ni_3Al. The dislocation emission results in local plastic deformation along grain facets neighbouring the extending macrocrack. The tip of the precrack blunts during loading, while intergranular microcracking develops in the process zone on the sample surface (only). Intergranular macrocracking occurs along grain boundaries after significant crack opening displacement, while intergranular macrocrack propagation occurs in a stable manner accompanied by significant local plasticity in the grains and at grain boundary regions. The mechanism proposed supports initiation of stable intergranular macrocracks, followed by energy dissipation through dislocation activity in the vicinity of grain boundaries and grain interiors, thereby contributing significantly to the high toughness and resistance curve behaviour in Ni_3Al.

Additionally, **Figure Appendix C1** (p.222) shows that grain boundary facets (in reality semi-dendritic boundaries) are interconnected by most probably secondary dendritic arms

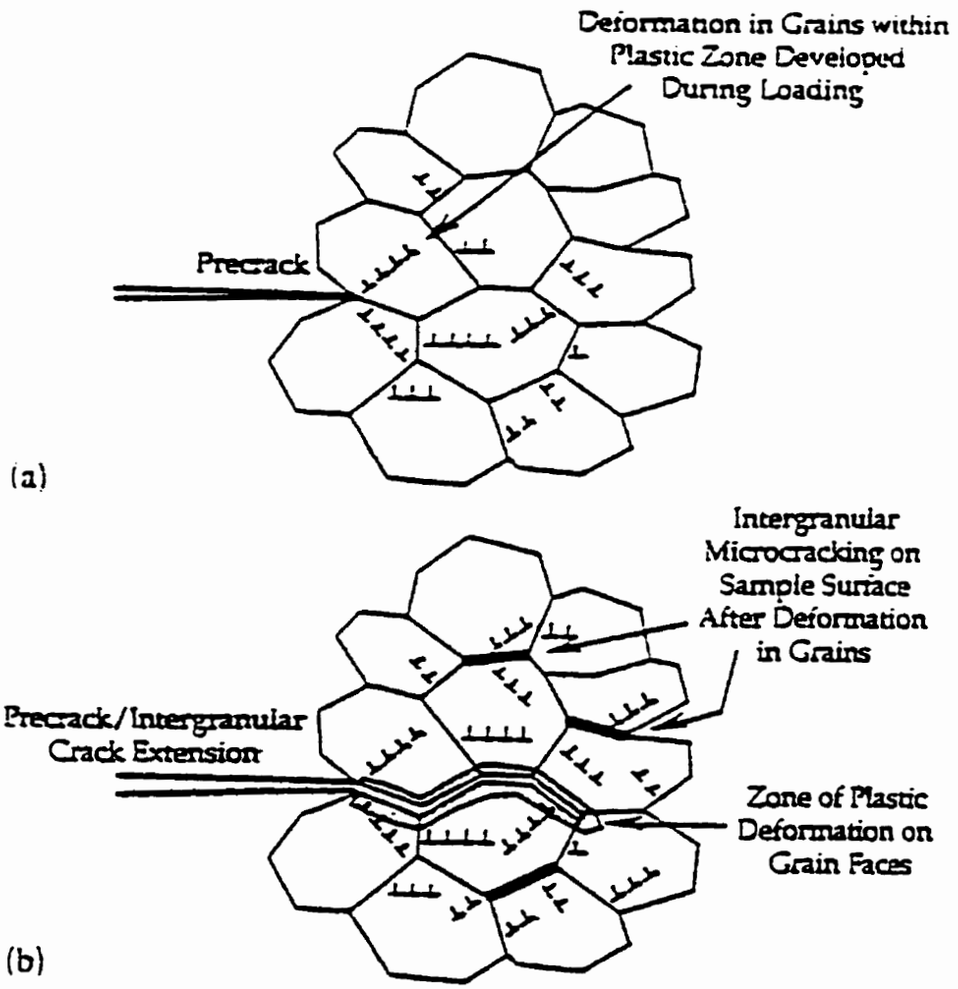

Figure 4.5 Schematic diagrams of the mechanisms contributing to high toughness and resistance curve behaviour in Ni_3AL. (a) With increasing in load, dislocation motion is promoted in grains contained within the plastic zone owing to high stresses and strains attained ahead of the precrack. (b) The blunting of the crack tip causes further yielding along the grain facets neighbouring the crack facets. A high degree of yielding in grains on the sample surface away from the macrocrack causes prior particle boundary and intergranular cracking. This process continues with crack growth [81].

which fracture last acting similarly to crack bridging mechanism. This may be somehow additive to the toughness resulting from the local plasticity developing during grain (semi-dendritic) boundary fracture (Rigney and Lewandowski [81]).

The Alloy after Ageing

As indicated in Section 4.1, the Ni_5Al_3 phase in the $Ni_{65.9}Al_{34.1}$ in-situ composite, was not observed nucleating at the grain boundaries, which is inconsistent with the results by Khadkikar et al. [78, 79, 90]. This fact indicates that the Ni_5Al_3 phase would not affect the intergranular fracture pattern in $Ni_{65.9}Al_{34.1}$ in-situ composite but might be beneficial for bowing or crack front trapping in the grains during the fracture toughness test. That is probably why this needle-like mat structure of fine Ni_5Al_3 particles is not embrittling the alloy and simultaneously increases the yield strength of the $Ni_{65.9}Al_{34.1}$ in-situ composite.

The Alloy with Ni Reinforcements

The non-catastrophic fracture and significant plasticity of the $Ni_{77.7}Al_{22.3}$ alloy with near-single Ni_3Al phase, as shown in **Figure 3.16**, prompted additional toughness testing utilizing *J*-integral technique in a *CNB* test. The present results from *J*-integral technique as shown in **Appendix G**, indicate that despite the observed intergranular fracture (**Figure 3.16a**) this alloy possesses extremely high toughness (=85 MPa$\sqrt{m}$ as shown in **Appendix G**). This might be due to the Ni phase residing within the grains as shown in **Table 3.3** and **Table 3.4** and seen in **Figure 3.3m**. The significant plastic deformation on the grain facets and in the specimen bulk, especially local tearing fracture mode as shown in **Figure 3.16b**, is definitely beneficial for such

high fracture toughness value of this alloy.

4.4 The Dependence of the Fracture Toughness on the Yield Strength for the Boron-Free, In-situ Composites

Materials with higher yield strength usually exhibit a lower tensile ductility and thus a lower fracture resistance (fracture toughness) [107, 108]. This general behaviour as shown in **Figure 4.6** is also true for the investigated boron-free, in-situ composites (**Figures 4.7** and **4.8**).

Figures 4.7 and **4.8** show the influence of the yield strength on the valid $K_{Ivm}{}^{W}$ and K_{Ivc} for the boron-free in-situ composites, respectively. It can be seen that the fracture toughness values decrease with increasing yield strength for most of the investigated in-situ composites. In addition, this rule can be expressed as follows for the boron-free, in-situ composites:

$$K_{Ivm}{}^{W} = 1609.2\ \sigma_{YS}{}^{-0.6859} \qquad (R^2=0.7767) \qquad (4.3)$$

$$K_{Ivc} = 953.18\ \sigma_{YS}{}^{-0.6084} \qquad (R^2=0.8625) \qquad (4.4)$$

where σ_{YS} is in MPa, and $K_{Ivm}{}^{W}$ and K_{Ivc} in MPa.$\sqrt{m}$.

However, it is interesting to note that the $Ni_{63.7}Al_{36.3}$ alloy (the circle symbols as shown in **Figures 4.7** and **4.8**) does not conform to this rule, which shows lower fracture toughness dependence on the lower rather than higher yield strength. The reason for such a behaviour is not clear.

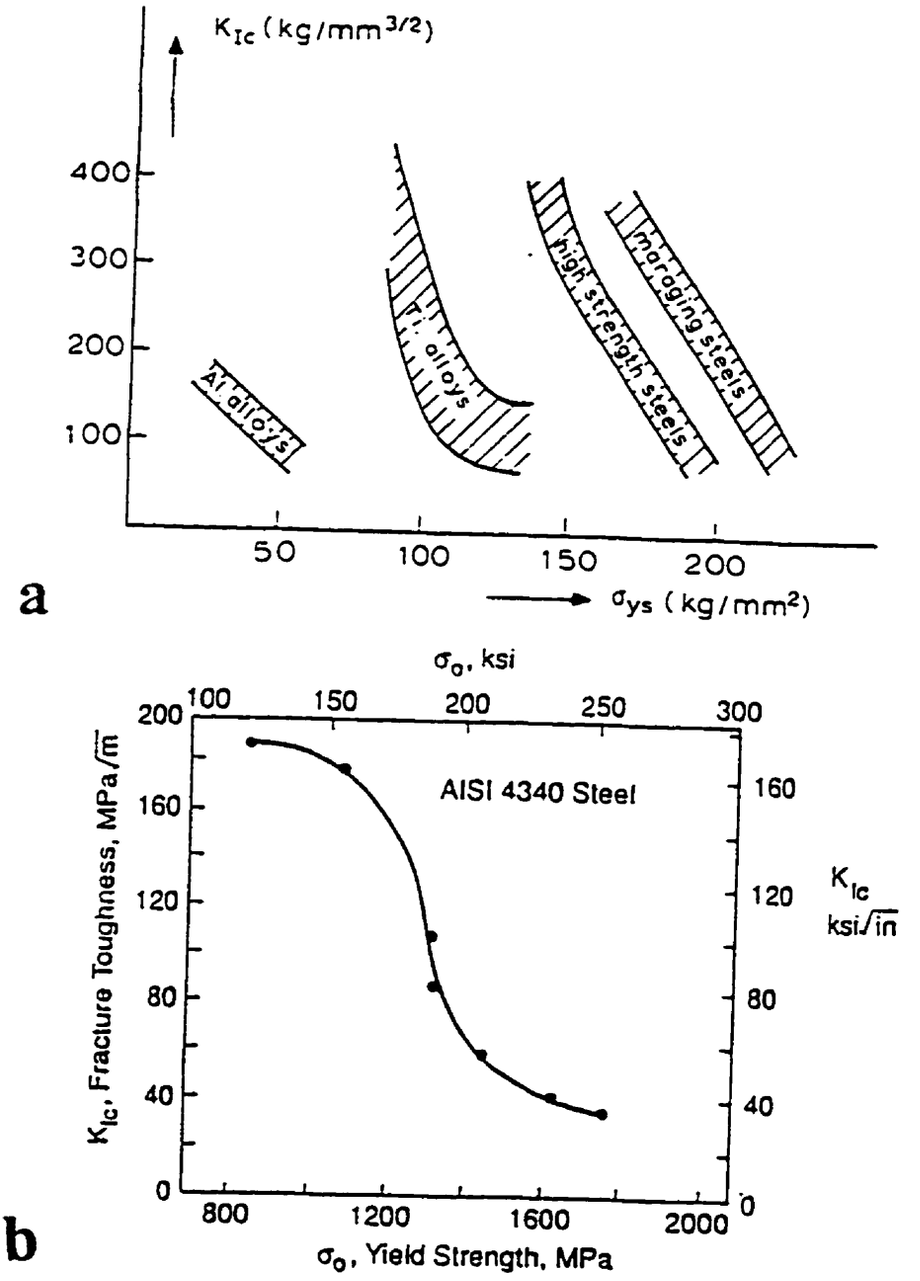

Figure 4.6 (a) Fracture toughness as a function of yield strength [108]. (b) Fracture toughness vs. yield strength for *AISI* 4340 steel quenched and tempered to various strength levels [107].

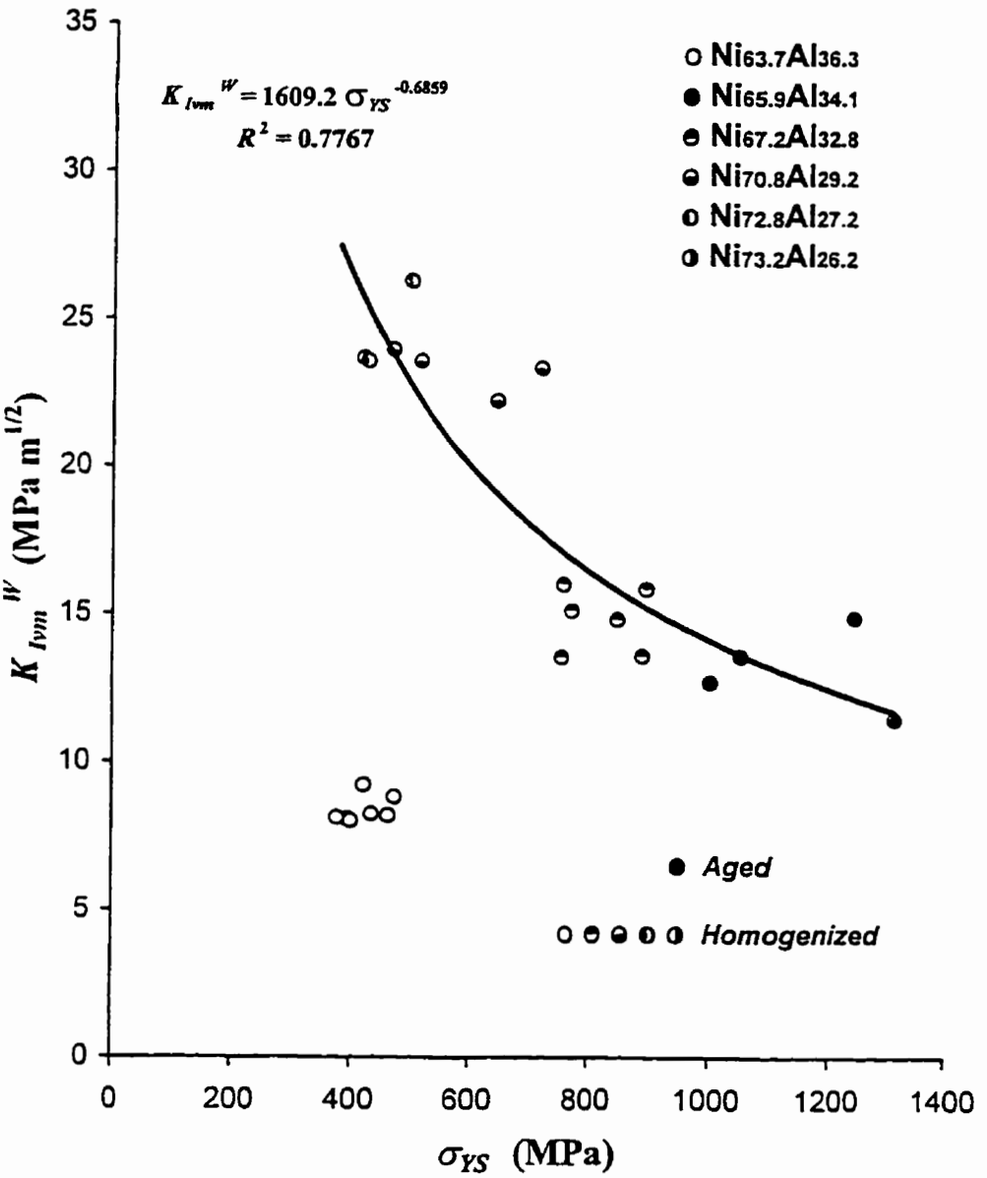

Figure 4.7 The valid $K_{Ivm}{}^{W}$ as a function of the yield strength for the boron-free, in-situ composites. The solid symbols show the aged alloy of $Ni_{65.9}Al_{34.1}$ and the open ones designate the homogenized alloys.

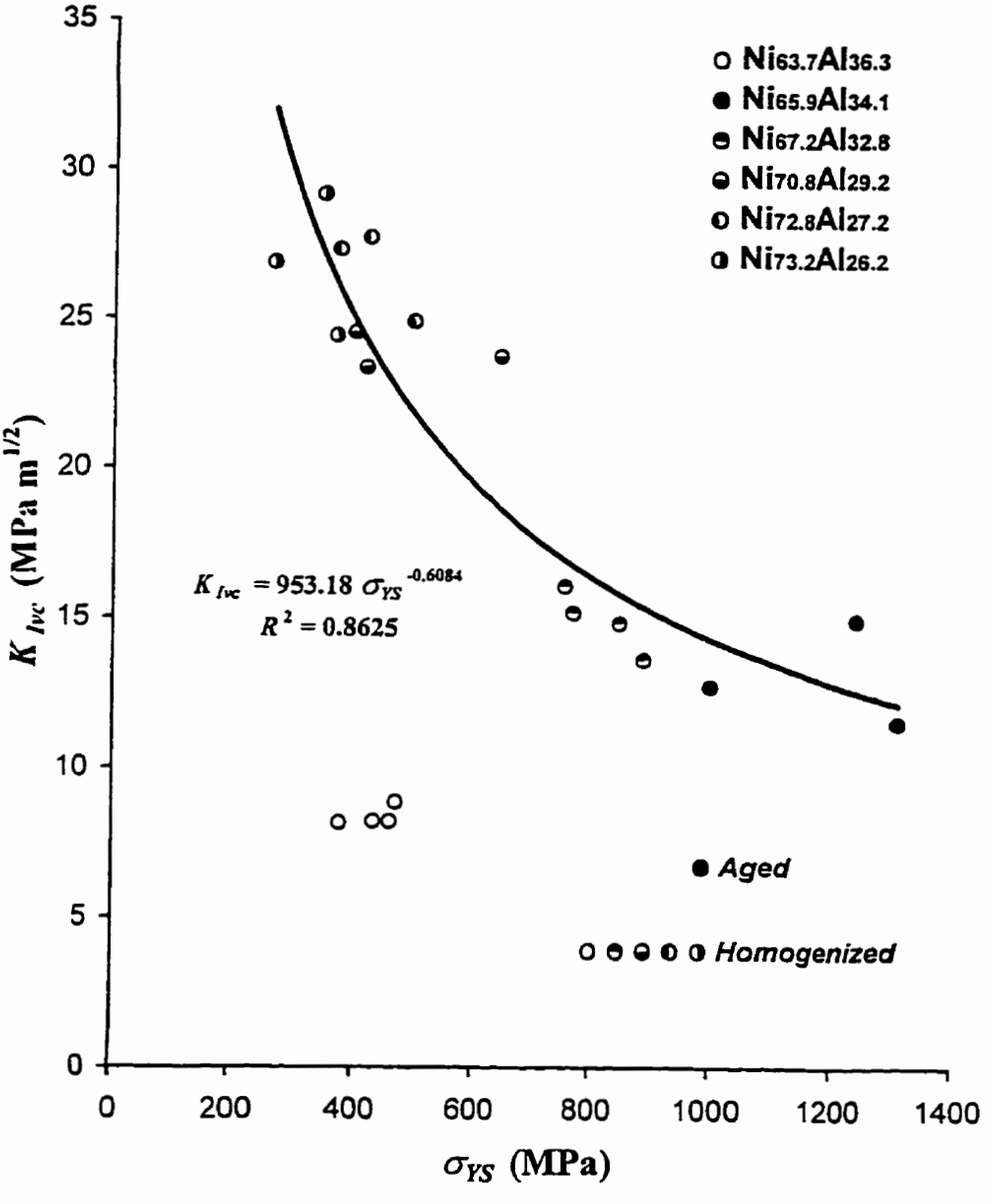

Figure 4.8 The valid K_{Ivc} as a function of the yield strength for the boron-free, in-situ composites. The solid symbols show the aged alloy of $Ni_{65.9}Al_{34.1}$ and the unsolid ones designate the homogenized alloys.

4.5 Engineering Implications-the Weakest Link Theory

The weakest link theory (*WLT*) originally proposed by Weibull [150, 151] was conventionally used to explain the large strength variation of ceramics by many researchers. Recently, Rogers et al. [152] first applied it for the analysis of fracture toughness results of fully lamellar γ-based titanium aluminides.

The *WLT* or so called Weibull analysis, assumes that the failure of the weakest element among all the elements which comprise an isotropic and statistically homogeneous component would cause the whole component to fail. The most important parameter in the *WLT* is Weibull modulus (m). For fracture toughness the parameter m can be obtained as the slope of a $lnln[1/(1-F)]$ versus lnK_{Ic} curve, where F represents a probability of failure. A high m value gives a narrow fracture-toughness range and little scatter, i.e. a high fracture reliability. Conversely, a low m value means a large scatter in fracture toughness. The function of m is somehow similar to that of the standard deviation or root mean square deviation from a normal distribution. The only difference is that when the standard deviation or root mean square deviation is large, the scatter of the properties is large and when the standard deviation or root mean square deviation is small, the variation of the properties is also small.

In the *WLT*, F is defined as follows [150, 151],

$$F \approx n/(1+N) \tag{4.5}$$

where n is the ordered data to rank the values of K_{Ic} from the small value to the large value, N

is the total number of the values.

The results of Weibull analysis on each in-situ composite are summarized in **Table 4.3** in detail. The three pairs of typical examples are shown in **Figures 4.9** to **4.11**. In particular, it is very interesting to note that the values of m=23.8 and m=5.8 are obtained for $Ni_{63.7}Al_{36.3}$ with lower fracture toughness ($K_{Ivm}^{W} \approx$ 8.7 MPa$\sqrt{m}$) and $Ni_{73.2}Al_{26.8}$ with a higher value of $K_{Ivm}^{W} \approx$ 23.6 MPa$\sqrt{m}$, respectively. The obtained results of m indicate that:

(1) The alloys $Ni_{63.7}Al_{36.3}$, $Ni_{67.2}Al_{32.8}$, $Ni_{70.8}Al_{29.2}$ and $Ni_{72.8}Al_{27.2}$ are very reliable materials for engineering design even $Ni_{63.7}Al_{36.3}$ with a lower value of average fracture toughness;

(2) The alloys $Ni_{65.9}Al_{34.1}$ and $Ni_{73.2}Al_{26.8}$ exhibit rather low Weibull modulus (m=5-9). This means that the fracture toughness values of these alloys are highly variable and no single value for K_{Ivm}^{W} can be assigned easily. This has very important implications for engineering design with these in-situ composites since safety factors will have to be high due to the uncertainty in the K_{Ivm}^{W}.

There is no microstructrual indication to explain such a difference in behaviour of these alloys.

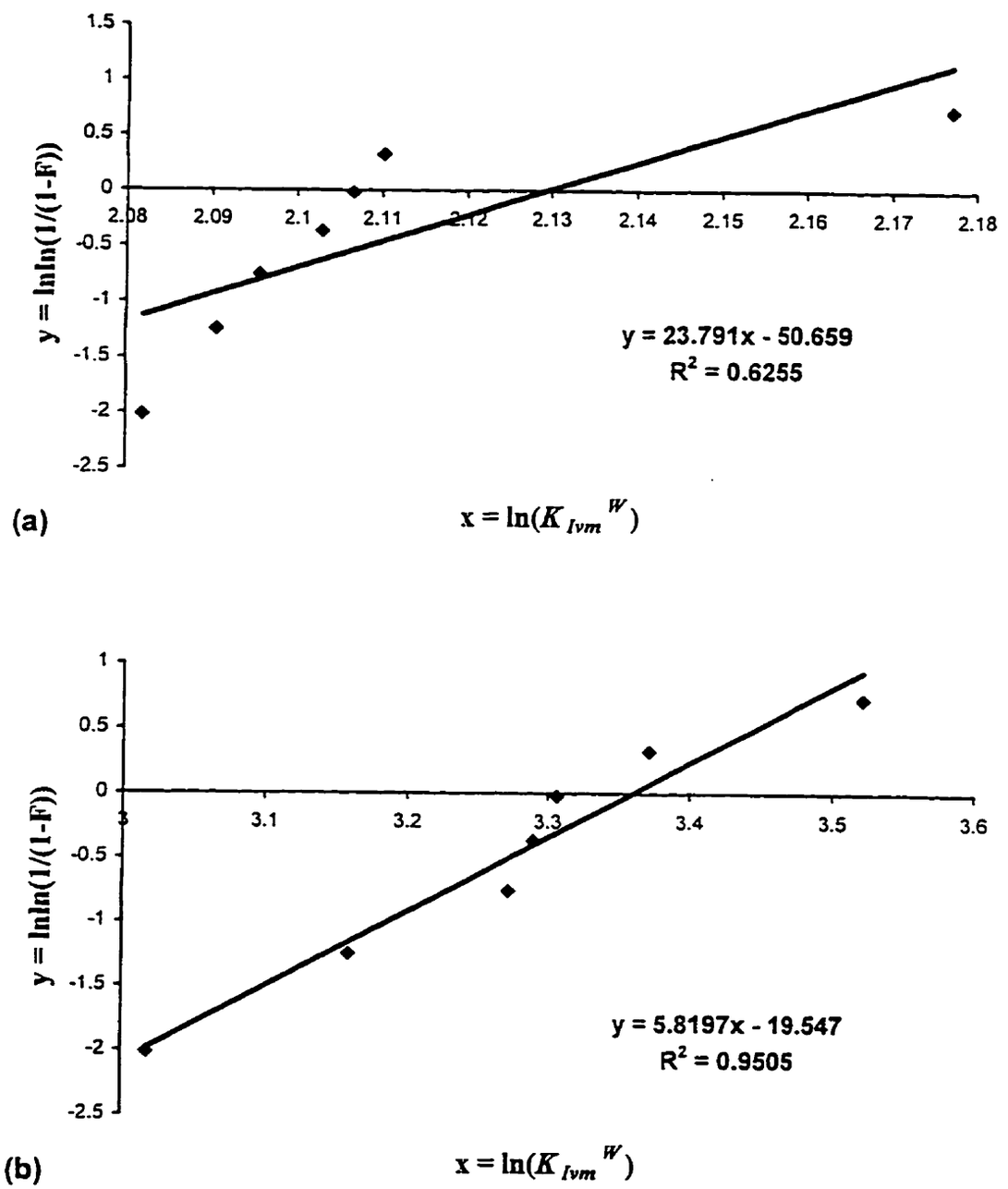

Figure 4.9 Two typical examples of Weibull analysis on the investigated boron-free in-situ composites: (a) $Ni_{63.7}Al_{36.3}$, and (b) $Ni_{73.2}Al_{26.8}$.

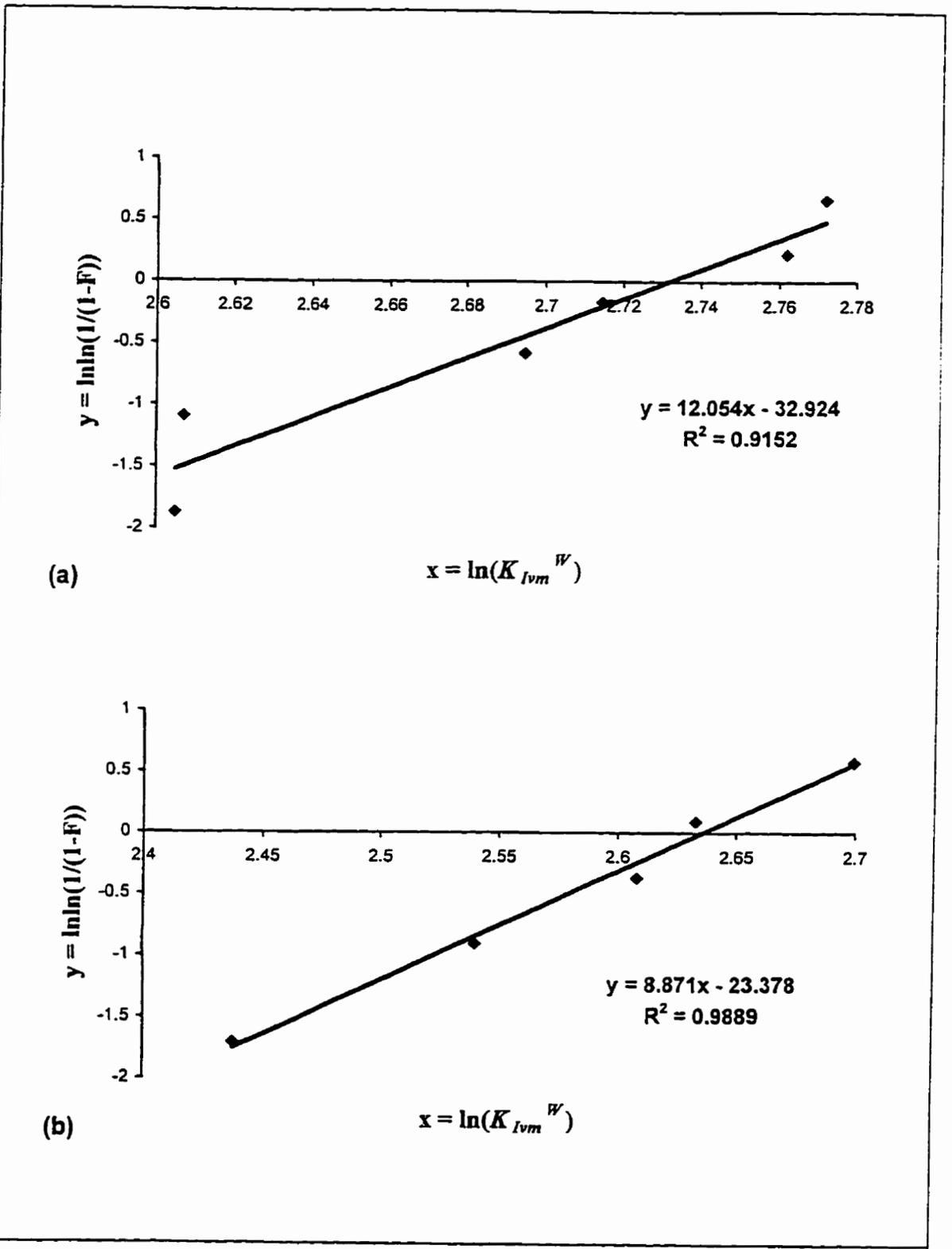

Figure 4.10 Two typical examples of Weibull analysis on the investigated boron-free in-situ composites: (a) $Ni_{67.2}Al_{32.8}$, and (b) $Ni_{65.9}Al_{34.1}$.

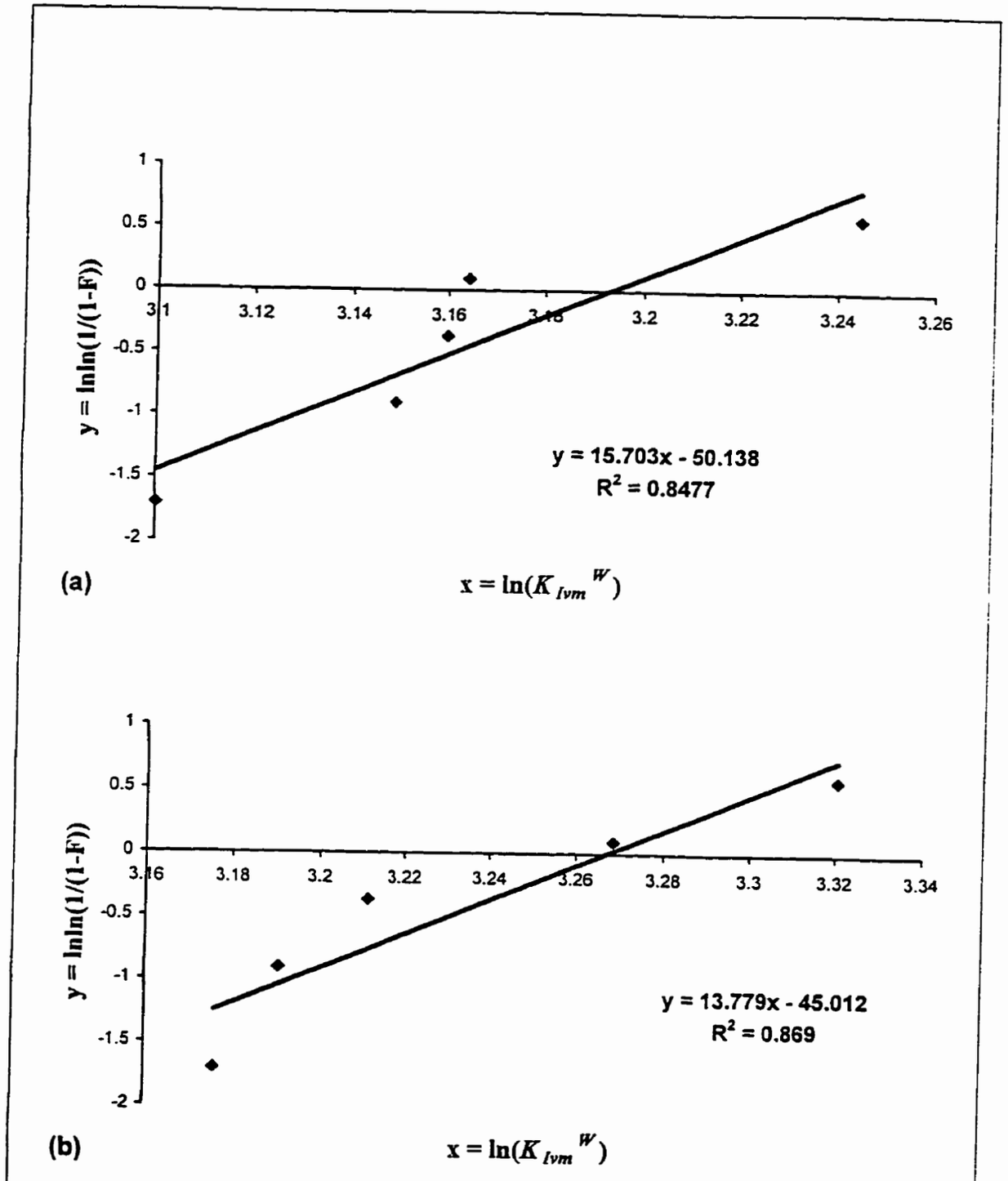

Figure 4.11 Two typical examples of Weibull analysis on the investigated boron-free in-situ composites: (a) $Ni_{70.8}Al_{29.2}$, and (b) $Ni_{72.8}Al_{27.2}$.

Table 4.3 Weibull analysis on each boron-free, in-situ composite.

			$Ni_{63.7}Al_{36.3}$ (m=23.8)			$Ni_{73.2}Al_{26.8}$ (m=5.8)		
n	N	n/(N+1)	K_{Ivm}^{W}	$\ln(K_{Ivm}^{W})$	lnln(1/(1-F))	K_{Ivm}^{W}	$\ln(K_{Ivm}^{W})$	lnln(1/(1-F))
1	7	0.125	8.02	2.081938	-2.013419	20.44	3.017494	-2.013419
2	7	0.25	8.09	2.090629	-1.245899	23.56	3.15955	-1.245899
3	7	0.375	8.13	2.095561	-0.755015	26.37	3.272227	-0.755015
4	7	0.5	8.19	2.102914	-0.366513	26.84	3.289893	-0.366513
5	7	0.625	8.22	2.10657	-0.019357	27.28	3.306154	-0.019357
6	7	0.75	8.25	2.110213	0.3266343	29.1	3.370738	0.3266343
7	7	0.875	8.82	2.177022	0.7320994	33.81	3.520757	0.7320994
			$Ni_{65.9}Al_{34.1}$ (m=8.9)			$Ni_{70.8}Al_{29.2}$ (m=15.8)		
n	N	n/(N+1)	K_{Ivm}^{W}	$\ln(K_{Ivm}^{W})$	lnln(1/(1-F))	K_{Ivm}^{W}	$\ln(K_{Ivm}^{W})$	lnln(1/(1-F))
1	5	0.16667	11.45	2.43799	-1.701983	22.2	3.100092	-1.701983
2	5	0.33333	12.68	2.540026	-0.90272	23.32	3.149311	-0.90272
3	5	0.5	13.57	2.607861	-0.366513	23.57	3.159975	-0.366513
4	5	0.66667	13.91	2.632608	0.0940478	23.67	3.164208	0.0940478
5	5	0.83333	14.87	2.699346	0.5831981	25.65	3.244544	0.5831981
			$Ni_{67.2}Al_{32.8}$ (m=12.1)					
n	N	n/(N+1)	K_{Ivm}^{W}	$\ln(K_{Ivm}^{W})$	lnln(1/(1-F))			
1	6	0.14286	13.53	2.604909	-1.869825			
2	6	0.28571	13.56	2.607124	-1.08924			
3	6	0.42857	14.8	2.694627	-0.580505			
4	6	0.57143	15.1	2.714695	-0.165703			
5	6	0.71429	15.83	2.761907	0.2253515			
6	6	0.85714	15.99	2.771964	0.6657298			
			$Ni_{72.8}Al_{27.2}$ (m=13.8)					
n	N	n/(N+1)	K_{Ivm}^{W}	$\ln(K_{Ivm}^{W})$	lnln(1/(1-F))			
1	5	0.16667	23.95	3.175968	-1.701983			
2	5	0.33333	24.31	3.190888	-0.90272			
3	5	0.5	24.81	3.211247	-0.366513			
4	5	0.66667	26.27	3.268428	0.0940478			
5	5	0.83333	27.67	3.320349	0.5831981			

4.6 The Influence of the Boron-Doping on the Fracture Toughness of the In-Situ Composites

As shown in **Figures 3.17** and **3.18**, in the boron-doped in-situ composites the fracture mode of Ni_3Al was not changed from intergranular failure to transgranular tearing as reported by Rigney and Lewandowski [81]. That is why the fracture toughness values (≈25 MPa) obtained from the boron-doped in-situ composites are almost equal to the ones (≈ 24 MPa) obtained from the boron-free in-situ composites (**Appendices E** and **G**).

Comparing the micrographs of the boron-free $Ni_{77.3}Al_{22.7}$ alloy (**Figures 3.6a** and **3.7a**) with the boron-doped in-situ composites of $Ni_{73.2}Al_{26.6}B_{0.2}$ and $Ni_{74.8}Al_{24.8}B_{0.4}$ (**Figures 3.6b** and **3.7b**), much less grain-boundary cracking can be seen for the water-quenched, 0.2 at.% boron-doped alloy (**Figure 3.6b**) and no grain-boundary cracking can be observed for Vickers indentation fracture testing under the highest load (2000g) on the 0.4 at.% boron-doped in-situ composites as shown in **Figure 3.7b**. The obtained results indicate that boron doping seems to be beneficial for the grain-boundary cohesion of polycrystalline Ni_3Al, which agrees with the work by Liu et al. [82, 110, 113]. In their research [82, 110, 113], due to boron addition (≈0.2 at.%) the ductility increases dramatically for the boron-doped Ni_3Al with less than 25 at.% Al. This is because boron is less electronegative with respect to the base metals of Ni and Al. Therefore, boron would share electrons with the metal atoms rather than draw charge off them and thus enhance bonding in the grain boundary of monolithic Ni_3Al.

However, the fractographs (**Figures 3.17** and **3.18**) and fracture toughness results (**Figure**

4.12) in this research indicated that the fracture toughness of Ni_3Al as shown in **Figure 4.12**, seems to be insensitive to boron addition. This might be because boron addition did not change the fracture mode of Ni_3Al from intergranular to transgranular as shown in **Figures 3.17** and **3.18**. The obtained results are obviously contrary to the recent results obtained by Rigney and Lewandowski [81, 115] and Liu et al. [82, 110, 113]. In their work [81, 115], 0.2 at.% boron doping raised the toughness value of monolithic Ni_3Al from 20 MPa$\sqrt{m}$ to 30 MPa$\sqrt{m}$ and the load-displacement curve showed much higher plastic deformation (**Figure 4.13a**) than that from Ni_3Al. Furthermore, Liu et al. [82] found that ductility increases dramatically and fracture mode changes from intergranular to transgranular due to boron doping (**Figure 4.13b**).

However, **Table 3.3** shows that the Ni3Al matrix in boron-doped alloys contain 24.9 at.% Al and 24.6 at.% Al for 0.2 at.% B and 0.4 at.% B, respectively. These Al contents are relatively high being close to a border-line content of 25 at.% Al. It is well-known [153] that Al contents much lower than 25 at.% are needed for full ductilizing effect of boron.

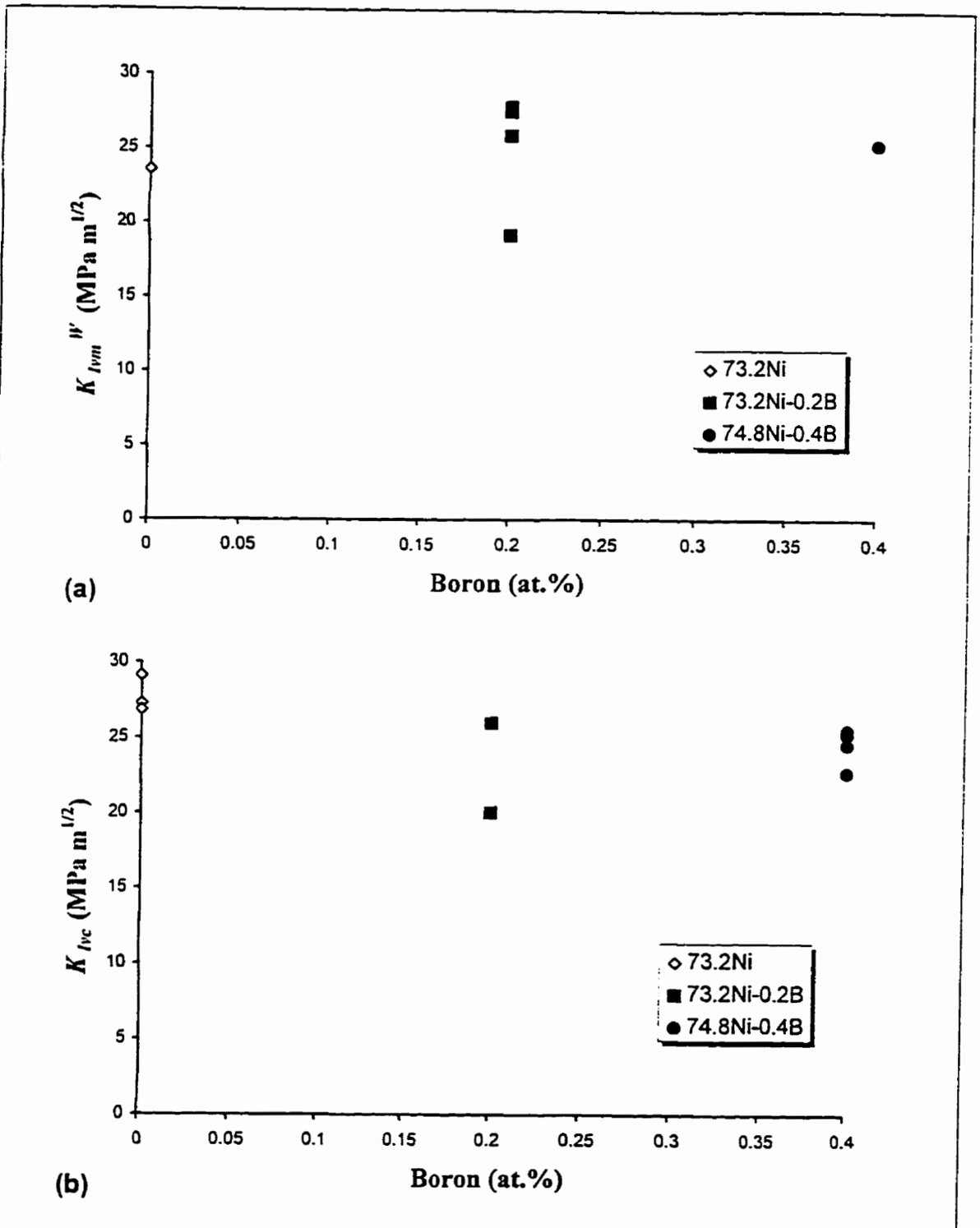

Figure 4.12 The dependence of (a) the valid $K_{Ivm}{}^{W}$ and (b) K_{Ivc} values on the boron content.

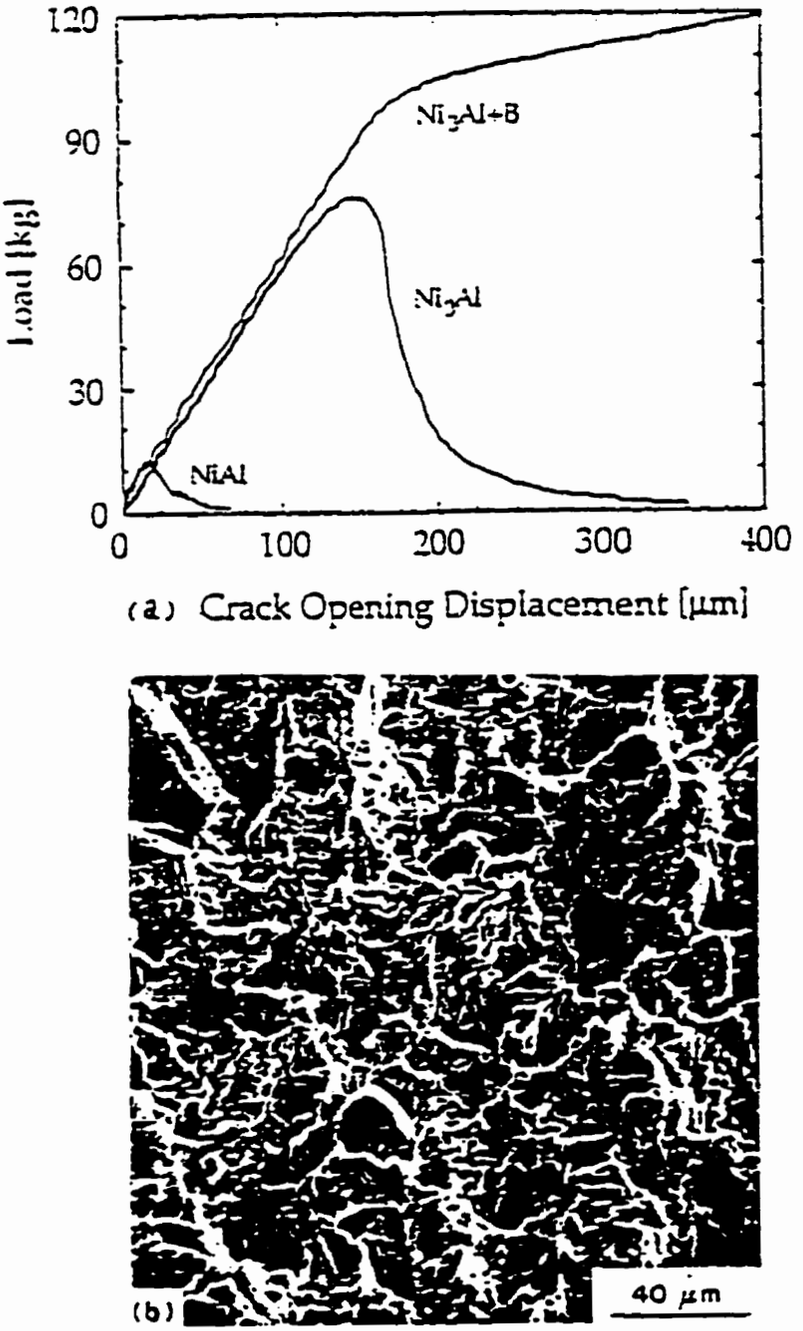

Figure 4.13 (a) Typical load-crack opening displacement toughness test traces for monolithic materials [81, 115]. (b) SEM fractographs of Ni_3Al doped with 0.05 wt.% B, showing tensile fractured surface of 24 at.% Al [82].

4.7 Work-of-Fracture and Apparent Fracture Toughness

In this research, critical stress intensity factors were also calculated from the work of fracture analyses performed simultaneously on the same specimen. This involved measuring the area under the load-load line displacement curve of an in-situ composite beam through integration and dividing by the total, projected area of the specimen to obtain the effective surface energy or "work of fracture", γ_{WOF}, as described by *Eq.(2.42)*. The designation of apparent fracture toughness [120] (or so called average fracture toughness in some references [154]) K_{WOF} is used to denote the work of fracture critical stress intensity factor in order to avoid confusion with the maximum load derived parameters, K_{Ivm} or the *J*-integral obtained values, K_{Ivc}.

Figure 4.14 shows a plot of apparent fracture toughness K_{WOF} and the valid $K_{Ivm}{}^{W}$ versus volume fraction of the ductile Ni_3Al phase (V_d) for the boron-free in-situ composites. It is worth noting that for every composite, $K_{WOF} > K_{Ivm}{}^{W}$, and that the magnitude of the separation becomes larger with increasing V_d. This is in very good agreement with the results obtained from the polymeric sintered Ni/α-Al_2O_3 composites [154]. It was found that there is an increasing separation between K_{WOF} and $K_{Ivm}{}^{W}$ with increasing content of Ni in the Ni/α-Al_2O_3 composite [154]. This separation between K_{WOF} and $K_{Ivm}{}^{W}$ clearly indicates that the energy consumed by the non-linear fracture processes of the in-situ composite is too large and the apparent fracture toughness K_{WOF} cannot be used to predict the *LEFM* K_{Ic}. However, because the plastic deformation increased with increasing volume fraction of the ductile Ni_3Al phase,

the non-linear fracture would cause a separation of the K_{WOF} and $K_{Im}{}^{W}$ since the two distinct stress intensity factors are probing different critical crack lengths (i.e. different regimes of beam failure) [120, 154]. This feature can be explained in the following.

In relation to this work, in the case of maximum load derived stress intensity factor, K_{Im}, primarily the early portion of the K_{Im} - Δa is being probed. This is because the maximum loads in the load/load line displacement plots occur at relatively small displacements or critical crack extension when compared to the total displacement at beam failure. The work of fracture stress intensity factor, K_{WOF}, on the other hand, serves more as an average fracture toughness in relation to the overall fracture resistance curve since its determination relies on integration of the entire load/load line displacement curve from start to finish. Furthermore, due to the unique geometry of the chevron notches (i.e. the crack encounters more and more material as it progresses), this "average" fracture toughness is also weighted in favour of the larger crack lengths.

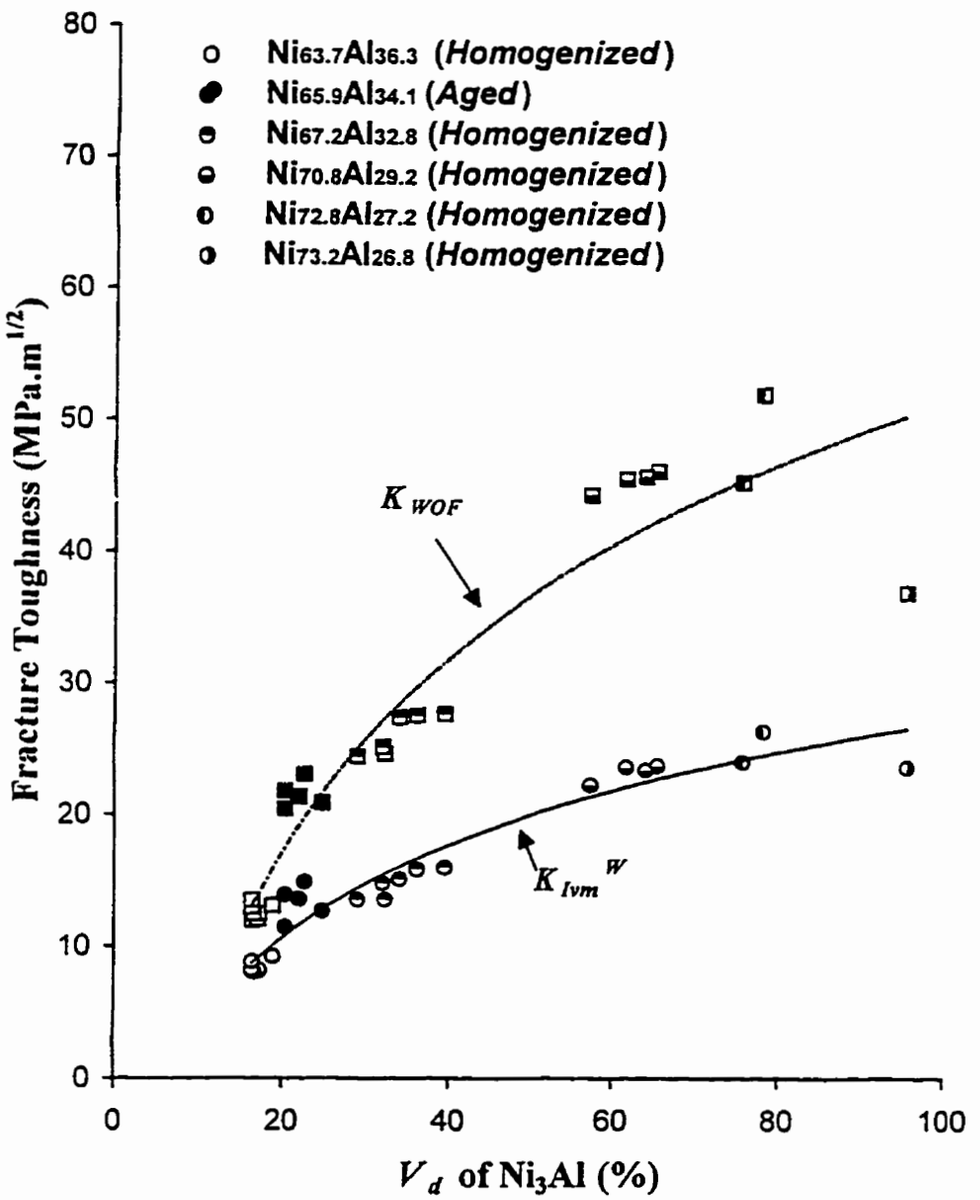

Figure 4.14 A comparison of the apparent fracture toughness K_{WOF} and valid $K_{Ivm}{}^{W}$ versus volume fraction of ductile Ni_3Al phase for the boron-free in-situ composites. The solid symbols show the aged alloy of $Ni_{65.9}Al_{34.1}$ and the void ones designate the homogenized alloys.

4.8 The Unique Features of K-Δa and J-Δa Curves for a *CNB* Bending Test

The important characterizations of the fracture resistance K-Δa and J-Δa curves derived from a J-integral method by a chevron-notch-beam (*CNB*) bending test could be observed in **Figure 3.28c**, **Appendices F1 (c)** thro **F8 (c)** and **Figure 3.29c**, **Appendices F1 (f)** thro **F8 (f)**, respectively, and summarized as follows:

1. As shown in **Figure 3.28c** and **Appendices F1 (c)** thro **F8 (c)**, the stress intensity factor K decreases with increasing crack extension Δa and besides, a PLATEAU usually appears right up to the critical crack extension Δa_m.

The fracture energy J decreases with increasing crack extension Δa only until the critical crack extension Δa_m, then starts to increase with increasing crack extension, forming a very special shape which can be called "HOOP HEAD" as shown in **Figure 3.29c** and **Appendices F1 (f)** thro **F8 (f)**. It is very interesting to note that this feature is distinct from the conventional power-law regression curve of J-Δa defined by *ASTM* Standard *E 813-89* [99] as shown in **Figure 2.13d**. Particularly, a critical value (J_{Ivc}) of the fracture energy for a CNB test can be now simply calculated by a horizontal line tangent to the "hoop head", i.e., a minimum value of J. It has to be pointed out that the above important features of K-Δa and J-Δa curves from a J-integral method for a *CNB* test has never been found in any other references so far up to best of author's knowledge.

To elucidate the main reasons for such special characterizations as pointed out above, it is

essential to consider the parameters P and Y^* because the stress intensity factor K and the fracture energy J are directly calculated from the product of the applied load P and the stress intensity factor coefficients Y^*. As discussed in Chapter 2, the stress intensity factor K and the fracture energy J are calculated from

$$K = PY^*/(B\sqrt{W}) \tag{4-6}$$

and

$$J = (PY^*)^2(1-\nu^2)/(B^2WE)+4A/[B(2W-a_1-a_0)] \tag{4-7}$$

respectively. Where, Y^* is calculated from *Eq.(2.25)* for a CNB specimen and $Y^* = f(a/W)/W$ [97] for a single-edge-straight-through (*SEST*) specimen. Therefore, the three important features as mentioned above are actually resulting form the following:

(1) The load-load line displacement (*P-LLD*) curves as shown in **Figures 3.21** thro **3.24**) start from zero, but the load-crack extension (P-Δa) curves (**Figure 3.28a** and **Appendix F (a)**) start from a load value much higher than zero, which corresponds to the end of elastic portion (straight line) of the *P-LLD* curve. This difference between the curves of *P-LLD* and P-Δa arises because the precrack in a *CNB* specimen can begin a stable growth only under a certain applied load, which is usually beyond the maximum elastic load on the *P-LLD* curve.

(2) When crack-length-to-width-ratio equals to a_0/W (i.e. Δa_0=0), $Y^* = \infty$ for a *CNB* specimen (a solid line as shown in **Figure 2.11**), however, $Y^* = f(a_0/W)/W$ for a *SEST* specimen (a dashed line as shown in **Figure 2.11**). This difference of the normalized stress-intensity factor coefficients (Y^*) between *CNB* and *SEST* specimens comes from the *CNB*'s and *SEST*'s configurations as shown in **Figure 2.11**. The detailed derivations for $Y^* = f(\Delta a)$ can be seen in Section 2.2.3 and references [97, 121-122,

126, 132-133].

Due to a peculiar shape of $Y^* = f(\Delta a)$ and P-Δa curves for a *CNB* specimen, *Eqs.(4.6)* and *(4.7)*, either a K-Δa or J-Δa curve would obviously not start from zero but a *K-LLD* or *J-LLD* curve would start from zero. In addition, a fracture resistance curve of either K-Δa or J-Δa for a *CNB* specimen would start from INFINITY rather than from a certain value (**Figure 1.2**) or zero (**Figure 2.13d**). In other words, the conventional fracture resistance curve of either K-Δa or J-Δa as schematically shown in **Figure 1.2** or **Figure 2.13d** is only suitable for any other specimen's geometries such as a single-edge-straight-through (*SEST*) specimens, but not for a *CNB* specimen.

Similarly, a PLATEAU in a K-Δa curve (**Figure 3.28c** and **Appendices F1 (c)** thro **F8 (c)**), or a flat bottom "HOOP HEAD" in a J-Δa curve (**Figure 3.29c** and **Appendices F1 (f)** thro **F8 (f)**), also results from a flat bottom Y^*-Δa curve (**Figure 3.28b** and **Appendices F1 (b)** thro **F8 (b)**).

4.9 Methodology of the Assessment of the Relationship between *LLD* and Δa

In this research crack extension Δa was not measured directly because of substantial experimental difficulties. Therefore, the load-crack extension (P-Δa) curves (**Figure 3.28a** and **Appendices F1 (a)** thro **F8 (a)**) were actually obtained from the experimental load-load line displacement (*P-LLD*) curves (**Figures 3.21** thro **3.24**) using three well-known points from the

P-LLD curve. In order to further elucidate the fundamental relationship between load-load line displacement *LLD* and crack extension Δa for a tested specimen, the technique used in this work can be summarised in more detail as follows:

Defining three pairs of points between the *P-LLD* and *P-*Δa curves:

Point 1 is crack extension starting point: (LLD_0, P_0), which is the end of the straight line portion (elastic) of the *P-LLD* curve in **Figures 3.21** thro **3.24**, and (Δa_0, P_0), where $\Delta a_0 = 0$;

Point 2 is maximum load point: (LLD_m, P_m) and (Δa_m, P_m), where Δa_m is calculated from *Eq.(2.25)*;

Point 3 is maximum extension point: (LLD_W, P_W), where LLD_W is the load line displacement taken at the load $P_W = 0$, and (Δa_W, P_W), where $\Delta a_W = W - a_0$, and W is the width of a *CNB* specimen.

Since a constant and very low cross-head speed of 0.05 mm/min (as pointed in Section 2.4) was used in the three-point bend test, a smoothly increasing *P-LLD* curve would be seen at the first stable section just after linear portion of the *P-LLD* curve. Therefore, the crack extension starting point of (LLD_0, P_0) can be found directly from the *P-LLD* curve because the *P-LLD* curve would show a pop-in phenomena, i.e., the applied load P would stop to increase suddenly when crack extension starts (**Figures 3.21** thro **3.24**). This is because the resistance stress in the bending specimen would not keep a balance with increasingly applied load since crack extension occurs suddenly.

The maximum load point of (LLD_m, P_m) and maximum extension point of (LLD_W, P_W) can be easily obtained from the highest point and the last point on the *P-LLD* curve, respectively.

Thereafter, the corresponding extension value of Δa_m can be calculated correspondingly from the minimum stress intensity factor coefficient of Y^*_m by *Eq.(2.25)*. This is because when the applied load reaches its maximum value of P_m, the stress intensity factor coefficient Y^* would decrease to its minimum value of Y^*_m and the corresponding crack extension Δa could be defined as Δa_m if the crack growth resistance curve of the tested material is flat [126, 133]. This assumption would be also true when the bottom part of stress intensity factor coefficient Y^* of are flat (**Figure 3.28b** and **Appendices F1 (b)** thro **F8 (b)**) because the fracture toughness value of K_{Im} would not be sensitive to Δa_m.

Connecting the three points on the *LLD*-Δa curve - simple linear assumption:

The two straight lines to connect point 1 (LLD_0, Δa_0) to point 2 (LLD_m, Δa_m), then to point 3 (LLD_W, Δa_W) are schematically shown in **Figure 4.15**. The two lines can be mathematically expressed as following:

$$\text{For } 0 \le \Delta a \le \Delta a_m: \qquad LLD = (LLD_m - LLD_0)\Delta a/\Delta a_m + LLD_0 \tag{4.8}$$

$$\text{For } \Delta a_m \le \Delta a \le \Delta a_W: \quad LLD = (LLD_m - LLD_W)(\Delta a - \Delta a_m)/(\Delta a_m - \Delta a_W) + LLD_m \tag{4.9}$$

These lines are made actually based on such an assumption that the crack extension Δa has the same average speed as the load-line-displacement (*LLD*) during bending. This assumption is true for a medium ductile material. In other word, a curved assumption could be more accurate for a material with different speed between load-line-displacement *LLD* and crack

extension Δa. For instance, crack extension could be much faster than load-line-displacement in a movement for a brittle material.

Calculating more data points according to the linear *LLD*-Δa curve

To obtain accurate shape of the parameters (*P*, *K*, *J*) vs. Δa curves, more data points must be calculated according to the *LLD*-Δa curve. According to *Eqs.(4.8)* and *(4.9)*, the inserting values (usually 6 (or 7) and 9 (or 10) points inserted between point 1 to 2 and point 2 to 3, respectively, as shown in **Figure 3.27**) can be calculated by the following formulas:

$$\text{For } 0 \le \Delta a \le \Delta a_m: \qquad LLD_i = (LLD_m - LLD_0)\Delta a_i / \Delta a_m + LLD_0 \tag{4.10}$$

$$\text{For } \Delta a_m \le \Delta a \le \Delta a_W: \qquad LLD_i = (LLD_m - LLD_W)(\Delta a_i - \Delta a_m)/(\Delta a_m - \Delta a_W) + LLD_m \tag{4.11}$$

where i = 1,..., n.

From the discussion above, it can be seen that the corresponding technique is very simple, useful and reliable method to overcome the difficulty of measuring crack extension directly in an experiment. Obviously, the patent to such an advanced approach should be applied soon.

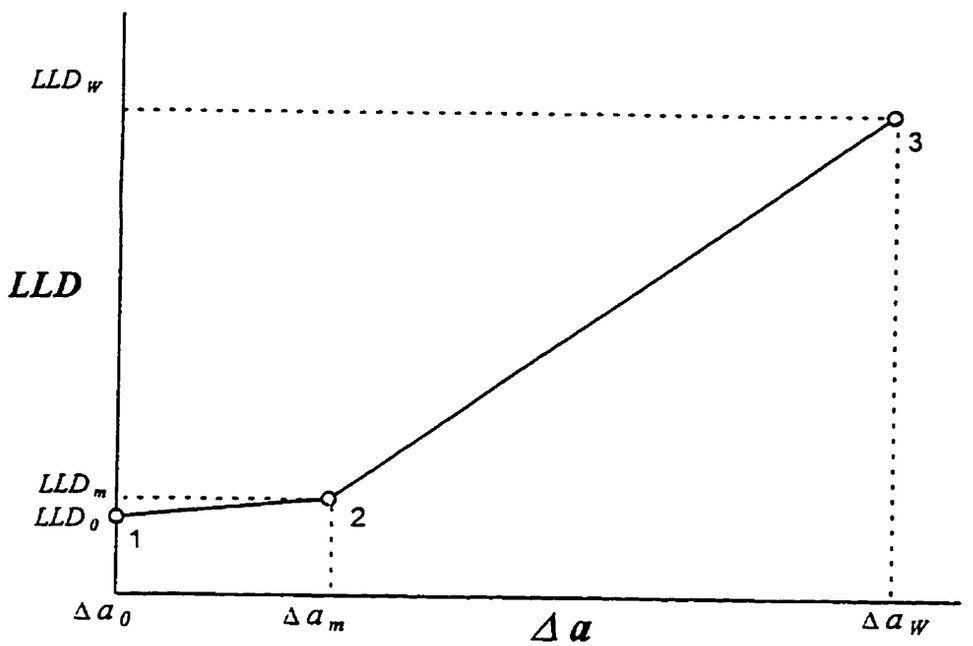

Figure 4.15 A schematic showing the fundamental relationship between load-load line displacement *LLD* and crack extension Δa.

4.10 Future Research

The first area for future research is an effort to improve the *J*-integral method for a chevron notched bend specimen test:

1. Validity of K_{Ivc} and J_{Ivc} :

In this research, the fracture toughness values of K_{Ivc} were calculated from J_{Ivc} by *Eq.(2.46)* and confirmed by the agreement with fracture toughness values of the valid K_{Ivm}^{W} rather than any validity requirement. The values of J_{Ivc} were obtained automatically from lines tangent to the "hoop head" of the J-Δa. The experimental values of J_{Ivc} and K_{Ivc} (K_{Ivm}^{W}) were validated using *Eqs.(2.20)* and *(2.40)*, respectively. These requirements might not be good enough for validity of K_{Ivc} and J_{Ivc} in a formal *ASTM* Standard document of the *J*-integral method for a *CNB* bend test. Some additional validity requirements such as validation of J_Q as J_{Ivc} might be necessary by analogy with *ASTM* Standard document [99] for a *CNB* specimen. In addition, the critical unloading slope ratio (r_c) as described in *ASTM* Standard document [98] or the value of plasticity p [98, 122] as shown in **Figure 4.16** might be also needed to be considered for such an unloading/reloading *J*-integral method used in this research. Limited by the difficulty to obtain the critical unloading slope ratio (r_c) and theoretical confirming of $K_{Ic} = [(1+p)/(1-p)]^{1/2}K_Q$ [122], the parameter r_c or p was not considered in this research.

2. Experimentally establishing the relationship between a real compliance from unloading/reloading a load-load line displacement curve and a geometry compliance from

Eq.(2.33) for the same *CNB* bend specimen:

In this research, a compliance from unloading/reloading the load-load line displacement curve is approximately at least ten times greater than the compliance calculated from *Eq.(2.33)* for the same *CNB* bend specimen for all the investigated in-situ composites. The reason why the two compliances are not equal to each other at the mean time, is unclear. The establishment of the experimental relationship between these two compliances might be necessary;

Other areas for the toughening mechanisms of the NiAl/Ni_3Al in-situ composites include:

1. Influence of grain size on fracture toughness:

   In this research, grain size effect of reinforcements and matrix on the in-situ composites are still not clear. An effort for a proper etching method of the in-situ composites might be essential;

2. Boron effect on Ni_3Al grain-boundary embrittlement:

In this research, the microscopy and surface indentation testing from the water-quenched alloys showed that boron looks beneficial for improving the Ni_3Al grain-boundary embrittlement because less grain boundary cracking for water-quenched alloys and no grain-boundary cracking under surface indentation were observed. However, the fractography and fracture toughness test from homogenized alloys indicated that boron appears no effect on the Ni_3Al grain-boundary embrittlement because no changes of fracture mode and toughness values for the alloys with or without boron addition. The reason for such contrary results is uncertain. An effort on confirming boron content in the in-situ composites by some advanced measuring technique looks necessary.

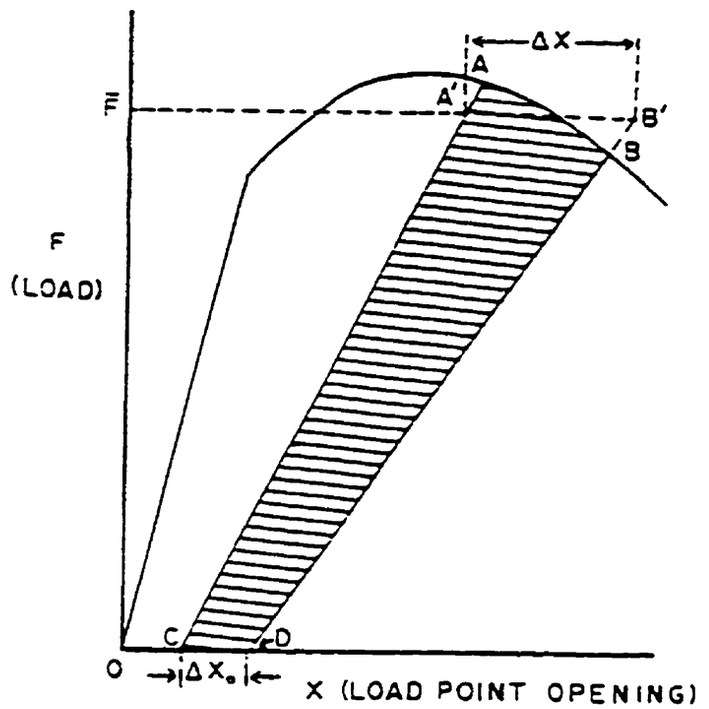

Figure 4.16 Schematic of a load-displacement illustrating the method of determining the plasticity, $p=\Delta x_0/\Delta x$ [122].

CHAPTER 5

SUMMARY

An overview of the toughening mechanisms in the intermetallic-base in-situ composites is presented. The toughening mechanisms and corresponding modelling formulas such as crack-tip blunting, crack trapping, microcrack renucleation, interface debonding, crack bridging, shear ligament toughening, crack deflection, microcrack shielding and so on have been discussed in detail.

The use of NiAl as a structural material has been hindered by its lack of tensile ductility or toughness at room temperature. The operative flow and fracture mechanisms in monolithic NiAl leading to these poor low temperature properties, demonstrate the need for ductile phase toughening. Based on the literature review and preliminary research, the two phase ($\beta + \gamma'$) region of Ni-Al system with and without boron adoption has been chosen as a model in-situ composite. This is because Ni_3Al is a good candidate for ductile phase toughening of NiAl since the two phase systems can be readily formed *in-situ* from the melt or by heat treatment.

The advantage for using Ni_3Al (γ') as a reinforcing second phase is its superior ductility and toughness compared to β-NiAl. A study of fracture toughness of the in-situ NiAl-Ni_3Al intermetallic composites is presented. The composition ranges investigated are 25-35 at.% Al for both as-solidified and as-heat-treated composites. Also, boron-doped (0.2 and 0.4 at.%) Ni_3Al is studied.

To evaluate fracture toughness, a non-linear fracture method such as *J*-integral unloading/reloading method, has been applied for the investigated in-situ composite. The method is based on a three point bending of chevron-notched specimens. Additionally, compression testing as well as Vickers microhardness testing are also used for the investigated composites.

The main results can be summarized as follows:

1. The volume fraction of ductile phase Ni_3Al increases with increasing Ni content in the investigated intermetallic composites under either the as-cast or as-annealed condition.
2. The volume fraction of ductile phase Ni_3Al of the as-cast composites increases after homogenization at 1000°C for 100h followed by a slow furnace cooling. The increment of the relatively more ductile γ' (Ni_3Al) phase by the heat treatment is an important means of modifying the local fracture processes in Ni-rich NiAl.
3. The grain boundary cracking was found for the boron-free Ni_3Al alloy after water quenching using Vickers indentation fracture testing under the highest load (2000g). Less grain boundary cracking was found for the boron-doped Ni_3Al alloy after both water quenching and Vickers indentations. The possible boron effect

might be attributed to boron increasing the grain boundary cohesive strength and allowing the deformation of grain interiors without premature intergranular failure. However, no effect was found on the fracture toughness of the in-situ composites.

4. The Orthorhombic D_{2h}^{19} Ni_5Al_3 in the aged alloy $Ni_{65.9}Al_{34.1}$ at 1000°C/100h + 550°C/100h both followed by a slow furnace cooling, was identified by X-ray analysis method.

5. The mat-like structure of fine particles of Ni_5Al_3 exhibits very high Vickers microhardness (≈690 kg/mm^2). The significant yield strength of =1151 MPa in $Ni_{65.9}Al_{34.1}$ in-situ composite is also contributed to this needle-like structure of Ni_3Al_5. It has to be pointed out that very high yield strength (≈1150MPa) and reasonable value of fracture toughness (≈13 MPa$\sqrt{m}$) of $Ni_{65.9}Al_{34.1}$ is a new promising alloy. To the contrary, this needle-like mat structure (Ni_5Al_3) is not embrittling to the alloy but is very beneficial for yield strength.

6. The brittle NiAl presents not much higher Vickers hardness of ≈400 kg/mm^2 than the ductile Ni_3Al phase (≈280 kg/mm^2) for both the as-cast and as-annealed composites. All of the Vickers hardness values for the investigated composites are almost independent on the load.

7. Delamination at interfaces of Ni_3Al and NiAl, crack bridging in the wake of Ni_3Al and crack-tip blunting are predominant toughening mechanisms in the in-situ composites.

8. The volume fraction of Ni_3Al in the in-situ composites has a significant effect on the fracture toughness. The valid K_{Im}^{W} and K_{Ic} values increase with increasing of

the volume fraction of ductile Ni_3Al phase in the boron-free in-situ composites. The power curve, describing exactly the relationship of $K_{Ivc}=f(V_d^n)$, is $K_{Ivc}=6.1+0.7V_d^{0.7}$.

9. All the values of the fracture toughness of the investigated in-situ composites are within the K_{max} and K_{min} models (or upper and lower bound) [63]. This behaviour experimentally conformed the *E*-modified *ROM* modes which was theoretically proposed by Ashby [63]. Furthermore, all the data are close to the upper bound (K_{max}), which is contrary to the results from the Nb-Si in-situ composites obtained by Davidson and Chan [61-62].

10. Weibull analysis was applied into the fracture toughness distribution of the investigated Ni_3Al/NiAl in-situ composites. Weibull's modulus m = 23.8 for $Ni_{63.7}Al_{36.3}$ indicates that this alloy is a very reliable material for engineering design even with lower fracture toughness value; however, $m \approx 7.0$ was also found in the in-situ composite of $Ni_{73.2}Al_{26.8}$. This means that the fracture toughness is highly variable and no single value for K_{Ivm} can be assigned easily.

11. A mixed transgranular-intergranular fracture mode was observed in most of the representative photographs of the boron-free and boron-doped in-situ composites. This behaviour is consistent with the results obtained by Rigney and Lewandowski [81].

12. The important characterizations of the K-Δa and J-Δa curves derived from a *J*-integral method by a chevron-notch-beam (*CNB*) bend test have been obtained first by this research. The stress intensity factor K decreases with increasing the crack

extension Δa and a PLATEAU usually appears right up to the critical crack extension Δa_m. The fracture energy J decreases with increasing of the crack extension Δa only until the critical crack extension Δa_m, then starts to increase with increasing of the crack extension, forming a very special shape which can be called "HOOP HEAD", which is obviously distinct from the conventional power-law regression curve of J-Δa defined by *ASTM* Standard *E 813-89* [99] as shown in **Figure 2.13d.**

13. Particularly, a critical value (J_{Ic}) of the fracture energy for a *CNB* test can be simply calculated by a horizontal line tangent to the "hoop head", i.e., a minimum value of J, which is much more simple than a blunting-line approach defined in *ASTM* Standard *E 813-89* [99].

14. In this research, a simple corresponding-insertion technique was successfully developed for exploring the fundamental relationship between load-load line displacement *LLD* and crack extension Δa. This advanced approach effectively solved the measuring problem caused by a small bend specimen.

REFERENCES

1. D.L. Anton and D.M.Shah, in "High-Temperature Ordered Intermetallic Alloys V", I. Baker, R. Darolia, J.D. Whittenberger and M.H. Yoo, eds., Mat. Res. Soc., Pittsburgh, Pennsylvania, 288(1993)141-150.
2. S. Reuss and H. Vehoff, in "Intermetallische Phasen Strukturwerkstoffe fur Hohe Temperaturen", ed. F.J. Bremer, Forschungszentrum Julich GmbH, (1991)65-73.
3. W.A. Kaysser, R. Laag, J.C. Murray and G.E. Petzow, Int. J. Power. Metall., 27(1991)43-49.
4. S.M. Russel, C. C. Law, M.J. Blackburn, P.C. Clapp, and D.M. Pease, "Lightweight disk alloy development", Report FR-19577-8, Pratt and Whitney, West Palm Beach. FL, 1989.
5. H. Vehoff, S. Reuß, W. Vogt and P. Specht, in "Structural Intermetallics", R. Darolia, J.J. Lewandowski, C.T. Liu, P.L. Martin, D.B. Miracle and M.V. Nathal, eds., The Minerals, Metals & Materials Society, (1993)657-663.
6. D.A. Hardwick, P.L. Martin, S.N. Patankar and J.J. Lewandowski, in "Structural Intermetallics", R. Darolia, J.J. Lewandowski, C.T. Liu, P.L. Martin, D.B. Miracle and M.V. Nathal, eds., the Minerals, Metals & Materials Society, (1993)665-674.
7. W.O. Soboyejo and S.M.L. Sastry, Mat. Sci. Eng., A171(1993)95-104.
8. K.S. Kumar, in "Structural Intermetallics", R. Darolia, J.J. Lewandowski, C.T. Liu, P.L. Martin, D.B. Miracle and M.V. Nathal, eds., The Minerals, Metals & Materials Society, (1993)87-96.
9. D. Banerjee, A.K. Gogia, T.K. Nandy, K.Muraleedharan and R.S. Mishra, in "Structural Intermetallics", R. Darolia, J.J. Lewandowski, C.T. Liu, P.L. Martin, D.B. Miracle and M.V. Nathal, eds., The Minerals, Metals & Materials Society, (1993)19-33.
10. L. Murugesh, K.T. Venkateswara Rao, and R.O. Ritchie, Scr. Metall. Mater., **29**(1993)1107-12.
11. H.E. Deve, A.G. Evans and D.S. Shih, Acta Metall. Mater., **40**(1992)1259-65.
12. S. Tsuyama, S. Mitao and K-N Minakawa, Mater. Sci. Eng., **A153**(1992)451-56.
13. K.S. Kumar, S.K. Mannan, and R.K. Viswanadham, Acta Metall., **40**(1992)1201-22.
14. K.S. Kumar, S.K. Mannan, J.D. Whittenberger, R.K. Viswanadham and L. Christodoulou, Final Report, MML TR 89-102 (C), Martin Marietta Corp., Baltimore. MD, 1989.

15. M.F. Ashby, Acta Metall. Mater., **37**(1989)1273-93.
16. M.R. Jackson, B.P. Bewlay, R.G. Rowe, D.W. Skelly, and H.A. Lipsitt, JOM, **48**(1996)39-44.
17. K.S. Chan, in "High-Temperature Ordered Intermetallic Alloys VI", J. Horton, I. Baker, S. Hanada, R. D. Noebe and D.S. Schwartz, eds., Mat. Res. Soc., Pittsburgh, Pennsylvania, **364**(1994)469-80.
18. K.S. Chan, Metall. Trans. A, **23A**(1992)183-199.
19. R.O. Ritchie, in "Mechanical Behaviour of Materials-V", M.G. Yan, S.H. Zhang and Z.M. Zheng, eds., Pergamon Press, **2**(1987)1399-1417.
20. K.S. Chan, Metall. Trans. A, **25A**(1994)299-308.
21. K.S. Chan, Metall. Trans. A, **21A**(1990)69-80.
22. R.O. Ritchie and A.W. Thompson, Metall. Trans. A, **16A**(1985)233-48.
23. K.S. Chan, Metall. Trans. A, **24A**(1993)569-83.
24. R.D. Noebe, NASA Technical Memorandum 106534, Cleveland, Ohio, April, 1994.
25. J.W. Hutchinson, J. Mech. Phys. Solids, **16**(1968)13-31.
26. J.R. Rice and G.R. Rosengren, J. Mech. Phys. Solids, **16**(1968)1-13.
27. G.R. Odette, H.E. Deve, C.K. Elliott, Hasegawa and G.E. Lucas, in "Interfaces in Metal-Ceramic Composites", R.Y. Lin, R.J. Arsenault, G.P. Martins and S.G. Fishman, eds., Warrendale, PA., MMMS, (1989)443-64.
28. A.F. Bower and M. Ortiz, J. Mech. Phys. Solids, **39**(1991)815-58.
29. F.E. Heredia, M.Y. He, G.E. Lucas, A.G. Evans, H.E. Deve, and D. Konitzer, Acta Metall. Mater., **41**(1993)505-11.
30. V.V. Krstic, P.S. Nicholson, and R.G. Hoagland, J. Am. Ceram. Soc., **64**(1981)499-507.
31. M.C. Shaw, D.B. Marshall, M.S. Dadkhah, and A.G. Evans, Acta Metall. Mater., **41**(1993)3311-22.
32. M.Y. He, F.E. Heredia, D.J. Wissuchek, M.C. Shaw, and A.G. Evans, Acta Metall. Mater., **41**(1993)1223-28.
33. A.G. Evans and D.B. Marshall, Acta Metall., **37**(1989)2567-83.
34. H.C. Cao and A.G. Evans, Acta Metall., **39**(1991)2997-3005.
35. K.S. Chan, M.Y. He and J.W. Hutchinson, Mat. Sci. Eng., **A167**(1993)57-64.
36. A.G. Evans, J. Am. Ceram. Soc., **73**(1990)187-206.
37. H.E. Deve, A.G. Evans, G.R. Odette, R. Mehrabian, M.L. Emiliani and R.J. Hecht, Acta Metall. Mater., **38**(1990)1491-1502.
38. T.L. Anderson, Fracture Mechanics, CRC Press, Second Edition, 1995.

39. B. Budiansky, J.C. Amazigo and A.G. Evans, J. Mech. Phys. Solids, **36**(1988)167-87.
40. C.K. Elliott, G.R. Odette, G.E. Lucas and J.W. Sheckherd, In"High Temperature/High Performance Composites", F.D. Lemkey, S.G. Fishman, A.G. Evans and J.R. Strife, Eds., Materials Research Society, Pittsburgh, Pennsylvania, **120**(1988)95-101.
41. M.F. Ashby, F.J. Blunt and M. Bannister, Acta metall., **37**(1989)1847-57.
42. P.A. Mataga, Acta metall., **37**(1989)3349-59.
43. B.D. Flinn, M. Rühle and A.G. Evans, Acta Metall., **37**(1989)3001-06.
44. C.D. Bencher, L. Murugesh, K.T.V. Rao and R.O. Ritchie, Intermetallics, **4**(1996)23-29.
45. X. Sun and J.A. Yeomans, J. Mater. Sci. Technol., **12**(1996)124-134.
46. H.C. Cao, B.J. Dalgleish, H.E. Deve, C. Elliott, A.G. Evans, R. Mehrabian and G.R. Odette, Acta metall., **37**(1989)2969-77.
47. L. Murugesh, K.T. Venkateswara Rao, L.C. EdJonche and R.O. Ritchie. In"Intermetallic Matrix Composite II", D.B. Miracle, D.L. Anton and J.A. Graves, eds., Pittsburgh, Pennsylvania, MRS, **273**(1992)433-38.
48. A.G. Evans and R.M. Cannon, Acta metall., **5**(1986)761-800.
49. L.S. Sigl, P.A. Mataga, B.J. Dalgleish, R.M. McMeeking and A.G. Evans, Acta Metall., **36**(1988)945-53.
50. K.S. Chan, Metall. Trans. A, **22A**(1991)2021-29.
51. K.S. Chan, Metall. Trans. A, **26A**(1995)1407-18.
52. K.S. Chan, Metall. Trans. A, **21A**(1990)2687-99.
53. S. Suresh, Metall. Trans. A, **16A**(1985)249-60.
54. W.O. Soboyejo, K.T.V. Rao, S.M.L. Sastry, and R.O. Ritchie, Metall. Trans. A. **24A**(1993)585-600.
55. W.O. Soboyejo, D.S. Schartz and S.M.L. Sastry, Metall. Trans. A, **23A**(1992)2039-59.
56. J.D. Rigney, P.M. Singh, and J.J. Lewandowski, JOM, (1992)36-41.
57. M. Enoki and T. Kishi, Mater. Sci. Eng., **A192/193**(1995)420-26.
58. L.R.E. Rose, Inter. J. Frac., **31**(1986)233-42.
59. V.D. Krstic, Phil. Mag. A, **48**[5](1983)695-708.
60. K.S. Ravichandran, Scr. Met. et Mat., **26**(1992)1389-93.
61. D.L. Davidson, K.S. Chan and D.L. Anton, Met. Mat. Trans. A, **27A**(1996)3007-18.
62. K.S. Chan and D.L. Davidson, JOM, **48**(September 1996)62-67.
63. M.F. Ashby, Acta metall. mater., **41**[5](1993)1313-35.

64. M.J. Strum and G.A. Henshall, in "High-Temperature Ordered Intermetallic Alloys V". I. Baker, R. Darolia, J.D. Whittenberger and M.H. Yoo, eds., Mat. Res. Soc., Pittsburgh, Pennsylvania, 288(1993)1093-98.
65. B.P. Bewlay, H.A. Lipsitt, W.J. Reeder, M.R. Jackson and J.A. Sutliff, in "Processing and Fabrication of Advanced Materials III", V.A. Ravi, T.S. Srivatsan and J.J. Moore, eds., TMS., (1993)547-65.
66. F. Ebrahimi, D.T. Hoelzer and J.R. Castillo-Gomez, Mater. Sci. Eng., A171(1993)35-45.
67. R.D. Noebe, R.R. Bowman and M.V. Nathal, International Materials Reviews, 38(1993)193-232.
68. R.A. Varin and G-H. Li, The 3rd Int. Conf. on High-Temperature Intermetallics, Materials Science and Engineering, Vol.A192/193, Part 1, 1995, pp.59-68.
69. Y.K. Song, MASc Thesis, University of Waterloo, 1996.
70. K.T. Venkateswara Rao, G.R. Odette and R.O. Ritchie, Acta Metall. Mater., 42(1994)893-911.
71. R.G. Rowe, J.A. Sutliff, and E.F. Koch, MRS Symp. Proc., B.G. Girssen, D.E. Polk, and A.I. Taub, eds., Pittsburgh, PA, 58(1986)359-64.
72. W.O. Soboyejo, Metall. Trans. A, **23A**(1992)1737-50.
73. Z. Li and E.M. Schulson, J. Mater. Sci., **30**(1995)2859-65.
74. T.N. Baker, in "Yield, Flow and Fracture of Polycrystals", T.N. Baker, ed., Applied Science Publishers, London and New York, (1983)235-73.
75. E.M. Grala, Investigation of the NiAl Phase of Nickel-Aluminum Alloys, NACA TN-3828, 1957.
76. R. Darolia, in "Structural Intermetallics", R. Darolia, J.J. Lewandowski, C.T. Liu, P.L. Martin, D.B. Miracle and M.V. Nathal, eds., PA. Warrendale, The Minerals, Metals and Materials Society, (1993)495-504.
77. I.M. Robertson and C.M. Wayman, Metallography, 17(1984)43-55.
78. P.S. Khadkikar, K. Vedula and B.S. Shabel, in "High-Temperature Ordered Intermetallic Alloys II", N.S. Stoloff, C.C. Koch, C.T. Liu and O. Izumi, eds., Mat. Res. Soc., Pittsburgh, Pennsylvania, 81(1987)157-64.
79. P.S. Khadkikar and K. Vedula, J. Mater. Res., 2(1987)163-67.
80. Y. Xu and E.M. Schulson, in "High-Temperature Ordered Intermetallic Alloys V", I. Baker, R. Darolia, J.D. Whittenberger and M.H. Yoo, eds., Mat. Res. Soc., Pittsburgh, Pennsylvania, 288(1993)635-40.
81. J.D.Rigney and J.J. Lewandowski, Mater. Sci. Eng., **A149**(1992)143-151.
82. C.T. Liu, C.L. White and J.A. Horton, Acta Metall., 33(1985)213-29.

83. E.P. George, C.T. Liu and D.P. Pope, Acta Mater., **44**(1996)1757-63.
84. M.F. Singleton, J.I. Murray, and P. Nash, Binary Alloy Phase Diagrams, T.B. Massalski, ed., ASM, 1(1986)140-43.
85. K. Hilpert, D. Kobertz, V. Venugopal, M. Miller and H. Gerads, Z. Naturforsch, **42a**(1987)1327-32.
86. F.J. Bremer, M. Beyss, E. Karthaus, A. Hellwig, T. Schober, J.-M. Welter, and H. Wenzl, J. Crystal Growth, **87**(1988)185-92.
87. J.D. Verhoeven, J.H. Lee, F.C. Loabs, and L.L. Jones, J. Phase Equilibria, **12**(1991)15-23.
88. J. Schramm, Z. Metallkd. **33**(1941)347-55.
89. J.H. Lee and J.D. Verhoeven, J. Crystal Growth, **144**(1994)353-66.
90. P.S. Khadkikar and K. Vedula, Matal. Tran. A, **24A**(1993)83-94.
91. W.S. Walston and R. Darolia, in "High-Temperature Ordered Intermetallic Alloys V", I. Baker, R. Darolia, J.D. Whittenberger and M.H. Yoo, eds., Mat. Res. Soc., Pittsburgh, Pennsylvania, 288(1993)237-42.
92. B. Dulmaine, Fall TMS meeting, Indianapolis, IN, Oct.1989.
93. I.M. Robertson and C.M. Wayman, Phil. Mag. A, **48**(1983)443-67.
94. D.R. Pank, M.V. Nathal and D.A. Koss, J. Mater. Res., **5**(1990)942-49.
95. I.M. Robertson and C.M. Wayman, Phil. Mag. A, **48**(1983)421-42.
96. I.M. Robertson and C.M. Wayman, Metallography, **17**(1984)43-55.
97. ASTM Standard E 399-90.
98. ASTM Standard E 1304-89.
99. ASTM Standard E 813-89.
100. R.W. Hertzberg, Deformation and Fracture Mechanics of Engineering Materials, John Wiley & Sons, Inc., fourth edition, 1995.
101. D. Munz, In "Fracture Mechanics of Ceramics", R.G. Bradt, A.G. Evans, D.P.H. Hasselman and E.E. Lange, Eds., Plenum Press.New York-London, **6**(1983)1-25.
102. G.R. Irwin, J.A. Kies and H.L. Smith, In "Fracture Strengths Relative to Onset and Arrest of Crack Propagation", Proceedings, Am. Soc. Testing Mats., **58**(1958)640-51.
103. J.E. Srawley, M.H. Jones and W.F. Brown, Jr., In "Materials Research and Standards", ASTM, **7**[6](1967)262-66.
104. T. Nose and T. Fujii, J. Am. Ceram. Soc., **71**[5](1988)328-33.
105. S.W. Freiman, In "Fracture Mechanics of Ceramics", R.G. Bradt, A.G. Evans, D.P.H. Hasselman and E.E. Lange, Eds., Plenum Press, New York-London, **6**(1983)27-45.
106. T.T. Shih, In "Chevron V-Notched Bend Specimen for K_{Ic} Measurement of Brittle Materials", Journal of Testing and Evaluation, JTEVA, **9**[1](1981)50-55.

107. N.E. Dowling, Mechanical Behaviour of Materials, Prentice Hall, 1993.
108. D. Broek, Elementary Engineering Fracture Mechanics, Martinus Nijhoff Publishers, Third Revised Edition, 1982.
109. W.F. Brown, Jr., and J.E. Srawley, Plane Strain Crack Toughness Testing of High Strength Metallic Materials, ASTM Special Technical Publication No.410, 1967.
110. C.T. Liu and J.O. Stiegler, in "Metals Handbook", J.R. Davis et al., eds., Tenth Edition, ASM, pp.913(1990).
111. J.J. Lewandowski, G.M. Michal, I. Locci and J.D. Rigney, In"Alloy Phase Stability and Design", G.M. Stocks, D.P. Pope and A.F. Giamei, Eds., MRS, Pittsburgh, Pennsylvania, **186**(1991)341-47.
112. R.A. Varin, In "Structure & Property Relationships for Interfaces", J.L. Walter, A.H. King and K. Tangri, Eds., ASM, The Materials Information Society, (1991)243-62.
113. C.T. Liu, In "Structural Intermetallics", R.Darolia, J.J. Lewandowski, C.T. Liu, P.L. Martin, D.B. Miracle, M.V. Nathal, eds., Teh Minerals, Metals and Materials Society, Warrendale, (1993)365-77.
114. R.D. Noebe, A. Misra and R. Gibala, ISIJ Inter., **31**(1991)1172-85.
115. D.B. Miracle, Acta metall. mater., **41**[3](1993)649-84.
116. M.L. Weaver, R.D. Noebe, J.J. Lewandowski, B.F. Oliver and M.J. Kaufman, Mater. Sci. & Eng., In press.
117. R.R. Bowman, R.D. Noebe, S.V. Raj, and I.E. Locci, Met. Trans. A, **23A**(1992)1493-1508.
118. R.D. Noebe and M.K. Behbehani, Scr. Met. et Mat., **27**(1992)1795-1800.
119. M. Nakamura, In "Intermetallic Compounds", J.H. Westbrook and R.L. Fleisher, Eds., John Wiley & Sons Ltd, (1995)873-93.
120. M.G. Jenkins, M.K. Ferber, A. Ghosh, J.T. Peussa, and J.A. Salem, In "Chevron-Notch Fracture Test Experience: Metals and Non-Metal", ASTM STP 1172, K.R. Brown and F.I. Baratta, Eds., American Society for Testing and Materials, Philadelphia, (1992)159-77.
121. J.C. Newman, In "Chevron-Notched Specimens: Testing and Stress Analysis", ASTM STP 855, J.H. Underwood, S.W. Freiman, and F.I. Baratta, Eds., American Society for Testing and Materials, Philadelphia, (1984)5-31.
122. L.M. Barker, Inter.J. Frac., **15**[6](1979)515-36.
123. A. Ghosh, M.G. Jenkins, K.W. White, A.S. Kobayashi and R.C. Bradt, In "Ceramic Materials and Components for Engines, V.J. Tennery, Ed., The American Ceramic Society, Westerville, OH, (1989)592-603.

124. L. Chuck, E.R. Ruller, Jr., and S.W. Freiman, In "Chevron-Notched Specimens: Testing and Stress Analysis", ASTM STP 855, J.H. Underwood, S.W. Freiman, and F.I. Baratta, Eds., American Society for Testing and Materials, Philadelphia, (1984)167-175.
125. C-W. Marshall, P.R. Held, and F.J. Dolan, In "Chevron-Notch Fracture Test Experience: Metals and Non-Metal", ASTM STP 1172, K.R. Brown and F.I. Baratta, Eds., American Society for Testing and Materials, Philadelphia, (1992)144-56.
126. S. Wu, Eng. Frac. Mech., **19**(1984)221-32.
127. W. Chizhi, Y. Maochan, and C. Tzeguang, In "Chevron-Notched Specimens: Testing and Stress Analysis", ASTM STP 855, J.H. Underwood, S.W. Freiman, and F.I. Baratta, Eds., American Society for Testing and Materials, Philadelphia, (1984)193-204.
128. J.A. Horton and J.M. Schneibel, In "High Temperature Ordered Intermetallic Alloys VI", J. Horton, I. Baker, S. Hanada, R.D. Noebe and D.S. Schwartz, Eds., MRS, **363**(1995)1107-10.
129. R.A. Varin and L. Zbroniec, In "High Temperature Ordered Intermetallic Alloys VII", (in press).
130. L.M. Barker, Eng. Fract. Mechanics, **17**(1983)289-312.
131. L.M. Barker, In "Chevron-Notched Specimens: Testing and Stress Analysis", ASTM STP 855, J.H. Underwood, S.W. Freiman, and F.I. Baratta, Eds., American Society for Testing and Materials, Philadelphia, (1984)117-33.
132. D. Munz, R.T. Bubsey, and J.L. Shannon, Jr., J. Am. Ceram. Soc., **63**(1980)300-305.
133. S. Wu, In "Chevron-Notched Specimens: Testing and Stress Analysis", ASTM STP 855, J.H. Underwood, S.W. Freiman, and F.I. Baratta, Eds., American Society for Testing and Materials, Philadelphia, (1984)176-192.
134. I. Bar-On, F.R. Tuler, and I. Roman, In "Chevron-Notched Specimens: Testing and Stress Analysis", ASTM STP 855, J.H. Underwood, S.W. Freiman, and F.I. Baratta, Eds., American Society for Testing and Materials, Philadelphia, (1984)98-113.
135. R.F. Krause, Jr., and E.R. Fuller, Jr., In "Chevron-Notched Specimens: Testing and Stress Analysis", ASTM STP 855, J.H. Underwood, S.W. Freiman, and F.I. Baratta, Eds., American Society for Testing and Materials, Philadelphia, (1984)309-23.
136. I. Merkel and U. Messerschmidt, Mat. Sci. Eng., **A151**(1992)131-135.
137. H. Nakamura and H. Kobayashi, Mat. Sci. Eng., **A143**(1991)119-26.
138. L.M. Barker, In "Fracture Mechanics Applied to Brittle Materials, ASTM STP 743, Richard Roberts, Ed., American Society for Testing and Materials, Philadelphia, (1981)456-75.
139. D. Munz, Eng. Frac. Mech., **15**(1981)231-36.

140. J.I. Bluhm, Eng. Frac. Mech., **7**(1975)593-604.
141. P.A. Whithey and P. Bowen, Int Journ of Fracture, **46**(1990)R55-59.
142. M. Sakai, K. Urashima, and M. Inagaki, J. Ame. Ceram. Soc., **66**(1983)868-74.
143. A.M. Gokhale, Trans. Indian Inst. Met., 34(1981)71-88.
144. G. Albinger, Java Jandel Video Analysis Software, Jandel Scientific, Corte Madera, CA, 1988, pp.4.4-4.10.
145. ASTM Standard E 9-89a (Reapproved 1995).
146. Shimadzu Micro Hardness Tester HMV-2000 Instruction Manual, Shimadzu Corporation, Kyoto Japan, 1984.
147. Selected Powder Diffraction Data for Metals and Alloys, JCPDS, Eds., **1**(1978)13, 32, 107, 185, 260, 471.
148. P.A. Withey and P. Bowen, In "Mechanical Behaviour of Materials-VI", M. Jono and T. Inoue, Eds., Pergamon Press, **4**(1991)153-58.
149. ASTM Standard E 8M-96.
150. D.W. Richerson, "Modern Ceramic Engineering", Marcel Dekker INC, 1982.
151. G.E. Dieter, "Mechanical Metallurgy", McGraw-Hill Book Company, third edition, 1986.
152. N.J. Rogers, P.D. Crofts, L.P. Jones and P. Bowen, Mater. Sci. Eng., **A192/193**(1995)379-86.
153. N.S. Stoloff, International Materials Reviews, **34[4]**(1989)153-183.
154. E.D. Rodeghiero, O.K. Tse, B.S. Wolkenberg, and E.P. Giannelis, In "Processing and Fabrication of Advance Materials IV", T.S. Srivatsan and J.J. Moore, Eds., The Minerals Metals & Materials Society, 1996.

APPENDIX A
THE DEDUCTION OF THE CRACK-TIP BLUNTING MODEL

The crack-tip blunting model of *Eq.(1.5)* resulted from the Hutchinson, Rice and Rosengren (*HRR*) crack tip field [25-27]. From the *HRR* theory [25-27], the near-tip effective strain distribution can be described by [18, 25-27]

$$\varepsilon_m = \alpha' \varepsilon_y^m \left[\frac{J_m}{\alpha' \varepsilon_y^m \sigma_y^m I_n r}\right]^{n/(n+1)} \varepsilon(\theta, n) \tag{A1}$$

for the matrix and

$$\varepsilon_c = \alpha' \varepsilon_y^c \left[\frac{J_c}{\alpha' \varepsilon_y^c \sigma_y^c I_n r}\right]^{n/(n+1)} \varepsilon(\theta, n) \tag{A2}$$

for a composite containing a brittle matrix, α, reinforced with a ductile second phase, β, when the hardening exponents, n, for the matrix and composite are identical. In Eqs.(1) and (2), I_n is a constant value corresponding to n, given by Hutchinson [25]; α' is a coefficient in the tensile stress-strain relations of certain metals: $\varepsilon=\sigma+\alpha\gamma^n$; r and θ are cylindrical co-ordinates.

Dividing *Eq.(A2)* by *Eq.(A1)* leads to

$$\frac{\varepsilon_c}{\varepsilon_m} = \frac{\varepsilon_y^c}{\varepsilon_y^m}\left[\frac{J_c}{J_m}\right]^{n/(n+1)}\left[\frac{\varepsilon_y^m \sigma_y^m}{\varepsilon_y^c \sigma_y^c}\right]^{n/(n+1)} \tag{A3}$$

or,

$$\frac{\varepsilon_c}{\varepsilon_m} = \left[\frac{J_c}{J_m}\right]^{n/(n+1)}\left[\frac{\sigma_y^m}{\sigma_y^c}\right]^{(n-1)/(n+1)}\left[\frac{E_m}{E_c}\right]^{1/(n+1)} \tag{A4}$$

when the relations $\varepsilon_y^c=\sigma_y^c/E_c$ and $e_y^m=\sigma_y^m/E_m$ are invoked. *Eq.(A4)* can be combined with $J=(1-\nu^2)K^2/E$ to give

$$\frac{K_c}{K_m}=\left[\frac{\varepsilon_c}{\varepsilon_m}\right]^{(n+1)/2n}\left[\frac{\sigma_y^c}{\sigma_y^m}\right]^{(n-1)/2n}\left[\frac{E_c}{E_m}\right]^{(n+1)/2n} \qquad \text{(A5)}$$

based on the assumption that the rule of mixtures for composite materials is applicable to a two-phase alloy: $\sigma_y=V_\alpha\sigma_y^\alpha+V_\beta\sigma_y^\beta$ and $\varepsilon_y=V_\alpha\varepsilon_y^\alpha+V_\beta\varepsilon_y^\beta$, *Eq.(1.5)* can be deducted.

APPENDIX B
A BASIC RELATION OF THE EVALUATING K_{Ivm} IN *CNB* BEND TESTING

A three-point-bend specimen with a chevron notch is characterized by the dimensions shown in **Figure 2.9**. The length of the crack front b at crack length a is

$$b = B[(a - a_0)/(a_1 - a_0)] = B[(\alpha - \alpha_0)/(\alpha_1 - \alpha_0)] \qquad \text{(B1)}$$

The relation between load P and fracture toughness K_{Ivc} is obtained by considering the available and the necessary energies for crack propagation. The available energy for the extension of the crack by Δa is

$$\Delta U = (P^2/2W)(dC_v/d\alpha)\Delta a \qquad \text{(B2)}$$

where C_v is the compliance of the specimen with a trapezoidal crack front. Extending the crack by the increment Δa increases the crack area by $\Delta A = b\Delta a$. The necessary energy for crack extension is

$$\Delta W = G_{Ivc} b\Delta a = (K_{Ivc}^2/E')b\Delta a \qquad \text{(B3)}$$

with $E'=E$ for plane stress and $E'=E/(1-\nu^2)$ for plane strain. During crack extension, $\Delta U=\Delta W$:

$$K_{Ivc} = P\left[\frac{(dC_v/d\alpha)E'}{2Wb}\right]^{1/2} = \frac{P}{BW^{1/2}}\left[\frac{dC_v}{2d\alpha}\frac{\alpha_1 - \alpha_0}{\alpha - \alpha_0}\right]^{1/2} \qquad \text{(B4)}$$

where the term in brackets $Y^*=\{(1/2)dC_v(\alpha)/d\alpha)[(\alpha_1-\alpha_0)(\alpha-\alpha_0)]\}^{1/2}$, is stress-intensity factor coefficient. For a stable crack growth of *CNB* bend testing, $K_{Ivc}=K_{Ivm}$, which could be calculated from P_{max}, which occurs at the minimum value of Y^*, i.e., Y^*_m.

APPENDIX C
MORE EXAMPLES OF FRACTURE SURFACES FROM THE INVESTIGATED IN-SITU COMPOSITES

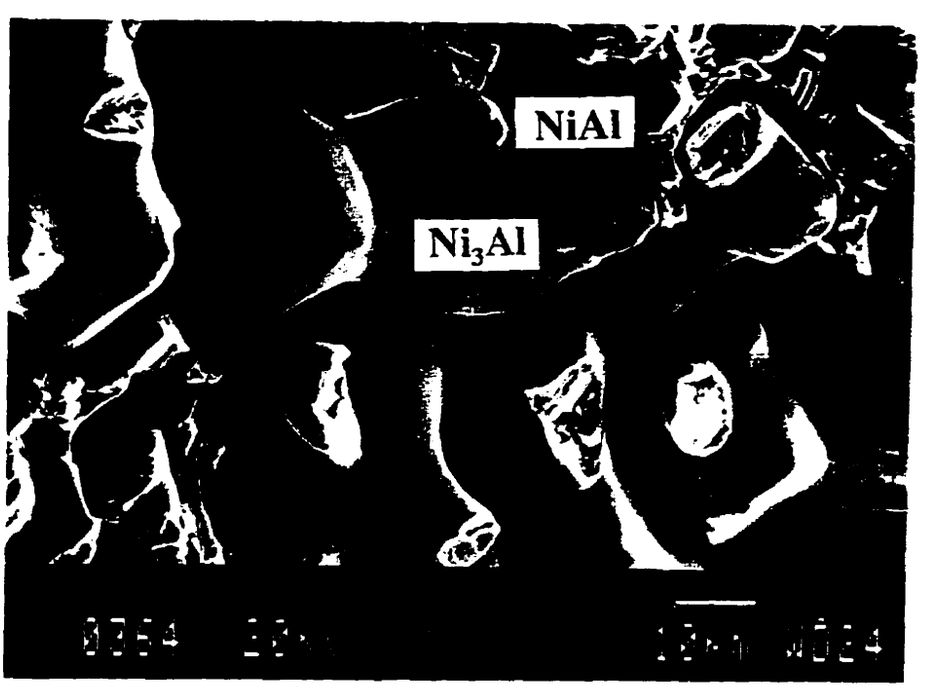

Appendix C1 Typical scanning electron microscope (SEM) fractographs of the homogenized $Ni_{70.8}Al_{29.2}$: small transgranular fractures occurred on the smooth intergranularly fractured grain boundary facets.

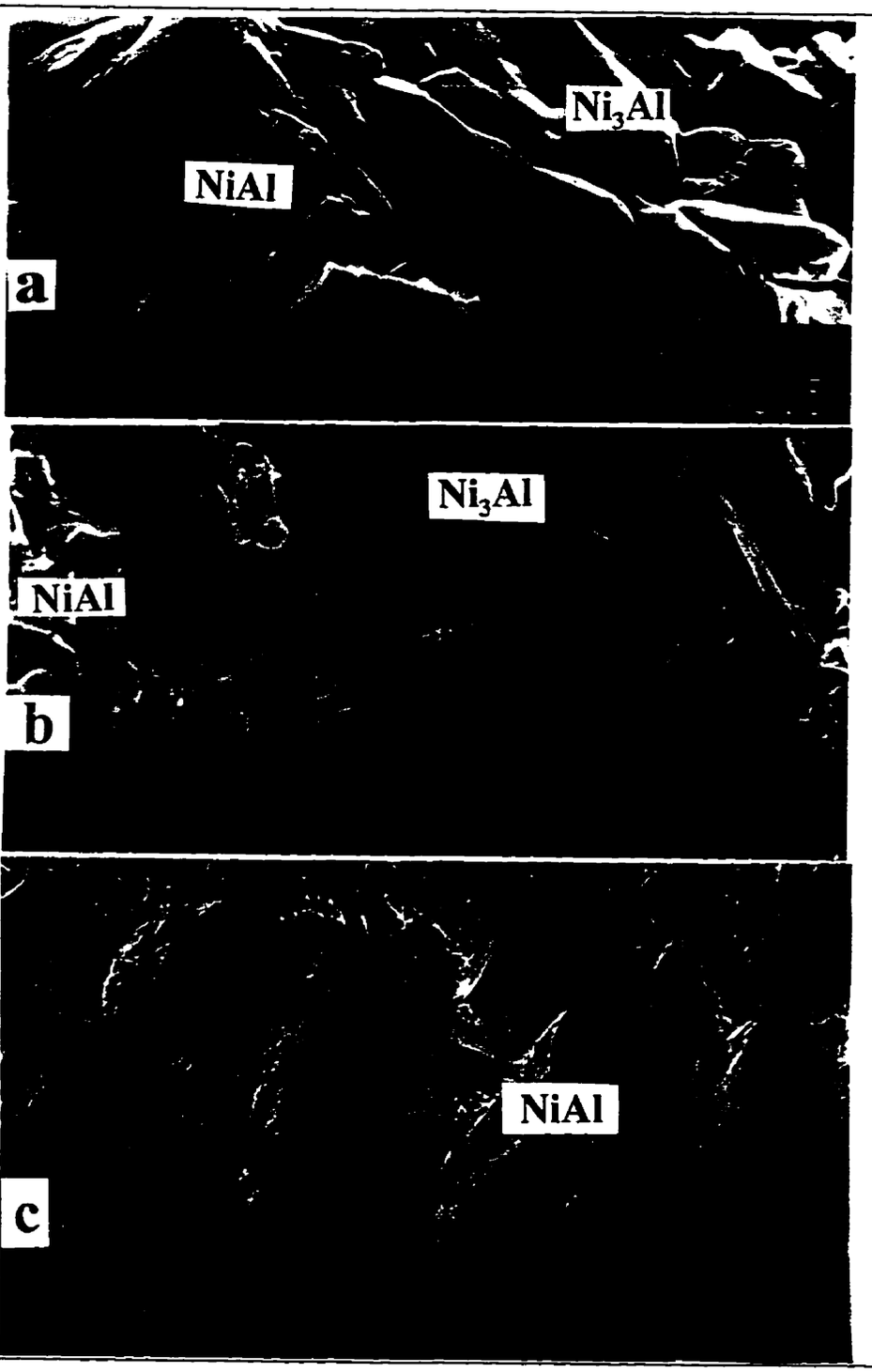

Appendix C2 Typical scanning electron microscope (SEM) fractographs of the homogenized $Ni_{63.7}Al_{36.3}$: (a) intergranular fracture of Ni_3Al phase, (b) secondary grain boundary cracks and (c) transgranular crack-path-deflection of cleavage fracture plane.

Appendix C3 Typical scanning electron microscope (SEM) fractographs of the homogenized $Ni_{67.2}Al_{32.8}$: (a) a mixed mode of tansgranular/intergranular fracture, (b) delamination at interfaces.

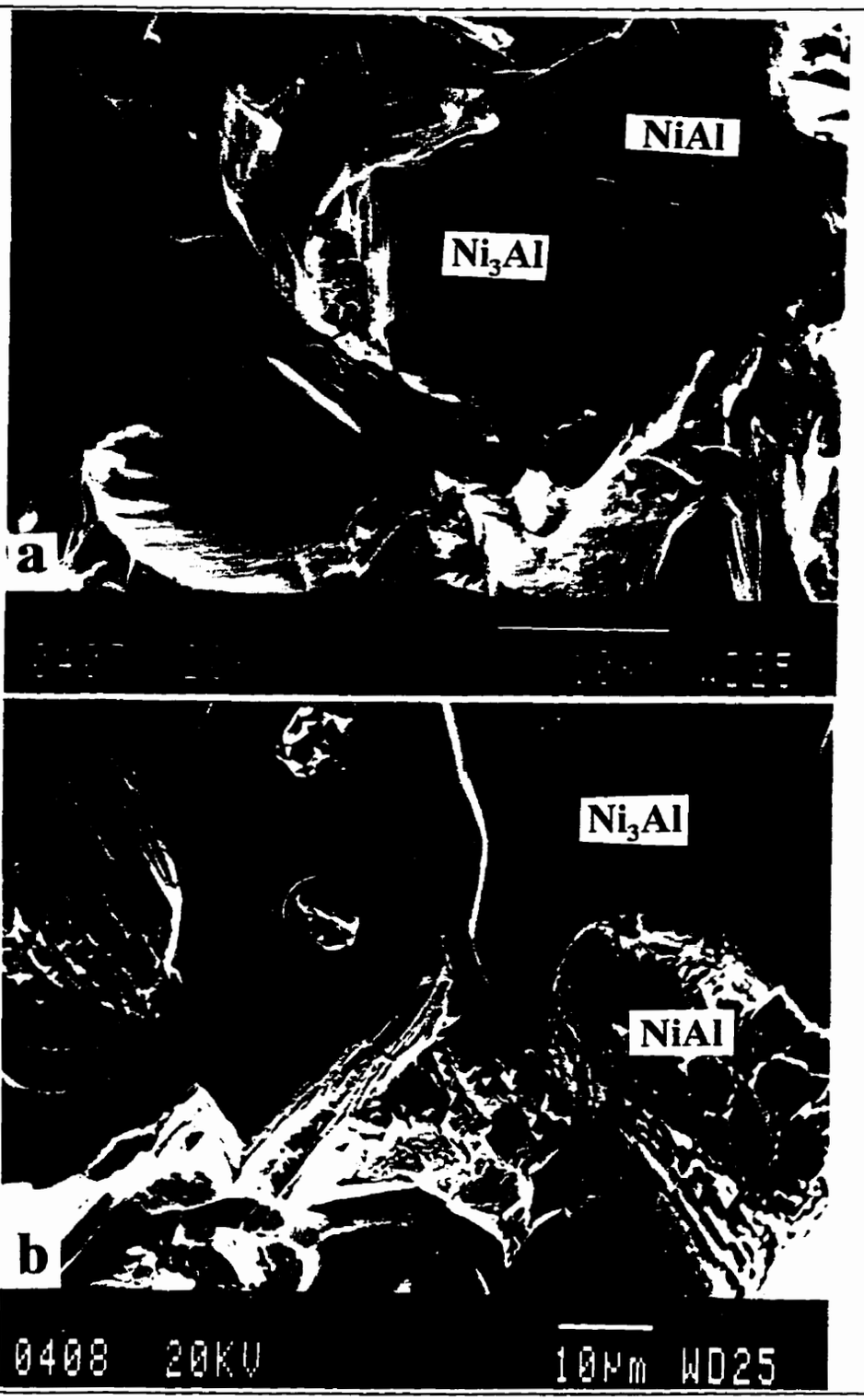

Appendix C4 Typical scanning electron microscope (SEM) fractographs of the homogenized $Ni_{72.8}Al_{27.2}$: (a) deep dimples surrounded by cleavage fracture with river pattern, (b) debonding occurs at interfaces.

APPENDIX D
THE MEASURED AND CALCULATED GEOMETRICAL PARAMETERS FOR EACH *CNB* BEND SPECIMEN.

Appendix D1
The Measured and Calculated Geometrical Parameters for Each CNB Bend Specimen.

Ni (at.%)	Ni_3Al (vol.%)	B (mm)	W (mm)	a_0 (mm)	a_1 (mm)	Δa_m (mm)	Y^*_m
63.7	16.53	4	4	0.35	3.4	0.68	10.94
63.7	17.16	3.9	3.9	0.7	3.89	0.72	16.55
63.7	17.27	3.5	4.1	0.89	3.4	0.65	13.19
63.7	18.86	3.74	3.92	0.3	3.72	0.73	12.56
63.7	16.7	3.83	4.07	1.27	4.05	0.65	20.95
63.7	16.48	3.9	3.95	0.81	3.34	0.64	13.75
63.7	16.48	3.81	3.87	0.62	3.86	0.72	16.04
65.9	22	4.43	4.66	0.99	4.37	0.83	13.5
65.9	24.7	4.39	4.84	1.1	4.61	0.83	13.65
65.9	20.3	4.38	4.79	1.15	4.52	0.81	13.99
65.9	22.6	4.39	4.83	1.09	4.53	0.83	13.35
65.9	20.3	4.31	4.65	1.77	4.64	0.68	21.52
67.2	36.14	4.06	3.82	0.25	3.7	0.73	12.96
67.2	34.09	4.06	4.26	0.5	3.86	0.76	11.77
67.2	39.43	3.79	4.11	0.35	3.65	0.73	11.18
67.2	28.98	3.96	4.09	0.18	3.39	0.67	9.49
67.2	32.33	4.04	4.22	0.25	4	0.79	11.21
67.2	32.1	3.87	4.09	0.32	3.47	0.69	10.47
70.8	61.65	3.92	3.94	0.15	3.51	0.7	10.68
70.8	57.44	3.48	4.32	0.55	3.85	0.76	11.58
70.8	65.48	3.67	4.13	0.3	3.57	0.71	10.49
70.8	64.03	4.05	4.07	0.37	3.97	0.77	12.87
70.8	61.36	3.75	4.07	1.29	4.06	0.65	21.27
72.8	85.97	4.04	3.94	1.09	3.83	0.65	19.35
72.8	91.31	4.22	4.3	0.85	4.29	0.78	15.51
72.8	92.56	3.57	4.82	1.87	4.81	0.7	21.1
72.8	92.1	3.81	4.73	1.76	4.72	0.7	20.69
72.8	93.47	5.33	4.54	0.82	4.02	0.77	12.07

Appendix D2

The Measured and Calculated Geometrical Parameters for Each CNB Bend Specimen.

Ni (at.%)	Ni_3Al (vol.%)	B (mm)	W (mm)	a_0 (mm)	a_1 (mm)	Δa_m (mm)	Y^*_m
73.2	93.18	3.62	4.44	1.48	4.36	0.69	19.67
73.2	96.25	3.64	4.04	0.55	3.94	0.75	14.19
73.2	94.43	3.78	4.65	1.25	4.45	0.77	15.63
73.2	95.45	3.85	4.68	1.77	4.61	0.69	21.24
73.2	95.74	4.36	4.73	1.4	4.71	0.77	17.27
73.2	95.82	3.42	4.5	1.72	4.48	0.66	22.28
73.2	96.65	4.56	4.84	1.85	4.43	0.68	17.87
77.7	100	4.71	6.13	2.33	5.74	***0.88***	***16.27***
77.7	99.8	4.27	4.35	1.08	4.15	0.73	15.99
77.7	99.9	4.08	4.19	0.35	3.96	0.77	11.82
77.7	100	5.07	5.95	1.92	5.45	***0.92***	***14.28***
73.2-0.2B	92	4.25	4.05	0.82	3.81	0.71	15.4
73.2-0.2B	93.7	3.95	4.08	1.25	4.05	0.66	20.55
73.2-0.2B	93.6	4.34	3.98	1.48	3.97	0.59	24.79
73.2-0.2B	94.6	3.98	4.57	1.52	4.55	0.71	19.46
74.8-0.4B	99.8	4.18	4.26	0.93	3.9	0.72	14.52
74.8-0.4B	99.8	4.26	4.79	0.74	4.38	0.85	11.32
74.8-0.4B	99.9	5.07	5.86	1.43	5.63	***1***	***13.2***
74.8-0.4B	99.9	5.04	5.85	1.48	5.6	***0.99***	***13.4***
74.8-0.4B	99.9	4.53	4.26	0.93	4.22	0.75	16.19

Note:

The bold and italic values were obtained using Bluhm's solution since Wu's solution did not work for these specimen geometries because S/W in Eq.(2.30) was greater than 2.9.

APPENDIX E
THE MECHANICAL PROPERTIES AND FRACTURE TOUGHNESS VALUES FOR EACH *CNB* BEND SPECIMEN.

Appendix E1

The Mechanical Properties, Maximum Load and Fracture Toughness Values for Each *CNB* Bend Specimen.

Ni	Ni_3Al	*Ec*	σ_{YS}	P_{max}	$K_{Ivm}{}^{W}$	$K_{Ivm}{}^{B}$	K_{WOF}	γ_{WOF}
(at.%)	(vol.%)	(GPa)	(MPa)	(kg)	(MPa $m^{1/2}$)			(J/m^2)
63.7	16.53	261.97	395.2	19.07	8.09	*8.93*	11.97	273.468
63.7	17.16	264.81	377.8	12.2	8.13	*8.92*	12.06	274.619
63.7	17.27	264.51	461.7	14.19	8.19	*9.07*	12.48	294.413
63.7	18.86	262.23	421.1	17.52	8.22	*9.12*	12.05	276.861
63.7	16.7	265.51	400	9.53	8.02	*8.81*	12.44	291.427
63.7	16.48	265.85	434.4	14.99	8.25	*9.11*	12.95	315.408
63.7	16.48	265.85	471.4	13.29	8.82	*9.67*	13.47	341.247
65.9	22	257.59	1051	30.97	13.57	*15.09*	21.32	882.298
65.9	24.7	253.74	1000	28.9	12.68	*14.13*	20.84	855.808
65.9	20.3	260.08	-	30.72	13.91	*15.49*	21.74	908.62
65.9	22.6	256.72	1241	34.64	14.87	*16.59*	23	1030.31
65.9	20.3	260.08	1311	15.94	11.45	*12.68*	20.4	800.062
67.2	36.14	238.6	895.2	31.27	15.83	*17.32*	27.49	1583.61
67.2	34.09	241.18	770.7	34.66	15.1	*16.72*	27.35	1550.76
67.2	39.43	234.58	756.4	35.42	15.99	*17.66*	27.6	1623.67
67.2	28.98	247.85	753.9	36.83	13.53	*14.94*	24.37	1198.1
67.2	32.33	243.44	889.2	32.36	13.56	*14.93*	24.6	1242.93
67.2	32.1	243.73	847.4	35.66	14.8	*16.36*	25.1	1292.43
70.8	61.65	210.59	514.3	55.38	23.57	*25.86*	**45.42**	4898.09
70.8	57.44	214.75	643.7	44.72	22.2	*24.63*	**44.2**	4548.64
70.8	65.48	206.76	417.6	54.23	23.67	***26.15***	**46**	5117.04
70.8	64.03	208.31	716.9	47.73	23.32	*25.63*	**45.59**	4988.83
70.8	61.36	210.87	400	29.41	**25.65**	***28.19***	**49.67**	5849.83
72.8	85.97	189.39	400	33.14	**24.81**	***27.25***	**47.22**	5886.61
72.8	91.31	185.3	422.4	50.31	**27.67**	***30.54***	**53.14**	7619.7
72.8	92.56	184.37	466.5	28.68	23.95	***26.59***	**45.17**	5533.25
72.8	92.1	184.71	496.4	33.91	26.27	***29.14***	**51.81**	7266.19
72.8	93.47	183.69	367.8	73.72	**24.31**	***27.07***	**46.5**	5885.6

Note:

(1) The bold values are invalid according to the validity requirements.

(2) The $K_{Ivm}{}^{W}$ values were calculated using Wu's solution.

(3) The italic values of $K_{Ivm}{}^{B}$ were obtained by Bluhm's solution.

Appendix E2

The Mechanical Properties and Fracture Toughness Values for Each CNB Bend Specimen.

Ni (at.%)	Ni_3Al (vol.%)	Ec (GPa)	σ_{YS} (MPa)	P_{max} (kg)	K_{Ivm}^{W} ($MPa\,m^{1/2}$)	K_{Ivm}^{B} ($MPa\,m^{1/2}$)	K_{WOF} ($MPa\,m^{1/2}$)	γ_{WOF} (J/m^2)
73.2	93.18	183.91	373.2	25.56	**20.44**	**22.6**	**34.79**	3290.59
73.2	96.25	181.66	396.1	56.19	**33.81**	**37.19**	**47.22**	6137.09
73.2	94.43	182.99	421.5	44.32	**26.37**	**29.29**	**40.19**	4413.45
73.2	95.45	182.24	425.5	29.77	23.56	**26.1**	**36.82**	3719.58
73.2	95.74	182.03	392.9	48.29	**27.28**	**30.29**	**38.13**	3993.56
73.2	95.82	181.98	264.7	28.17	**26.84**	**29.66**	**37.62**	3888.52
73.2	96.65	181.38	346.3	52.64	**29.1**	**32.38**	**41.55**	4759.08
77.7	100	179	128.8	96.56	***41.76***	**41.8**	**122.9**	42191.1
77.7	99.8	180.41	193.1	48.78	**27.18**	**30.06**	**106.74**	31576.5
77.7	99.9	179.7	350	85.15	**37.38**	**41.22**	**137.82**	52850.2
77.7	100	179	214.2	97.29	***34.84***	**34.85**	**112.33**	35245.9
73.2-0.2B	92	184.78	549	49.74	27.78	30.62	**35.31**	3373.73
73.2-0.2B	93.7	183.52	543	34.38	27.48	30.21	**35.26**	3387.28
73.2-0.2B	93.6	183.6	517	29.11	25.86	28.37	**32.78**	2926.28
73.2-0.2B	94.6	182.86	532	26.97	19.14	13.27	**28.91**	2285.32
74.8-0.4B	99.8	179.14	355	43.7	**22.82**	**25.25**	**53.21**	7902.49
74.8-0.4B	99.8	179.14	350	65.31	**24.59**	**27.46**	**55.07**	8464.62
74.8-0.4B	99.9	179.07	-	75.84	***25.24***	**25.31**	**52.51**	7698.94
74.8-0.4B	99.9	179.07	334	66.58	***25.28***	**22.71**	**48.36**	6530.1
74.8-0.4B	99.9	179.07	489	46.97	25.24	**27.85**	**56.72**	8982.96

Note:

(1) The bold values are invalid according to the validity requirements.

(2) The K_{Ivm}^{W} values were calculated using Wu's solution.

(3) The italic values of K_{Ivm}^{B} were obtained using Bluhm's solution.

APPENDIX F
TYPICAL RELATIONSHIPS BETWEEN THE PARAMETERS (a) Y^*, (b) P_{max}, (c) K, (d) J_{el}, (e) J_{pl}, (f) J AND THE CRACK EXTENSION FOR EACH ALLOY.

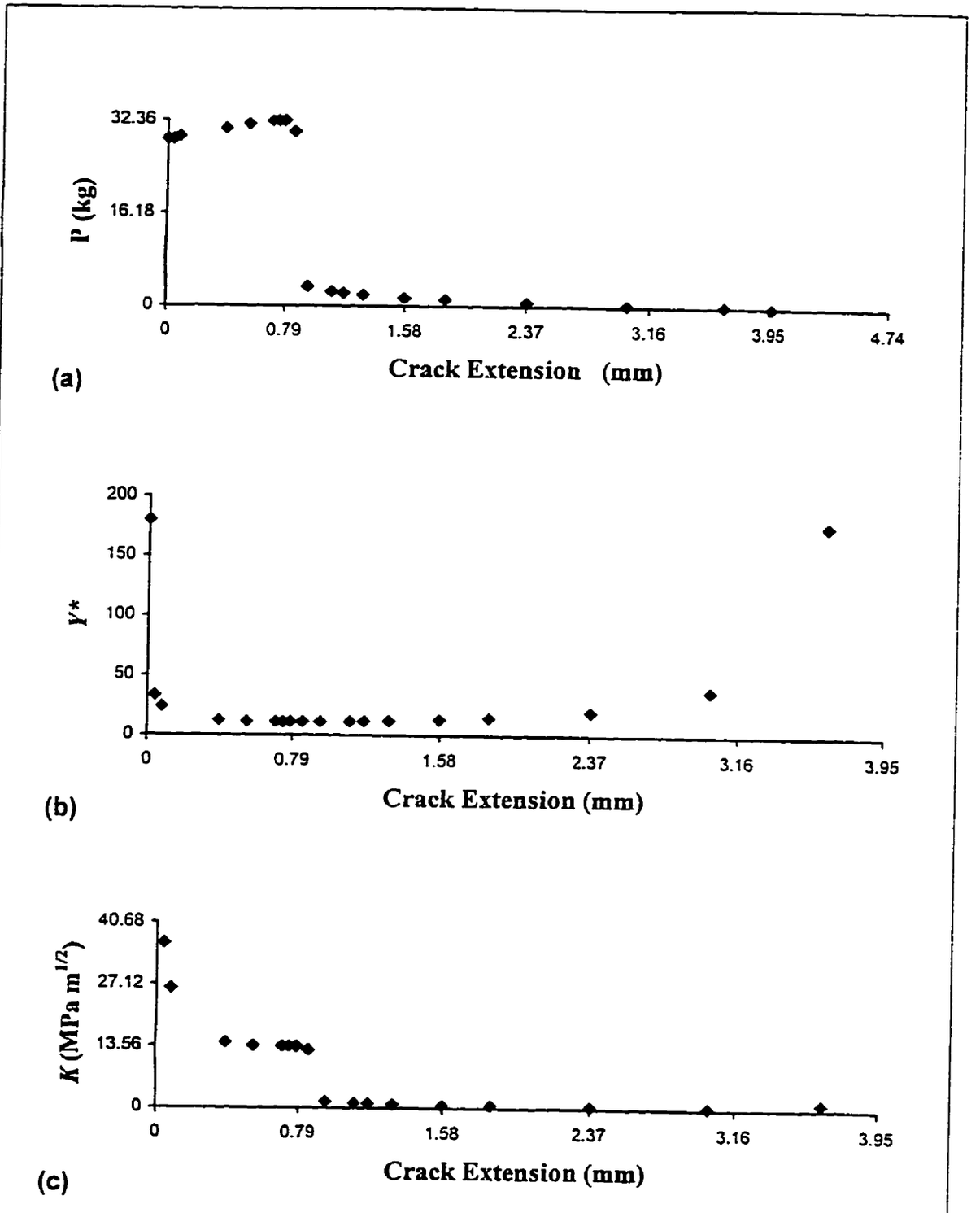

Appendix F1 A typical relationship between the parameters (a) P_{max}, (b) Y^* and (c) K, and the crack extension of $Ni_{67.2}Al_{32.8}$.

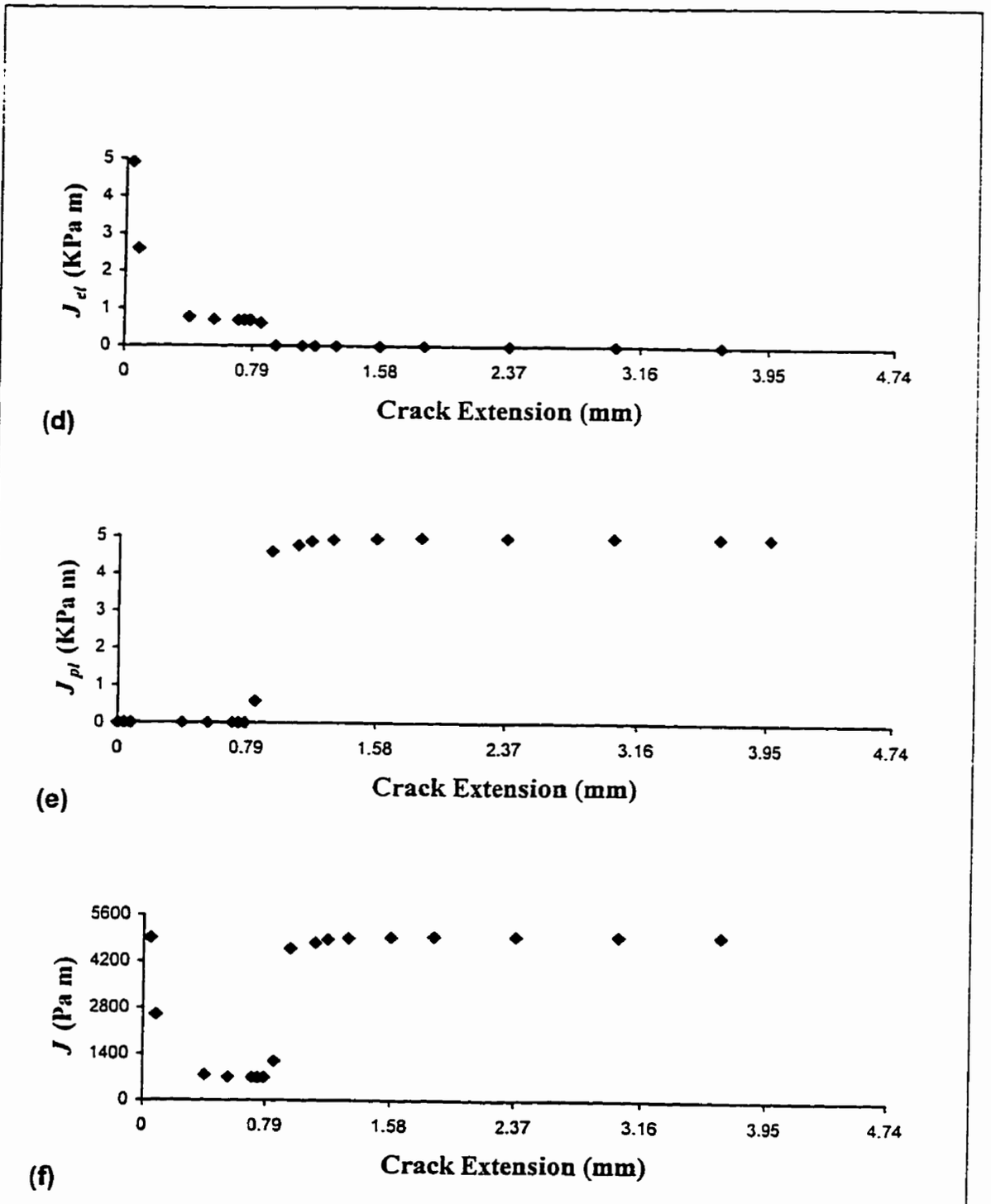

Appendix F1 A typical relationship between the parameters (d) J_{el}, (e) J_{pl} and (f) J, and the crack extension of $Ni_{67.2}Al_{32.8}$.

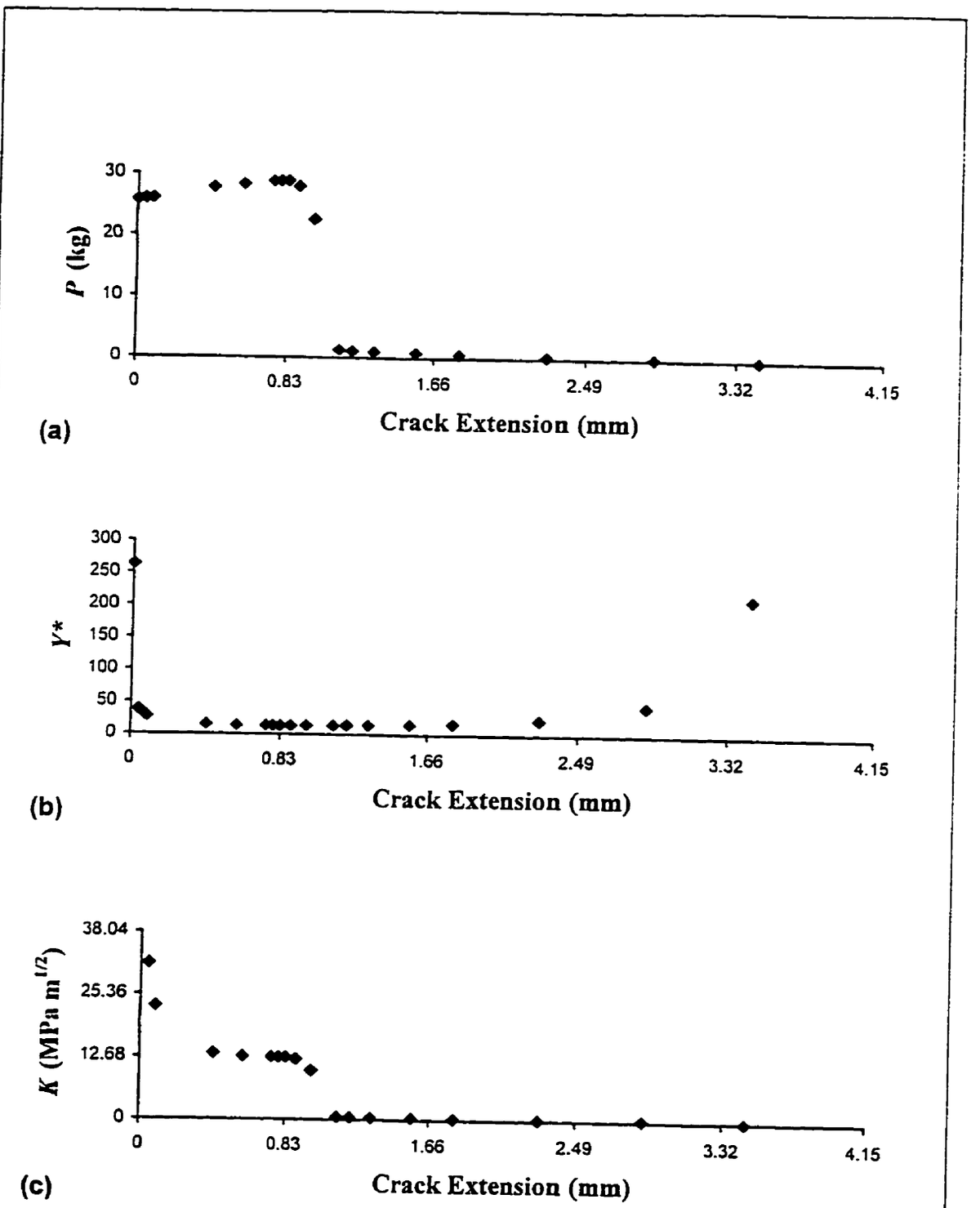

Appendix F2 A typical relationship between the parameters (a) P_{max}, (b) Y^* and (c) K, and the crack extension of $Ni_{65.9}Al_{34.1}$.

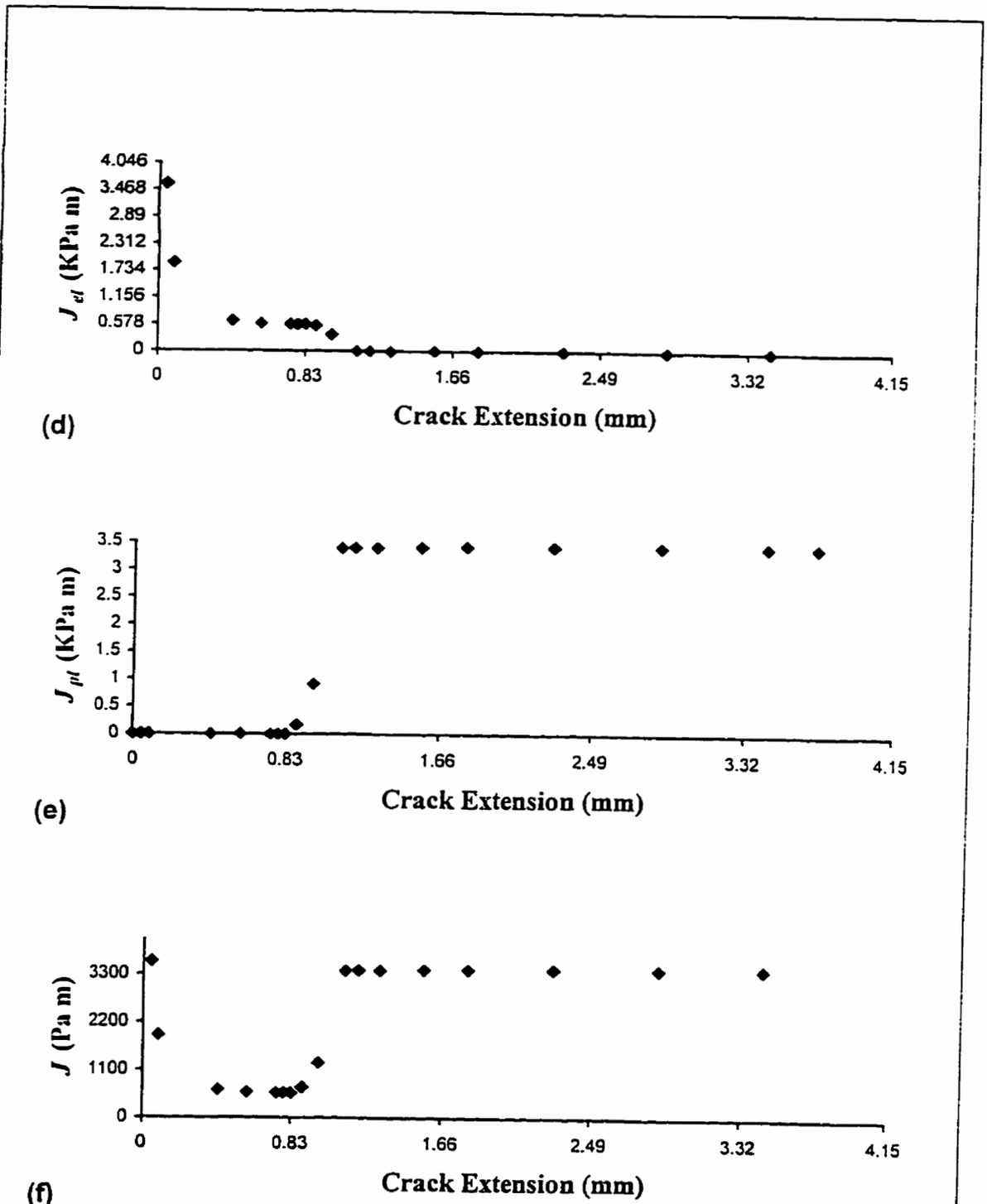

Appendix F2 A typical relationship between the parameters (d) J_{el},(e) J_{pl} and (f) J, and the crack extension of $Ni_{65.9}Al_{34.1}$.

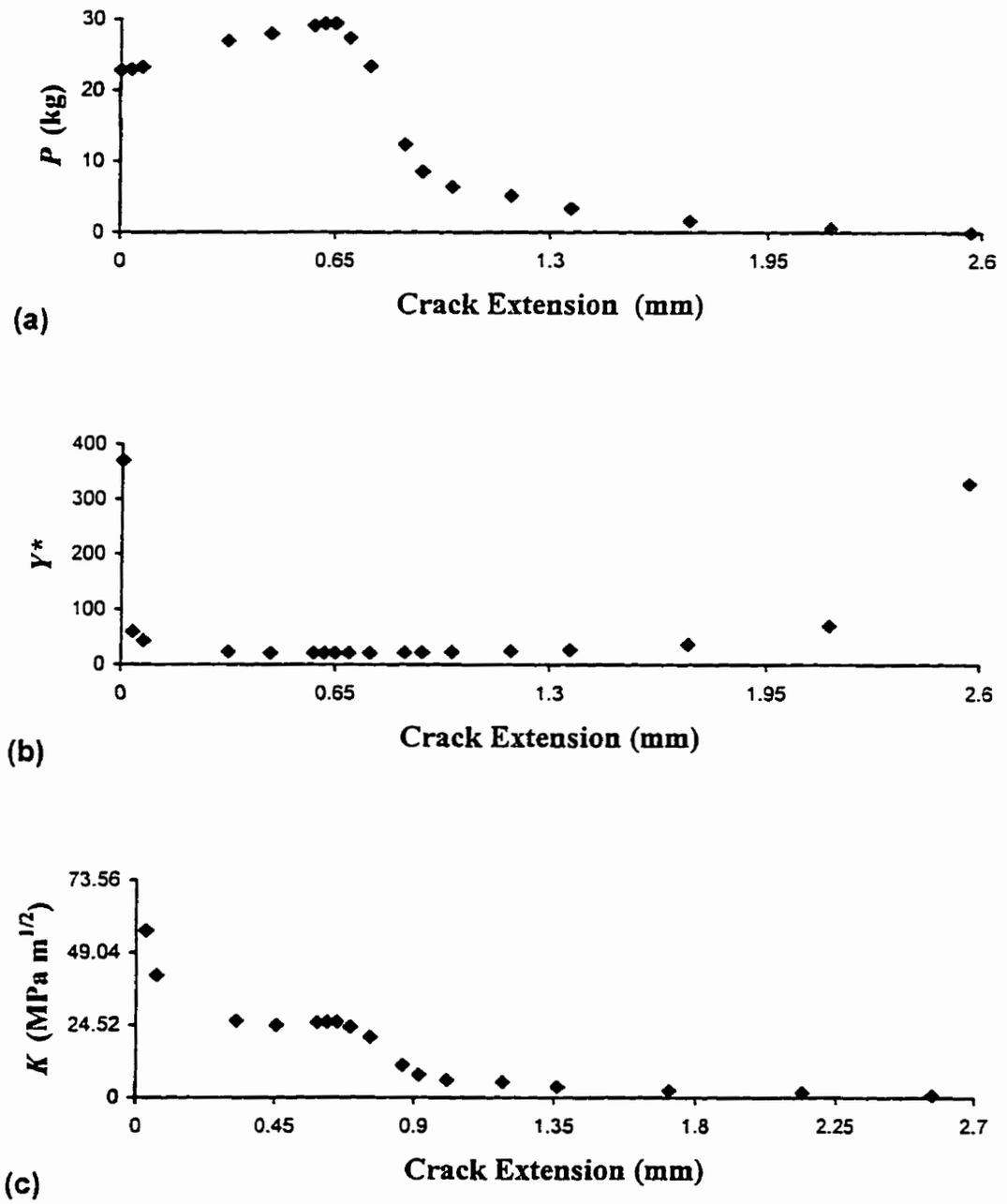

Appendix F3 A typical relationship between the parameters (a) P_{max}, (b) Y^* and (c) K, and the crack extension of $Ni_{70.8}Al_{29.2}$.

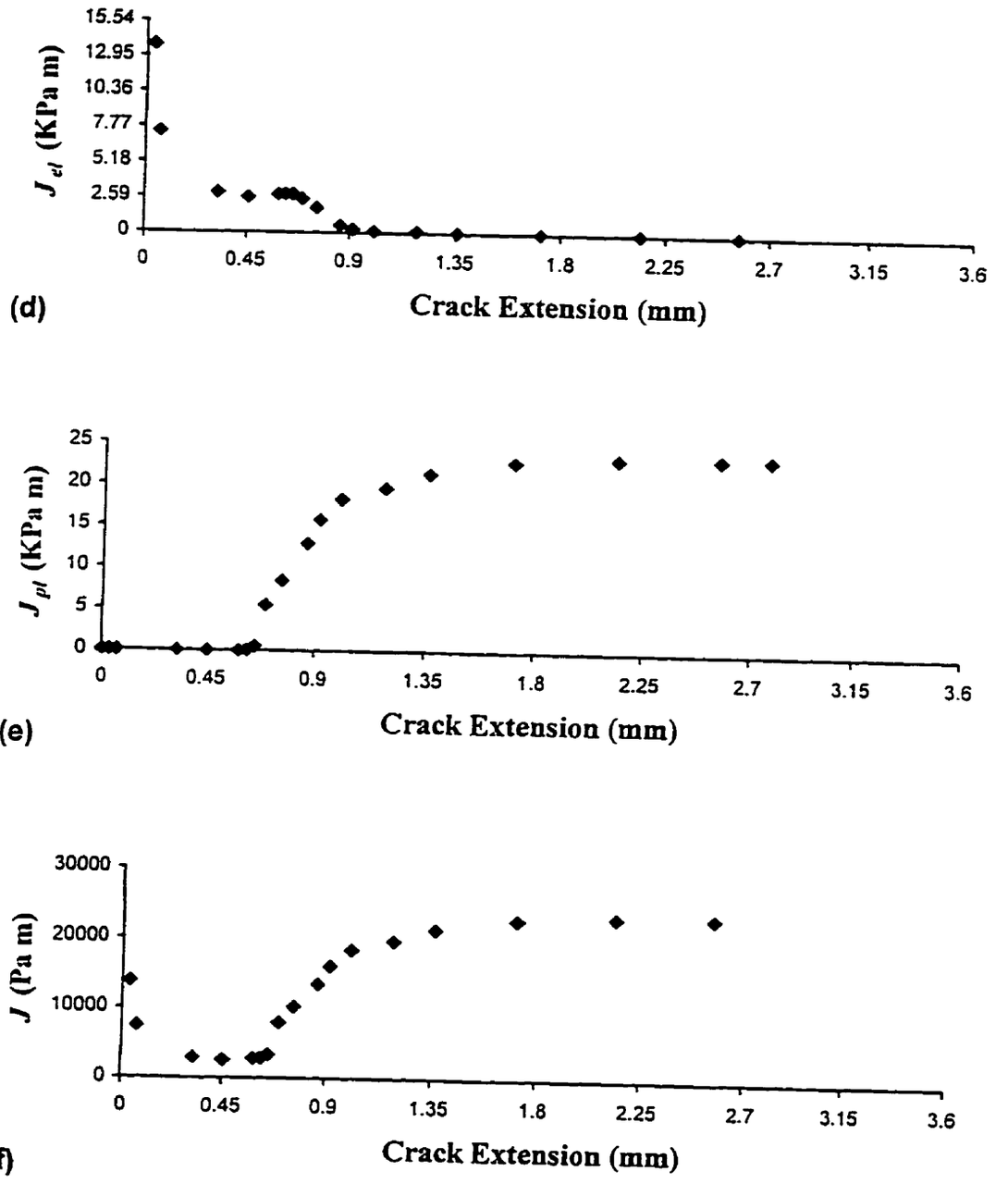

Appendix F3 A typical relationship between the parameters (d) J_{el},(e) J_{pl} and (f) J, and the crack extension of $Ni_{70.8}Al_{29.2}$.

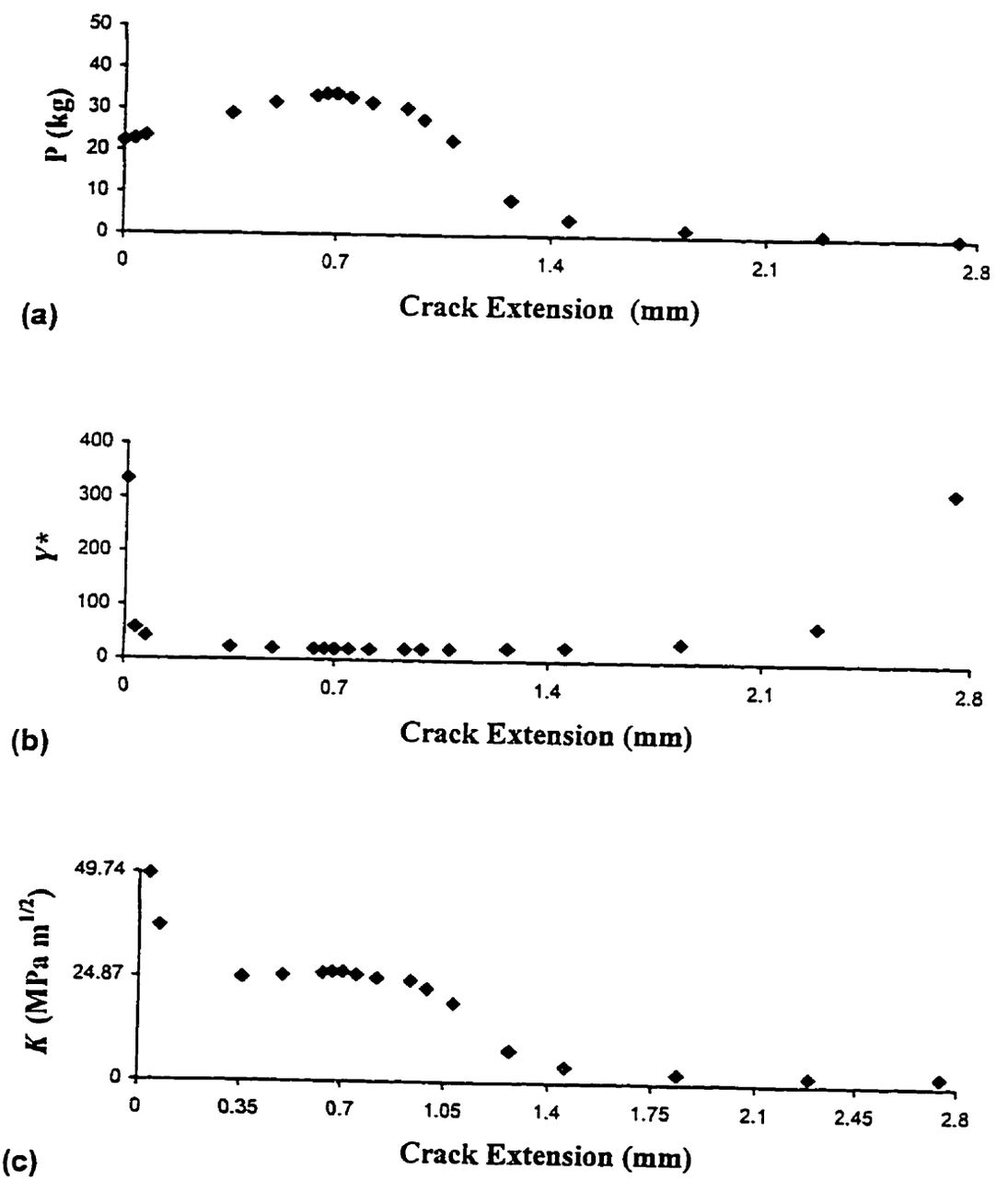

Appendix F4 A typical relationship between the parameters (a) P_{max}, (b) Y^* and (c) K, and the crack extension of $Ni_{72.8}Al_{27.2}$.

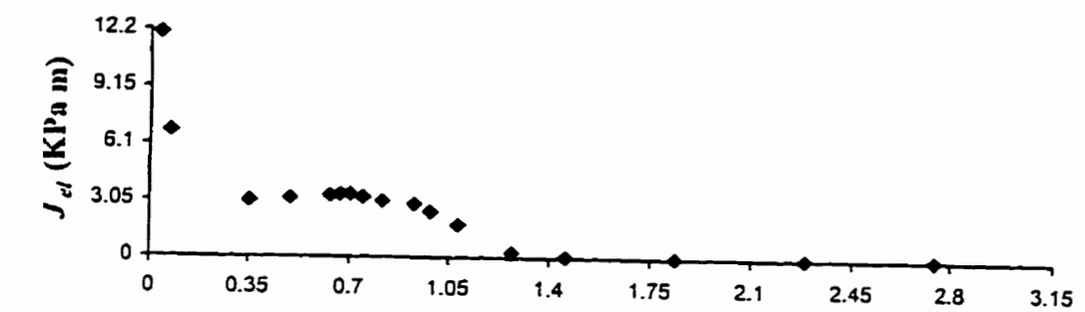

(d)

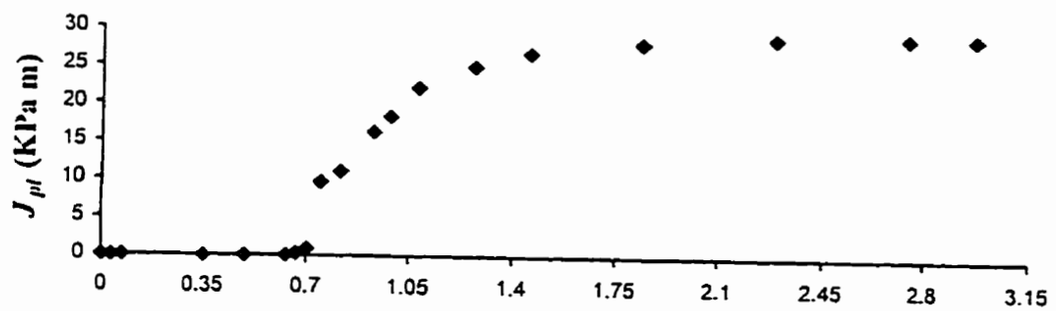

(e)

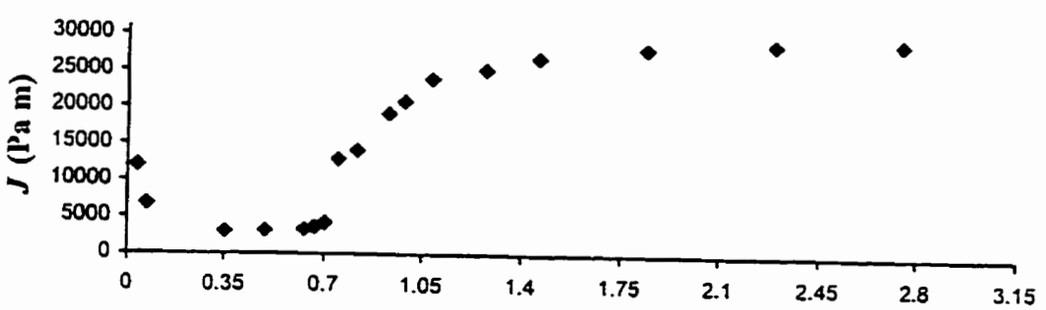

(f)

Appendix F4 A typical relationship between the parameters (d) J_{el},(e) J_{pl} and (f) J. and the crack extension of $Ni_{72.8}Al_{27.2}$.

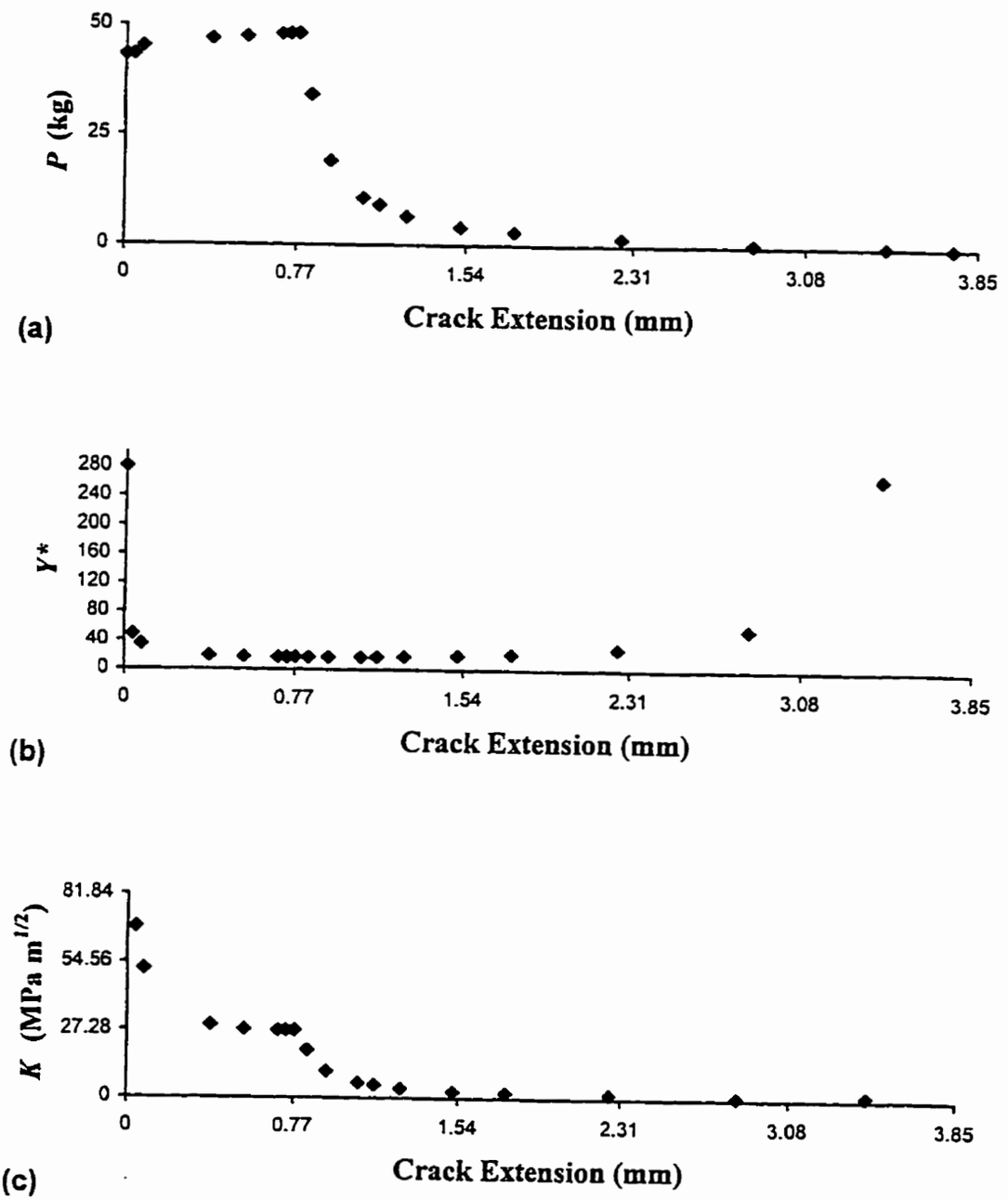

Appendix F5 A typical relationship between the parameters (a) P_{max}, (b) Y^* and (c) K, and the crack extension of $Ni_{73.2}Al_{26.8}$.

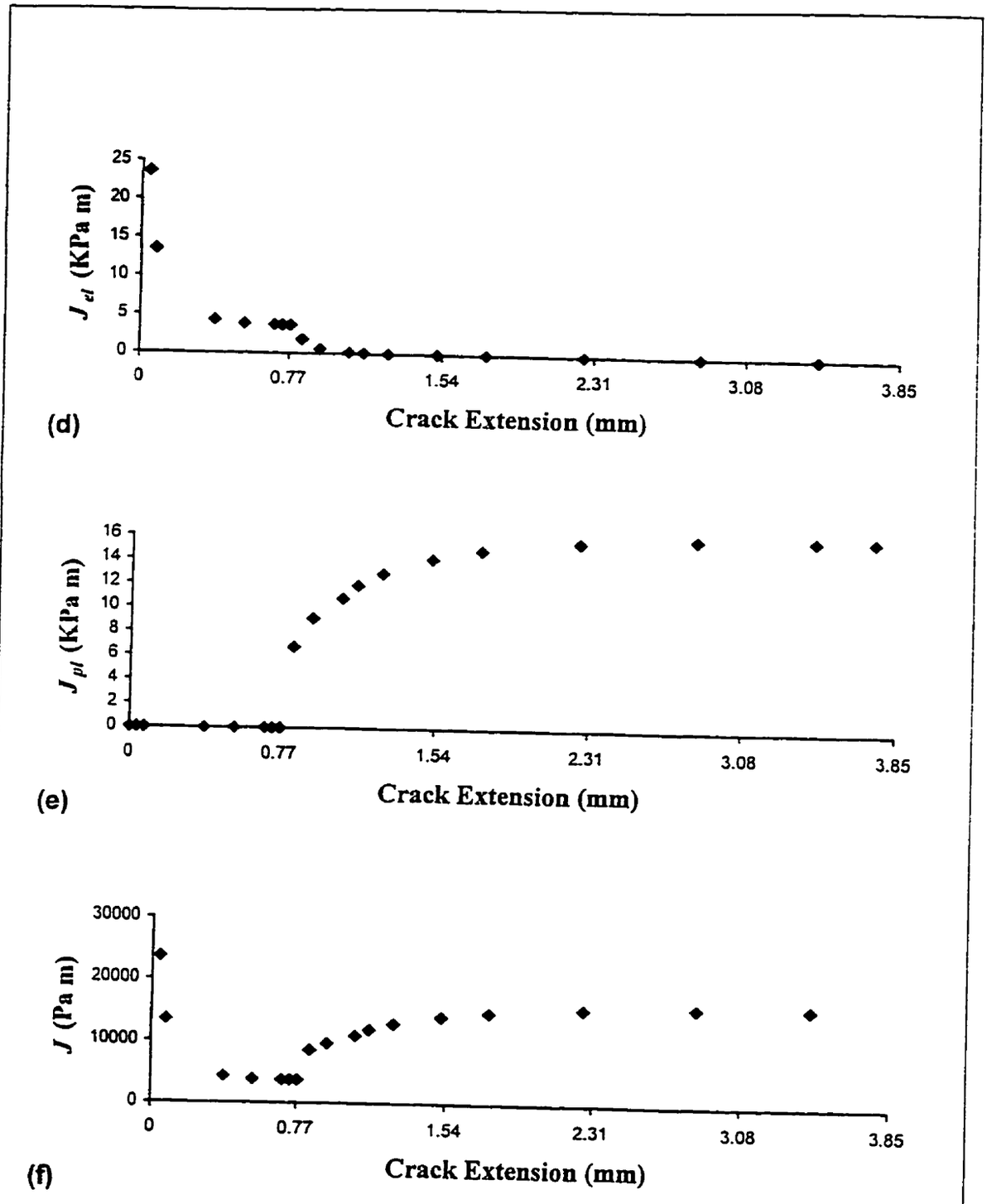

Appendix F5 A typical relationship between the parameters (d) J_{el},(e) J_{pl} and (f) J, and the crack extension of $Ni_{73.2}Al_{26.8}$.

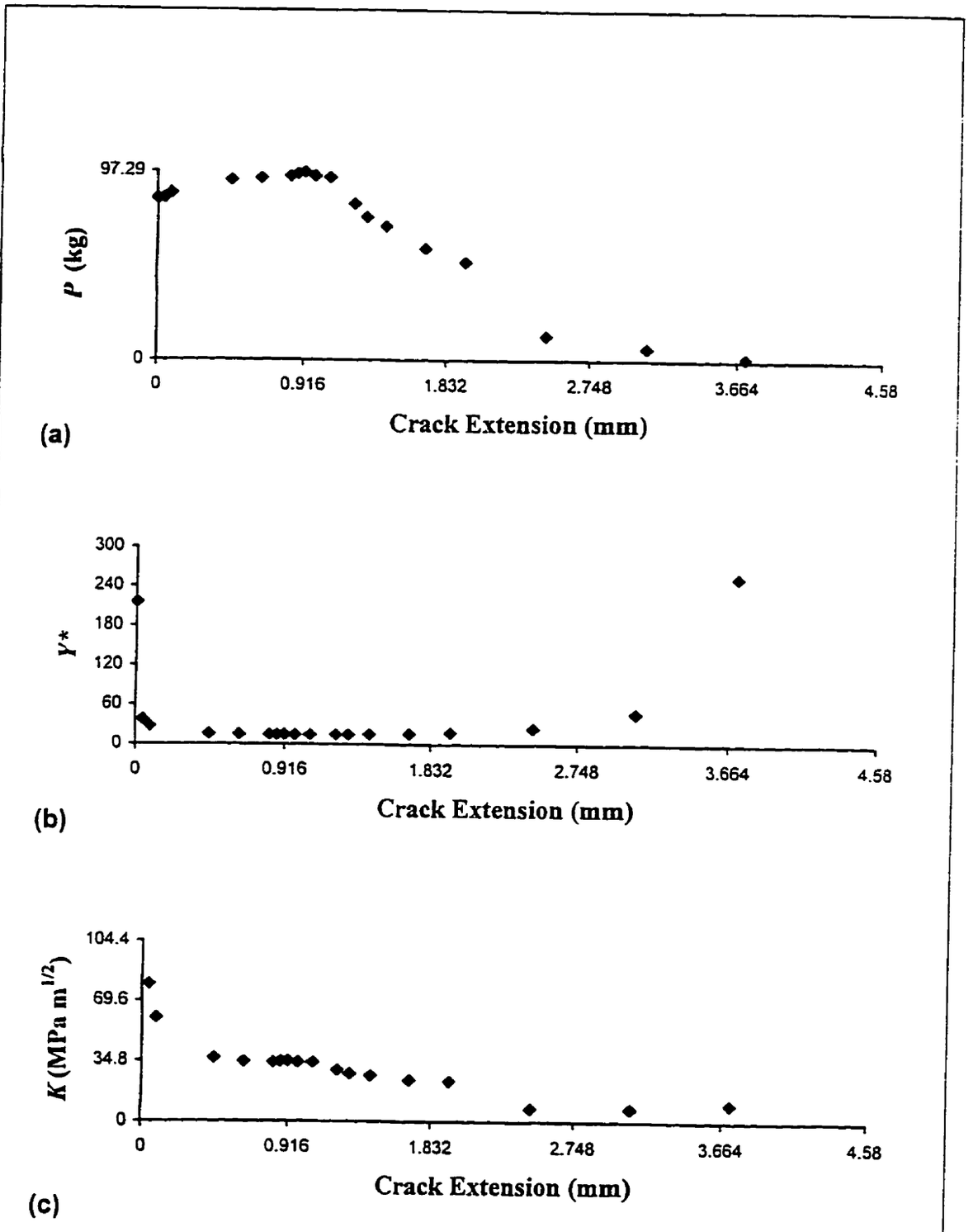

Appendix F6 A typical relationship between the parameters (a) P_{max}, (b) Y^* and (c) K, and the crack extension of $Ni_{77.7}Al_{22.3}$.

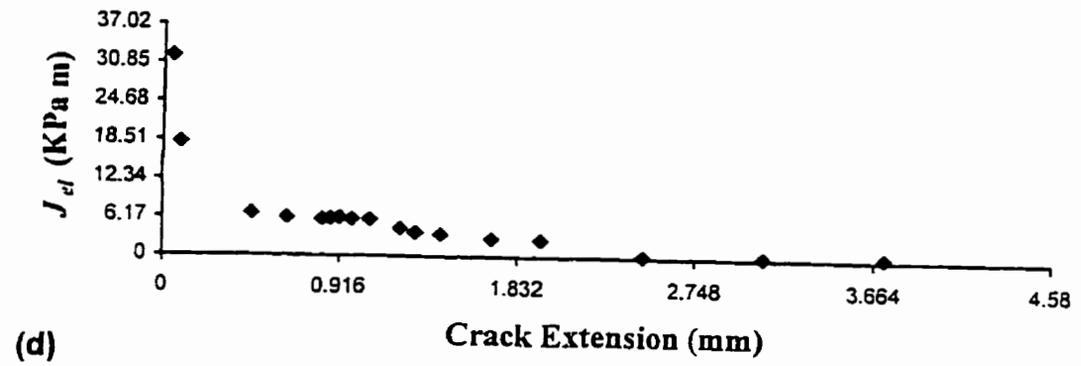

(d)

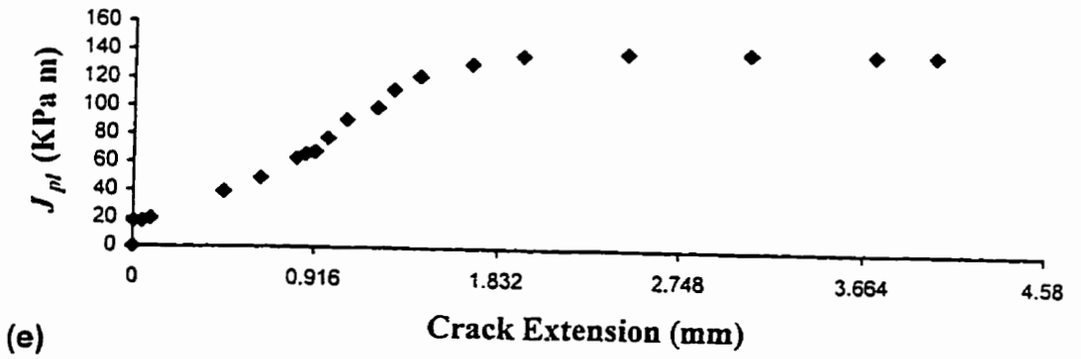

(e)

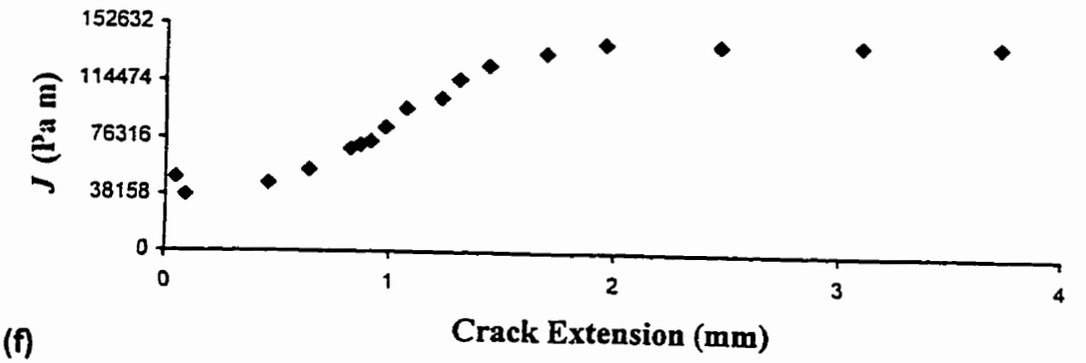

(f)

Appendix F6 A typical relationship between the parameters (d) J_{el},(e) J_{pl} and (f) J. and the crack extension of $Ni_{77.7}Al_{22.3}$.

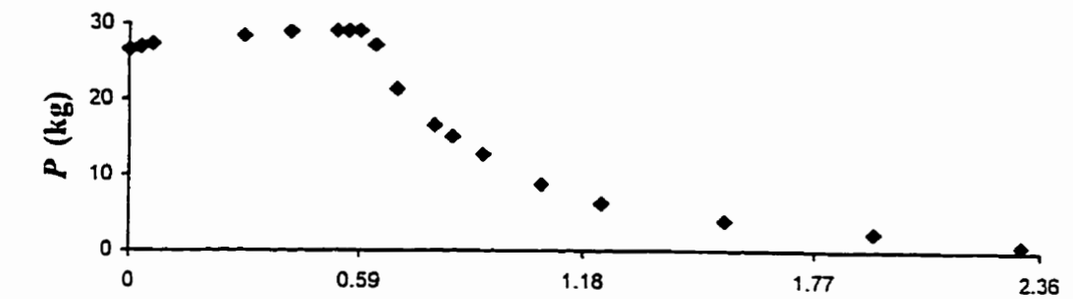

(a)

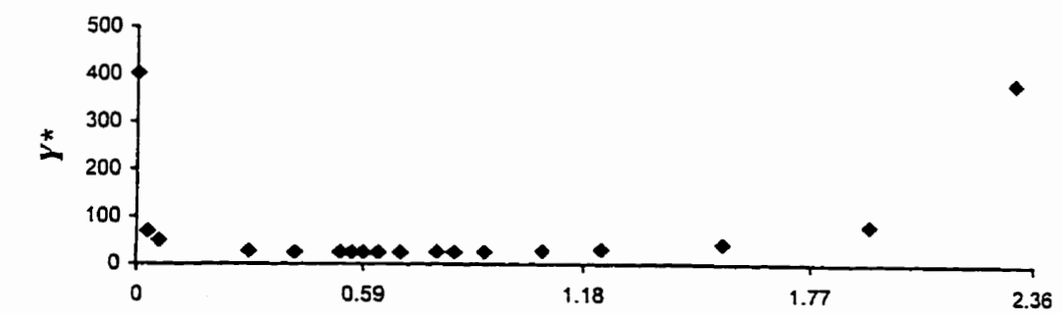

(b)

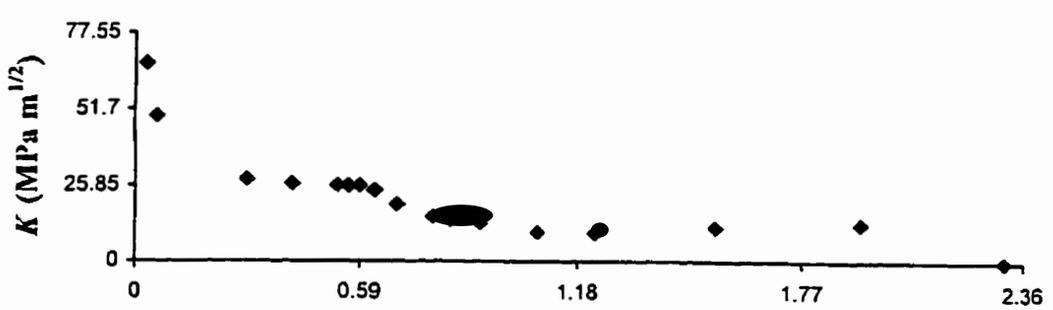

(c)

Appendix F7 A typical relationship between the parameters (a) P_{max}, (b) Y^* and (c) K, and the crack extension of $Ni_{73.2}Al_{26.6}B_{0.2}$.

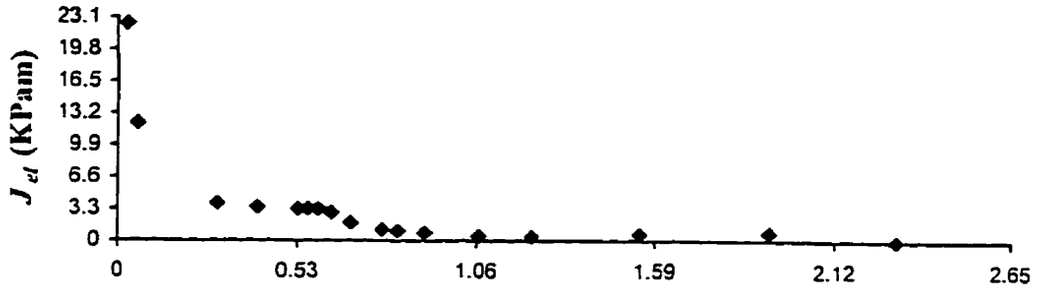

(d)

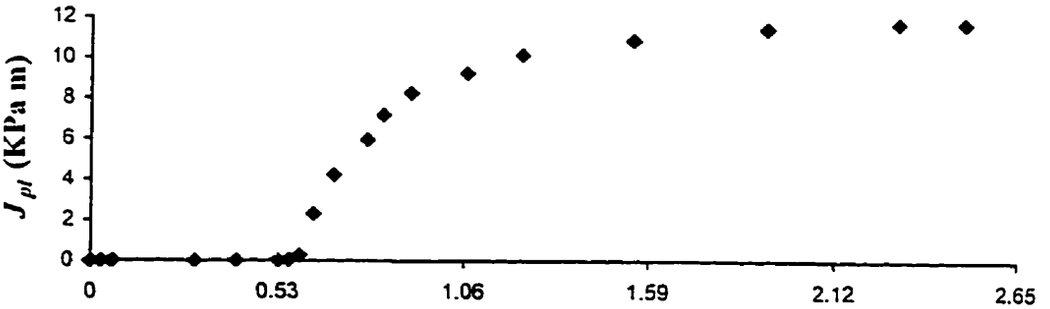

(e)

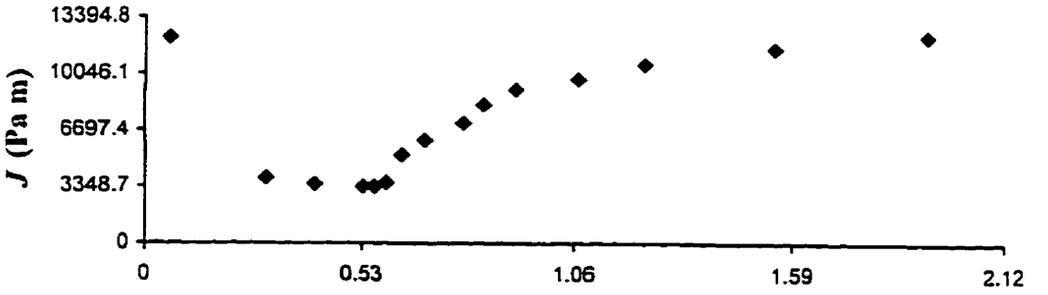

(f)

Appendix F7 A typical relationship between the parameters (d) J_{el},(e) J_{pl} and (f) J, and the crack extension of $Ni_{73.2}Al_{26.6}B_{0.2}$.

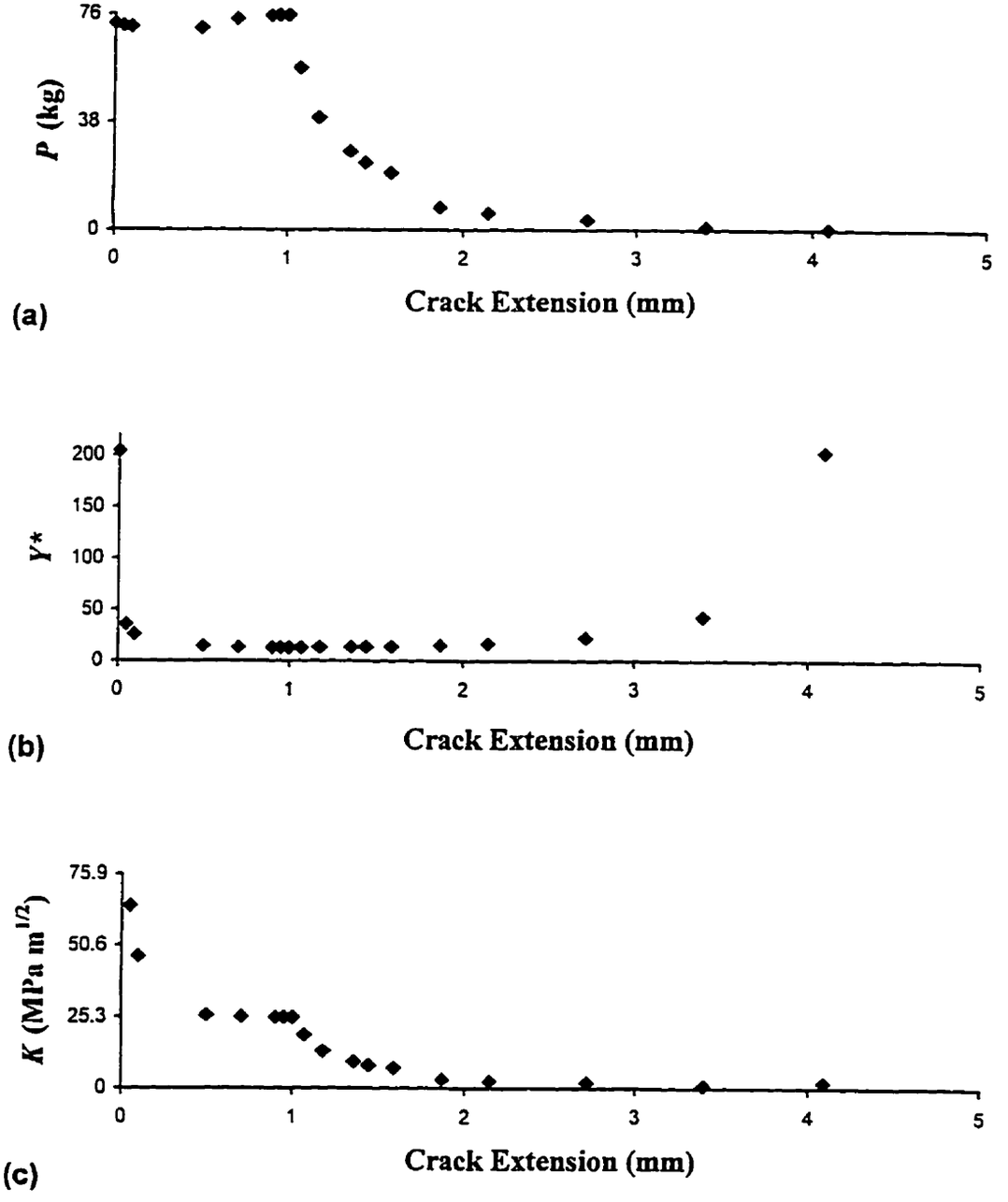

Appendix F8 A typical relationship between the parameters (a) P_{max}, (b) Y^* and (c) K, and the crack extension of $Ni_{74.8}Al_{24.8}B_{0.4}$.

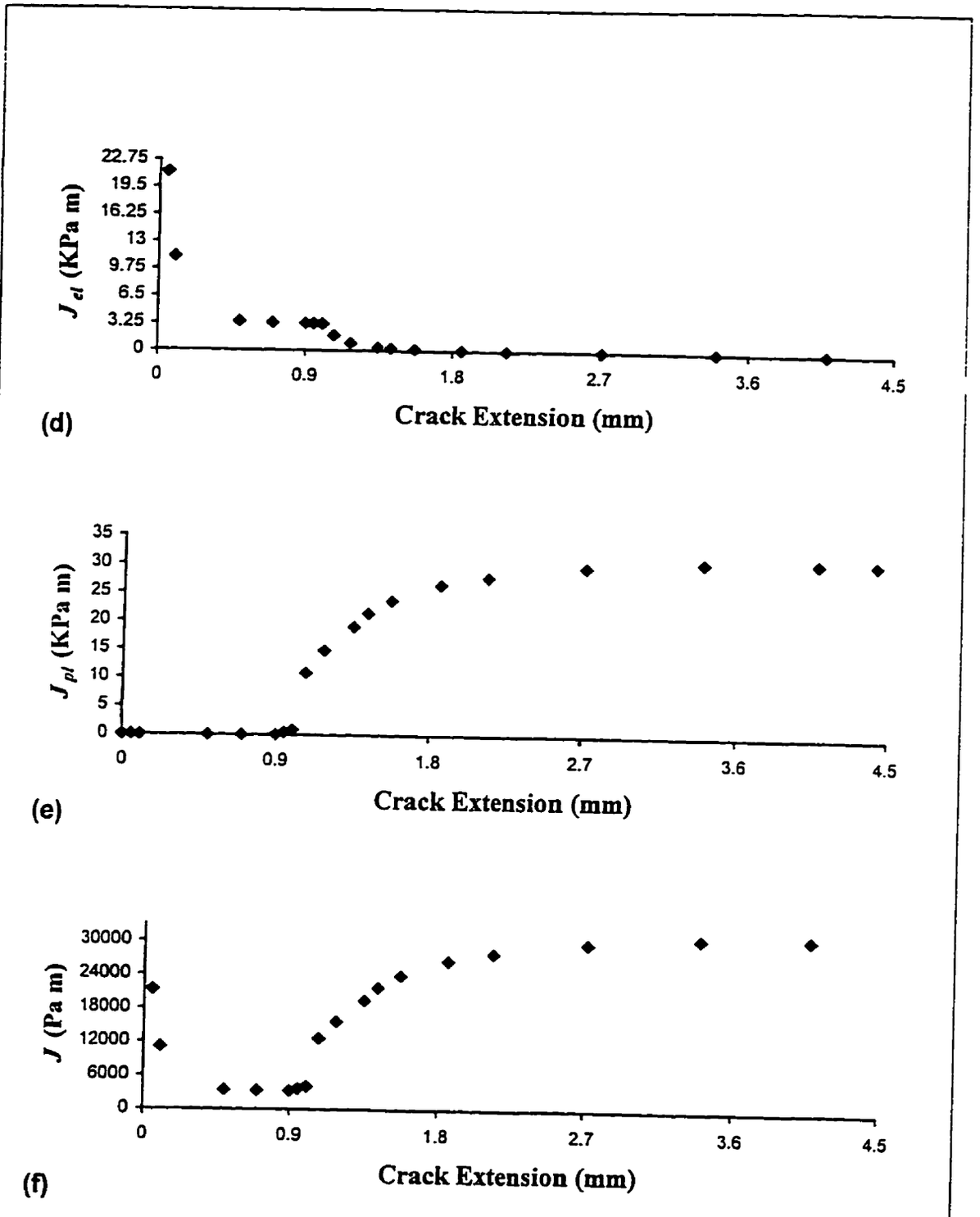

Appendix F8 A typical relationship between the parameters (d) J_{el},(e) J_{pl} and (f) J, and the crack extension of $Ni_{74.8}Al_{24.8}B_{0.4}$.

APPENDIX G
THE CALCULATED J_{Ivc} AND $K_{Ivc,}$ AND CORRESPONDING PARAMETERS FOR EACH *CNB* BEND SPECIMEN

Appendix G
The Calculated J_{Ivc} and K_{Ivc}, and Corresponding Parameters for Each *CNB* Bend Specimen.

Ni	Ni_3Al	J_{Ivc}	K_{Ivc}	*Jel*	*Jpl*	Δa_c	Pc	Y^*_c	LLD_c
at.%	vol.%	J/m^2	$MPam^{1/2}$	J/m^2	J/m^2	mm	kg		*mm*
63.7	17.16	227.41	8.13	227.23	0.18	Δa_m	P_{max}	Y^*_m	LLD_m
63.7	17.27	230.9	8.2	230.53	0.37	Δa_m	P_{max}	Y^*_m	LLD_m
63.7	16.48	231.27	8.2	230.9	0.53	Δa_m	P_{max}	Y^*_m	LLD_m
63.7	16.48	266.89	8.83	266.44	0.45	Δa_m	P_{max}	Y^*_m	LLD_m
65.9	24.7	577.61	12.69	576.23	1.38	Δa_m	P_{max}	Y^*_m	LLD_m
65.9	22.6	785.91	14.89	783.46	2.45	Δa_m	P_{max}	Y^*_m	LLD_m
65.9	20.3	460.32	11.47	460.01	0.31	Δa_m	P_{max}	Y^*_m	LLD_m
67.2	34.09	864.87	15.14	864.55	0.32	Δa_m	P_{max}	Y^*_m	LLD_m
67.2	39.43	995.85	16.02	995.03	0.55	Δa_m	P_{max}	Y^*_m	LLD_m
67.2	32.33	688.86	13.57	688.24	0.62	Δa_m	P_{max}	Y^*_m	LLD_m
67.2	32.1	817.82	14.8	817.39	0.43	Δa_m	P_{max}	Y^*_m	LLD_m
70.8	57.44	2382.2	23.71	2381.5	0.65	Δa_m	P_{max}	Y^*_m	LLD_m
70.8	65.48	2397.6	23.34	2397	0.57	Δa_m	P_{max}	Y^*_m	LLD_m
70.8	61.36	2593.8	24.52	2593.1	0.72	0.45	28	21.35	0.14
72.8	79.03	3765.4	27.69	3765.1	0.35	Δa_m	P_{max}	Y^*_m	LLD_m
72.8	78.18	3048.1	24.87	3047.1	1.03	0.35	29	22.91	0.135
72.8	76.08	2949.4	24.4	2949.2	0.17	Δa_m	P_{max}	Y^*_m	LLD_m
73.2	95.74	3720.3	27.28	3719.7	0.57	Δa_m	P_{max}	Y^*_m	LLD_m
73.2	95.82	3548.8	26.86	3548.2	0.54	Δa_m	P_{max}	Y^*_m	LLD_m
73.2	96.65	4257.3	29.13	4257	0.28	Δa_m	P_{max}	Y^*_m	LLD_m
77.7	100	40504	89.26	19342	21180	0.07	86.02	40.13	0.57
77.7	99.8	32614	80.41	15948	16666	0.06	42.56	44.29	0.24
77.7	100	38158	86.64	18196	19962	0.09	86.4	27.6	0.48
73.2-0.2B	93.6	3348.7	25.99	3327.1	21.61	0.53	29.08	24.87	0.12
73.2-0.2B	94.6	2071	20.04	2070.4	0.68	Δa_m	P_{max}	Y^*_m	LLD_m
74.8-0.4B	99.8	3071.6	24.59	3071.2	0.37	Δa_m	P_{max}	Y^*_m	LLD_m
74.8-0.4B	99.9	3315	25.54	3251.9	63.11	0.9	75.6	13.64	0.21
74.8-0.4B	99.9	2623.2	22.72	2623	0.21	Δa_m	P_{max}	Y^*_m	LLD_m
74.8-0.4B	99.9	3240	25.25	3239.6	0.41	Δa_m	P_{max}	Y^*_m	LLD_m

Note: The values of P_c, Y^*_c and LLD_c are the load, stress-intensity-factor coefficient and load-line-displacement corresponding to J_{Ivc}, respectively.